INFORMATION TO USERS

This manuscript has been reproduced from the microfilm master. UMI films the text directly from the original or copy submitted. Thus, some thesis and dissertation copies are in typewriter face, while others may be from any type of computer printer.

The quality of this reproduction is dependent upon the quality of the copy submitted. Broken or indistinct print, colored or poor quality illustrations and photographs, print bleedthrough, substandard margins, and improper alignment can adversely affect reproduction.

In the unlikely event that the author did not send UMI a complete manuscript and there are missing pages, these will be noted. Also, if unauthorized copyright material had to be removed, a note will indicate the deletion.

Oversize materials (e.g., maps, drawings, charts) are reproduced by sectioning the original, beginning at the upper left-hand corner and continuing from left to right in equal sections with small overlaps. Each original is also photographed in one exposure and is included in reduced form at the back of the book.

Photographs included in the original manuscript have been reproduced xerographically in this copy. Higher quality 6" x 9" black and white photographic prints are available for any photographs or illustrations appearing in this copy for an additional charge. Contact UMI directly to order.

UMI

University Microfilms International
A Bell & Howell Information Company
300 North Zeeb Road, Ann Arbor, MI 48106-1346 USA
313/761-4700 800/521-0600

Order Number 9205863

A search for very high energy gamma ray emission from Hercules X-1

Kelley, Linda Ann, Ph.D.

University of Hawaii, 1991

U·M·I
300 N. Zeeb Rd.
Ann Arbor, MI 48106

A Search for
Very High Energy Gamma Ray Emission
from Hercules X-1

A dissertation submitted to the graduate division of the University of Hawaii in
partial fulfillment of the requirements for the degree of
Doctor of Philosophy
in
Physics
August 1991

by
Linda Ann Kelley

Dissertation Committee:
John G. Learned, Chairperson
Frederick Harris
Charles Hayes
Sandip Pakvasa
Brent Tully

Acknowledgments

I owe a great dept of gratitude to many people who have contributed both to the completion of this thesis and to making it possible in the first place. Certainly, my advisor and good friend John Learned has been vital in helping me achieve this goal. I would like to thank him for his many useful suggestions and comments. John is a very good person and an excellent, creative physicist.

Many people here in Hawaii have helped me along the way. Andy Acker, Daniela Paluselli, Dan O'Connor, Steve Dye, John Babson, John Clem, Shige Matsuno, Will Wilson, and Dan Weeks should all be thanked for their efforts and friendship. I especially want to thank Gus Sinnis and Jake Hudson for their assistance and many interesting conversations (especially at 3 am on shift), but I refuse to thank Jake for his puns! Sandip Pakvasa, Brent Tully, Chuck Hayes, Fred Harris, and Xerxes Tata should be thanked for their many insightful comments. Thanks also to the High Energy Physics Group at the University of Hawaii, especially our secretaries. Without them, none of us would get anything done.

Many people involved in the construction and operation of the Haleakala Gamma-ray Telescope should also be thanked. Those include: Bob Morse, Leo Resvanis, Bob March, Ugo Camerini, Jack Fry, Jim Gaidos, Glenn Sembroski, Chuck Wilson, Matty Jaworski, Mike Frankowski, Andy Szentgyorgi, Pat Slane, Almus Kenter, John Jennings, John Finley, Robert Austin, Mary Kertzman, Mark Skinner, and many others. Matty, thanks also for the daffodils.

I am very thankful to my parents and my brothers who have always encouraged me to pursue my interests, no matter how odd those interests might seem. Finally, my husband, Ralph, deserves much praise, both for putting up with me, and especially for his contributions and his many intelligent, "stupid questions". I am truly fortunate to have him as a friend.

Abstract

Data from the Haleakala Gamma-ray Observatory taken during 1987 and 1989 is searched for the presence of TeV Gamma-rays from the direction of Hercules X-1. These two data sets were compiled on two different instruments: the first in operation from 1985 through the end of 1987 and the second, upgraded instrument in operation from early 1989 to the present. After the initial data selection and calibration, the two data segments were analyzed for periodicity near the interpolated pulse period, a counting rate (or DC) excess during short intervals, and an integrated DC excess over longer periods of time.

The 1987 data set revealed one interval of significant periodicity. The detected period, 1.23578 ±0.00020 s, is not in agreement with the expected X-ray pulse period, but it is in agreement with periodicity observed from Her X-1 by several groups during 1986 in the TeV – PeV energy range. No significant rate excess was observed during this interval. A integrated DC excess calculation was not possible on these data because of the mode in which the data were taken.

The 1989 data set contained no periodicity; however, an integrated excess corresponding to two of the three high on X-ray intervals during which data was taken was observed. The overall flux observed during this year was $(5.9 \pm 2.6) \times 10^{-11}$ cm^{-2}s^{-1} above 0.15 TeV. No significant short (15 minute) bursts of VHE gamma-rays were detected in this data set.

Contents

Acknowledgments iii

Abstract v

List of Tables x

List of Figures xi

1 Introduction and Motivation 1

1.1 VHE Gamma-ray Astronomy 3

1.2 X-rays and Lower Energy Gamma-rays 4

1.2.1 Gamma-ray Production at Lower Energies 7

1.3 VHE Gamma-ray Emission 10

1.3.1 Neutron Stars and X-ray Binary Stars 10

1.3.2 Accretion in a Disk-fed System 13

1.3.3 Gamma-ray Emission at Higher Energy 21

1.4 Cascades in the Atmosphere 25

1.4.1 Čerenkov Radiation 26

1.4.2 Cosmic Ray Initiated Showers 28

1.4.3 Gamma-ray Initiated Showers 30

1.4.4 Electromagnetic Cascades 31

- 1.5 Monte-Carlo Studies 33
  - 1.5.1 Characteristics of Proton and Gamma-ray Initiated Showers 34
  - 1.5.2 Cosmic Ray Rejection Based on Aperture Cuts 38

2 The Binary Pulsar Hercules X-1 57
- 2.1 Optical Observations 57
- 2.2 X-ray Observations 59
- 2.3 VHE Observations 66

3 The Old and New HGRO Telescopes 74
- 3.1 The Old Telescope 75
- 3.2 The Retrofit Telescope 77
  - 3.2.1 Changes on the telescope mount 78
  - 3.2.2 Electronics 81
  - 3.2.3 Data Acquisition 84
  - 3.2.4 System Performance 85
- 3.3 Pulse Shape Analysis with a Waveform Digitizer 90
  - 3.3.1 Analysis of the Waveform Data Set 92
  - 3.3.2 Conclusions from the Waveform Analysis 102
- 3.4 The Air Shower Array 103

4 Data Preparation, Calibration, and Analysis 107
- 4.1 Preliminary Data Preparation 107
- 4.2 Pulse Height and Timing Calibration 111

4.2.1 ADC Calibrations 113

4.2.2 TDC Calibrations 114

4.3 Barycentering 117

4.4 Periodicity Analysis 122

4.4.1 The Rayleigh Test 123

4.4.2 The H_m Test 125

4.4.3 Estimation of the Signal Strength 127

4.5 DC Analysis 130

4.5.1 The Gini-test 130

4.5.2 The Cosmic Ray Rate as a Function of Zenith Angle 132

4.5.3 Errors in the Rate Excess Calculations 138

5 Time Series and DC Analysis of the Haleakala Data 140

5.1 1987 Data 144

5.1.1 Preparation of the 1987 Her X-1 Data 145

5.1.2 Periodicity Analysis 149

5.1.3 DC Analysis 156

5.1.4 A Look at the Barrels During 1987 168

5.2 The 1989 Data 174

5.2.1 Preparation of the 1989 data 174

5.2.2 DC Analysis 181

5.2.3 Periodicity Analysis 190

5.3 Summary and Conclusions 195

A Calibration for the Waveform Tests 201

B Phase Linking of the 1986 Anomalous Period Data 204

C Summary of Periodicity and Rate Excess Consistency for Haleakala and Whipple data, 1984 - 1986 207

Bibliography 210

List of Tables

1.1 Signal to background rejection compared to a 0.35° aperture. 56

2.1 Source parameters 64

2.2 VHE detections of Her X-1 67

3.1 Waveform shape statistics 96

3.2 Total excess from Figure 3.10. 98

3.3 Spatial coordinates of the individual particle counters 105

5.1 Zenith angle fit parameters for 1987. 148

5.2 Combined probabilities for run 1162. 164

5.3 Zenith angle fit parameters for 1989 180

5.4 Integrated number excess for each 35 day phase. 186

A.1 A Aperture timing calibration 203

C.1 Summary of Whipple and Haleakala results. 209

List of Figures

1.1 A map of binary X-ray pulsars. 6

1.2 Differential γ-ray spectrum from the Crab. 12

1.3 Neutron star model. 13

1.4 Sample field lines in the Standard Model. 19

1.5 Proton acceleration and VHE γ production. 24

1.6 The geometry of a Čerenkov photon. 27

1.7 The development of a γ initiated cascade. 32

1.8 The photon distribution from 0.75 TeV γ shower at Haleakala altitude. 35

1.9 The photon distribution from 2 TeV proton shower at Haleakala altitude. 36

1.10 The photon density of a 0.75 TeV γ shower and a 2 TeV proton shower as a function of radius. 37

1.11 A diagram of the aperture position in front of the PMT. 39

1.12 The photon density of a 0.75 TeV γ shower and a 2 TeV proton shower for 0.35° aperture. 40

1.13 The arrival time of photons from a 0.75 TeV γ shower and a 2 TeV proton shower with a 0.35° aperture. 41

1.14 The trigger distribution for a 0.75 TeV and 2 TeV shower. 43

1.15 Effective area for proton showers. 44

1.16 The Area as a function of angle off-axis for $\theta_{ap} = 0.35°$ and $\theta_{ap} = 0.5°$ 45

1.17 The proton rate as a function of energy for a 0.35° aperture. 47

1.18 The effective area for γ showers as a function of energy. 48

1.19 The relative rate for gamma showers as a function of energy for a 0.35° aperture. 48

1.20 The photon density of a 0.75 TeV γ shower and a 2 TeV proton shower for an annular aperture. 50

1.21 The arrival times of photons for a 0.75 TeV γ shower and a 2 TeV proton shower for an annular aperture. 51

1.22 The trigger distribution for a 0.75 TeV γ shower and a 2 TeV proton shower. 52

1.23 The arrival times of photons near a radius of 90 m for a 0.75 TeV γ shower and a 2 TeV proton shower for an annular aperture. 53

1.24 The effective area for on-axis and off-axis proton showers. 54

2.1 The orbital inclination angle (ABC) for a binary orbit. 59

2.2 Her X-1's 35 day variation from Uhuru and EXOSAT X-ray data. . 61

2.3 The pulse period of Her X-1 as a function of observation date. . . . 63

2.4 The differential flux measured as a function of energy. 69

3.1 A diagram of the old telescope aperture separation. 76

3.2 The placement of the 26 mirrors on the telescope. 79

3.3 A sketch of the main Čerenkov telescope on Haleakala. 80

3.4 An individual mirror and aperture placement. 80

3.5 Total photon acceptance for the two different filter, PMT, and Čerenkov light combinations. 82

3.6 Spectral response of the current PMTs+filters. 82

3.7 Mirror alignment for the A aperture, A – Z mirrors. 86

3.8 Rate as a function of declination for apertures AA and AK. 87

3.9 Rate as a function of multiplicity. 90

3.10 Fraction of out of time pulses for runs 1686, 1687, and 1688. 95

3.11 On source events after cuts. The dashed histogram is the estimated background. The dotted lines separate wobbles. 97

3.12 Number of pulses observed versus pulse width (in ns) for runs 1686, 1687, and 1688. 99

3.13 Three sample waveforms: A typical narrow pulse (A), a clipped pulse with overshoot (B), and a multiple pulse (C). 100

3.14 Layout of the barrel air shower array. The Čerenkov telescope is at the center of the diagram. 104

4.1 The word count (on a log scale) for a typical event. 109

4.2 An example of weather contaminated data. 110

4.3 The change in scaler rates, raw event rates, and cut event rates with the rise of the moon. 112

4.4 The pedistal, one PE, and total ADC distributions for a typical channel (AC). 115

4.5 Pulse height slewing in the new telescope. 116

4.6 Calibration corrections and 1 σ errors for July '89. 118

4.7 A definition of the distance to shower maximum. 134

5.1 Rate as a function of zenith angle for run 1162, A and B apertures. 142

5.2 Orbital phase and 35-day phase of all 1987 Her X-1 runs. 144

5.3 Orbital phase and 35-day phase coverage of all 1987 Her X-1 runs. . 146

5.4 On and off source Rayleigh distributions for run 1162. 151

5.5 Light curve for the 12th interval of run 1162 at P=1.23578 s. 152

5.6 All reported VHEGR detections of Her X-1 through 1987. 153

5.7 Run 1162, on source light curve for t_o = 6613.17379361 JD. 154

5.8 Rayleigh power as a function of the multiplicity cut. 155

5.9 Rayleigh power spectrum for the on and off source for all '87 data tested. 157

5.10 Distribution of Gini numbers for the 1987 off source data set. 158

5.11 The sigma rate excess for each interval in runs 1162 and 1174. . . . 160

5.12 Rate as a function of time for a portion of run 1162. 161

5.13 Rayleigh distribution for ± 1 IFP around the interpolated X-ray period. 162

5.14 Rayleigh distribution for ± 1 IFP around the detected anomalous period. 163

5.15 The difference between the expected and observed number of events for both a delta-function and sinusoidal light curve. 166

5.16 The distribution of the Rayleigh power and rate excess. 168

5.17 Barrel events for run 1116. 170

5.18 Individual interval excess and integrated number excess for the barrels. 171

5.19 Pulsar, orbital, and 35-day phase plots for all Her X-1 barrel data. . 173

5.20 Orbital phase and 35-day phase coverage of all 1989 Her X-1 runs. . 175

5.21 The distribution of γ, A and B aperture. 177

5.22 Average χ for each zenith angle fit. 178

5.23 χ as a function of zenith angle during one run. 179

5.24 The Gini numbers for all off source Her X-1 data passing zenith angle fit cuts. 182

5.25 Distribution of the number excess for each 900 s interval, expressed in σs. 184

5.26 Number excess as a function of wobble number. 185

5.27 Integrated number excess as a function of wobble number. 187

5.28 Rate as a function of wobble number for the high on, low on, and off 35 day variation phases. 188

5.29 Integrated rate as a function of wobble number for the high on, low on, and off 35 day variation phases. 189

5.30 The number excess as a function of the orbital phase. 191

5.31 The number excess as a function of the 35 day phase. 192

5.32 On and off source H_m distributions. 193

5.33 On and off source H_m distributions for ±1 IFP around the X-ray and the anomalous period. 194

A.1 The difference between standard calibrations and those obtained using the 337 nm laser. 202

B.1 The light curve at P=1.2357701 s for run741, using an ephemeris of $t_0 = 2446613.17379361$ JD. 205

B.2 The light curve at P=1.236 s for run741. 205

Chapter 1

Introduction and Motivation

Very High Energy (VHE) and Ultra High Energy (UHE) gamma-ray astronomy provide an opportunity to observe the highest energy photons currently available for study. VHE range spans $\sim 10^{11}$ to 10^{13} eV while the UHE range can be defined as energies $\geq 10^{14}$ eV. The boundaries between these energy regimes, and that between High Energy (HE) gamma-ray astronomy and VHE are defined primarily by observation technique. The HE energy range (10^{8}–10^{10} eV) is limited to satellite detectors, although balloon-born detectors have been used in this energy range. The upper limit of this range is set by the the decreasing flux of photons at the higher energies combined with the limited observation time and area of satellite and balloon detectors. At $\sim 10^{11}$ eV, ground based telescopes are capable of detecting short flashes of Čerenkov light from photon and cosmic ray induced showers in the atmosphere. This technique defines the VHE energy band. At still higher energies, particles produced in electromagnetic and hadronic cascades may penetrate through the atmosphere to the ground, and be detected by particle detectors, defining the UHE band.

Observations of Cygnus X-3 made by the Fly's Eye group at $E \geq 10^{18}$ eV (Cassiday, 1989) extend the UHE region even further. Such observations of γ's and observations of cosmic-rays of a similar energy (center of mass energies of $>$ 100 TeV) push the UHE particle region higher than energies attainable at the SSC in its current proposed design for p-p collisions with beam energies of $<$ 20 TeV. It is reasonable to assume that any knowledge of particle interactions at these ultra high energies obtained in the next 10–12 years will come from astrophysical particle detectors, such as UHE γ-ray telescopes.

In addition to these direct applications to particle physics from the study of high energy particle production and interaction, the astrophysical interest in these high energy particles is great. Most identified sources of γ's in these energy ranges are neutron stars in a stellar binary system. Other sources include isolated neutron star systems such as the Crab pulsar and nebula. Although much information is available about these systems at lower energies, primarily through radio and X-ray observations, the picture of particle production must be completed at higher energies in order to more fully understand these objects. Investigation of VHE and UHE emission from neutron star systems will help to form a coherent model of particle production near these highly magnetized stars over a wide range of energies.

1.1 VHE Gamma-ray Astronomy

Early experimenters in the field of VHE γ-ray astronomy did not anticipate much of the difficulty that was to be encountered in the observation of these high energy photons. Initially, γ-ray astronomers at the beginning of the 1960′s met only with null results and marginal detections. Although progress has been made in the 30 years since the first air-Čerenkov experiments were constructed, and many results have been reported during those years, the main body of VHE γ-ray detections are sporadic and at a low significance level (3-4 σ). We have yet to identify a "standard candle" γ source in the VHE range (such as the Crab in the HE range) which can be seen constantly with a detectable flux. This simply may be a result of the current sensitivity of our detectors, or it may be the nature of γ emission at these energies. Recently, detections with a high significance (9 σ and above) been reported which appear to be stable over several years of observations.

The slow progress of VHE γ-ray astronomy may be attributed to the difficulty of separating photon-induced showers from the overpowering cosmic-ray background (composed mainly of $\sim$ TeV protons). Certainly, many improvements in the recent generation of air-Čerenkov detectors, such as better timing resolution, faster electronics, and larger collection area, have increased the sensitivity of these instruments as compared to that of the first telescopes constructed in the ′60s; however, the basic observational technique has remained the same for the most part, with a small number of photomultiplier tubes (PMTs) in the focal plane(s) of the telescope. Recent changes to the light collection technique, such as attempts to use an array of PMTs in the focal plane to spatially image the shower over a large angle ($\sim 4^\circ$), have shown promise for separating γ and proton showers.

In this dissertation, I will begin with a brief discussion of both lower energy and early VHE γ-ray astronomy, which is the basis of the current work to be discussed here is. Following this is a discussion of the type of sources observed to be emitting VHE γ-rays, in particular Hercules X-1, and a general discussion of the observation technique. Then, a specific description of the Haleakala Gamma-ray Telescopes (both the telescope in operation from '85 through '88 and the new telescope currently in operation), the data taken on Her X-1 during '87 and '89 with these 2 telescopes and its analysis, and finally the results and conclusions from this analysis are presented.

1.2 X-rays and Lower Energy Gamma-rays

The brightest X-ray source in our sky, Sco X-1, was the first such source to be observed. It was detected in X-rays on a rocket flight using a Geiger counter as the detector (Giacconi, *et al.* 1962). Since the duration of this first flight was very short (less than 6 minutes above a height of 80km), only a hint of other possible X-ray sources was seen. It was not until the Uhuru satellite was launched in 1970 that X-ray sources were firmly established with high statistics not possible from balloon flights. It is worth noting that, although VHE γ-ray candidate sources are generally drawn from X-ray and lower energy γ-ray sky surveys, VHE γ-ray astronomy observations actually predated the first X-ray or lower energy γ-ray telescopes, since they can be made from earth. Cynically, one must also note that once X-ray astronomy got off the ground, it produced more results with its first satellite detector, than all of VHE γ-ray astronomy has produced in its entire history.

It was the accidental discovery of PSR1919+21 (Hewish, 1969), the first radio pulsar which was detected during observations of the variations in radio sources due to irregularities in the solar wind, that served as a motivation to look for pulsation in the X-ray and γ-ray energy bands. The Crab pulsar, after being established as a radio source, was the first pulsar to be observed at X-ray energies. This discovery was followed by many other such discoveries by the Uhuru satellite (Giacconi, *et al* 1971). Since the launch of Uhuru, 11 other X-ray observatories have been launched on satellites to date, discovering over two dozen X-ray pulsars. Unlike the Crab, many of these pulsars discovered are X-ray binary stars rather than isolated pulsars. A map of all such binary pulsars discovered, including several new sources discovered by Ginga in 1989, is shown in Figure 1.1.

A large range of companion stars to the X-ray pulsar (presumably a neutron star) exist, though these companions can be divided into three general classes: low mass binaries (LMB), Be stars, and massive binaries (MB). Her X-1 is an example of a LMB system: its companion star, HZ Hercules, has a mass which is only marginally larger than the neutron star's mass. In such LMBs, it is assumed that the system has evolved sufficiently so that accretion by Roche-lobe overflow is the driving mechanism of the pulsar. In general, Be star companions, such as 4U0115's companion, have intermediate mass ($\sim 5\ M_\odot$ in this case). Cen X-3,

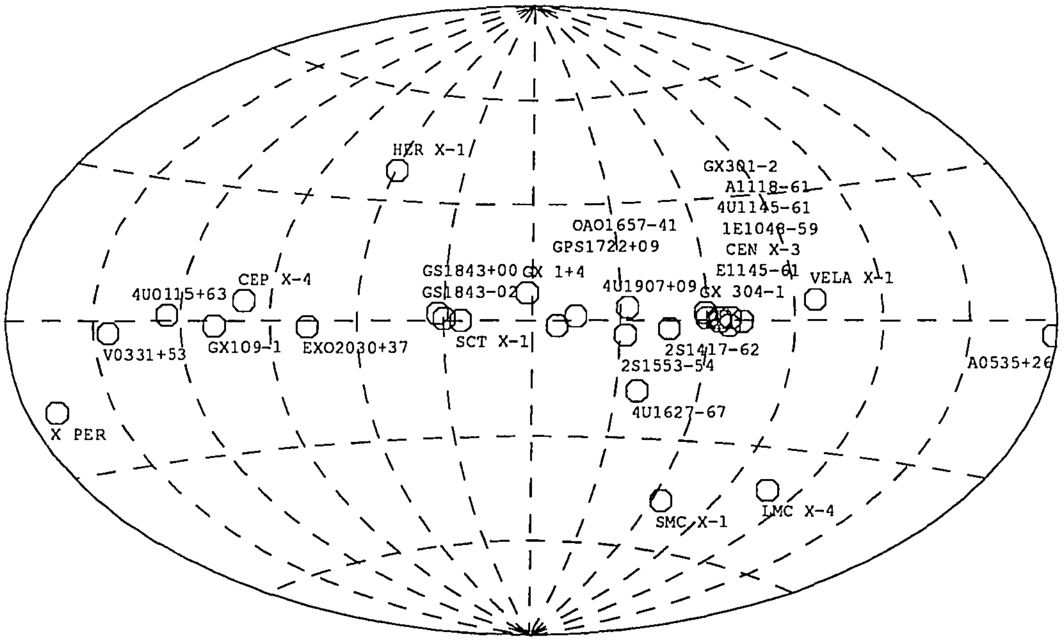
HER X-1
GX301-2
A1118-61
4U1145-61
1E1048-59
CEN X-3
E1145-61
VELA X-1
OAO1657-41
GPS1722+09
GS1843+00
GX 1+4
GS1843-02
4U1907+09
GX 304-1
4U0115+63
CEP X-4
V0331+53
GX109-1
EXO2030+37
SCT X-1
2S1417-62
2S1553-54
4U1627-67
A0535+26
X PER
SMC X-1
LMC X-4

Figure 1.1: A map of binary X-ray pulsars.

with a 20 M$_\odot$ companion, is a MB system. Be binaries and MBs, more massive and generally early-type stars, are usually powered by accretion through stellar wind capture of matter. Pulse periods for these three classes of pulsars depend more on the evolution of the system than the mass of the companion, though observations indicate that MBs tend to have either very short (a few second) periods or very long (several hundred second) periods. Many X-ray pulsars, such as Her X-1, have been studied for over 10 years by many detectors. As we will discuss in Chapter 2, detailed knowledge of the pulse spin up (or down) rate, as well as precise measurements of the orbital parameters have been obtained over this time in the X-ray region.

Meeting with similar atmospheric limitations as those encountered by the early X-ray astronomers, those attempting to observe low energy to HE γ-rays were largely thwarted until the first γ-ray satellites were launched. Measurements from balloon-born γ-ray detectors were both exposure time and background limited from the secondary γ's produced by cosmic rays in the upper atmosphere. The first sources observed in this energy range of about 30MeV - 100 MeV were all by low resolution satellite experiments, thus although γ-ray fluxes were detected as early as 1961, by instruments such as the Explorer XI satellite (Kraushaar, 1965), many of these sources were not positively identified until the 1970's.

Both balloon and satellite γ-ray detectors share a common background of γ's produced by cosmic rays interacting with interstellar matter (ISM). This is the source of diffuse γ emission near the galactic plane. We will discuss the processes of γ production at these energies in Section 1.2.1. It has been suggested that incorrect estimates of this background put the detection of some of the 29 COS-B (2CG) catalogue sources on dubious statistical ground (Ramana Murthy and Wolfendale, 1986); though the detection of strong γ-ray sources, such as the Vela pulsar and the Crab are firmly established.

1.2.1 Gamma-ray Production at Lower Energies

The diffuse γ-ray background can be attributed to the electron processes of Bremsstrahlung and Compton scattering, and to π^o decay from nucleonic interactions in the ISM. We will discuss these processes briefly and made an estimate of the contribution of each to the HE γ-ray background. In practice, to determine the expected γ background at any point in the sky, the column density and content of ISM gas must be considered, as well as the γ production mechanisms.

Bremsstrahlung radiation is produced in the presence of a magnetic field (in the coulomb field of a nucleus in the ISM). The differential cross section for this process can be written as (Ramana Murthy, 1986):

$$\sigma_B(E_o, E_\gamma)dE_\gamma = 4\sigma_o Z^2 \frac{dE_\gamma}{E_\gamma} f(E_\gamma, E_o) \tag{1.1}$$

Here, E_γ is the photon energy, E_o is the initial electron energy, $\sigma_o = \alpha(e^2/mc^2)^2$ and $f(E_\gamma, E_o)$ is a slowly varying function of energy. From this cross section, we can calculate the rate of energy loss for electrons by Bremsstrahlung for an electron traveling through matter with a number density n:

$$-\left(\frac{dE}{dt}\right)_B = cn \int_0^{E_o} E_\gamma \sigma_B(E, E_\gamma) dE_\gamma \tag{1.2}$$

For electrons traveling through the galactic plane ($n = 1$ cm^{-3}), this leads to a characteristic energy of photon emission of E_o and a radiation length of $\sim$ 10kpc.

Another process by which HE γ's may be produced is by Compton scattering. This process involves the scattering of a relativistic electron off of a photon, increasing the energy of the photon. The photons considered in this application are either stellar light ($E_\gamma \sim$ 2eV) or cosmic ray background photons ($E_\gamma = 2.7kT \sim 6 \times 10^{-4}$ eV. In this case, the rate of electron energy loss can be written as:

$$-\left(\frac{dE}{dt}\right)_C = cn\sigma\bar{E}_\gamma \tag{1.3}$$

The mean energy of the scattered photon is $\bar{E}_\gamma = \frac{4}{3}\bar{E}_{\gamma 0}(E/mc^2)^2$. To produce energies in the HE range, the incident electron energy must be large. In the case of scattering of star light, the required electron energy to produce a 100 MeV photon would be $E \sim 3 \times 10^9$ eV. For scattering of the cosmic background radiation, this would be $E \sim 2 \times 10^{11}$ eV. As a result, Compton scattering is more important at lower γ energies.

The decay of π^os produced in p–p interactions is another possible source of HE γ's. The energy of the photons produced in this decay can be considerable. In the rest frame of the pion, the photon energy will be $(m_\pi c^2)/2 \sim 68$ MeV. We will discuss this process further as a mechanism for the production of higher energy γ's near neutron stars in Section 1.3. Then, in Section 1.4 we will return to a discussion of these three processes, and also a discussion of pair production in the context of atmospheric cascades.

In the HE γ range, several point sources have also been identified in addition to the diffuse background. The two most significant sources identified by COS-B, the Crab and Vela, are both neutron stars. It has been suggested that inverse Compton scattering of X-ray photons is responsible for this γ flux (Schlickeiser, 1981). At TeV energies, pair production and p–p collisions are the basis of many suggested production mechanisms. These may be a factor at COS-B and EGRET energies ($\geq$ 100 MeV) as well. We will now discuss γ production by binary neutron stars in the VHE range.

1.3 VHE Gamma-ray Emission

Because of limitations in the amount of exposure time and in the observed strength of VHE γ-ray emission, it is not practical to perform an all-sky search for potential VHE γ-ray sources using the current generation of detectors. For these reasons, most of the potential sources observed, and all of the sources discovered were chosen from the list of known radio, X-ray and lower energy γ-ray sources. In this section, I will discuss some of the basic properties of neutron stars, specifically a neutron star in a stellar binary system, and I will describe the accretion process that is believed to produce X-rays and lower energy γ-rays; and that may also produce higher energy photons.

1.3.1 Neutron Stars and X-ray Binary Stars

As was mentioned in the introduction, neutron stars were positively identified by an accidental observation of pulsed radiation at radio energies, though the existence of such stars was theorized long before this discovery in the late '60′s. A neutron star may be formed from a supernova explosion where the mass of the remaining matter is 1-2 $M_\odot$. With such a mass, the collapsing supernova remnant will cease its infall when the neutron degeneracy pressure balances the gravitational force, producing a neutron star with a radius of about 10 km. The existence of such dense stars ($\rho \sim 10^{16}$ g/cm^3) is often one of most surprising facts learned by Freshman astronomy students: as it is often stated in introductory texts, a teaspoon of this dense neutron core will weigh over a billion tons.

The photon flux observed from these objects is predictable over large ranges of energy. As is demonstrated for the Crab in Figure 1.2, the differential flux spectrum:

$$\frac{dN}{dE} \simeq AE^{-2} \tag{1.4}$$

is a good approximation to the data over many orders of magnitude in energy (Ramana Murthy and Wolfendale, 1986). This power law spectrum is the product of particle acceleration over these large range of energies.

Here, no attempt will be made to describe the process of stellar evolution or the eventual collapse of the star. We will begin our discussion by examining the properties of neutron stars. Specifically, we will address the production of X-rays and higher energy photons from neutron stars in a binary star system. The neutron star's companion may be assumed to be a main-sequence or post main sequence non-degenerate star, though in principle, it could be another neutron star, or black hole. It is this combination of a neutron star which is driven by the accretion of matter from its companion that is assumed to be responsible for many of the observed X-ray pulsars.

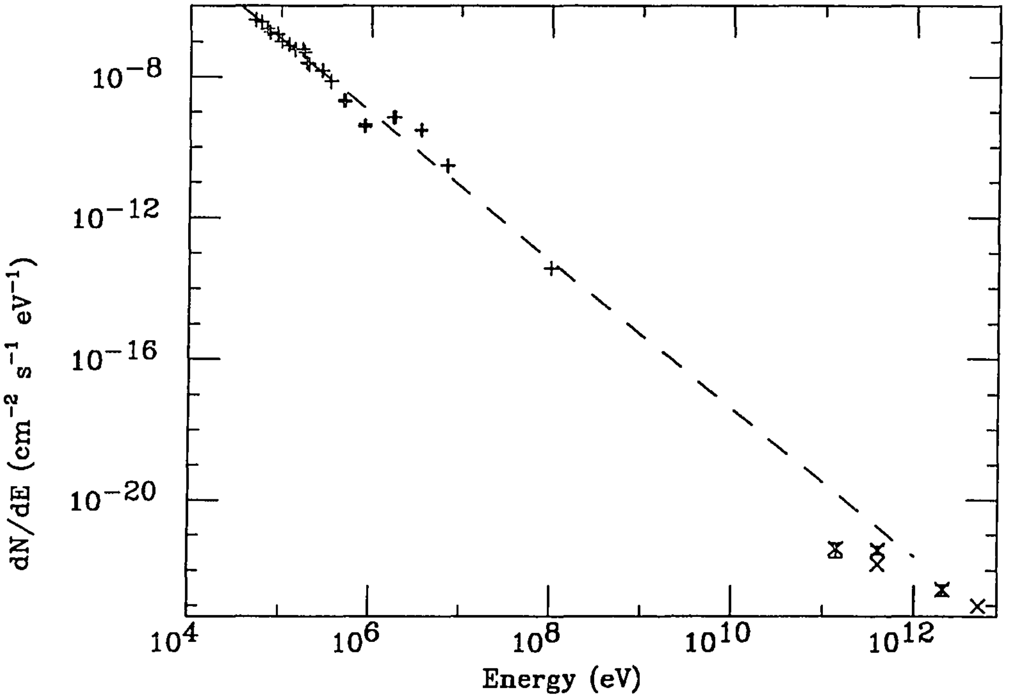

Figure 1.2: Differential γ-ray spectrum from the Crab from HEAO-3, COSB, and VHE measurements. The dashed line is a $E^{-2.1}$ fit to the HEAO-3 data.

In order to understand (or at least comprehend a possible model for) high energy photon emission from a neutron star binary system, a brief description of the production of such photons at lower energies is given. This is far from being complete and even farther from being rigorous: a more complete description of accretion is presented by Ghosh and Lamb (Ghosh, Lamb, and Pethick, 1977; Gosh and Lamb, 1979(a) and 1979(b)). A good summary of magnetospheric theory is presented by Michel (Michel, 1982).

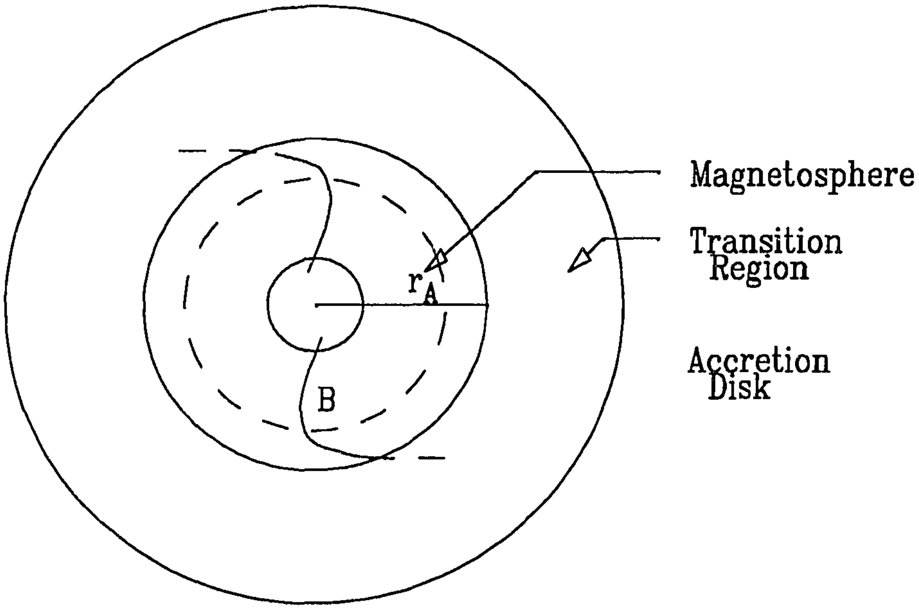

Figure 1.3: A model of the regions around a neutron star.

1.3.2 Accretion in a Disk-fed System

The neighborhood around the neutron star may be divided into three regions: a region inside the magnetosphere where the stellar magnetic field lines dominate all matter flow, a region outside of the influence of these field lines, and a transition region where these two zones meet (Figure 1.3). In this transition region, magnetic coupling between the neutron star and the accreted matter still exists but it is screened to some extent. The radial structure of this transition region is very complex. We will present some general statements about it's structure as well as about the transport of matter through this region and into the magnetosphere.

The Alfv́en radius, r_A, defines a surface within which matter moves along these magnetic field lines in a reference frame that is co-rotating with the star. It will be assumed in the model discussed that the magnetospheric radius, r_m is roughly equal to r_A, and both are much larger than the neutron star radius, R. Additionally, we will restrict ourselves to a discussion of disk-fed pulsars where the neutron star can be classified as a rapid rotator, so that the co-rotation radius (r_{co}) is not much larger than r_m. Here, we will take the co-rotation radius as the boundary within which the matter is forced to co-rotate with the neutron star. This will occur within the light cylinder for the models we will discuss. The location of r_{co} as influenced by internal and external factors (such as the accretion rate) will determine whether a spin-up or a spin-down torque is exerted on the pulsar. For Her X-1, it is assumed that r_{co} is close enough to the critical value that, depending on the mass accretion rate, either a spin-up or spin-down torque can be exerted.

Using the model of Ghosh and Lamb, we can now estimate the size of, and the characteristics of matter flow in, the three regions around the neutron star. We will begin by discussing the outer region of the accretion disk, and work our way inward to the surface of the star.

Beyond the Magnetosphere

The outer accretion disk is assumed to exhibit Keplerian matter flow, completely decoupled from the stellar magnetic field. The angular velocity of matter in the disk is then just:

$$\omega_d(r) = (GM/r^3)^{\frac{1}{2}} \tag{1.5}$$

In the transition region, the stellar magnetic field begins to penetrate and reconnects with the very small magnetic field present in the disk. This reconnection near the surface of the disk, along with vertical turbulent diffusion of the matter and other instabilities near the boundary of the disk cause the field to penetrate (or thread) the disk for some distance into this transition region. The movement of matter in the disk across these threading stellar field lines produces screening currents which will eventually contain the intrusion of the stellar field into the disk. Throughout most of this transition region, the motion can be treated in a Keplerian fashion, with the dominant mechanism of angular momentum transport being viscous stress. One can write down the equations for the accretion flow and the magnetic field in this transition (Ghosh and Lamb, 1979(a)), leading to a numerical solution for the magnetic field, the mass flow rate, and the radial and angular velocities of the matter.

From these solutions, some general observations can be made: The magnetic field strength which remains weak in the outer part of the transition region will increase approximately exponentially as the magnetopsheric boundary is approached. The radial mass flow rate decreases rapidly throughout the transition region. The radial velocity of the infalling matter, which is very small in the region outside of the field's influence, increases as the centrifugal force on the matter increases. Before reaching the magnetospheric boundary, the outward pressure produced by the magnetic field begins to dominate, slowing down the radial infall. As the matter passes the magnetospheric boundary, coupling to the field lines will become more complete. The angular velocity is reduced from its Keplerian value by magnetic stress until it reaches the corotation velocity at r_{co}

From this analysis, the rotation speed of the star may be given in terms of a dimensionless rotation velocity which is proportional to the mass accretion rate, $\dot{M}$ as:

$$\omega_s = \frac{\Omega}{(GM/r^3)^{\frac{1}{2}}}$$

$$\omega_s = \frac{1.19\mu_{30}^{\frac{6}{7}}}{P\dot{M}_{17}^{\frac{3}{7}}(M/M_{\odot})^{\frac{5}{7}}} \tag{1.6}$$

Ω is the stellar angular velocity, P is the rotation period of the neutron star in seconds, M is the mass of the neutron star, and $\dot{M}$ is the mass accretion rate. μ_{30} is the magnetic moment in units of 10^{30} gauss cm^3. For Her X-1 (Ghosh and Lamb, 1979(b)) we find that:

$\mu_{30} = 0.47\ (10^{30} Gcm^3)$

$r_o = 1.1 \times 10^8 cm$

$\omega_s = 0.35$

$$\dot{M} = 2.4 \times 10^{17} g/s$$

This puts a limit on the rotation speed of the star according to the model. If $\omega_s > 1$, the centrifugal force on the accreting matter will become so large in the transition zone that it will overcome the magnetic force, so that at some point in this region the infall velocity will drop to zero. In this case, accretion into the magnetosphere will not occur, or will be very unstable. The minimum pulse period can be estimated for $\omega_{max} \sim 1$ to be on the order of several milliseconds. We have assumed that $\dot{M}_{max} \sim 10^{18}$ g s^{-1} as imposed by the Eddington luminosity limit.

Within the Magnetosphere

The extent of the Alfv́en surface can be approximated by noting that near the magnetospheric boundary region, the energy density of the neutron star's magnetic field $(\frac{\mathbf{B}^2}{4\pi})$ must be roughly equal to the kinetic energy of the accreting matter onto the star $(\frac{1}{2}\rho\ v^2)$. As the distance from the star increases beyond this radius, the magnetic energy density becomes less important until eventually, at a large enough distance from the star, the matter flow is spherically symmetric. The Alfv́en radius is then:

$$r_A = \frac{2.5X10^8(\frac{M}{M_\odot})^{\frac{1}{7}}\mu_{30}^{\frac{4}{7}}}{L_{37}^{\frac{2}{7}}R_6^{\frac{2}{7}}} \tag{1.7}$$

L_{37} is the luminosity in units of 10^{37} erg/s, and R_6 is the neutron star radius in units of 10^6 cm. We have assumed that the mass accretion is constant over this region, and that we may write the velocity as just $v(r_A) = (2GM/r_A)^{1/2}$ in the near free-fall approximation.

Several theories have been proposed to explain the transport of matter within the magnetosphere. Most of these theories are variations on the Goldreich-Julian model, known as the standard model, by which one is able to calculate properties of the field given certain assumptions (Goldreich and Julian, 1969). This model was developed to explain radio signals from pulsars, and it can be modified, to explain radiation up to the X-ray regime. Among the simplifying assumptions made in the standard model are the following: The magnetic field is taken to be a dipole field with its axis aligned with the spin axis of the star, $\mathbf{E} \cdot \mathbf{B} = 0$ everywhere in the magnetosphere so charged particles are not accelerated along closed field lines, the motion of the matter is taken to be along the magnetic field lines with a component of $\mathbf{E} \times \mathbf{B}$ drift, and gravity and centrifugal forces near the star are neglected. Using these assumptions, the magnetic field in the co-rotating plasma can be derived.

Before reaching the poles, the matter must rapidly decelerate to match the angular velocity of the neutron star. It then interacts with matter near the stellar surface, producing anisotropic X-ray emission at the two poles. The area of this accreting column can be estimated. Near r_A, the last closed, undistorted field line must occur. In the dipole field approximation this determines the cross-sectional area of the accreting column, since:

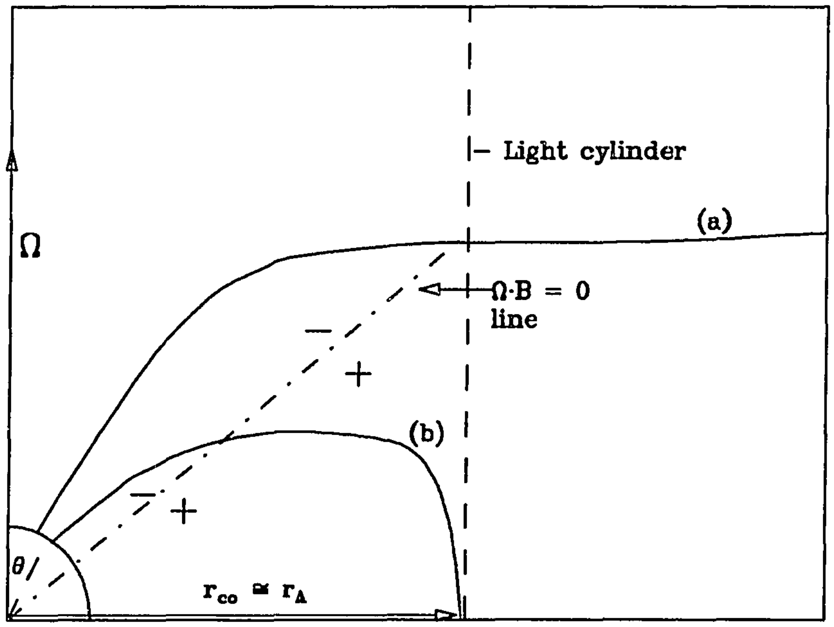

Figure 1.4: Sample field lines in the Standard Model of a pulsar magnetosphere. The magnetic and rotation axes are aligned in this view.

$$\sin^2\theta = \frac{R}{r_A} \tag{1.8}$$

Using Equation 1.7, we find that in this approximation the accretion column has a cross sectional area of about 10^6 m^2. In Figure 1.4, the last closed field line is labeled as (b). It closes at a radius approximately equal to the Alfv́en radius (recall that for the specific case discussed here, $r_A \sim r_{co}$).

There are many problems with this standard model, and many modifications have been made to address, or subvert these problems (Ostriker and Gunn,1969;

Ruderman and Sutherland, 1975 to name two). Both of these are oblique rotator models (unlike the standard model diagram presented in Figure 1.4), that is to say they assume that the axis of rotation of the neutron star does not correspond to the star's magnetic axis, so that there is the possibility that pulsed radiation is produced in these models. Charge separation of the matter in the magnetosphere will occur as a result of the larger gravitational forces on the positive charges (protons and nuclei) in the plasma. The boundary between these two regions has been the subject of debate, since if the two regions are separated by only a $\mathbf{\Omega} \cdot \mathbf{B} = 0$ line as in the standard model, then the difference in rotation needed to satisfy $\mathbf{F} \cdot \mathbf{B} = 0$ in the two regions is a problem. Another modification to the standard model assumes that the outflow of charged particles from the star along the open field lines will form a gap region near the polar cap where the magnetospheric density is zero. Within this vacuum gap, $\mathbf{E} \cdot \mathbf{B} \neq 0$. The gap size is limited by $e^+ \, e^-$ production by photons which enter the gap with an energy greater than $2m_e c^2$. The gap thickness, h, can be approximated to be 5×10^3 cm for Her X-1 according to the Ruderman and Sutherland model. A potential drop is produced along a field line from the stellar surface passing through this gap. This potential is proportional to the gap thickness as:

$$\Delta V = \Omega B h^2 / c \tag{1.9}$$

Acceleration of the electrons and positrons created in the gap along the open field lines by this potential increases their energy to $\sim e\Delta V$. The electrons flow back toward the polar region while the ultrarelativistic positrons flow outward along the field lines, producing lower energy radiation in the magnetosphere.

1.3.3 Gamma-ray Emission at Higher Energy

To explain VHE and UHE γ-ray production, a mechanism that differs from those mentioned above is needed. Any photons produced near the neutron star surface with such high energy would interact with matter, producing e^+ e^- pairs. Several models have been proposed: two of these will be brief discussed here. Both of these involve the production of high energy photons by charged particles funneled out of the polar cap region of the neutron star. These are in essence an extension of X-ray production mechanisms: The charged particle beam is assumed to be produced by the infall of accreting matter, which was the production mechanism for X-rays we discussed in the previous section. The charged particles produced near the surface of the star are accelerated outwards along field lines in most models. Various mechanisms such as steering along these lines producing a very narrow beam and Fermi shock acceleration near the light cylinder, are then assumed to increase the charged particle's energy so that VHE protons may be produced. It should be noted that neither of the models discussed below, nor any model so far proposed, is completely successful in explaining all radiation observed in the X-ray through UHE γ range. In particular, pulsed emission detected in the VHE and UHE range from Her X-1 at a period significantly different from the X-ray pulse period was not predicted by any model. This anomalous periodicity will be discussed further in Chapter 2, along with extensions to existing γ production models proposed to explain this periodicity.

At the polar regions of the neutron star, near where X-ray production may take place, charged particles (specifically e^+ e^-) are also present. One model, proposed by Cohen and Mustafa in 1987, assumes that these particles are accelerated to extreme relativistic energies along open magnetic field lines directed out from the pole. As these field lines bend, the relativistic electron will emit synchrotron radiation with a maximum energy of:

$$E_c = \hbar\omega = \frac{3\gamma^3\hbar c}{\rho} \tag{1.10}$$

Where ρ is the instantaneous bending radius of the particle and γ is the Lorentz gamma factor: $\gamma = e/(mc^2)$. This corresponds to a maximum energy of $\sim\ 3\ \times\ 10^{-23}\ \frac{E^3}{\rho}\ m/eV^2$ with E in electron volts and ρ in meters. Above this energy , negligible radiation is emitted. For Her X-1 this energy is about $10^{15}\ eV$ for a magnetic field of about 10^{12} Gauss.

The size of the resultant beam is estimated to be:

$$\sin\theta_s \sim \frac{4R}{3\rho_s} \tag{1.11}$$

Here, ρ_s is the radius of curvature of the open field line meeting the surface at a radial distance of θ_s from the pole. For Her X-1, this distance is calculated to be 0.00078° , which is only about .01% of the total angular extent estimated for the polar cap region. Thus, γs are expected to be produced in a tight beam near the polar region. One problem with this production mechanism is that it assumes that the VHE photons emerge from this small region fairly near (but not at) the neutron star surface. The authors consider attenuation by pair production, and dismiss its effect as minor if the photons travel along the magnetic field through a region where $\mathbf{E}\times\mathbf{B} = 0$ (but $\mathbf{E} \neq 0$). Others have argued that the interaction of these VHE γs with thermal photons will lead to pair production when the incident γ has an energy of $\sim$ 1TeV or more (Johnson, 1989). This photon induced pair production could lead to near total annihilation of the outgoing γs.

VHE photons may also be produced by protons moving through the disk material outside of the magnetosphere. In this model proposed by Király and Mészáros a beam of protons can be produced near the polar cap by a radiative shock transition of the infalling accretion matter (Király and Mészáros, 1988). This process is also expected to produce X-ray radiation near the polar region. The protons which are ejected along the magnetic field axis are able to pass through r_A, experiencing a collisionless shock near this radius. This shock will be the result of pressure from accretion matter in the transition region of the star if the accretion rate is large enough (Eicher and Vestrand, 1985). At or near r_A, these shocks produce a narrow jet of accelerated protons. Once the jet has passed through the inner part of the transition region and out of the influence of the neutron star's magnetic field, the jet will continue out approximately radially. As the jet intersects the accretion disk, p–p collisions will occur, producing pions of all varieties from which VHE photons are produced with an energy which is approximately an order

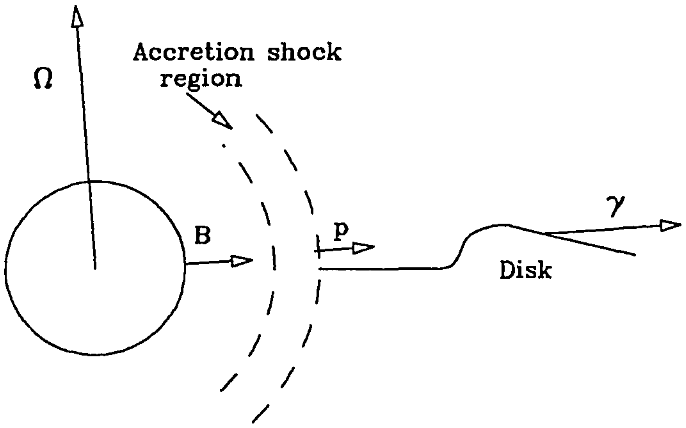

Figure 1.5: A possible scenario for the production of VHE γ's from accelerated protons (Király and Mészáros). The accretion shock region, near r_A, also produces γ's which may escape at lower (X-ray) energy but will pair produce at higher energy.

of magnitude lower than the incident proton energy (see Figure 1.5). Muons and neutrinos are also produced from the charged pions. If the interaction takes place at the edge of the disk, or if the disk is thin near the interaction region (less than $\sim$ 100 g/cm^2 of matter), then the photons may escape without significant loss to pair production.

The protons that survive the accretion disk still may interact with the companion star. As these protons approach the companion, they may be bent or steered somewhat into a curved path by the companion's magnetic field (Gorham and

Learned, 1986). Protons which interact at or near the star surface may produce neutrinos. Those that pass through the less dense material around the star can produce a beam photons with energies up to $\sim 10^{15}$ eV. Since the optical depth in this region is very small, most of the photons produced will survive. If this proton beam is steered as mentioned above, then the possibility exists for the detection of γ emission just after eclipse for Her X-1. This would then be a unique signature for VHE photon production, indicating that such production must take place in a region different from that where X-ray production occurs.

Both of these models are powered by accretion, and the Eddington luminosity ($\sim 10^{38}$erg s^{-1}) provides an upper limit to the accretion rate. This sets a limit on the maximum energy of photons produced which is slightly above the UHE threshold, though it is possible through the jet model of Király and Mészáros to achieve slightly higher energies than through more isotropic acceleration models. Other models based upon rotation powered shock acceleration (Gaisser, Harding, and Stanev, 1989) have been proposed recently, but these are designed primarily to explain UHE radiation up to 10^{18} eV from short period sources, such as Cygnus X-3, which is may have a pulsar period of $\sim$ 12 ms, according to observations by the Durham group (Chadwick, *et al.* 1985)

1.4 Cascades in the Atmosphere

VHE gamma-rays cannot be directly observed on the earth since they do not survive through more than about 35 g/cm^2 of the earth's atmosphere on the average;

nor can they currently be observed from space because of their low flux. Because of this, they must be observed indirectly, through the detection of the Čerenkov flash produced by shower particles from the incident γ-ray. What follows is a brief description of Čerenkov light, and the cascades produced by γ-rays and protons in the atmosphere. A complete treatment of Čerenkov radiation and electromagnetic and hadronic cascades can be found elsewhere (Jackson, 1975; Longair, 1981).

1.4.1 Čerenkov Radiation

Čerenkov radiation was first observed in about 1910 by several people performing experiments with radioactive materials, including Madame Curie who noticed a faint, blue glow from radioactive samples. It wasn't until the mid 1930's that specific experiments by Frank and Tamm were conducted in an attempt to determine the cause of this blue light (Frank and Tamm, 1937). This effect can be described qualitatively by a dipole field generated by a charged particle moving at a rapid velocity. In the case where the particle's velocity is greater than the velocity of light in the medium, the electromagnetic pulse produced at each point in the particles path can constructively interfere, causing radiation to be produced at an angle that is a function of the type of medium and the velocity of the particle traveling through it. A diagram of this, Figure 1.6, shows that $\cos\,\theta = 1/(\beta n)$. This also implies that the particle will continue to emit light as long as its velocity is greater than c/n.

In the case of Čerenkov radiation produced by a charged particle in the atmosphere, the angle of emission increases as the atmospheric index of refraction,

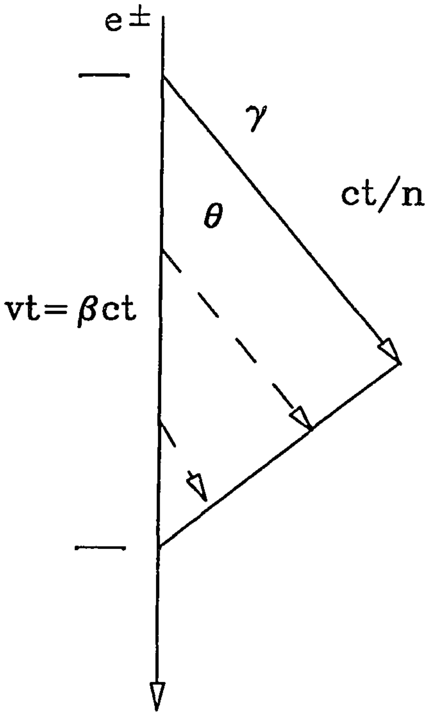

Figure 1.6: The geometry of a Čerenkov photon.

n, increases. Since $n - 1$ is always very small in the atmosphere, we can approximate $\beta \sim 1$ in order for these particles to be producing /vCerenkov light. For showers produced at the point at which the maximum number of electrons and positrons are present, which is often called shower maximum and which will be discussed further in the next section, the index of refraction is about 1.0000798, thus $\theta = 0.72°$ at this altitude.

The theory of classical Čerenkov radiation was developed at about the same time that P.A. Čerenkov was conducting his original experiments. According to this theory, the energy radiated in the form of Čerenkov light can be calculated as the energy loss per unit length for interactions (Jelley, 1967). Substituting the Fourier Transform of the E field at a perpendicular distance from the path (the impact parameter):

$$\frac{dE}{dx} = \frac{e^2}{c^2} \int_{\beta > \frac{1}{n}} \left(1 - \frac{1}{\beta^2 n^2}\right) \omega d\omega \tag{1.12}$$

The number of photons produced within a given wavelength range is found from this simply by substituting in the energy per photon; so for a path length l:

$$\frac{dN}{dl} = 2\pi \frac{e^2}{c\hbar} \left(1 - \frac{1}{\beta^2 n^2}\right) \left(\frac{1}{\lambda_2} - \frac{1}{\lambda_1}\right) \tag{1.13}$$

So the number of Čerenkov photons produced is inversely proportional to the wavelength of the photons. Considering the spectral response of our telescope ($\sim$ 300 – 450 nm)* the number of Čerenkov photons produced near shower maximum would be $\sim$ 8 photons m^{-1}.

1.4.2 Cosmic Ray Initiated Showers

Cosmic rays produce nuclear cascades in the atmosphere. The incident charged particle, which is usually a proton for energies above several GeV, hits an oxygen or nitrogen nucleus in the upper atmosphere, initiating the hadronic cascade. From this initial interaction, approximately equal numbers of π^+, π^-, and π° are produced at high energies with the total number of charged particles $\sim 2E^{\frac{1}{4}}$ (E in GeV) in the shower (Longair, 1981). The incident particle and secondary particles produced may interact many times. The cascade continues until the proton energy is less than that necessary for multiple pion production, which is on the order of 1 GeV. The π° produced decays almost immediately into two photons. This electromagnetic component of the shower provides nearly all of the observed Čerenkov light. The $\pi^{\pm}$ decay via:

---

*Here, I have taken a wavelength range covering both the new and old telescope spectral responses. See Figure 3.4 for the response of each telescope.

$$\begin{array}{llllll} \pi^{\pm} \longrightarrow & \mu^{\pm} & + \; \nu_{\mu} & & & \\ & \llcorner\!\!\longrightarrow & e^{\pm} & + \; \nu_{e} & + \; \bar{\nu}_{\mu} & \end{array}$$

The muon lifetime is two orders of magnitude larger than the pion lifetime ($c\tau_{\mu} = 658.65\ m$ and $c\tau_{\pi} = 7.804\ m$) so that above several GeV, the muons produced in $\pi^{\pm}$ decay will penetrate to detector altitudes. The detection of these accompanying muons can be used as a veto by high energy experiments with muon identification capability, since purely electromagnetic cascades are not predicted to have this large muon component*. The electromagnetic cascade produced by the π° decay is indistinguishable from that produced by a γ-initiated shower; however, the cascade produced by the proton shower contain an inhomogeneous component from π^{o}s produced from other hadronic decays of the primary or secondary particles. In addition, the lateral component of the momentum of the pions is much larger than that for the photon initiated electomagnetic cascade, which produces more spread in the photon density at a given altitude. The difference in the photon 'footprint'

---

*In Section 2.3, observations of both Her X-1 and Cyg X-3 which do *not* show a muon-poor signal will be discussed. These observations are not in agreement with what is expected from γ initiated showers as discussed in this section.

produced on the ground is obvious from Monte-Carlo simulations, but, as we will see, it is very difficult to exploit these differences when only a small portion of the shower is sampled. More detailed explanation of this can be found in Section 1.4 where the Monte-Carlo simulations of γ and proton initiated showers are discussed.

The integral cosmic ray spectrum goes as $N(E) \simeq C_I\, E^{-1.6}\ \mathrm{m}^{-2}\mathrm{s}^{-1}\mathrm{sr}^{-1}$ for energies up to the UHE region, with $C_I = 0.16$ and E in TeV. Above a primary energy of about 10^{15} eV, this spectrum appears to fall more steeply as $\sim E^{-2}$.

1.4.3 Gamma-ray Initiated Showers

When a VHE photon enters the earth's atmosphere, it produces an electromagnetic cascade. To understand this, let's look at the processes involved:

A photon with $E_\gamma > 2\, m_e c^2$ can pair produce in the coulomb field of a nucleus (another particle is necessary to allow both energy and momentum to be conserved). This is the dominant process for energy loss at energies greater than several 10's of MeV. The cross section for this process in the relativistic limit can be approximated as:

$$\sigma_p \simeq \frac{4Z^2\alpha^3}{m_e^2c^2/\hbar^2} \ln(183Z^{-\frac{1}{3}}) \tag{1.14}$$

where Z is the atomic number, and α is the fine structure constant. The interaction length is inversely proportional to this:

$$\xi_p \simeq \frac{554M_A}{Z^2 \ln(183Z^{-\frac{1}{3}})} \tag{1.15}$$

Equation 1.15 is the interaction length in g/cm^2. In this equation, M_A represents the atomic weight of the material.

The $e^{\pm}$ produced from the γ emit photons via Bremsstrahlung. The cross section for this process is approximately the same as that for pair production at these energies, thus the radiation length for Bremsstrahlung is about the same as that for pair production:

$$\xi_b = \frac{716M_A}{Z(Z+1.3)[\ln(183Z^{-\frac{1}{3}}) + \frac{1}{8}]} \tag{1.16}$$

For photons and electrons in the atmosphere, this gives $\xi_p \simeq 35$ g/cm^2 and $\xi_b \simeq 37$ g/cm^2.

At lower energies (below several 10's of MeV), photoelectric absorption is the main form of energy loss for photons. The cross section for this drops as $E^{-\frac{7}{2}}$ at non-relativistic energies and more softly, as E^{-1} at higher energy.

1.4.4 Electromagnetic Cascades

After this brief description of the interactions of photons and electrons in the MeV to TeV energy range, it can now be seen qualitatively how a γ-ray initiated cascade propagates and then dies. The photon will pair produce in the atmosphere, the

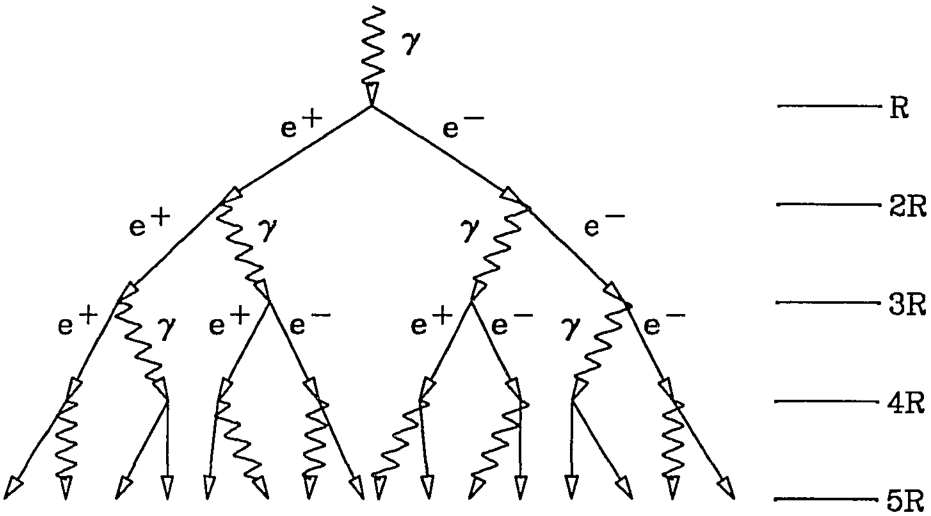

Figure 1.7: The development of a γ initiated cascade.

electron and positron produced will then radiate via Bremsstrahlung (see Figure 1.7) . These radiated photons then can pair produce; and the process continues until the energy per particle drops below a critical value, which is on the order of 80 MeV. At this point, the cross section for photoelectric absorption has risen to the point that this process begins to deplete the number of photons in the shower. At about 10 MeV, this process takes over, and the shower quickly dies.

When the energy per particle is near the critical energy mentioned above, the maximum number of particles are present. This energy corresponds to a height of shower maximum of about 10 km above sea level. Recalling that $\xi_p \sim \xi_b$, the energy drops off as $\frac{E_o}{E_c} = 2^n$ where E_c is the critical energy and n is the number of radiation lengths, or:

$$n = \frac{\ln(\frac{E_o}{E_c})}{\ln(2)} \tag{1.17}$$

For a γ near our threshold energy (.3 TeV for the old telescope) this corresponds to $n \simeq 12$ or a height of about 9 km above sea level. The distance to shower maximum is often taken in approximation as the altitude at which **all** of the Čerenkov photons are emitted. As will be seen, this is a reasonable approximation for some calculations, such as the determination of the theoretical rate as a function of zenith angle (Section 4.5).

1.5 Monte-Carlo Studies

A complete study of the expected properties of photon and proton initiated cascades just discussed is essential to determine how to distinguish between the two showers. The monte-carlo simulation employed here was originally written by Todor Stanev of Bartol Research Institute as solely a hadronic shower simulation program. This original program has been extensively modified by Glenn Sembroski of Purdue University and other members of the Haleakala collaboration. Sembroski's modifications include adding the ability to generate not only proton initiated cascades but also γ initiated showers. In a separate step, the Čerenkov light from this cascade is generated and a simulation of the telescope is added to help to determine the telescope's response to γ and hadronic initiated showers.

Many of the details of this program have been discussed elsewhere (for example Slane, 1988) so I will not go into them here. This program has been compared to other similar programs (Macomb and Lamb, 1990), and it is consistent with other such simulations.

1.5.1 Characteristics of Proton and Gamma-ray Initiated Showers

One of the main reasons for generating Monte-Carlo simulations of proton and γ initiated showers is to identify the differences in the Čerenkov light "footprint" produced by each on the ground, and exploit these differences in order to separate the γs from the cosmic-ray background. From basic assumptions about the propagation of γ and proton showers at primary energies near 1 TeV, several general differences can be inferred.

As was discussed in Section 1.3, the largest number of electrons in a γ shower are present at an altitude of about 10 km above lea level and, after this altitude the number of electrons dies off rapidly as the energy drops below about 80 MeV per particle. A large number of the Čerenkov photons that are produced originate from this shower maximum. These photons are produced at a angle of about 0.7°, leading to an abundance of photons at a radius corresponding to this Čerenkov angle. For a shower from zenith, this distribution is approximately symmetric about the shower core. From straight forward calculation (taking the Čerenkov photons to originate between 12 km and 8 km for a shower at zenith, and taking the electron to be near the core of the shower) this would produce a dense photon

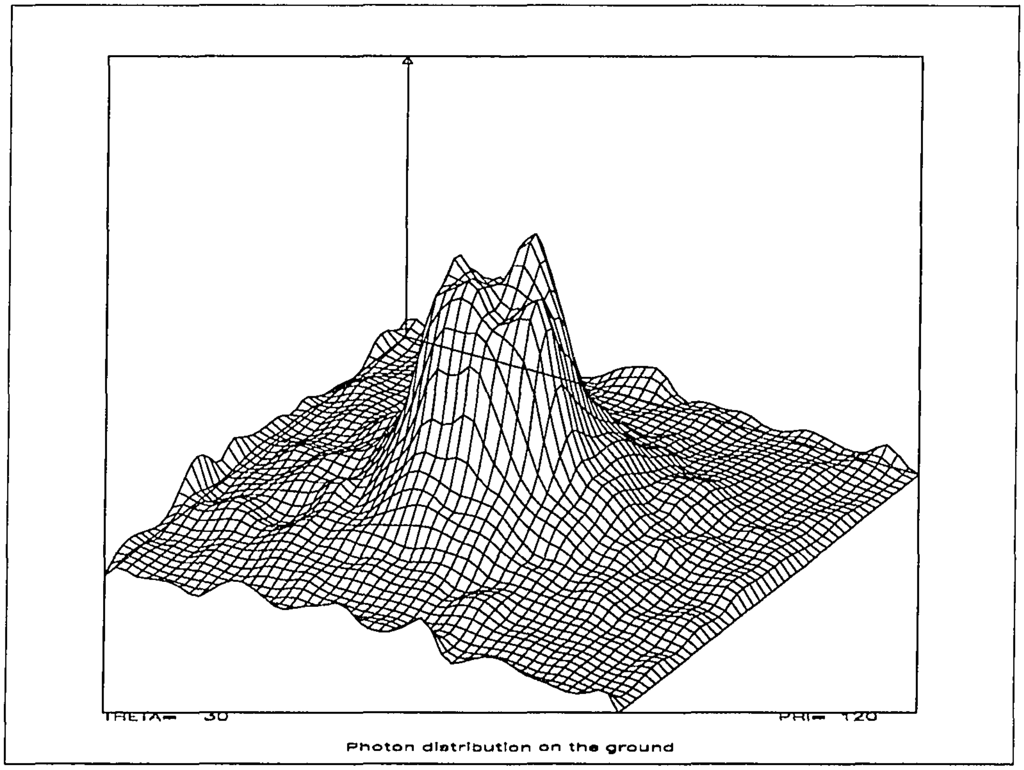

Figure 1.8: The photon distribution from 0.75 TeV γ shower at Haleakala altitude.

"ring" at about 80–100 m from the shower core at Haleakala altitude. Since most of the photons in this ring come from nearly the same altitude, the relative arrival times of these photons on the ground should be tight in time. A plot of a Monte-Carlo simulation of the Čerenkov light footprint of a electromagnetic shower is shown in Figure 1.8. A hint of a photon ring is seen in this 0.75 TeV shower.

Hadronic cascades are much more complicated and less predictable than purely electromagnetic cascades; however, a few basic characteristics can be inferred from a simple look at their development. The large transverse component of momentum imparted to shower pions in a proton shower leads to the conclusion that

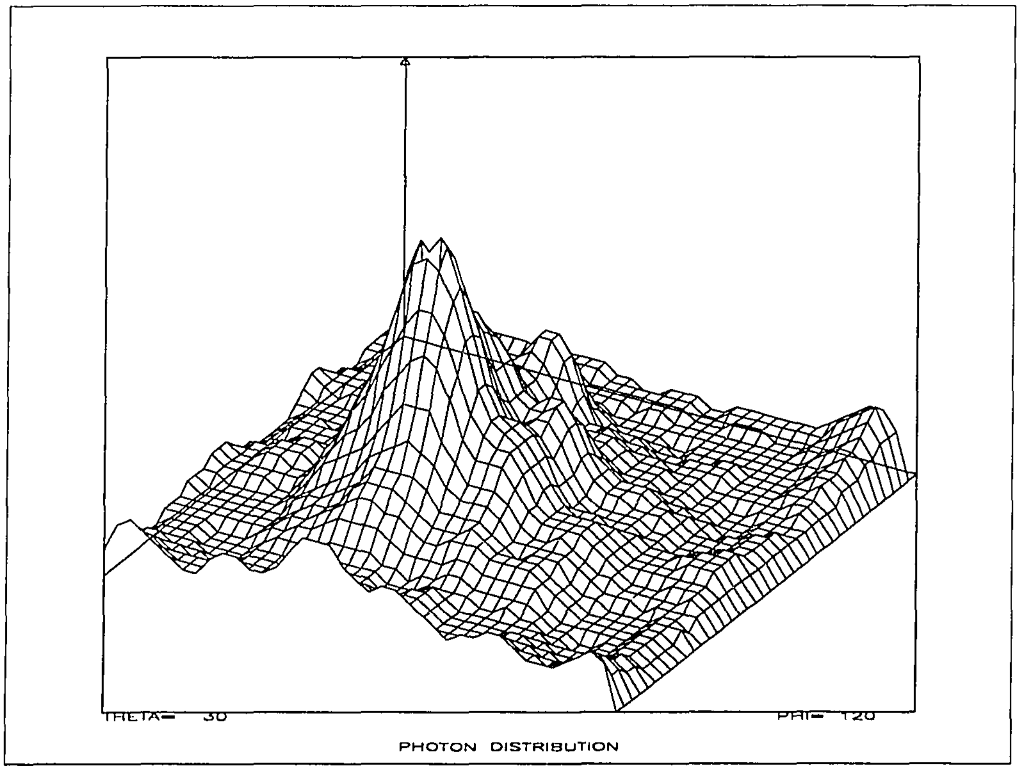

Figure 1.9: The photon distribution from 2 TeV proton shower at Haleakala altitude.

these showers should have a larger "footprint" than γ showers. More importantly, one can guess that these showers should produce a less uniform (or a less radially symmetric) footprint than γ showers, both because of the angular spreading and because Čerenkov light can be produced both from the products of π^o decay from the initial hadronic interaction, and from subsequent hadronic interactions. A representative Monte-Carlo proton shower is shown in Figure 1.9. Here, the Čerenkov light footprint does not look dramatically different than Figure 1.8; however, it does appear to be less uniform.

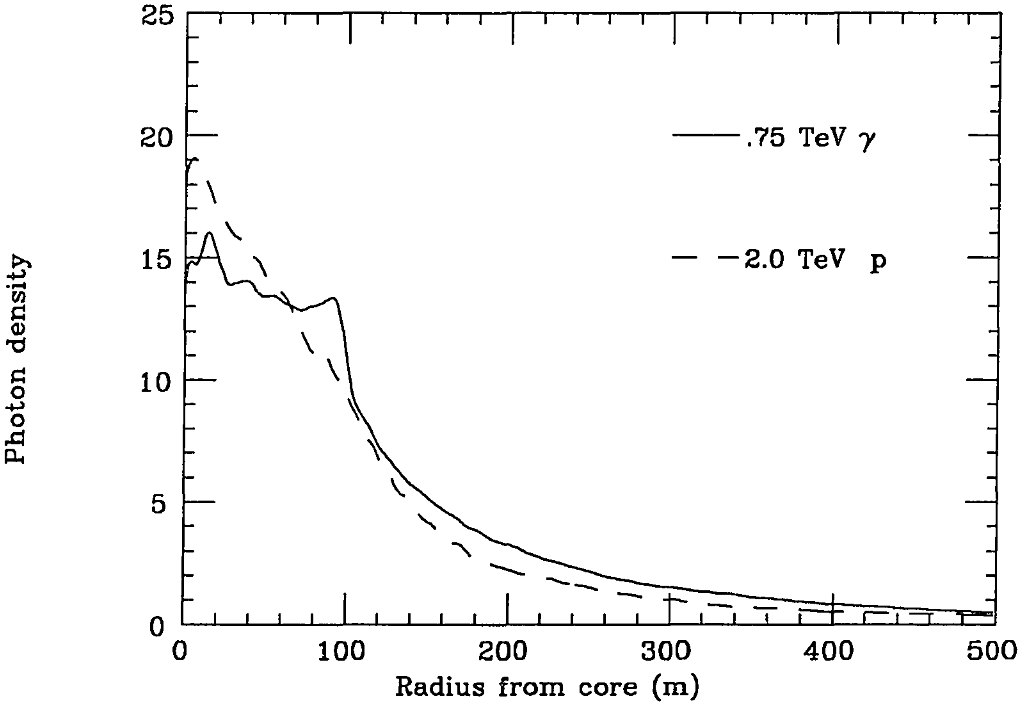

Figure 1.10: The photon density of a 0.75 TeV γ shower and a 2 TeV proton shower as a function of radius.

Figure 1.10 represents the photon density of both a 2 TeV proton and a 0.75 TeV γ shower as a function of distance from the core of the shower. The total number of photons contained in the two showers is approximately the same, but the shape of these distributions show a different radial dependence. The γ shower is relatively flat out to a radius of about 100 m, increasing slightly at the ring of the shower, then falling off. The proton shower falls off approximately exponentially from the core of the shower.

If one could look at the entire light distribution on the ground (as displayed in Figures 1.8 or 1.9) or the entire cross section of this distribution, hadronic and electromagnetic showers could be separated with a reasonable efficiency in the air Čerenkov energy range. With just one telescope sampling a small fraction of the light, this is not directly possible using a small aperture. Sampling light over several degrees, using a segmented detector with a common focus to obtain both a spacial and temporal image of the light from a shower, can aid in separating these two shower types. Such an imaging technique has been successfully employed by the Whipple group producing the detection a significant rate excess from the Crab (Kwok 1989).

It is possible to reject a small part of the cosmic ray background through adjusting the aperture of the telescope so as to attempt to select photons making up the electromagnetic shower ring. Such an aperture cut, combined with a very tight timing cut can be marginally effective is differentiating between the two showers; however, this hardware and software cut is not as effective as an imaging cut.

1.5.2 Cosmic Ray Rejection Based on Aperture Cuts

The data that will be discussed in this dissertation were taken with an aperture stop with a half opening angle of about 0.35°. This aperture is located in the focal plane of each mirror ~1/4 inch above the surface of the PMT (see Figure 1.11). The current telescope operates with a $\theta_{ap} = 0.32^\circ$ aperture, while the old telescope had $\theta_{ap} = 0.38^\circ$ for the 1987 Her X-1 data season.

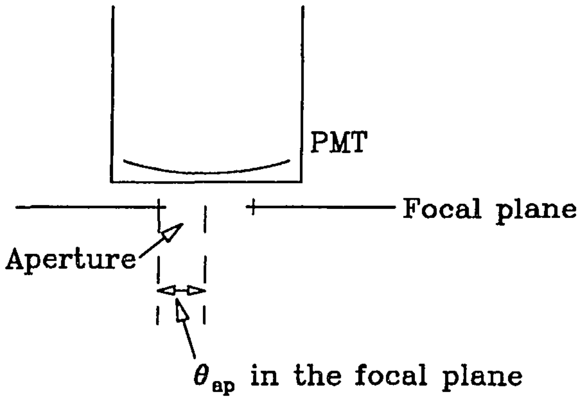

Figure 1.11: A diagram of the aperture position in front of the PMT.

The photon density as a function of radius employing a 0.35° half angle aperture (or angle) cut is shown in Figure 1.12. As in Figure 1.10, a 0.75 GeV γ shower and a 2 TeV proton shower are compared. Unlike Figure 1.10, there is little obvious difference between the two distributions, which is to be expected since in both cases, the photons accepted by the aperture cut are mainly those near the core of the shower, and the two showers look very similar near the core. The photon arrival time versus radius for these two showers is shown in Figure 1.13. The arrival times for the proton photons are not as uniform as those for the γ shower; however, there is very little difference in the width of these two showers as seen by a single telescope of a typical size.

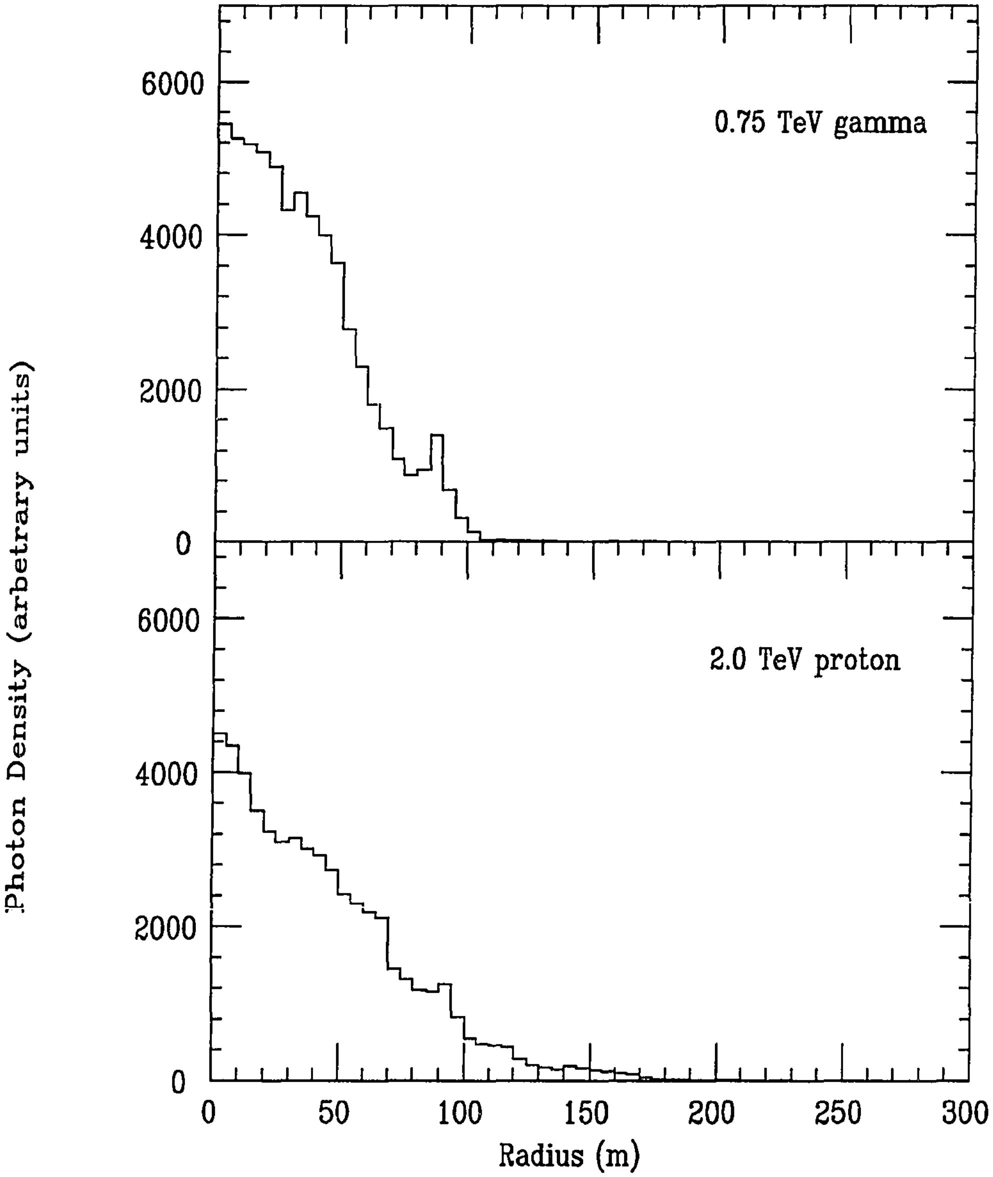

Figure 1.12: The photon density of a 0.75 TeV γ shower and a 2 TeV proton shower as a function of radius for an aperture with half angle 0.35°.

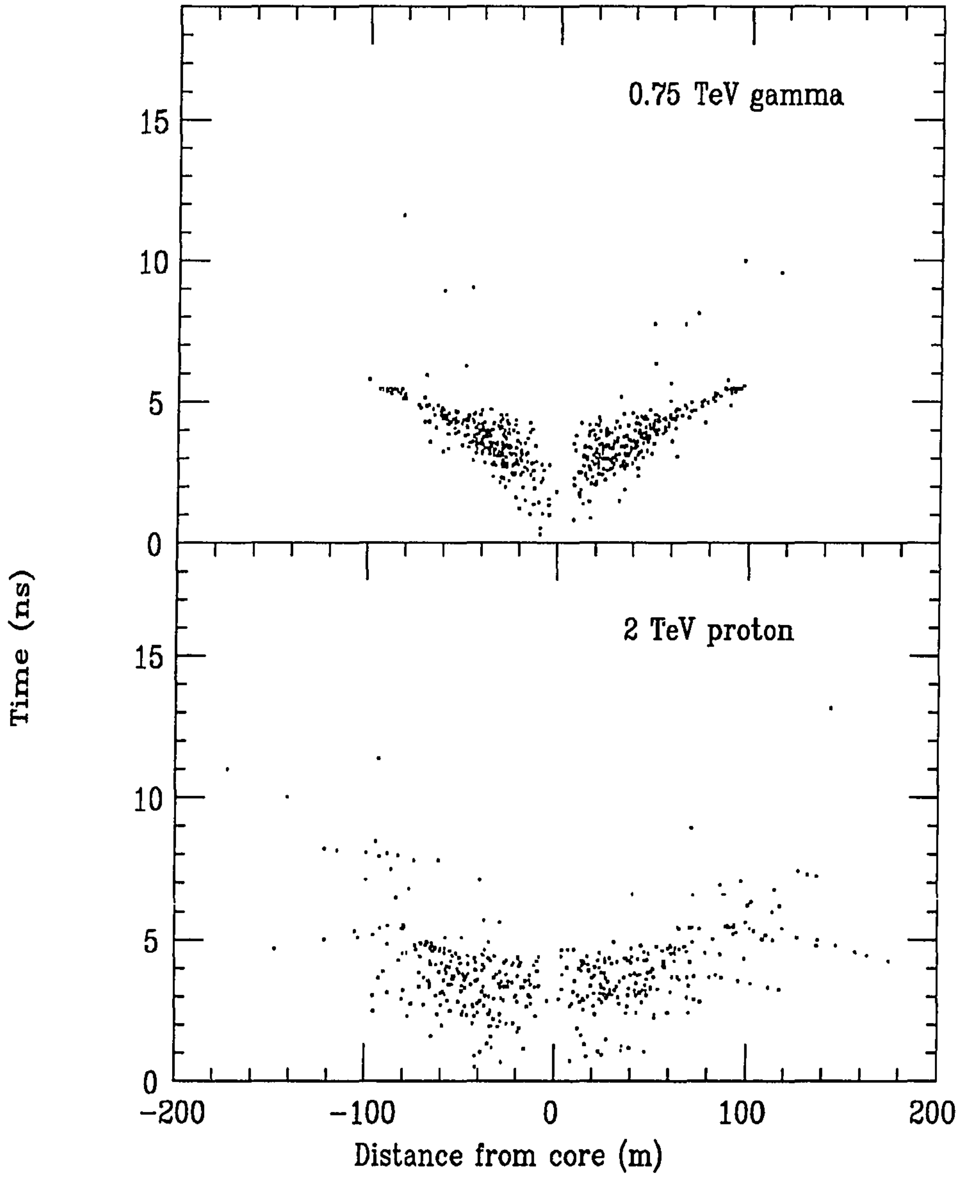

Figure 1.13: The arrival time of photons from a 0.75 TeV γ shower and a 2 TeV proton shower with for an aperture with half angle 0.35°.

In the final step of the Monte-Carlo simulation, the probability that a shower will trigger the telescope is estimated by moving a simulation of the new Haleakala telescope in 4 meter steps through a grid at the altitude of the observatory (4×4 m^2 are the approximate overall dimensions of the telescope). The total size of the grid is 400×400 m^2. At each step in the grid, the total telescope multiplicity can be calculated for a given time window. The efficiency of the PMT's, the reflectivity of the mirrors, the transmissivity of the filters, and other possible attenuation factors are taken into account through the introduction of an overall efficiency factor of 0.065. One can then determine if the telescope would be triggered, or if it would pass any other software cuts based on multiplicity at that position in the grid. Figure 1.14 are these trigger distributions for both proton and γ showers for a 0.35° aperture.

After the total number of triggers in the grid has been determined for showers of a given energy, the expected rate at that energy is calculated. Since proton showers are assumed to be isotropic, the contribution from off-axis protons must also be calculated. This contribution is calculated at an incident energy of 1 TeV, at angles out to 2° off-axis. The position of the telescope remained the same in these simulations, that is it remained pointed at zenith, while the direction of the incident particle was rotated in the y direction by multiples of 0.25° out to 1.0° , then in 0.5° steps out to 2.0° . As we will see, past 2.0° off-axis, the contribution to the total detected rate is small. From this determination of the rate as a function of angle off-axis, the total contribution to the proton rate can

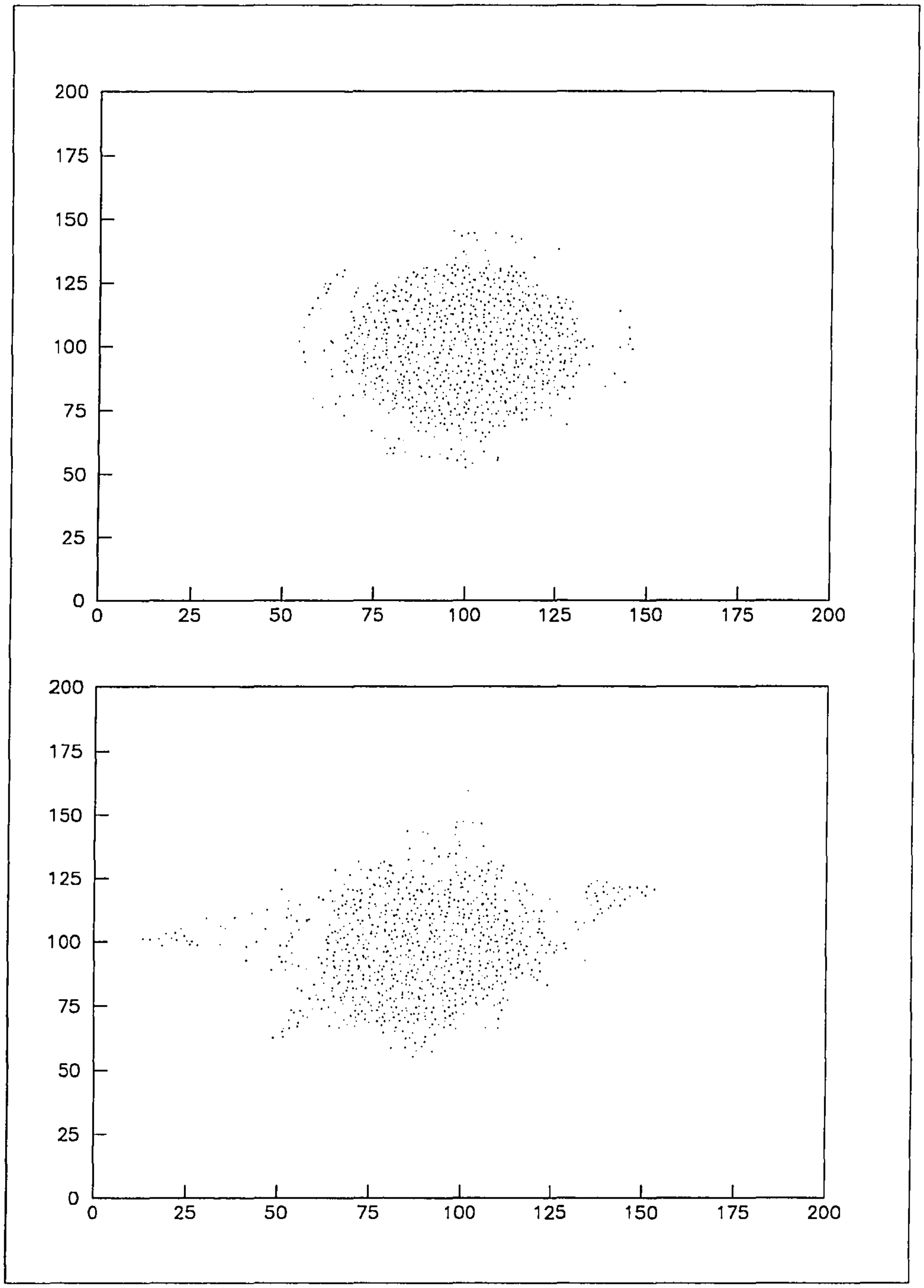

Figure 1.14: The trigger distribution for a 0.75 TeV γ shower (upper plot) and a 2 TeV proton shower (lower plot) with the usual 0.35° half angle aperture. The shower core is at 100,100 and the scale is 2 m/count.

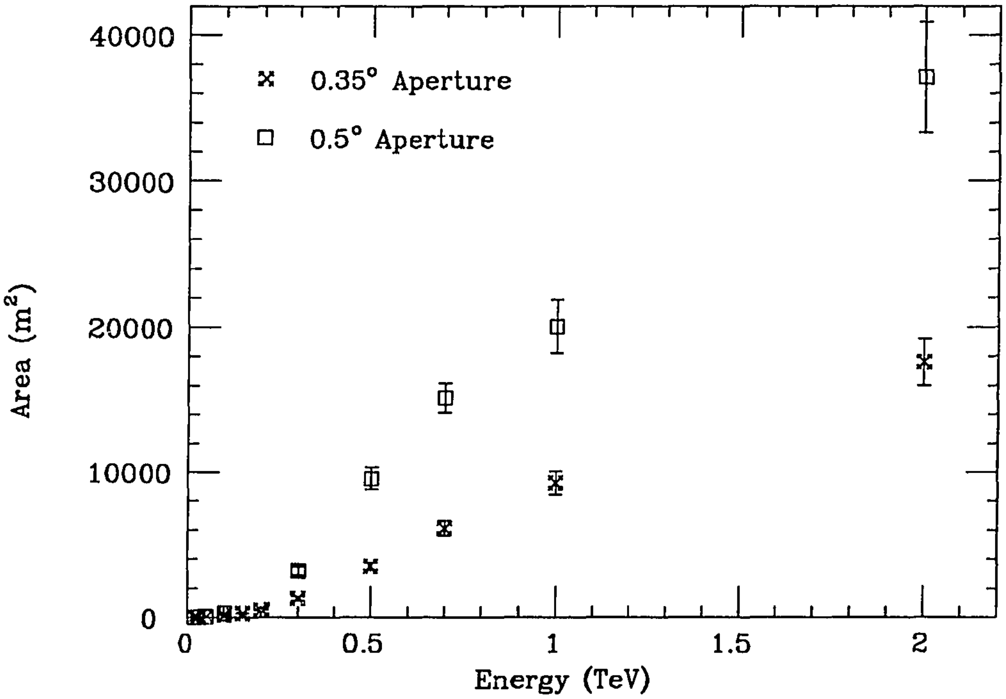

Figure 1.15: Effective area for proton showers.

be determined for different aperture sizes. A cut of 12 hits in a 5 ns window was used for the following analysis.

The effective area for a simulation, presented in Figure 1.15, is found by multiplying the number of triggers by the total area of the simulated array (16 m^2). In this figure, the effective area for a 0.35°aperture and a 0.5°aperture are presented. A functional fit is performed to determine the area as a function of the angle off-axis:

$$A(\theta) = A\theta_{ap}^2(0.5 + \theta)^B \exp(-C\theta) \tag{1.18}$$

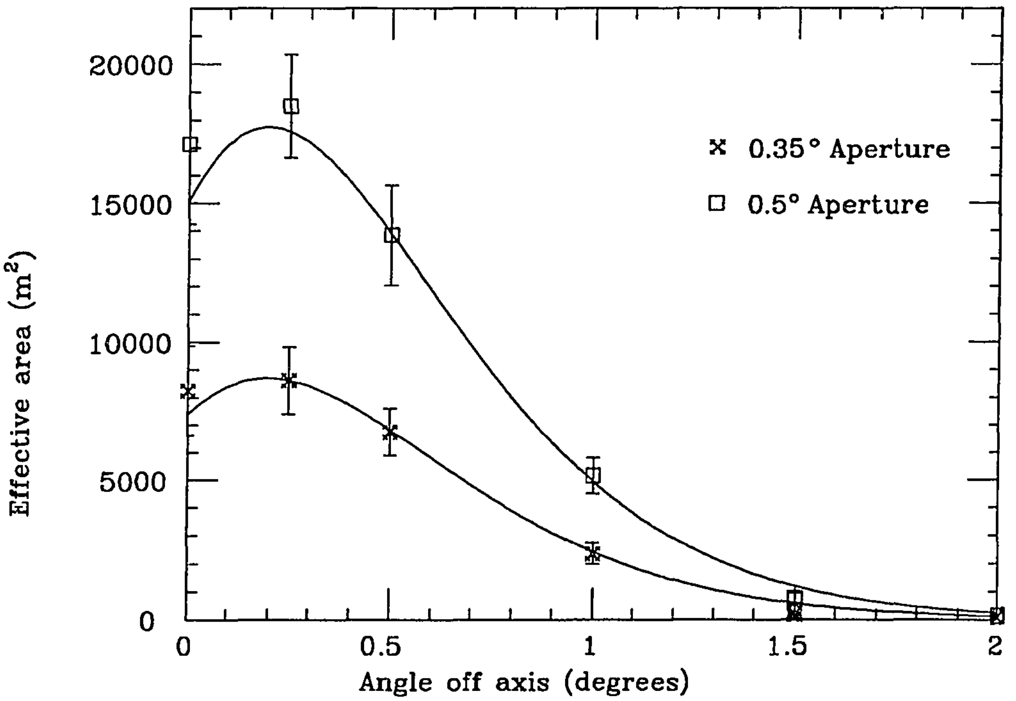

Figure 1.16: The Area as a function of angle off-axis for $\theta_{ap} = 0.35°$ and $\theta_{ap} = 0.5°$.

The dependence on θ_{ap}^2 is expected from geometric considerations, since the effective target area increases as θ_{ap}^2. A, B, and C are constants chosen to fit the data. From this fit we find:

$$A = 5.9565 \times 10^5 \text{ m}^2$$

$$B = 3.3062$$

$$C = 4.7435$$

$A(\theta)$ is presented for two different apertures in Figure 1.16. This same functional fit, with a different scaling factor A determined from the on-axis area, can be used to approximate the off-axis contribution for different aperture sizes.

$A(\theta)$ must be integrated over all θ to determine the total rate. To simplify the integration, we choose the angle limits of 0° → 30°, since as we can see from Figure 1.16, the area has dropped to zero long before this off-axis angle. The rate is then:

$$R = \int_0^{\frac{\pi}{2}} 2\pi \sin\theta A(\theta) d\theta \tag{1.19}$$

This is integrated numerically. Figure 1.17 is the result of this at a range of energies for $\theta_{ap} = 0.35°$. Notice from this figure that, even Figure 1.15 appears to indicate that the effective area for proton showers has dropped to zero at $\sim$ 0.15 TeV, the Monte-Carlo detected rate does not begin to fall until $\sim$ 0.03 TeV. This indicates that, because of the rapidly falling cosmic ray spectrum, even a very small effective area at low energies will translate into an appreciable detected rate.

Since γ showers are assumed to come from point objects, we need only consider the on-axis contribution. The effective area for these showers is presented for these showers in Figure 1.18.

The expected rate as a function of energy, Figure 1.19, may be determined by multiplying the effective area by a flux, which was chosen here to be 10^{-11} sec^{-1}cm^{-2}, for an integral spectrum $\propto E^{-1}$. This rate is presented for a telescope aperture of 0.35°. From this the predicted threshold for γ showers is about 0.1 TeV.

Using the information learned from Figures 1.15 and 1.18, as well as the expected off-axis dependence for different apertures, we are in a position to determine

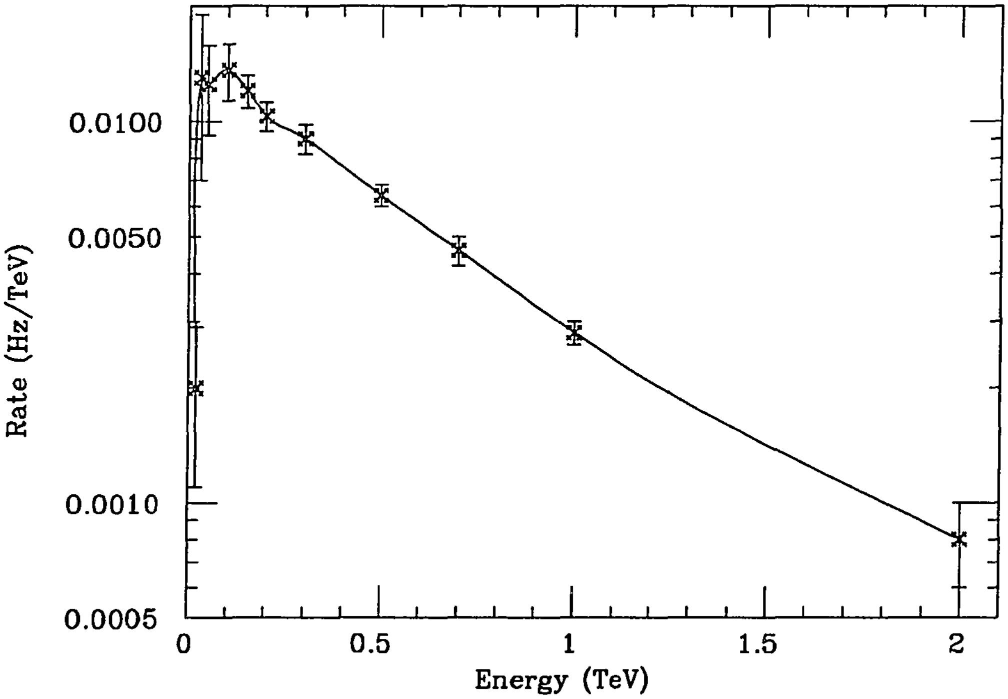

Figure 1.17: The proton rate as a function of energy for a 0.35° aperture.

an optimum (or at least a better) aperture configuration for the Haleakala telescope. We will consider two different strategies: the first attempts to select photons in the tight timing ring, while the second is just an increase in the aperture size to accept a larger portion of shower photons.

Annular Aperture and Other Aperture Sizes

A simple minded approach to select the photons that make up the tight timing ring is to require that the photons arrive at a half angle of about 0.7°, since this corresponds to the angle of Čerenkov emission at shower maximum. Using an

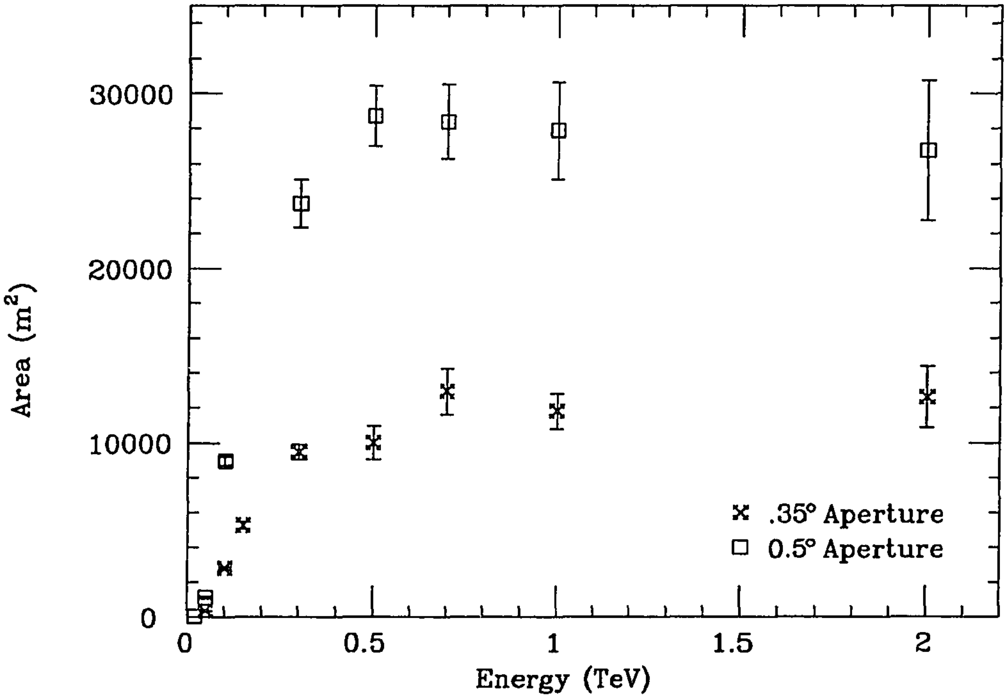

Figure 1.18: The effective area for γ showers as a function of energy.

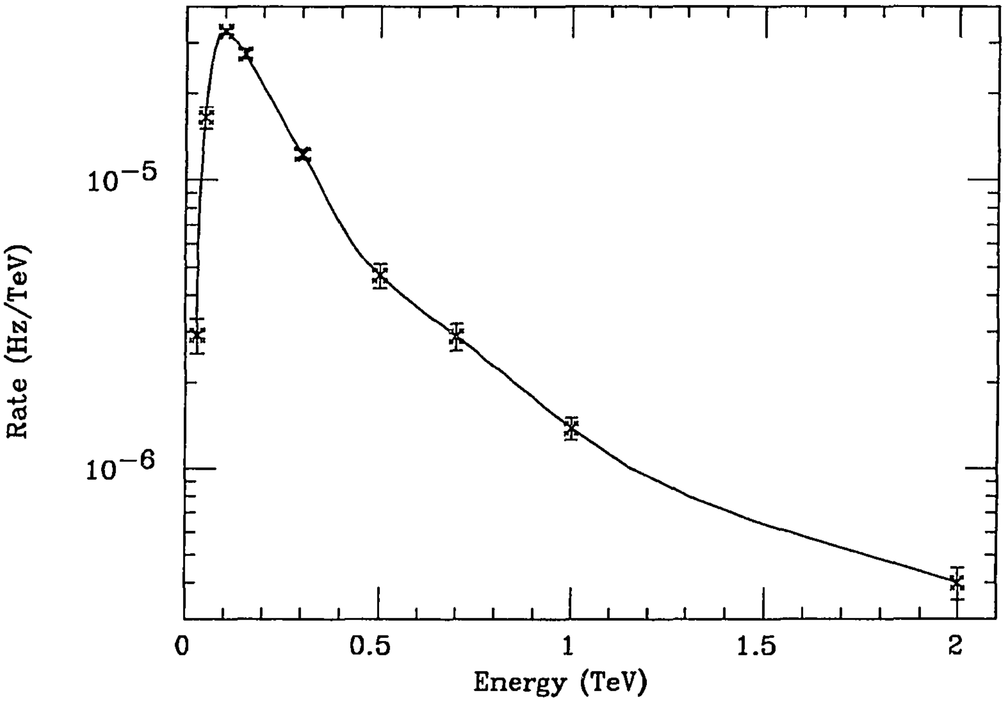

Figure 1.19: The relative rate for gamma showers as a function of energy for a 0.35° aperture.

annular cut with the opening angle of the annulus being 0.7° - 0.75°, the same set of photon density and arrival time plots are generated in Figures 1.20 and 1.21. The arrival times for the γ photons are very tight over nearly the entire area within which the telescope would be triggered. As is shown in Figure 1.22, which is the trigger distribution for a γ and proton shower using this annular aperture, the cut does trigger on photons in the ring of the γ shower. Comparing these plots to those for a 0.35° aperture from Figure 1.14, it appears that the number of proton triggers has been reduced. We will examine this more quantitatively below. Representative plots of the arrival time of photons for a telescope located at 90 m from the core of both showers is shown in Figure 1.23. The FWHM of the γ shower is typically 0.7 ns whereas the FWHM for a proton shower is $\sim$ 2 ns. For these Monte-Carlo generated showers, it is possible to separate proton and γ showers using both an annular aperture and a tight timing software cut.

The effectiveness of these cuts for rejecting off axis showers must also be investigated. Although the line corresponding to the direction of both proton and γ showers is referred to as the core of the shower (for the γ shower, it does represent the sole core of the shower) the proton shower, as we have seen, may contain several sub-cores from showers generated from cascade pions. These sub-cores may be as tight in time as the ring of γ showers, so they are a concern for both on- and off-axis showers. The degree of proton rejection was determined for showers ranging from on-axis to 2° off-axis using the same method as was described above: the telescope was simulated over a grid in 4 m steps. The grid was enlarged to a

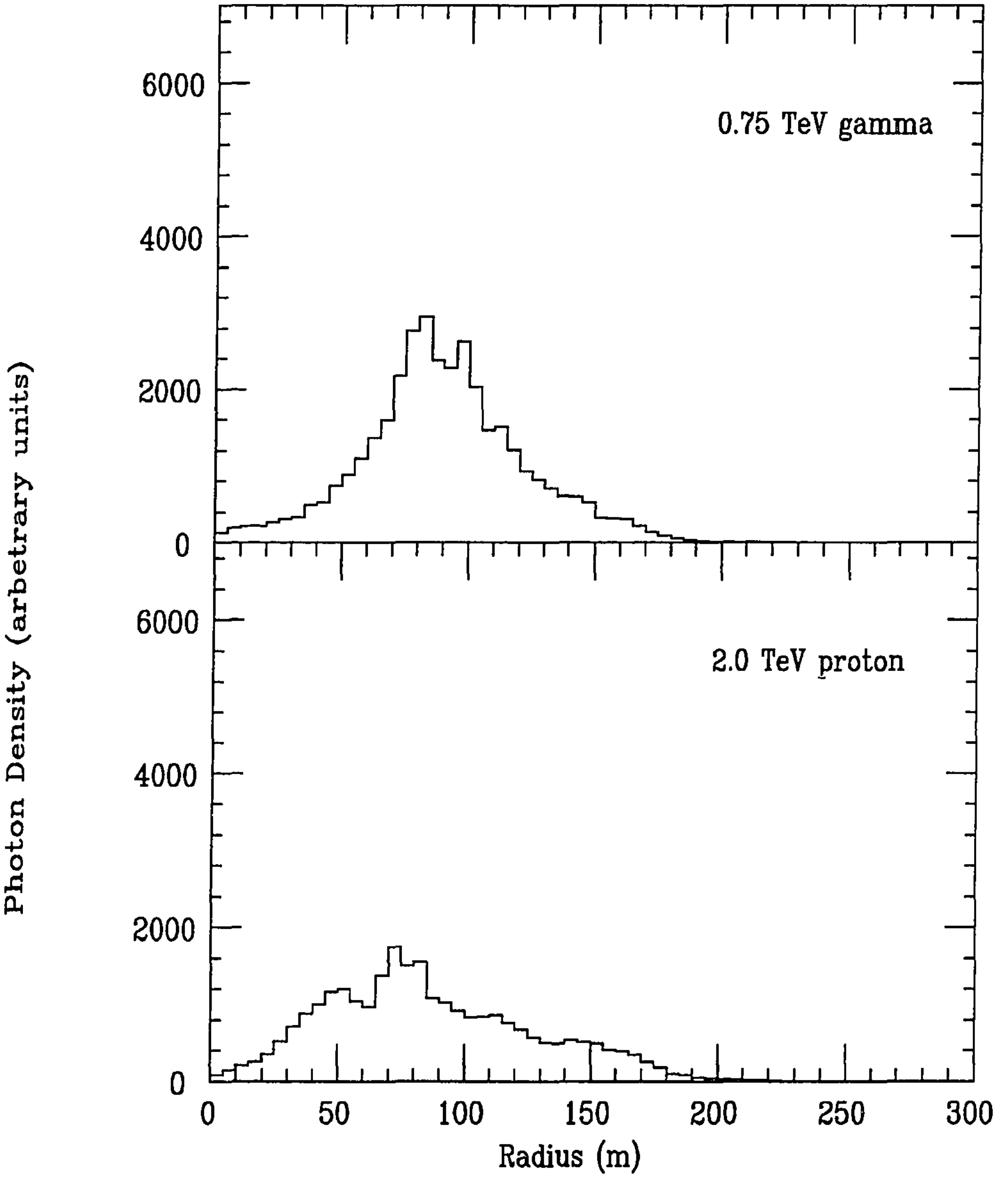

Figure 1.20: The photon density of a 0.75 TeV γ shower and a 2 TeV proton shower as a function of radius for an annular aperture with half angle 0.7° - 0.75°.

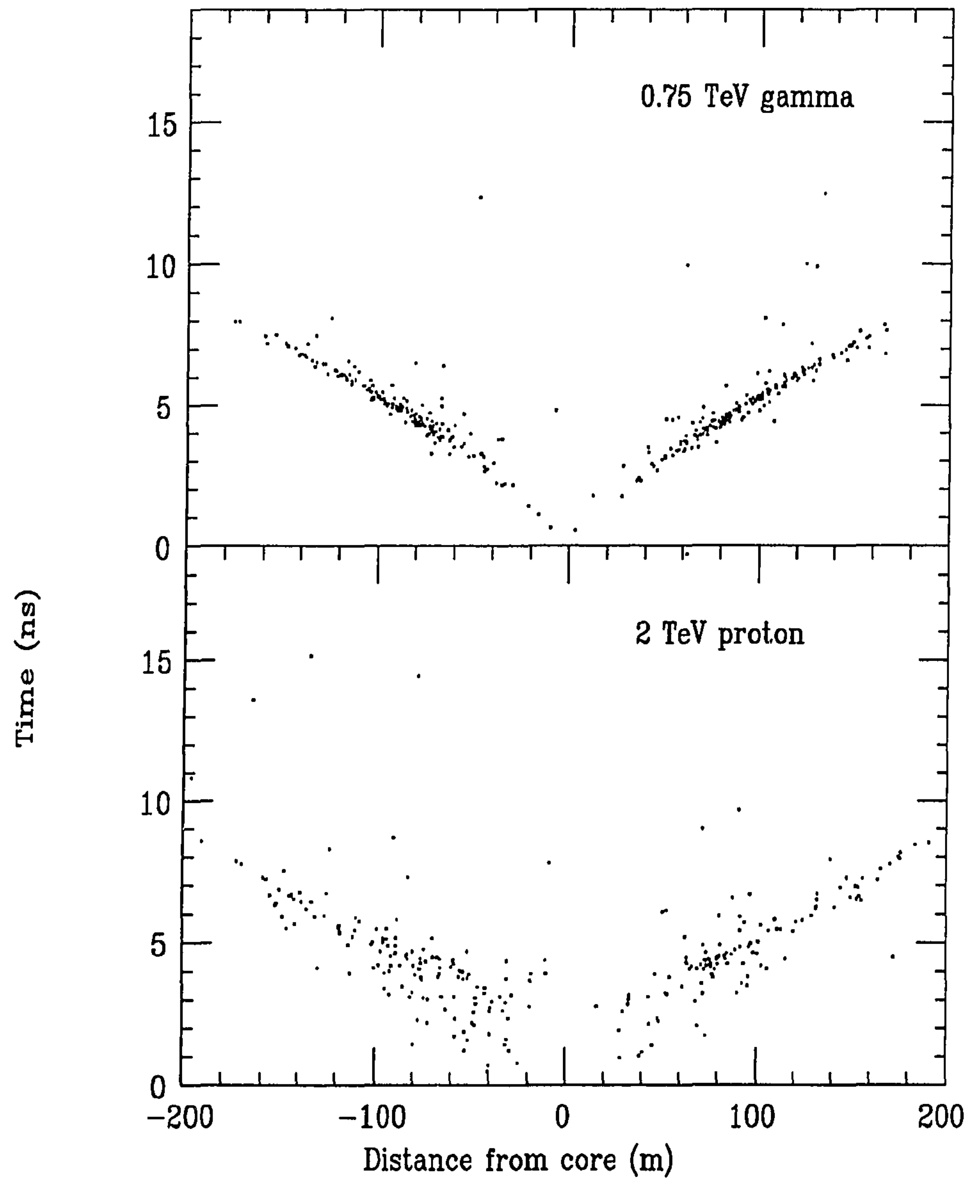

Figure 1.21: The arrival times of photons for a 0.75 TeV γ shower and a 2 TeV proton shower as a function of radius for an annular aperture with half angle 0.7° - 0.75°.

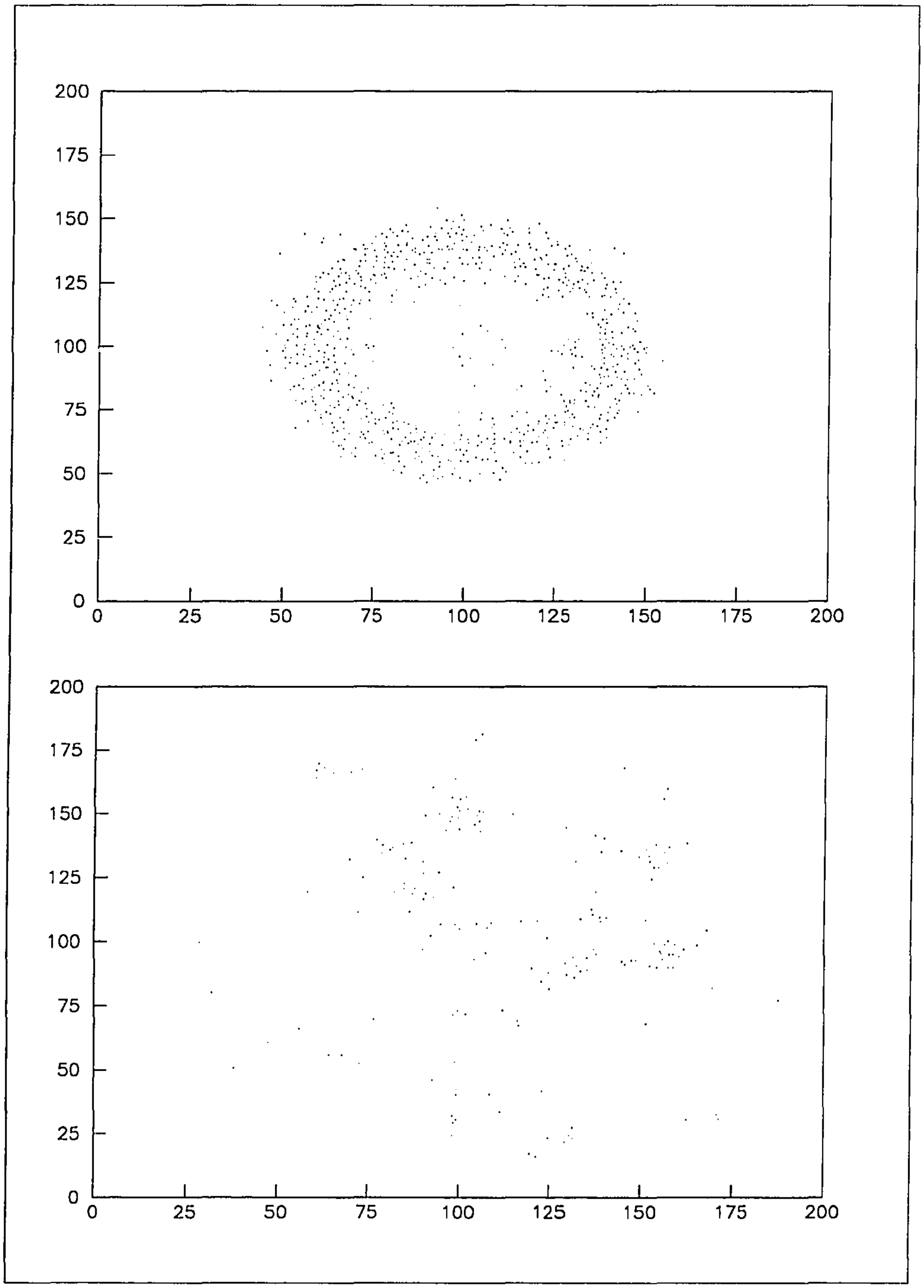

Figure 1.22: The trigger distribution for a 0.75 TeV γ shower (upper plot) and a 2 TeV proton shower (lower plot) with an annular aperture. The shower core is at 100,100 and the scale is 2 m/count.

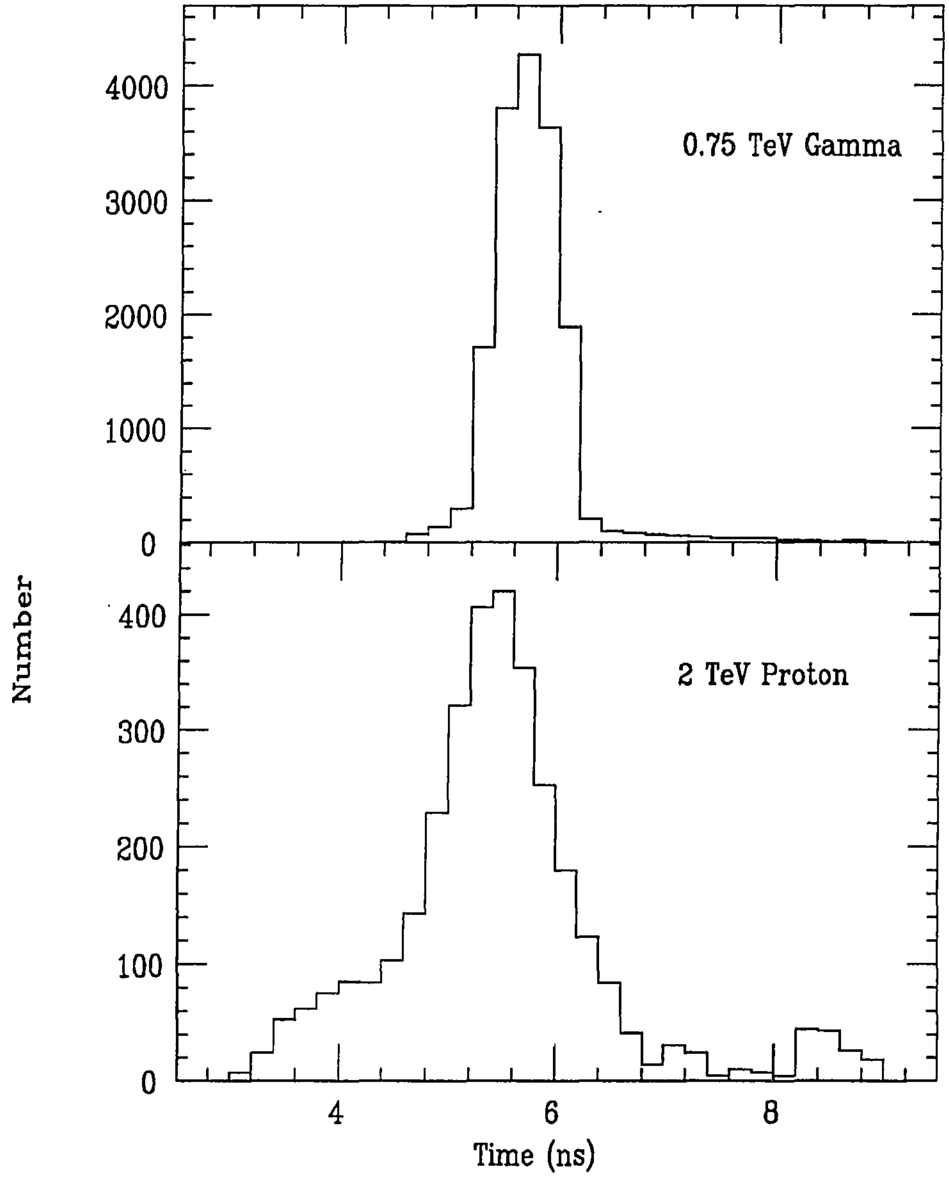

Figure 1.23: The arrival times of photons near a radius of 90 m for a 0.75 TeV γ shower and a 2 TeV proton shower for an annular aperture with half angle 0.7° - 0.75°.

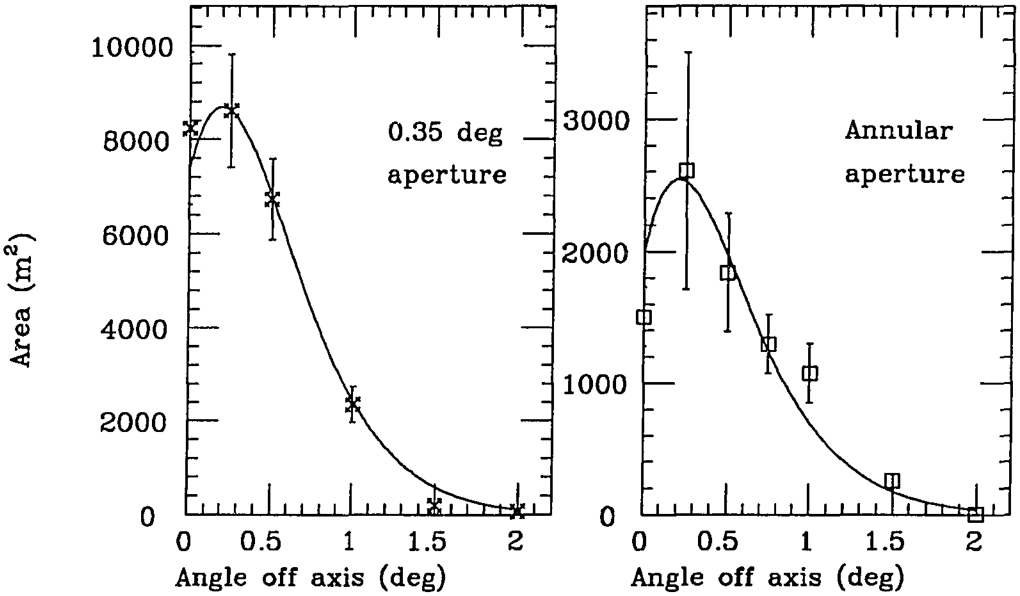

Figure 1.24: The effective area for on-axis ($\theta = 0.$) showers and off-axis showers averaged for five 2 TeV proton showers.

total area of 440 × 440 m^2, and as before, the shower was rotated in 0.25° steps away from zenith.

Again, 2 TeV proton and 0.75 TeV γ showers were simulated. The degree of shower rejection was comparable for both the 0.35° half-angle aperture and the 0.65° - 0.75° annular aperture (Figure 1.24), though the annular aperture shows a slightly worse off-axis rejection for small off-axis angles. This plot represents the average of 5 proton showers.

Figures 1.13 and 1.21 indicate that a tight timing cut can also aid in proton shower rejection for this annular aperture. The problem here is a practical one. In order to make a tight timing cut pay off in this case, one needs to make a *very* tight timing cut, which is only possible to the precision of ones timing calibrations. If one *could* make a 1 ns window cut, then based on telescope trigger simulations (specifically, requiring the total number of hits (N) to be greater than 10 and requiring that N-2 of these hits occur within 1 ns), the signal to background enhancement would be approximately a factor of 1.8. Here, signal to background is defined as the rate of gamma showers divided by the square root of the proton rate.

We can use Figures 1.15 and 1.18, along with the expected off-axis contribution for proton showers, to determine the expected signal to background rate for larger telescope apertures. These estimates are presented in Table 1.1. The signal to background ratio increases as the aperture size increases, up to an aperture of about 1.5°–2.0° after which it should decline, as off-axis proton showers become more of a problem. This result is not so surprising when one considers Figure 1.10. The photon density for γ showers falls off more slowly than that for proton showers out to a radius of $\sim$ 400 m from the core after the ring at $\sim$ 100 m.

An important point to be made here is that we have considered the background as just $\sqrt{R_p}$, we have not included background from random light, and other such noise. This background will decrease our signal to background ratio for larger apertures. For the Haleakala telescope, this background will limit our aperture size,

Table 1.1: Signal to background rejection compared to a 0.35° aperture.

Aperture Size (°)	$S/B(\theta_{ap})/S/B(\theta_{0.35})$
0.50	1.4
0.75	2.0
1.5	2.7
2.0	2.8
2.5	2.7

since event rates become unmanageable, unless the individual phototube sensitivity threshold is raised above the 1 PE level.

Chapter 2

The Binary Pulsar Hercules X-1

The eclipsing binary system Her X-1/HZ Her has been observed in many energy bands, from infrared and visible energies, up through VHE and UHE gamma-rays. In this chapter, a brief summary of past observations of Her X-1 in the higher energy range (X-rays and beyond) is presented. The orbital parameters measured and derived from X-ray and optical observations are also discussed. We will approach these in order of increasing photon energy, rather than in a chronological order of time of discovery.

2.1 Optical Observations

Optical pulsations from the HZ Her/Her X-1 system were discovered shortly after the discovery of X-ray emission from this source (Davidsen, *et al.* 1972). Through and investigation of the observed pulse period, three separate sites of optical pulse production were identified in the system (Middleditch and Nelson, 1976). Two of these are at or near the surface of HZ Her, as identified by the very small Doppler shift observed in their periodicity. They are clustered around two orbital phases separated by 0.5 in phase ($\phi_{orb} = 0.25$ and 0.75), and are assumed to be the product of reprocessing of X-rays (heating of the surface of HZ Her by X-rays from Her X-1). The third region exhibits a Doppler shifted period in close agreement with that of the pulsar, indicating that it must originate from very near the neutron star. This region could be from interactions of X-rays with matter near the neutron star, or directly from the neutron star, though the exact cause of these pulsations is not fully understood.

The small Doppler shift in these two regions near HZ Her allows a calculation of a range of mass ratios (M_{HZHer}/M_{HerX-1}) expected from the models of X-ray reprocessing . Geometric considerations allow the determination of this expected ratio as a function of the inclination angle of the orbit (i), which is angle ABC in Figure 2.1. If we assume that HZ Her fills its Roche lobe* then the mass ratio and the orbital inclination angle must be related for a given, fixed total time of eclipse. This time of eclipse is given from X-ray measurements to be 0.14 of the 1.7 day phase (Deeter, *et al.* 1981). These two constraints fix the value of the orbital inclination to be $i = 87 \pm 3^\circ$. From the mass function (Section 2.2) the individual masses can be calculated. Thus, it is the combined information from pulsations at orbital and X-ray energies that allow a precise determination of many of the orbital parameters which will be listed in Table 2.1.

---

*More recent calculations relax this requirement. Hutchings, *et al.* also use absorption and emission line spectroscopy to determine the radial velocity of HZ Her. Combining this with X-ray data for Her X-1 they find a much smaller neutron star mass (Table 2.1).

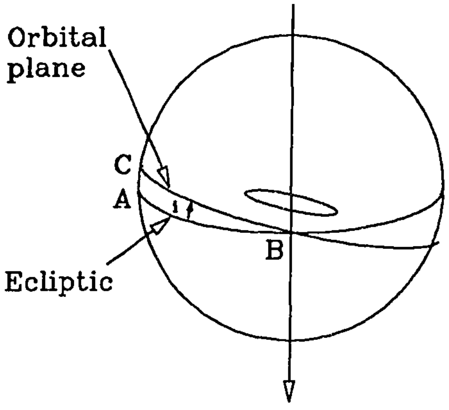

Figure 2.1: The orbital inclination angle (ABC) for a binary orbit.

2.2 X-ray Observations

Her X-1 has a relatively long history of observations in the field of X-ray astronomy. It was among the first of the X-ray binary sources observed by the Uhuru satellite. The observations of Centaurus X-3 (Giacconi, *et al.* 1971) and of Her X-1 (Tananbaum, *et al.* 1972) were the first two reported detections of X-rays coming from eclipsing binary systems. Subsequent observations of these and other such sources at both X-ray and radio energies, as well as optical observations of a (slightly higher mass) companion star established that the compact object in the binary system is a neutron star based upon the orbital parameters derived from these observations. Her X-1 exhibits three distinct periodicities: a ~ 1.24 second pulse period, a ~ 1.7 day orbital period and a ~ 35 day variation in the X-ray intensity. We will discuss these beginning with the least understood periodicity: the 35 day variation.

The 35 day variation in the observed X-ray flux may be divided into a "high on" region, which covers a 35 day phase (ϕ_{35}) of $0.0 \leq \phi_{35} \leq 0.4$, and a "low on" region, covering $0.6 \leq \phi_{35} \leq 0.8$. These are separated by "off" regions, during which the X-ray flux decreases by at least 97% from the high on maximum (Figure 2.2). Typically, the high on X-ray maximum is ~ 100 mcrab (where 1 crab is the X-ray intensity of the Crab, the brightest pulsed X-ray source in the sky). The low on X-ray maximum is typically 30 mcrab.

Several possible explanations for this 35 day variation exist. Two widely discussed models involve the precession of the accretion disk obscuring an X-ray beam, or the precession of the neutron star around its rotation axis. In support of a neutron star precession, one group has proposed that differences in the pulse profile between the two on regions suggest that they are due to two thin X-ray beams originating from two separate poles of the star (Trümper, *et al.* 1986). Using EXOSAT data, the X-ray light curves during the high on portion of the cycle show a main, two peaked pulse followed by a small interpulse. During the low on portion of the 35 day phase, the interpulse is actually larger than the main pulse, as defined from the high on interval. In addition, substructural changes occur in these pulses between the two on regions. They suggest that the main pulse and the interpulse are two separate polar X-ray beams. One beam which is nearly in the

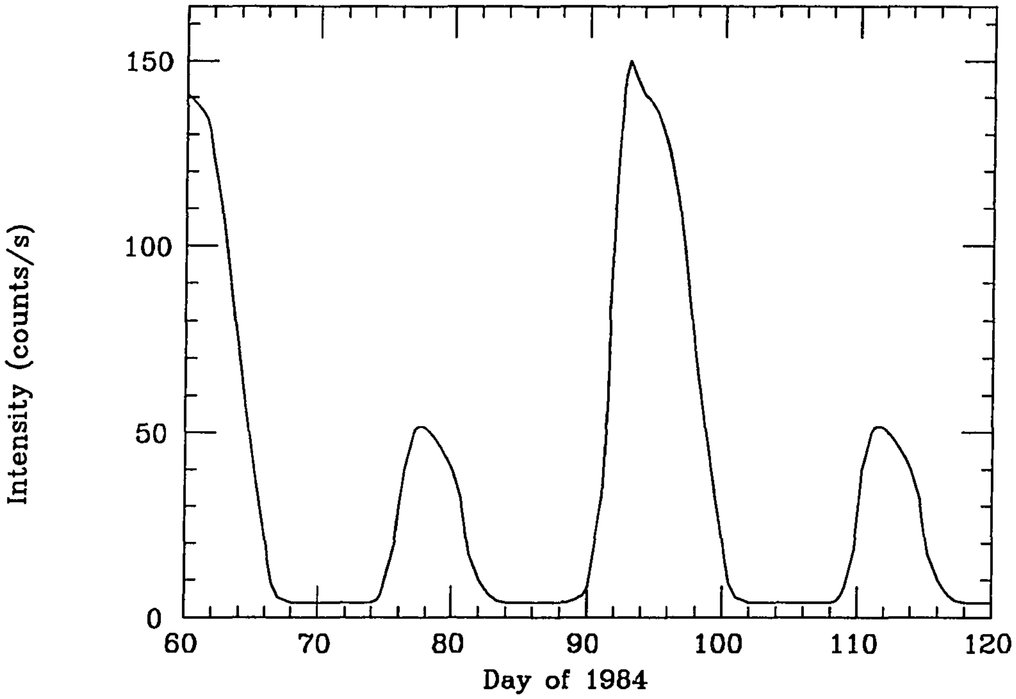

Figure 2.2: Her X-1's 35 day variation from Uhuru and EXOSAT X-ray data.

line of sight during the high on phase, and a weak second beam which produces the small interpulse during the high on phase. As the neutron star precesses, this weak beam is viewed more strongly during the low on phase, while the main beam is now reduced in observed intensity by the precession. While precession is expected to produce a precise periodicity (which the 35 day periodicity is not: variations of as much as 10% are observed from interval to interval), Trümper, *et al.* estimate that perturbations, such as could be caused by movement of the stellar crust could account for such variations.

It has been established that the observed change in the spin-up rate which began in 1980 corresponded to a change in the 35 d cycle as well (Ögelman, *et al.* 1985). This change in the spin-up rate will be mentioned further below. If the change in $\dot{P}$ is attributed to a change in the mass accretion rate ($\dot{M}$) then this change is on the order of $(\delta\dot{M}/\dot{M}) \sim -10^{-2}$. If this is the case, then such stellar precession models could be questioned, since one would not expect such a direct correlation between a change in $\dot{M}$ and the precession rate of the star. Since the precession model discussed above was based upon data taken while the spin-up rate was nearly zero, this data would first need to be compared to data taken during a (normal?) spin-up torque interval*, before statements could be made about the observed effect of $\delta\dot{M}$ on the precession.

The pulse period of Her X-1, originally observed by the Uhuru satellite, has been recorded by many satellite and balloon X-ray detectors (Figure 2.3). The rotation of Her X-1 has been observed to undergo a spin-up phase with a measured period change of $\dot{P} = -2\ X\ 10^{-13}$, and a time of relatively constant rotation. From it's detection in 1971 through 1980, the neutron star is observed to be spinning up, while from 1980 through 1984 no significant change in the pulse period is observed. Recent measurements from the GINGA satellite indicate that Her X-1 is once again spinning up with approximately the same period derivative as was observed in the 1970's (Boynton, 1990).

The fluctuations in the rotation rate are caused by either a change in the accretion rate, and thus the accretion torque produced (as was mentioned before),

---

*Such an interval appears to be currently occurring during recent GINGA measurements.

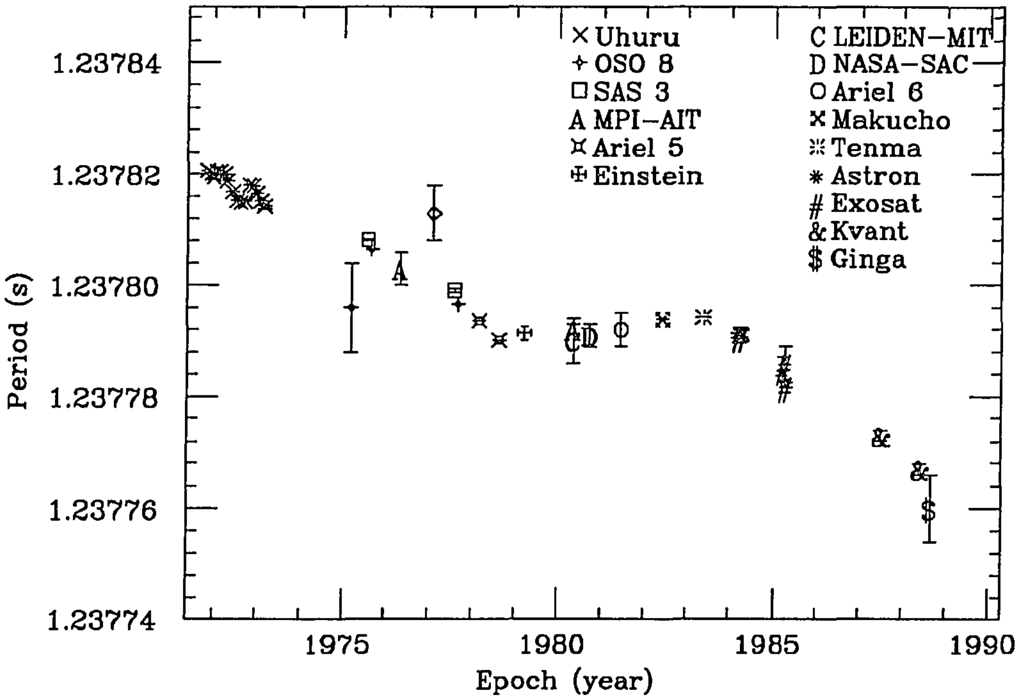

Figure 2.3: The pulse period of Her X-1 as a function of observation date.

or by internal effects, such as the coupling between the neutron star crust and its superfluid core. It is difficult to determine whether it was an external or internal event causing the spin up change, since only the final effect of the event is observed, and that final observation is consistent with both events. In any case, the impact of these changes in $\dot{P}$ is negligible for the VHE γ-ray observer since, over the span of a year, they are small compared to the period resolution of typical VHE measurements. Also, intervals searched for periodicity are typically very short (less than about 30 minutes) so that the period shift due to $\dot{P}$ is negligible over this interval. Usually, it is possible to obtain pulse measurements from X-ray data taken within one year of the VHE data being analyzed.

Table 2.1: Source parameters

Quantity	Symbol	Value	Reference
Pulsar epoch	T_{0p}	5478.0 JD-2440000.	(a)
Pulsar period	P	1.2377914 ± .00000010s	(a)
Pulsar period derivative	$\dot{P}$	-2×10^{-13}	(b)
Orbital epoch	T_{0orb}	2859.726688 JD-2440000.	(c)
Orbital period	P_{orb}	1.700167788 ± 0.000000011d	(c)
Orbital period derivative	$\dot{P}_{orb}$	$< 2 \times 10^{-10}$	(d)
Projected semimajor axis	$a_x \sin \imath$	13.1831 ± 0.0003ls	(c)
Eccentricity	e	< 0.0002	(c)
Orbital velocity	$v \sin i$	169.049 ± 0.004 km/s	(c)
Companion orbital velocity	K_c	83 ± 3 km/s	(e)
Her X-1 projected velocity	$v_x \sin i$	169.049 ± 0.004 km/s	(c)
X-ray eclipse 1/2 angle	Θ_c	24.4 - 24.7°	(e)
Mass function	f(M)	0.8510 ± 0.0001 $M_\odot$	(c)
35 day epoch	T_{035}	7642.2 JD-2440000.	(f)
35 day period	P_{35}	34.875 d	(c)
Other derived parameters (g)			
Her X-1 mass	M_x	0.98 ± 0.12 $M_\odot$	
HZ Her mass	N_c	$1.99^{+0.12}_{-0.14}$ $M_\odot$	
HZ Her radius	R_c	$3.86^{+0.28}_{-0.34}$ $R_\odot$	
Stellar separation	a	$8.61^{+0.22}_{-0.25}$ $R_\odot$	
Inclination angle	i	87. ± 3. °	

(a) Nagase, *et al.* 1984.

(b) From 1983 - 1989 measurements of the pulse period by the Tenma, EXOSAT, and Ginga satellites.

(c) Deeter, *et al.* 1981.

(d) Joss, *et al.* 1980.

(e) Hutchings, *et al.* 1985.

(f) Boynton, 1990.

(g) Nagase, 1989.

The orbital period of Her X-1 is well measured and its orbit is known to be nearly circular (no eccentricity has yet detected from the system). This was well determined by Deeter, *et al.* (Table 2.1) using data from Uhuru, OSO 8, and HEAO 1. Pulse timing analysis was performed on these data assuming a circular orbit, and the parameters obtained were found to agree with this orbit. The 2σ limit placed on the eccentricity was $e < 0.0003$, which is small enough to be ignored in orbital calculations. Deeter, *et al.* also measured the length of X-ray eclipse. This was found to be about 14% of its total orbit. The orbital period was calculated from this same, large set of X-ray measurements, allowing it to be determined to reasonable precision.

Table 2.1 summarizes the parameters associated with the pulse period, the orbital period and the 35 day long term variation. From the measurement of these parameters, other derived quantities are listed. The derived mass for Her X-1 is near the lower limit allowable for a neutron star.

This low mass is consistent with evolutionary models of accretion-induced collapse (AIC) for Her X-1 (Sutantyo, *et al.* 1986). Hz Her/Her X-1 is located very far from the galactic plane. Constraints on magnetic field decay from observations of radio pulsars lead to a maximum age of $\sim 10^7$ yr for the system. In order for this binary to reach its current position with a magnetic field of $\sim 10^{12}$ G, it would need to have acquired a large velocity in a direction out of the galactic plane when the neutron star was formed. The scenario investigated by Sutantyo, *et al.* assumes that Her X-1 was a white dwarf with a mass near the Chandrasekhar limit ($1.4\ M_\odot$). Its companion is a post-main sequence star with a mass of $\sim 2\ M_\odot$ that expands to fill its Roche lobe, after which, matter accreted onto the white dwarf pushes it over the Chandrasekhar limit. In the resulting explosion and collapse, a large amount of mass loss from Her X-1 is required to impart the necessary velocity to the system. This would produce a neutron star of $\sim 1\ M_\odot$ with a companion of slightly less than $2\ M_\odot$. They calculate that it would take HZ Her approximately 10^7 years to "refill" its Roche lobe (It must expand from a radius of $3.1\ R_\odot$ for Roche lobe filling in the white dwarf system to $3.7\ R_\odot$), which is in agreement with magnetic field constraints.

2.3 VHE Observations

In recent years, several observations of an apparent pulse period in the VHE and UHE ranges which is significantly different from the measured X-ray pulse period have raised questions about high-energy photon production mechanisms. UHE measurements of anomalous muon content associated with these showers have also raised additional questions concerning the behavior and nature of these particles at ultrahigh energies. A summary of these and other detections of Her X-1 above 10^{11} eV is presented in Table 2.2. If pulsed emission was observed, the period detected is listed. The column labeled "sig." represents a measure of the significance of the result: for a periodic detection, this is the chance probability and for a non-pulsed result, this is the DC excess in standard deviations. As can be seen in Figure 2.4, the differential flux approximately follows an E^{-2} spectrum throughout this energy range.

Table 2.2: VHE detections of Her X-1

Date	Period (s)	ϕ_{35}	ϕ_{orb}	Flux $(cm^{-2}s^{-1})$	E_{th} (TeV)	Sig.	Ref.
4/17/83	1.23739 ±0.00115	0.98	0.76	$3.0 \pm 1.5 \times 10^{-11}$	1.	.001	(a)
7/83	1.23771 ±0.0004	–	–	$3.3 \pm 1.1 \times 10^{-12}$	500.	.016	(b)
4/4/84	1.23770 ±0.00014	0.20	0.40	$3.1 \pm 1.5 \times 10^{-10}$	0.25	.16	(c)
5/5/84	1.23726 ±0.00006	0.08	0.60	$1.8 \pm 1.1 \times 10^{-10}$	0.25	.003	(c)
5/23/84	1.23721 ±0.00014	0.60	0.18	$3.7 \pm 2.0 \times 10^{-10}$	0.25	.05	(c)
6/16/85	1.23673 ±0.00004	0.36	0.95	1.5×10^{-10}	0.6	.007	(d)
5–7/85	–	–	–	$3.9 \pm 1.6 \times 10^{-13}$	100.	2.4σ	(e)
4/11/86	–	0.31	0.19	1.8×10^{-8} (!)	0.4	42σ	(f)
5/13/86	1.23593 ±0.00018	0.22	0.81	5×10^{-10}	0.3	.007	(g)
6/11/86	1.23579 ±0.00025	0.30	0.70	2×10^{-10}	0.6	.01	(h)
7/24/86	1.23575 ±0.00040	0.23	0.80	2×10^{-11}	50.	.00005	(i)
7-12/86	1.2358 ±0.0001	–	–	–	100.	.0062	(k)
7/12/88	1.2376 ±0.0002	0.02	0.66	4.7×10^{-10}	2.	.013	(j)

(a) Dowthwaite, *et al.* 1984. (Dugway)
(b) Baltrusaitis, *et al.* 1985. (Flys Eye)
(c) Gorham, *et al.* 1986a. (Whipple)
(d) Gorham, *et al.* 1986b. (Whipple)
(e) Sinha, *et al.* 1990. (KGF)
(f) Vishwanath, *et al.* 1989. (Pachmarhi)
(g) Resvanis, *et al.* 1988. (Haleakala)
(h) Lamb, *et al.* 1988. (Whipple)
(i) Dingus, *et al.* 1988. (Cygnus)
(j) Rawat, *et al.* 1990. (Gulmarg)
(k) Gupta, *et al.* 1990. (Ooty)

Two VHE γ-ray groups (employing our telescope on Haleakala and the Whipple telescope on Mt. Hopkins in Arizona) observed an anomalous periodicity from Her X-1 during the summer of 1986. The 15 minute interval observed on Haleakala (Slane, 1988; Resvanis, 1988) occurred on May 13, 1986 beginning at 48940.98 s UT. The observed period was 1.23593 ± 0.00018 s. The probability that this event was due to random background fluctuations is 0.007 The Whipple group observed an interval of 25 minutes in length on June 11 of that same year. This interval had $P = 1.23579 \pm 0.00025$ s and a chance probability of 0.01. These two periodicities are in very good agreement, and both differ from the interpolated X-ray period by more than two times the expected orbital doppler shift (Figure 5.6). This difference cannot be explained by the changes in $\dot{M}$ we discussed earlier.

Above 10^{15} eV, the Cygnus air shower array observed a significant excess of events from Her X-1 on July 24, 1986 in two 30 s intervals (Dingus, 1988). The two intervals were found to exhibit periodicities of 1.23572 ± 0.00040 s and 1.23575 ± 0.00030 s, in agreement with those quoted above. The chance probability of this observation is 2×10^{-5}. This anomalous periodicity was accompanied by two other curious observations: the events in these two bursts were well above the energy threshold for the detector (calculated assuming the primary particle was a proton), and they contained a muon content which is over an order of magnitude larger than that expected from γ-ray simulations. The muon content was even larger than that expected from cosmic-ray showers, though this excess is only on a 2σ level overall. The anomalous muon content, which has also been observed from Cygnus X-3 (Samorski and Stamm, 1983), raises several questions. Either we are

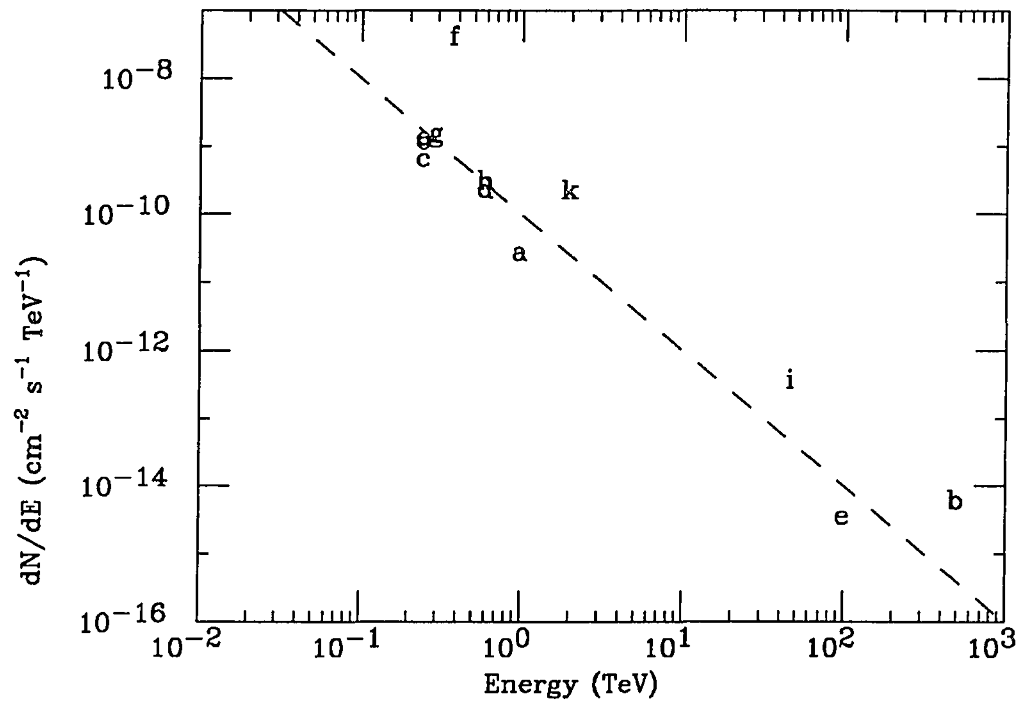

Figure 2.4: The differential flux measured as a function of energy for Her X-1. The dashed line is a $E^{-2.0}$ fit to the VHE pulsed data. The key to the symbols is found in table 2.2.

observing cosmic ray background which is mimicking a periodic signal and rate excess, or we do not understand photon interactions at very high energies, or it has been proposed that perhaps we are observing a new, previously undiscovered light, neutral particle.

Recently, the Ooty air shower array announced the detection of four episodes of periodicity from Her X-1 at the anomalous period (Gupta, 1990). These intervals, occurring during July – December of 1986, were further analyzed by the Ooty group and found to be nearly phase aligned (Gupta, 1991). They find that 26 of the 34 showers observed fall within the pulsar phase region of 0.11 – 0.38 given a search period of 1.2357701 s. From many simulations of four intervals exhibiting periodicity within the range observed by Ooty and separated by the interval spacing they observe, they estimate that the chance probability of this alignment is 6.2×10^{-3}. As additional confirmation, the Ooty group tested the Cygnus detection, which occurred between the first two Ooty intervals, using their phase aligned period. The Cygnus events fell nearly within the Ooty interval (0.14 – 0.49). If these events are correlated in pulsar phase over such a long time, it would indicate that this blue shifted period could be a stable feature of the Her X-1 system.

There is an obvious danger in attempting to phase lock signals in gapped data, since a small change in the search period will cause two intervals to align for an interval separation that is much larger than the search period (as is the case here). Objections have been raised to such searches of gapped data (Lewis, *et al.* 1991) claiming that the incoherent signals have a high probability of adding coherently when performing such a period search. Lewis, *et al.* determine the 0.01 and 0.001 probability thresholds for a value they call the coherence parameter, $\Gamma = P_{max}/P_{inco}$, which is a measure of the amount of the incoherent contribution to the observed power when a scan has been made in period space to attempt to align a given number of intervals of periodicity. P_{max} is the observed Protheroe or Rayleigh power and P_{inco} is the incoherent sum of the Protheroe or Rayleigh amplitudes (as defined in Section 4.4). Using the duty cycle estimated by the Ooty group (8.3%) and their reported Protheroe statistic (10.3) the chance probability of coherence according to Lewis, *et al.* would be on the order of 1% for 4 measurements, which they claim is not strong evidence for source coherence. This observed Protheroe statistic was determined from the 26 phase aligned events in the 34 event sample. If all 34 events are used, then the observed Protheroe power is 8.3, and the interval is not statistically significant according to the Lewis, *et al.* criteria.

Models to explain the shifted period were proposed after the anomalous periodicity was observed. One such model (Cheng and Ruderman, 1988) assumes a situation similar to the Király and Mészáros model for VHE photon emission discussed in Chapter 1. A beam of protons traveling out along polar field strikes the accretion disk. They assume that the main part of the disk is dense enough to absorb the produced γs. A less dense window in the disk is formed traveling inward toward the magnetospheric surface with a radial velocity v_r. Protons that strike matter in this window produce photons that can escape without appreciable pair production losses. Both the radial movement of this target and the radial dependence of the magnetic field will produce a period which is slightly shorter than the rotational period of the star. In another model (Slane and Fry, 1989), the target is a small piece of the accretion matter that has broken away from the accretion disk and is rotating at an increased Keplerian angular rotational velocity. If the polar beam is wide, then the target will be struck by different portions of this beam during each stellar rotation, producing a shorter period for the larger angular target velocity. It should be stressed that prior to these off period observations, no model predicting such a large period shift had been discussed, since such a periodicity was not expected. In fact, searches of early Her X-1 data taken by the Whipple and Haleakala groups, were not broad enough in period space to include this anomalous period.

An additional complication was added to the already confusing picture of Her X-1 by the Whipple group recently (Reynolds, 1990). They perform an analysis of their entire set of Her X-1 data taken with the 37 element imaging camera in operation. This total sample, 275 hours in length, is divided into 30 minute intervals and each interval is searched for periodicity near both the fundamental and 2nd harmonic. The distribution of the highest Rayleigh power found in each interval is compared to an equivalent distribution compiled from a search of the same data at a period different from the expected fundamental and 2nd harmonic. The observed cumulative Rayleigh distribution shows an excess in the source distribution above a Rayleigh power of about 3. They calculate the chance probability of this distribution to be 6×10^{-4}. This intriguing observation was made more puzzling by the application of imaging cuts to the data set. Imaging cuts had been used successfully to detect a strong DC signal from the Crab. This was the first strong evidence that γ-rays in the TeV range have characteristics similar to those predicted by Monte-Carlo calculations. Following the same procedure that was applied to their Crab data (Kwok, 1989), they applied cuts to the Her X-1 data sample based upon the spacial image of each event to select γ showers*, eliminating approximately 99% of the raw data. This cut, which was very successful in producing a $\sim 20\sigma$ rate excess from the Crab, reduced the Her X-1 Rayleigh power excess so that it was in agreement with background estimates.

---

*They have assumed that γ showers behave according to Monte-Carlo simulations.

If one assumes that the observed Rayleigh power excess from the raw Her X-1 data is a real signal, and not an improbable fluctuation, then this result is very difficult to understand. The apparent low level signal observed from Her X-1 does not behave as γ showers are expected to behave from Monte-Carlo predictions, and, just as worrisome, they do not behave like the particles (assumed to be photons) that have been observed from the Crab. This inconsistency, taken together with the anomalous muon content and the anomalous periodicity produces a complicated quagmire out of which no current VHE pulsar model can successfully emerge.

Obviously, the easiest way to solve this problem is to dismiss all, or most, of the above results as background fluctuations. Given the fact that Her X-1 is one of the most frequently observed and one of the best understood binary systems in the X-ray regime, the confusion at higher energies is very difficult to understand. At these lower energies, the pulsar period is very well known, and even though $\dot{P}$ is not constant, variations in the pulse period are not observed to be large compared to errors in the VHE measurements. If these anomalous observations of Her X-1 are correct, then this may be hinting toward dramatic, non-standard model physics which would be the most exciting particle physics discovery made by VHE astronomy in the last decade.

Chapter 3

The Old and New HGRO Telescopes

The original HGRO telescope was constructed during '83 - '84. It was tested in '84, and it began reliable data taking during '85. This instrument was in operation for 3 years, after which, substantial changes were made to the telescope's optics and collection area, and in '88 the "new" HGRO telescope was born. When the original telescope was being designed, relatively little quantitative information about γ and proton induced showers was known from Monte-Carlo simulations. Early simulations of these showers hinted at the possibility that the two showers could be discriminated by exploiting a small timing difference between the shower widths. As we have seen in Section 1.4, proton showers can be as narrow, or even narrower in time than γ showers if a only small cross-sectional area of the shower is sampled. Although this difference can not be exploited, the fast timing necessary to produce 1 ns accuracy does provide for a very low energy threshold for a given total mirror area compared to a telescope with the same area but a wider coincidence window. Thus, the first HGRO telescope was designed to have very fast timing accuracy, and one photoelectron sensitivity, providing a low energy threshold. Additionally, the simultaneous off source capability was a unique feature of the original Haleakala telescope. We will speak more of the advantages and also disadvantages of this technique in section 3.1.

The new telescope has kept all of the original timing accuracy, while adding simplified and better optics, and in the process, more light collection area. The simplified optics provided for better pointing accuracy, which was proven to be a problem for the old telescope. In this chapter, I will very briefly describe the old telescope, and I will describe the new instrument now in operation on Haleakala. In addition to the HGRO telescope, the collaboration operates an air shower array in coincidence with the telescope which was originally designed, in part, to provide a muon content veto. This array will also be briefly described.

3.1 The Old Telescope

A complete description of the original telescope can be found elsewhere (Szentgyorgi, 1986; Slane, 1988). Here, I will primarily mention aspects of the design that were changed in the rebuilding of the telescope. Nearly all of the electronics and data acquisition remained unchanged, thus these aspects will be mentioned in the discussion of the new telescope.

The original telescope consisted of 6 mirrors, each 1.5 m in diameter, providing a total mirror area of 10 m^2. It had a total of 36 channels, 18 of which looked at the desired source, while the other 18 surveyed the background at a distance of 3.6° in declination from the source (Figure 3.1). These 36 channels were divided evenly over the 6 mirrors, with 3 PMTs making up each aperture of each mirror. This

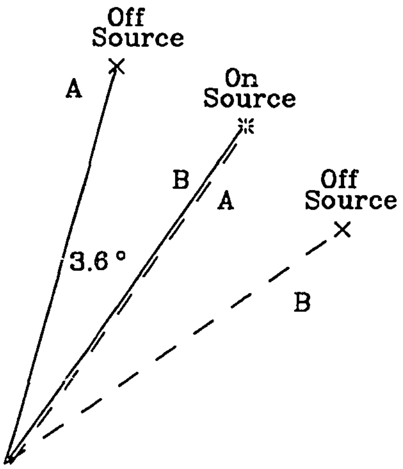

Figure 3.1: A diagram of the old telescope aperture separation.

design made alignment of the apertures difficult since it required the simultaneous alignment of 3 PMTs for each mirror aperture.

Both the old and new telescopes have the capability to observe both an "on source" and an "off source" (or background) region of the sky. The simultaneous off source has some obvious advantages, and some disadvantages as well. The ability to monitor a background portion of the sky while data is being taken on a given object increases the total time that can be spent on source. The most popular alternatives to this with only one aperture would be to perform driftscans, halting the mount and allowing the source to drift through the aperture, or to track the source for some amount of time then track the background for the same amount of time.

One of the disadvantages of this method of data taking, compared to a drift scan mode, is that our two apertures are looking at slightly different zenith angles, thus the expected background rate in the two apertures is different. Though this difference is not large, it must be corrected for if one hopes to accurately determine the significance of a constant, low level rate excess accumulated over many hours of data. A drift scan, by definition looks at a fixed zenith angle, so that no corrections for zenith angle differences are necessary. As will be seen, difficulties encountered by surveying different zenith angle regions can be overcome by performing a careful fit to the rate as a function of zenith angle; however, one does pay a price in the error associated with the zenith angle fit. Additionally, the two apertures possesses a slightly different response to showers, thus one must be careful when comparing the two apertures directly since one is comparing two slightly different instruments.

3.2 The Retrofit Telescope

This discussion of the new telescope will encompass much of the design of the old telescope as well. Where the design was improved, this will be noted. Otherwise, just a brief description of the setup will be given.

3.2.1 Changes on the telescope mount

The equatorial mount was left unchanged, as were the digital encoders and stepper motors used to drive the mount in Right Ascension and Declination. This drive has a precision of better than 0.05° as determined by the step size of the motors. The 6 large mirrors were replaced by 26 smaller (0.85 m diameter) mirrors, each with a small (15 cm diameter) hole in the center for use in mounting the mirror. The mirrors were produced at Purdue University by slumping flat glass blanks and then aluminizing the front surfaces by evaporation. These new mirrors are also approximately f=1 mirrors, with a focal length of 0.9 m. The net effect of this is mirrors with better resolution, and an increase in total mirror area to 13.5 m^2. The previous mirrors had a measured point source spread of 0.5° , while for the new mirrors, this is reduced by about a factor of 2 to 0.2° . The placement of the mirrors can be seen in Figure 3.2. From this figure, mirrors A, B, and D are referred to as edge mirrors, while mirrors E and G are center mirrors.

Two Hamamatsu R1450 PMTs are located at the focus of each mirror. These PMTs are separated by 3.0° (4.75 cm in the focal plane) and are aligned along the north-south axis. The 3/4″, 10 stage Hamamatsu tubes have a bialkali photocathode, with a maximum spectral response at $\sim$ 420 nm. They were originally chosen for the old telescope for their spectral response and timing accuracy (their transit timing spread is less than 1 ns). Figure 3.3 shows a rough sketch of the current telescope without cabling or space frame support. The two PMTs are held in the cans suspended by tripods above the mirrors in this drawing. An individual

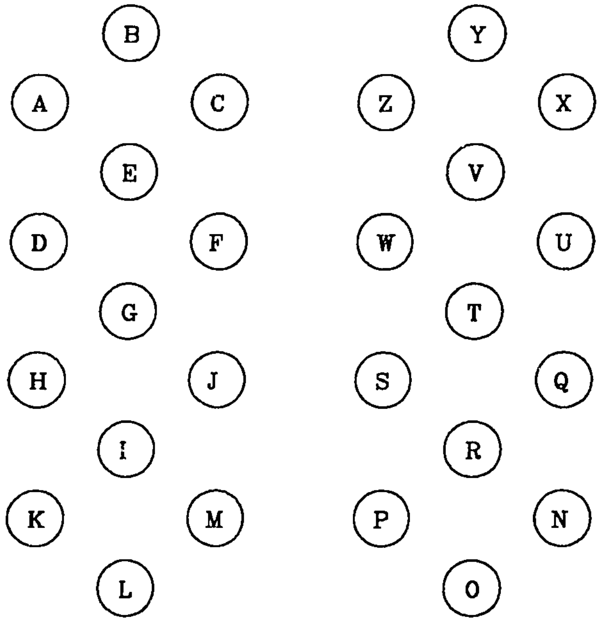

Figure 3.2: The placement of the 26 mirrors on the telescope. The mirrors are labeled A – Z, while the 2 channels in each mirror are called A and B.

mirror with tripod and can is shown in Figure 3.4. The two aperture separation is also depicted in this figure.

The filters in front of the PMTs were changed for the new telescope to be more sensitive in the ultraviolet. The new U-340 filters can take advantage of the abundance of UV Čerenkov photons. Currently, the PMTs and filters are not a perfect match. The filters cut off at the peak of the phototube's quantum efficiency; however, when folding in the Čerenkov light spectrum, the advantage gained by extending the spectral response down to $\sim$ 300 nm nearly offsets the loss at higher

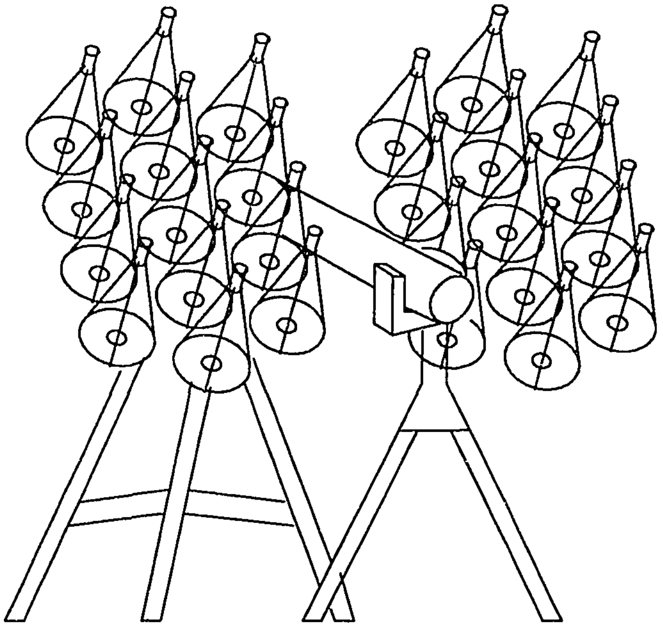

Figure 3.3: A sketch of the main Čerenkov telescope on Haleakala.

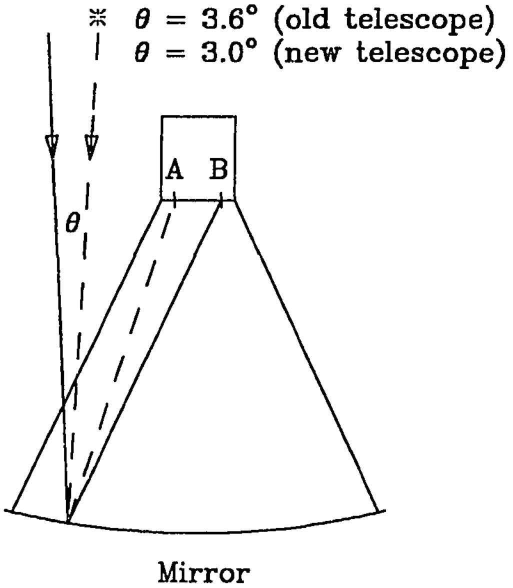
θ = 3.6° (old telescope)
θ = 3.0° (new telescope)
A
B
θ
Mirror

Figure 3.4: An individual mirror and aperture placement.

wavelengths (Figure 3.5). Figure 3.6 is a plot of the PMT's spectral response, the U-340 spectral response, the Čerenkov light spectrum, and the background night sky spectrum*.

Other additions to the telescope included light shielding around each aperture and around the edges of each mirror. A 5 cm high black cylinder around each aperture helps to prevent stray light from entering the aperture, and in a later modification, a cylindrical guard placed around each mirror, extending approximately 1/3 m above the mirror surface helps to prevent scattered light from the edges of mirrors or the space frame behind the mirrors from reaching the PMTs. The addition of these guards was seen to reduce the singles rates† in each channel by about 25%, depending on the position of the mirror on the mount. Edge mirrors saw a 20% rate reduction, while center mirrors showed a 30% reduction in singles rates.

3.2.2 Electronics

Also out at the mount, the PMT bases and amplifiers were modified to achieve better timing resolution. The new pre-amplifiers provide a factor of 20 multiplication of the initial pulse and a more narrow pulse than the previous amplifiers. This pulse is again amplified when it arrives in the counting room after traveling through 100 ft of RG-8 and about 15 ft of RG-58 cable. This second amplification

---

*As can be seen in Figure 3.5, it is advantageous to observe Čerenkov light in the blue-UV end of the spectrum, both because this light peaks in the UV and because the background sky shine is rather red.

†The singles rate is the total number of pulses counted in a PMT integrated over one second.

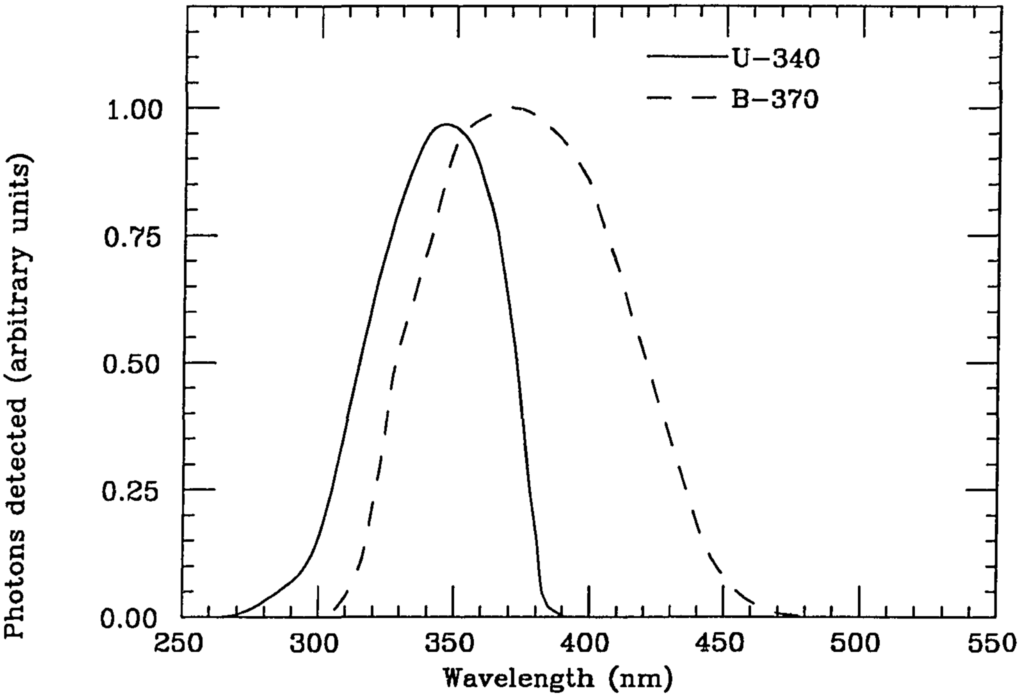

Figure 3.5: Total photon acceptance for the two different filter, PMT, and Čerenkov light combinations.

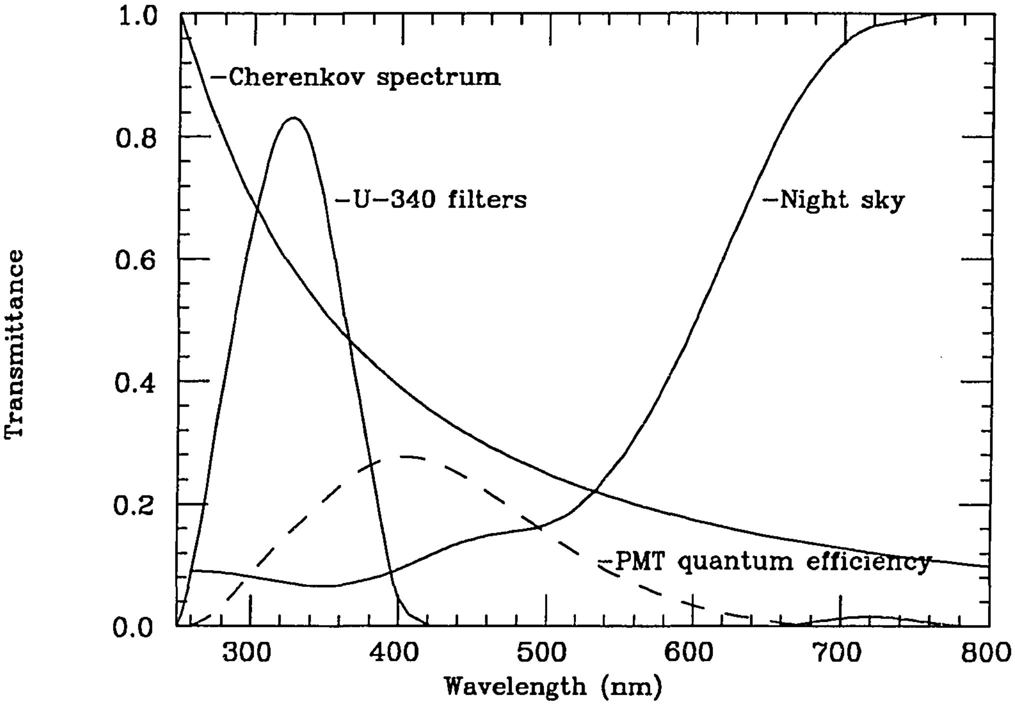

Figure 3.6: Spectral response of the current PMTs+filters.

takes place in the analog fan-outs (AFOs) which also split the signal into two separate paths: the timing (TDC) path and the pulse height (ADC) path. The TDC path signal is first discriminated to produce a logic pulse. This path then splits to perform the trigger decision in a Majority Logic Unit (MLU). The MLU sum is sent to a discriminator whose threshold is currently set at a a level corresponding to a multiplicity of 9 hits in the $\sim$ 8 ns gate. If this condition is met, the MLU sends a start pulse to the TDC, and gates to the ADCs and the latches. It also sends a logic pulse to the appropriate interrupt input of the interrupt box, which is sent on to be recorded in the data record, along with other interrupt register status words. The other branches of the TDC path go to the scalers, which are recorded in the data record at a rate of 1 Hz in an environmental record and via a discriminator and delay cable, to the TDCs and latches. The ADC path is a single delay cable that goes to the ADCs. If a trigger interrupt was produced, then the gate is opened and these pulses are integrated in the charge ADCs.

Each PMT runs at a plateau voltage that is in the range 1350 V – 1700 V. This high voltage is regulated by 4 high voltage controllers (HVC) and controlled by a fine adjust for each channel. As a precaution against damage to the PMT photocathodes caused by unusually high light levels (such as car headlights) the integrator current from the PMTs is monitored. If this current exceeds a certain value, then the +5 V control voltage sent to the HVC is dropped to zero. Without this reference voltage, the high voltage to the PMTs is cut off.

3.2.3 Data Acquisition

The event read out of the CAMAC TDCs, ADCs, scalers, and other registers is conducted through a Jorway 411 branch driver. It is written via a PDP 11/73 computer to 1600 bpi tape. Because of the low data rate of approximately 1 Hz, an entire night's data can fit onto one tape, so there is currently no need to streamline the data record or increase the the density of the recorded data. There is also no problem with dead time in the system with this low rate. An increase in the aperture size for the new telescope, as well as the addition of a new trigger based upon the pulse height sum of the event rather than the multiplicity, has brought the overall data rate up to 3-5 Hz. This rate is still manageable, though it is near the upper limit for our current system.

The data record is currently divided into three main areas: the indicative area which contains information about the event type, the time, and the telescope motion status, the barrel data area, which contains the timing and pulse height information for the particle counters, and the telescope data area. The position of the telescope, as determined by the encoders, is recorded at the start of the telescope data area. The status area for each CAMAC crate is located in a status area before the beginning of each of the two data areas. The clock time recorded is referenced to a cesium clock located at the Lunar Ranging facility (LURE). We receive a 1 MHz signal and a 1 Hz reference pulse from this clock. Since the cesium clock is corrected by the GPS network of satellites, it has an absolute accuracy of about 2 μs to UTC. A "wobble" bit is set in the indicative area whenever the telescope is given the command to switch between the two apertures during a data run, and it is then removed when the motion is completed. This bit, which was added shortly after the new telescope came into operation, is very useful when analyzing the data, since it properly defines the beginning and end of an analysis interval.

3.2.4 System Performance

The new telescope was tested extensively during the first 6 months of 1988. In February and March, the initial alignment and focusing of the mirrors was performed. The initial, approximate alignment was done by tracking the moon with the telescope*. The image is aligned visually to a mark at the center of the can holding the PMTs by three adjusting screws on the mount behind each mirror. In March, each mirror was aligned on Jupiter, most to within ± .2° (Figure 3.7). Periodically, the alignment is checked by performing a raster scan on a star (recording the light profile in each aperture by moving the telescope over a $\sim 1^\circ \times 1^\circ$ grid around a star). This also checks the focus and the image produced by each mirror. Figure 3.8 shows the rate as a function of declination for apertures AA and AK. The solid line represents the full extent of the aperture in place during this raster scan (0.64°). Note that the two apertures are misaligned by about 0.1° , also note that a difference in the image quality is apparent in the two distributions. The FWHM of AA is about 0.07° more narrow than AK, but both images are acceptable.

---

*without high voltage to the PMTs!

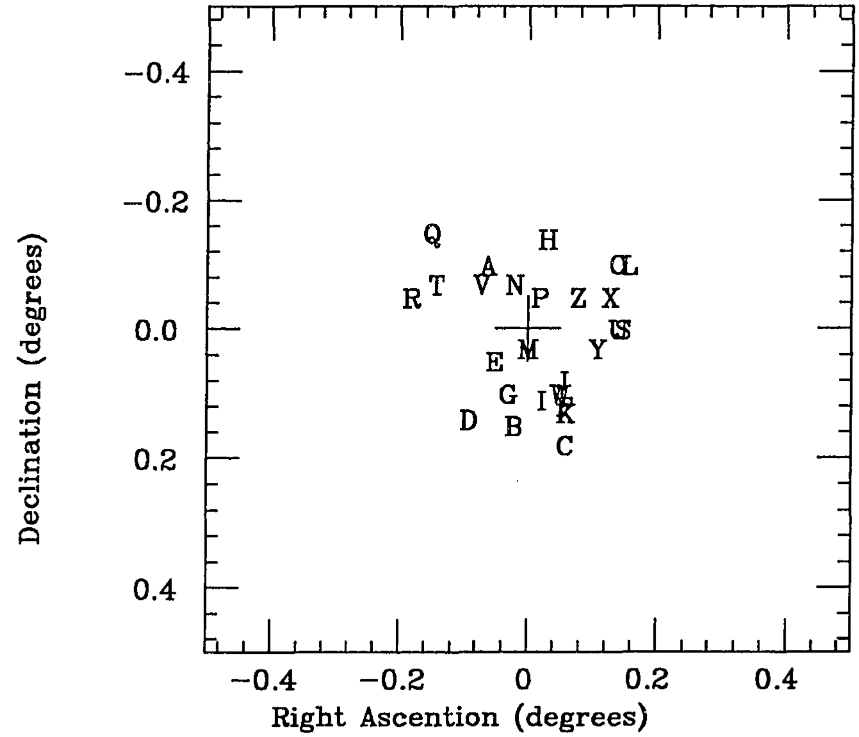

Figure 3.7: Mirror alignment for the A aperture, A – Z mirrors.

The North-South alignment of the two apertures was initially performed by measuring each aperture in reference to a survey line drawn on the cement pad under the telescope. The line was determined earlier by sighting Polaris. This preliminary alignment was also checked and adjusted if necessary by performing raster scans for each aperture.

After all PMTs were plateaued and the preliminary alignment and focusing was done, the behavior of the telescope to background light and Čerenkov light from showers was investigated. The telescope response to background, or random light from sky shine is referred to here as the accidental trigger rate. The spectral distri-

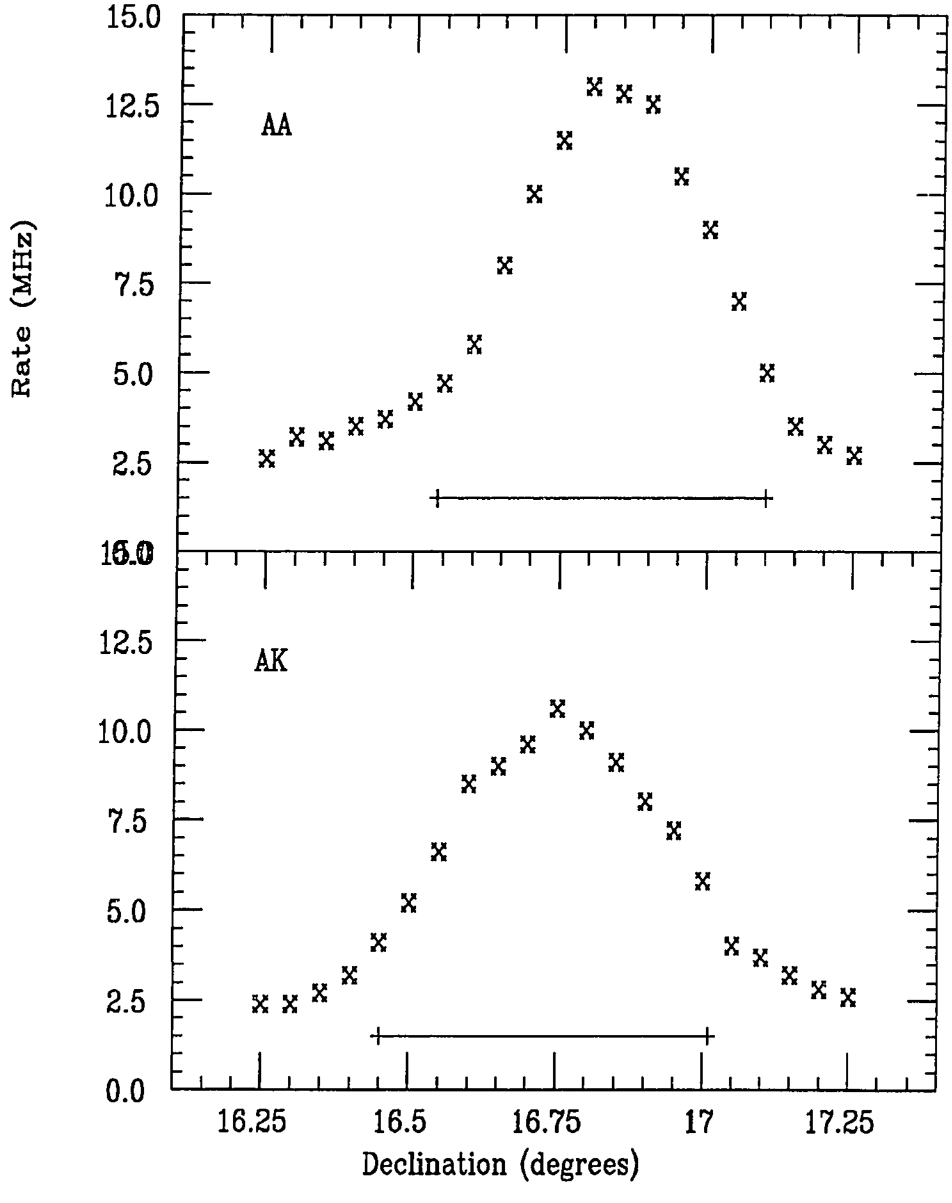

Figure 3.8: Rate as a function of declination for apertures AA and AK.

bution of this light, plotted in Figure 3.6, goes as $\log(f_\lambda(m)) = -0.4m + \log(f_\lambda(0))$, where f_λ is the spectral irradiance in units of erg/(cm^{2}sÅ) and here m is the mean sky brightness ($\sim$ 22.5 $\times$ 10^{11} photons/(m^2 s sr)) (Zombeck, 1982). The expected accidental trigger rate as a function of the number of channels hit in a given time window, which is usually called the multiplicity of the event, is given by the binomial distribution. So, the probability that one channel is hit with a photon is just P = $(1 - e^{-rt})$ where r is the individual singles rate for that channel, and t is the time interval. The rate for this one channel (the singles rate) is proportional to this for a constant wavelength acceptance. Typical singles rates for the telescope are between 1 - 2 MHz for a 0.35° half-angle aperture and the U-340 filters.

If we require that one channel is hit to define the start of our time interval, and then ask for the observed rate for a total of N out of a possible M channels getting hit (or N-1 *additional* channels getting hit after our time interval was begun by the initial hit), then the expected rate will be:

$$R_{ran}(N,M) = Mr \begin{pmatrix} M-1 \\ N-1 \end{pmatrix} (1 - e^{-rt})^{N-1} \, (e^{-rt})^{M-N} \tag{3.1}$$

Practically, the telescope is set to trigger at a multiplicity of N or greater, thus the actual expression we want to express the rate is just the sum:

$$R_{ran}(n > N, M) = M \sum_{n=N}^{M} r \begin{pmatrix} M-1 \\ n-1 \end{pmatrix} (1 - e^{-rt})^{n-1} (e^{-rt})^{M-n} \tag{3.2}$$

For typical singles rates of about 1 MHz, the calculated trigger rate for a multiplicity of 10 or greater is about 1 Hz from the night sky. This is approximately the trigger rate observed at this multiplicity.

The cosmic-ray rate can be estimated if one assumes that the photon density on the ground, ρ, is proportional to the energy of the primary cosmic ray particle as E $\propto \rho^{-\gamma}$, ignoring the large fluctuations present in the photon distributions of proton induced showers. If the probability for one channel to detect at least one photon in a given time window can be give by $(1 - e^{-k\rho})$, then the expected cosmic ray rate is:

$$R_{cr}(n > N) \propto \sum_{n=N}^{M} \left(\begin{array}{c} M \\ N \end{array} \right) \int_{\rho_{min}}^{\infty} \rho^{-\gamma}(1 - e^{-k\rho})^{n}(e^{-k\rho})^{M-n} d\rho \qquad (3.3)$$

Here, ρ_{min} is the minimum photon density required to trigger the telescope at the threshold of N channels registering at least one photon. It is assumed that most of the shower photons arrive within the trigger window, which for the new telescope is $\sim$ 7 ns. This is a reasonable assumption since the width of proton showers at the core is typically less than 5 ns (see Section 1.4).

The observed rate is the sum of the accidental rate and the shower trigger rate. In order to determine at what multiplicity to operate the telescope so that the contribution to the total trigger rate due to accidental events is at a reasonable level, the total event rate as a function of multiplicity is determined by adjusting the threshold of a discriminator that receives the summed pulse from the MLU (Figure 3.9). Each 50 mV of the MLU output corresponds to one channel reg-

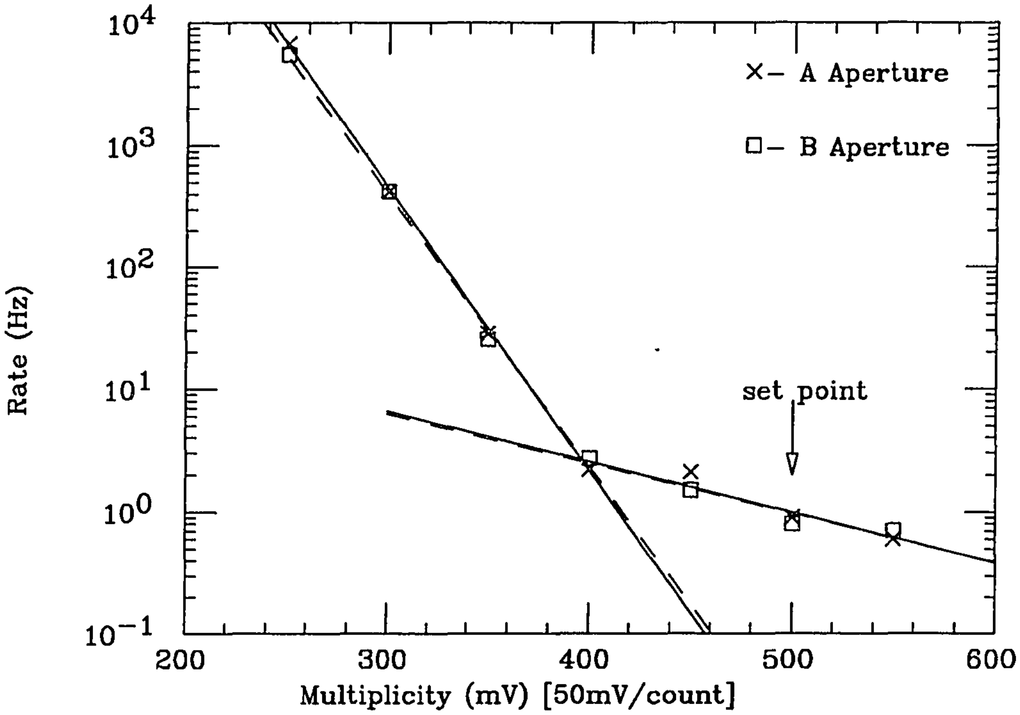

Figure 3.9: Rate as a function of multiplicity.

istering light. As is seen in Equation 3.1, the rate from accidental triggers falls off exponentially. This background rate drops below the cosmic ray rate at about a multiplicity of 9, thus the trigger trigger threshold for the telescope was set originally at 10-folds, and later this was dropped to 9-folds.

3.3 Pulse Shape Analysis with a Waveform Digitizer

During August of 1989, we had the opportunity to investigate the pulse shape of our PMTs using a LeCroy 6880A waveform digitizer. We were interested in this both as a diagnostic check for the new instrument and to attempt to use the pulse shape to reject proton showers:

1. The new telescope had just begun consistent operation in May of that year, and we were interested investigating the individual channel waveforms for diagnostic purposes. Although the phototubes remained the same in the upgrade, the amplifiers (both out at the mount and in the AFO) were modified (Section 3.2.2), so we wanted to determine if any irregularities, such as a greater pulse overshoot for large PE events, may have been introduced by the new amps.
2. We were also interested in the sum of the PMT pulses to determine the fraction of pulses with overshoot or clipped pulses.
3. Additionally, discrimination on the basis of pulse shape has been used successfully to separate γ and proton induced showers (Tumar, *et al.* 1990). We were interested in attempting to use a similar event classification on the basis of pulse width and number of sub-pulses within an event to separate protons and γs.
4. In an attempt to separate proton and γ showers, we wanted to discriminate on the basis of pre and after pulses observed, either from PMTs not participating in the main trigger pulse or in multiply hit PMTs.

To meet these goals, both individual channels and the summed output from the A and the B apertures were recorded. The PMT signals were taken from one of the spare outputs of the AFOs, and the trigger for recording a waveform was taken from the appropriate telescope trigger interrupt. Required for this operation were: the 6880A digitizer and the 6010 'MAGIC' (Manual and Automatic General purpose Interface to CAMAC) crate controller to digitize and temporarily store the waveforms, a IBM-compatible PC to run the data acquisition software to display and record the waveforms, and a passive adder to sum the PMT signals. The 6880A digitizer has a sampling period of .742 ns and has a maximum trigger rate of about 1 trigger per second. The actual recording rate was on the order of 1 trigger every 2-7 seconds because of limitations caused by the recording time of the PC.

As has been stated, our objectives for doing this included both system checks such as checking the pulse shape from each individual channel, and also an investigation of the shower profile through looking at the summed PMT pulses. Individual channels were checked for unusually large pulse "overshoot" and corresponding clipping of large pulses, and other irregularities in the pulse shape. The summed pulse profile was investigated for pre- or after-pulsing caused by out of time shower photons, which is more likely to occur in a proton shower, where one may be observing the (tight timing) core of a "daughter" shower and photons from other components of the shower, whose arrival times are not as tight. In addition, the summed output from the on-source and the off-source were compared in an attempt to determine any difference between the two sets of waveforms.

3.3.1 Analysis of the Waveform Data Set

Because the pulses observed with the waveform digitizer were taken from the output of the AFOs, a separate calibration from that normally employed for data analysis was needed. The calibration of each channel used in the waveform analysis is described in Appendix A. Approximately 2000 waveforms were recorded of the sum of the first 18 A aperture channels during three observing runs. Run1686 was started at 27884. s UT on August 3, 1989 with Cyg X-3 as the source. Run1687 was taken on 4U0115 that same evening beginning at 46585. s UT. Run1688 was taken the following evening beginning at 24228. s UT with Her X-1 as the source. For these waveforms, general statistics were compiled for the on and off source.

Waveforms taken of each of the individual channels revealed some minor problems, such as a noisy amplifier producing large fluctuations in the pulse shape and large noise fluctuations in the background. All problems discovered in the individual channels were easily corrected while the waveform recording was taking place by either replacing or repairing the PMT amplifier/base.

The magnitude of the pulse overshoot on the high PE pulses was much larger than expected. It is difficult to obtain a quantitative measure of this from looking at an oscilloscope trace of the PMT output, since these pulses make up less than 10% of the total number of pulses. The extent to which this overshoot is reflected in the ADC value should be reduced, since the LeCroy 2282A charge ADCs should clip off pulses with a magnitude *greater* than $\sim$ 0.1 mV, however, as is seen in Figure 3.13, the overshoot continues for $\sim$ 20 ns after the pulse. Integrating a portion of this "positive" charge will reduce the recorded ADC value for each channel with a large pulse.* Since we do not currently make cuts that are sensitive to small differences in observed PEs, this is not a major problem. It should be kept in mind when any pulse height selection is made. In practice, the signal gain is lower for the new telescope, so *any* selection based upon PE cuts is made more difficult.

---

*The effective ADC gate is about 40 ns wide, so it can be open for $\sim$ 10-30 ns after the pulse.

The degree of pre- and after- pulsing caused either by multiply hit PMTs or by PMTs not contributing to the trigger is seen in Figure 3.10. These pre- or after-pulses were separated from the main trigger pulse by at least 7 ns. The rate of these out of time pulses is the same in the on and off source apertures.

This observation is not surprising: the out of time hits caused by random light will be present in both the on and off source, and both of these apertures are dominated by the cosmic ray background. Since it is less likely for γ showers to exhibit such out of time behavior, most of (or all) of these triggers are cosmic ray events.

Pulse shape discrimination has been used successfully to reject cosmic ray showers (Tumar, *et al.* 1990). Tumar, *et al.* visually scan $\sim$ 3000 waveforms from data taken in drift scan mode on the Crab with two 11 m diameter solar collectors at the Solar Thermal Test Facility, Scandia Laboratory. These waveforms were recorded on video tape from a Tektronix 2467 oscilloscope. They reject events which show multiple pulses (such as the waveform in part C of Figure 3.13) and those below a certain pulse height. After the removal of these pulses, they are left with a data set of 236 potential γ shower events. They find a 4.2 σ excess of events near the Crab after the waveform cuts are applied.

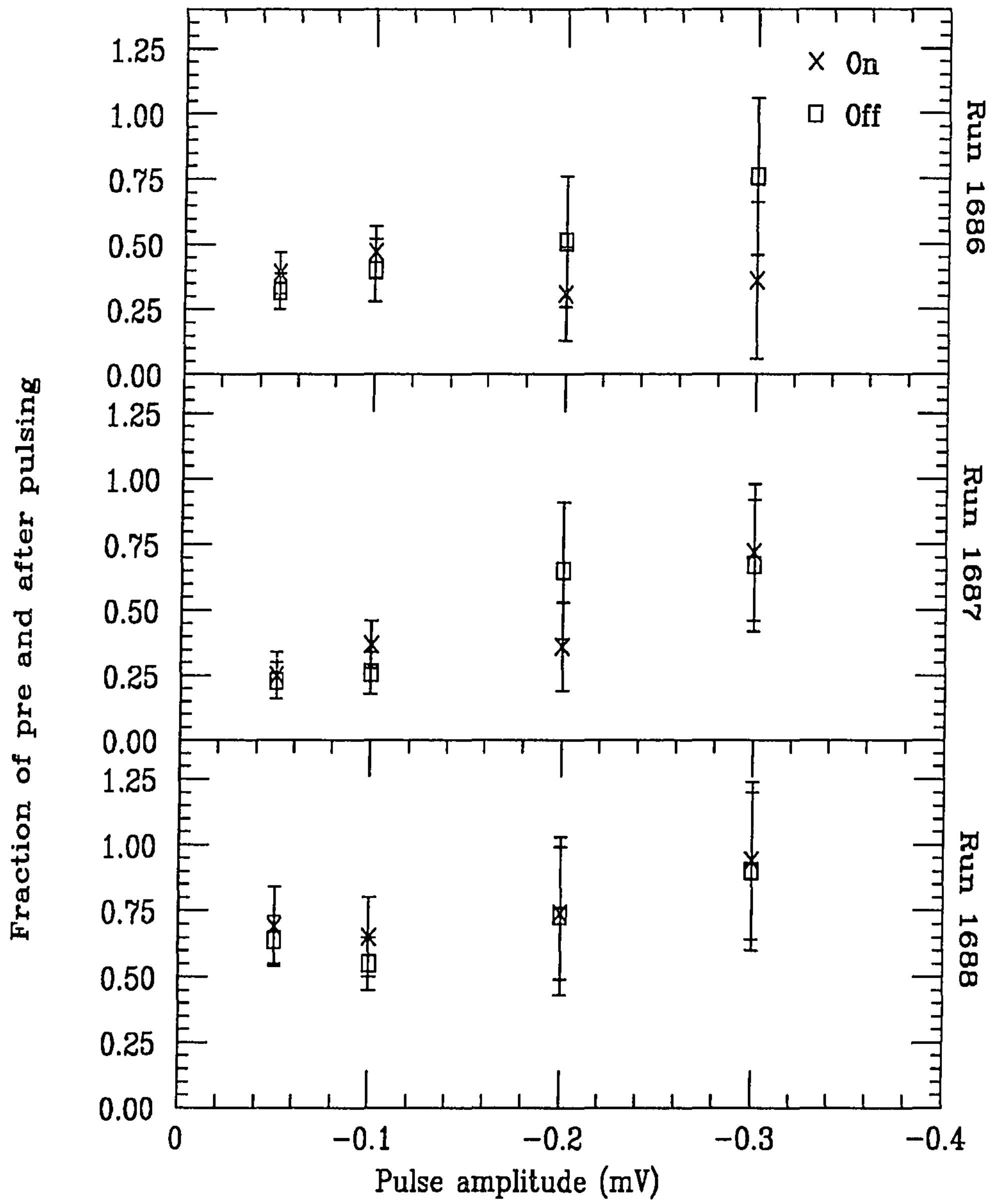

Figure 3.10: Fraction of out of time pulses for runs 1686, 1687, and 1688.

Table 3.1: Waveform shape statistics

	Run 1686		Run 1687		Run 1688	
	On	Off	On	Off	On	Off
Total events	346	380	89	87	241	267
Pass all cuts	143	169	42	36	83	91
Multiple pulses (1)	77	83	28	31	60	66
Pre-pulses (2)	20	32	2	3	21	27
After-pulses (3)	41	38	8	9	18	33
(1) and (2)	23	17	4	0	24	21
(1) and (3)	27	22	4	6	22	18
(2) and (3)	9	12	0	0	8	8
(1), (2), and (3)	6	7	0	2	5	3

Our three data sets may be analyzed in a similar manner. Our ~ 2000 waveforms were not visually scanned. Since they are recorded digitally, they may be searched analytically for the absolute minimum in the expected trigger window, the number of additional minima in that window (multiple pulses) , and any pre- or after- pulsing, as described above. Because we only had the ability to record one aperture at a time, on and off source waveform data could not be taken simultaneously. Table 3.1 is the result of this analysis for all complete, 900 s wobble intervals summed for the on and off source for each run. For run 1686, three complete on source and three off source intervals were recorded. For run 1687, only one on source and one off source interval was recorded, while for run 1688 two of each were recorded.

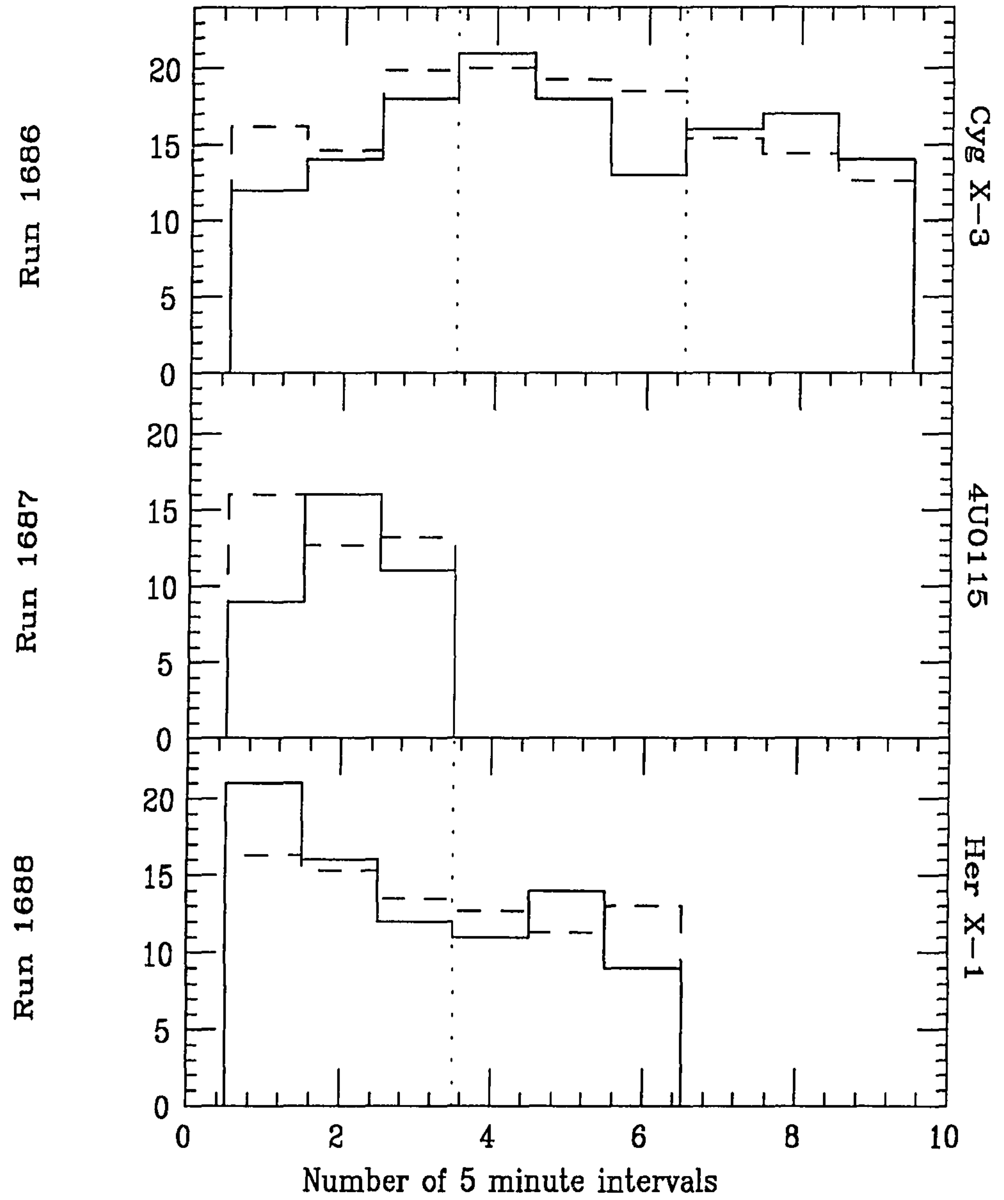

Figure 3.11: On source events after cuts. The dashed histogram is the estimated background. The dotted lines separate wobbles.

A plot of the total number of events that contain neither pre- or after- pulsing or multiple pulsing and which pass a maximum pulse depth cut* is presented in Figure 3.11. The solid histogram is the number of on source events passing all cuts plotted in 5 minute intervals. The vertical dotted lines represent breaks in time between wobble intervals. The dashed histogram is the estimated background based upon the total number of on source events in the interval *before* cuts are made and the fraction of off source events that survive all cuts in the adjacent wobble interval. The overall excess for each run based upon this estimated background is (Table 3.2):

Table 3.2: Total excess from Figure 3.10.

Run and Source	Num. Excess	σ Excess
Run 1686 (Cyg x-3)	143 ±150.9	-0.4σ
Run 1887 (4U0115)	36 ±41.9	-0.7σ
Run 1688 (Her X-1)	83 ±82.1	0.1σ

From Figure 3.11, there is no obvious excess in any bin. Nor is there an overall integrated excess present for any source. During this run, Her X-1 was in an X-ray off portions of the 35 day phase ($\phi_{35} = 0.88$). We could not take data on the Crab while we had the waveform digitizer set up, so we cannot attempt to reproduce the result of Tumar, *et al.*

---

*For the first part of run 1686, this cut was 50 mV. For the remainder of the runs this was changed to 100 mV, because the summed output was amplified by a factor of two.

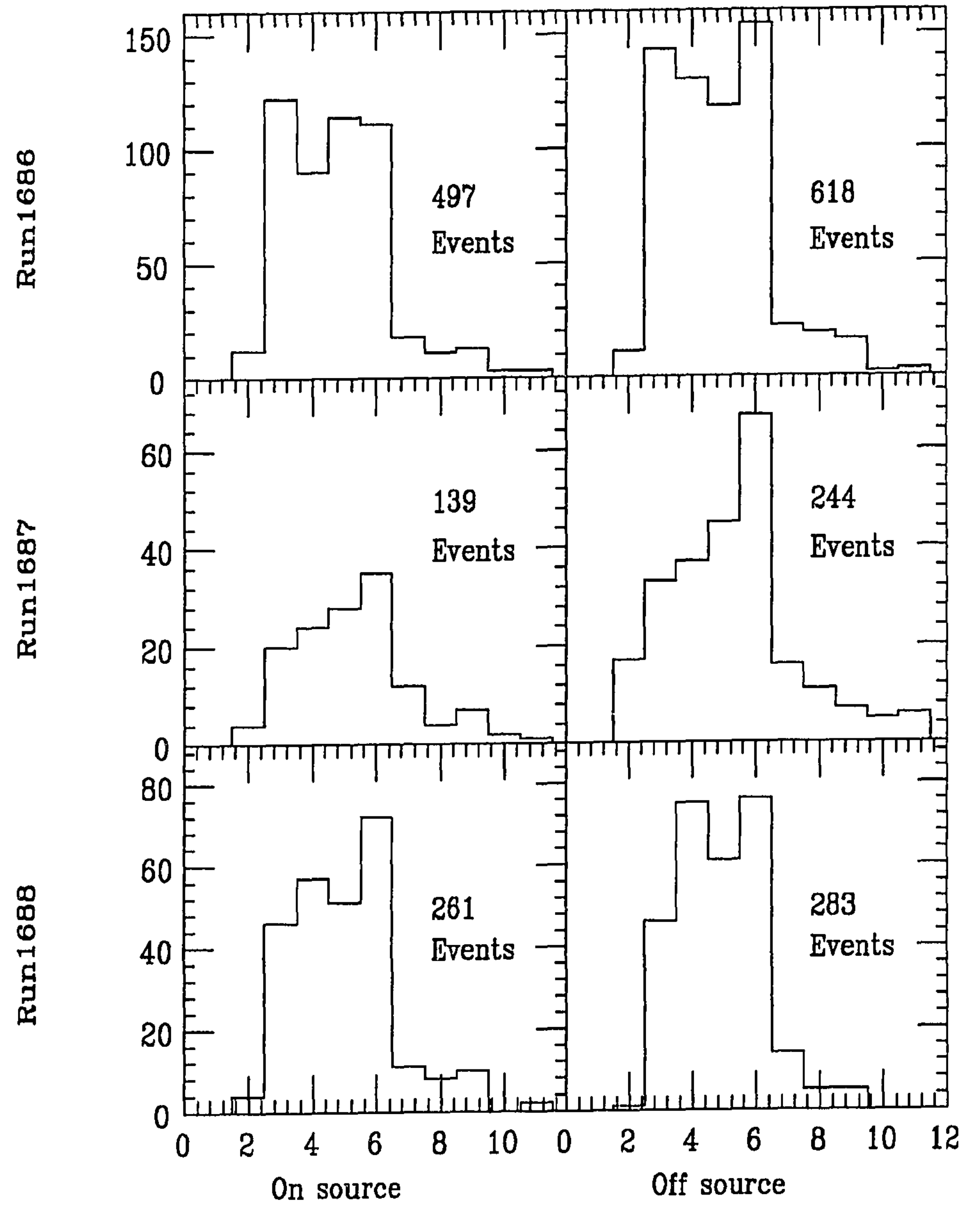

Figure 3.12: Number of pulses observed versus pulse width (in ns) for runs 1686, 1687, and 1688.

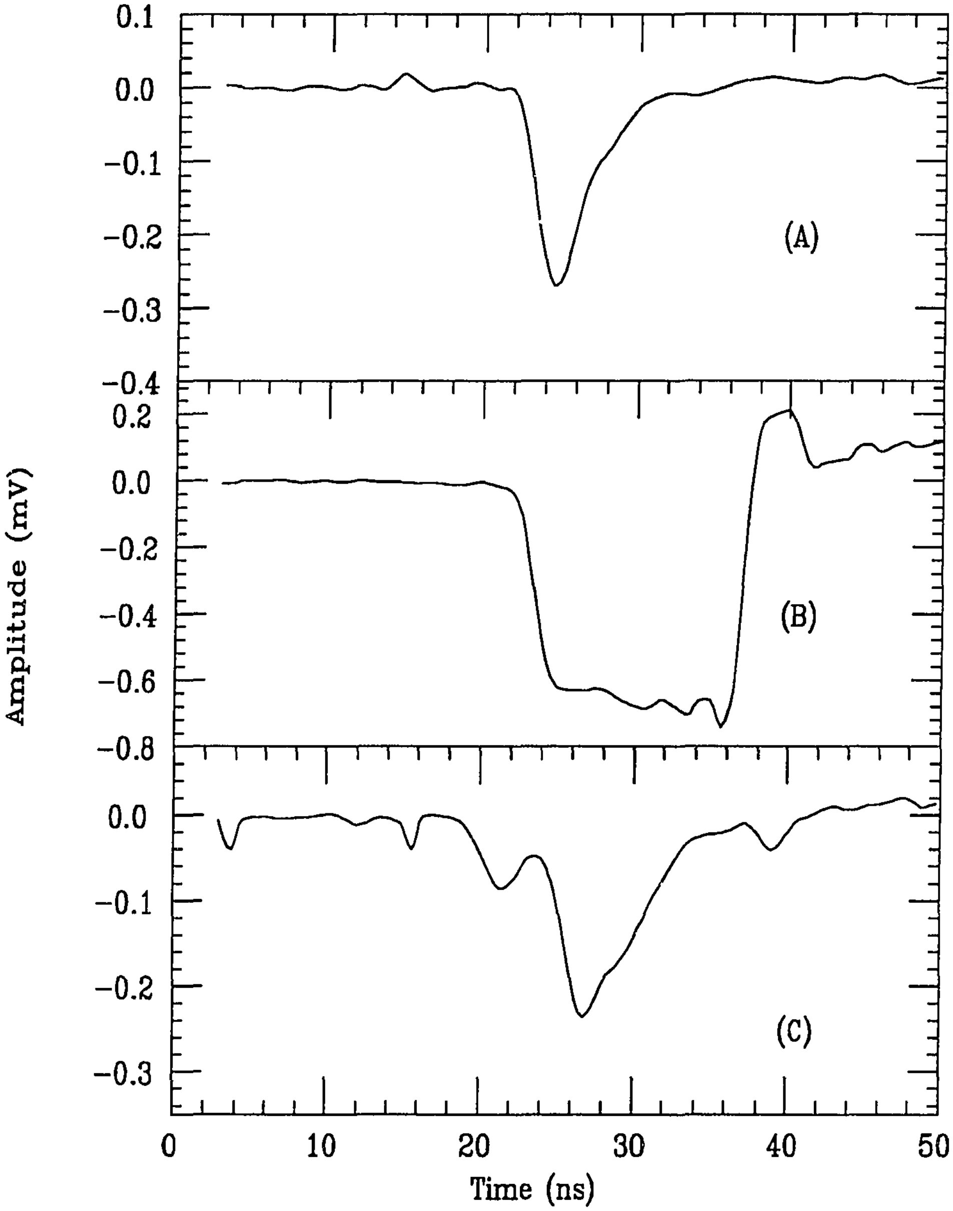

Figure 3.13: Three sample waveforms: A typical narrow pulse (A), a clipped pulse with overshoot (B), and a multiple pulse (C).

A study of the occurrence of the most narrow pulses in the sampled data set (those pulses with a FWHM of 2 ns or less and those pulses with a FWHM of 3 ns or less with no out of time pulses present) is presented in Figure 3.12 for all three runs. Here, there is some reason to believe that the narrower, non-multiple pulses may either be γ induced showers or possibly a sub-cores of a proton shower. Since as we gave seen these sub-cores can be highly temporally correlated over a small area of the shower footprint, it is not possible to reliably distinguish γs from protons in this manner. None of the runs showed any significant difference in ≤ 3 ns pulse frequency between the on and off source.

Some examples of the waveforms recorded are presented in Figure 3.13. These three are not representative samples of the waveform data set; they were chosen to depict characteristics and problems mentioned above. The largest fraction of the waveforms recorded were typically -0.05 – -0.10 mV deep and 4–6 ns wide (FWHM). The first pulse is typical of the subset of narrow pulses. It has a 3 ns width. The second is an example of a large PE, clipped pulse, which has a large amount of overshoot after the pulse. These clipped pulses made up 1% to 4% of the recorded waveforms in the three data runs. All of the large pulses (pulse height less than -0.3 mV) exhibited some overshoot. The final pulse is an example of a multiple pulse, with a pre-pulse preceeding the main pulse by 6 ns and a small after-pulse following the main pulse by about 11 ns.

3.3.2 Conclusions from the Waveform Analysis

Based upon the analysis of the waveform data, there are several criteria which one can use to accept an event as a γ candidate shower. For both the Her X-1 and Cyg X-3 data sample, there are a larger percentage of narrow pulses in the on source data, but in both cases, this excess is not significant. A more useful criteria which one can apply is a cut based upon the presence of slightly out of time pulses or multiple pulses within the main pulse. The number of waveforms with out of time pulses was large, making up about 30% of the entire data set. The number of waveforms with multiple pulses within the trigger window is 38% (including those pulses with both multiple pulses and other out of time pulses). 40% of the events pass the pulse shape cuts applied above, which is in agreement with the total number of pulses defined as "smooth" by Tumar, *et al.* (41.9%), where these smooth pulses showed no multiple or out of time hits. Their final sample of γ candidate events includes a pulse height cut as well, which is made because the low pulse height events are more difficult to scan.

We do not observe a rate enhancement in the waveform events accepted as γ candidate showers employing cuts which are similar to those applied by Tumar, *et al.*, but we have a much smaller data sample on each source. In addition, we have no information on the Crab using this analysis. Although investigations of the actual waveforms of events was useful as a diagnostic tool for the new telescope, we did not demonstrate that we were effectively able to discriminate against proton-induced showers employing event selection based upon the waveforms.

3.4 The Air Shower Array

The Haleakala group also operates an air shower array, positioned around the air Čerenkov telescope. This array has been maintained primarily by Jacob Hudson, who has made this detector the subject of his thesis research here at the University of Hawaii. Here, I will present a brief description of the array, since data from this instrument is discussed briefly in Chapter 5.

This array is known in our group as the "Barrel array", since each of the particle detectors is made from a 55 gallon drum. The entire drum is painted with titanium dioxide paint for reflectivity and filled with water*. An 8-inch PMT is inserted in a watertight PVC housing attached to the lid, and this lid is then sealed onto the barrel. There are 32 barrels, each with an effective area of $\sim$ 0.8 m^2, arranged approximately in 4 circles around the air Čerenkov telescope (Figure 3.14). The inner and outer most circles (dotted in the figure) were added in the upgrade. What is now know as barrels 9 – 24 were in place during the 1987 Her X-1 season. Each barrel was surveyed to an accuracy of ± 6 in with a transit, using the center of the air Čerenkov telescope on the cement pad as a reference. The position of each of the barrels is presented in Table 3.3.

During the 1989 Her X-1 data taking season, the barrels were operated in a slave mode to the telescope. The barrel timing and pulse height information was

---

*Obviously, the paint on the outer surface does not increase the array's performance. It was thought that the bright white barrels would be very visible against the brown rock background of the mountain top thus protecting them from accidental damage; however, one barrel was still run over by a truck shortly after the 32 barrels were installed.

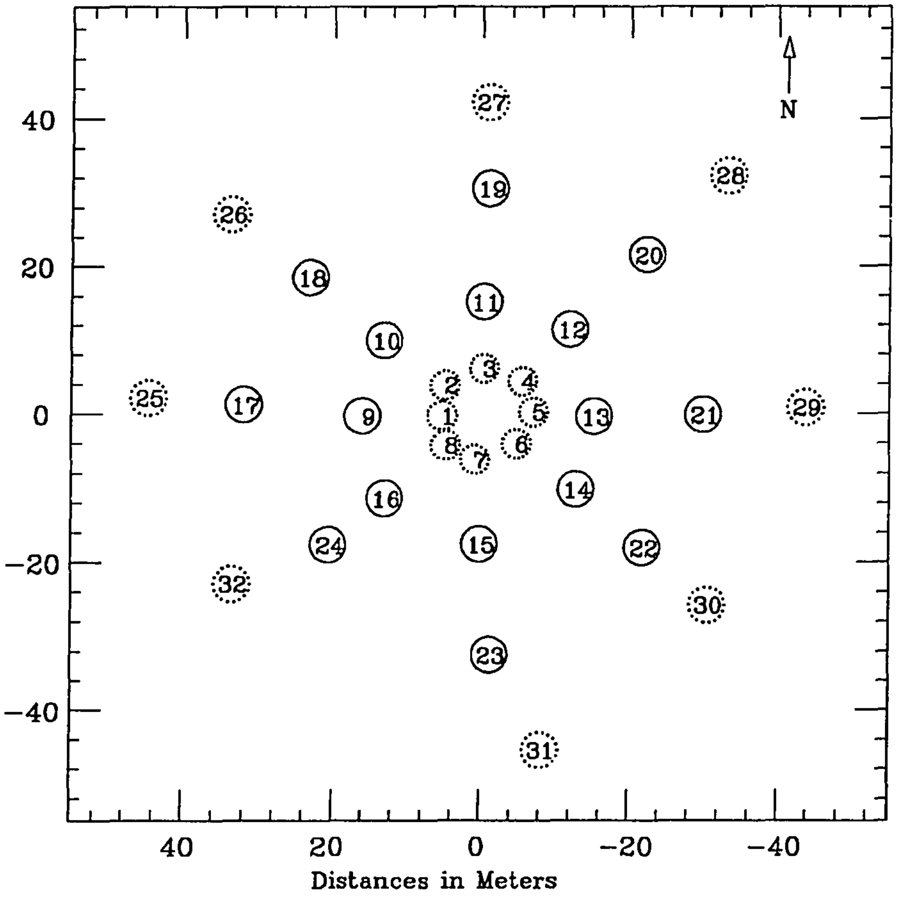

40
20
0
−20
−40
N
1
2
3
4
5
6
7
8
9
10
11
12
13
14
15
16
17
18
19
20
21
22
23
24
25
26
27
28
29
30
31
32
40
20
0
−20
−40
Distances in Meters

Figure 3.14: Layout of the barrel air shower array. The Čerenkov telescope is at the center of the diagram.

only recorded when a telescope trigger was recorded, thus the direction of the shower was *usually* the direction of the on-source or off-source of the telescope. The individual counting rate in each barrel is ~ 300 Hz, and the coincidence window used is 400 ns wide. The transit time for light across the entire array is ~ 320 ns, so this window is wide enough to accept all hits corresponding to a shower at any telescope angle. The rate of random hits can be calculated from the binomial distribution for a given barrel multiplicity (as was done for the telescope

Table 3.3: Spatial coordinates of the individual particle counters

Counter	X (m)	Y (m)	Z (m)
1	-0.218	5.293	-0.685
2	3.884	4.903	-0.202
3	6.156	-0.289	-0.018
4	4.412	-5.493	0.321
5	0.281	-7.026	0.844
6	-4.006	-4.753	-0.075
7	-6.114	0.924	-0.078
8	-4.186	4.772	-0.864
9	-0.295	15.914	-1.128
10	9.923	12.982	0.033
11	15.150	-0.308	-0.423
12	11.397	-11.980	2.300
13	-0.383	-15.241	2.296
14	-10.149	-12.788	1.485
15	-17.539	0.136	-0.187
16	-11.356	12.940	-1.352
17	1.255	31.986	-1.419
18	18.479	23.187	-2.502
19	30.540	-1.018	0.814
20	21.539	-22.272	3.366
21	-0.152	-29.992	4.144
22	-18.041	-21.857	3.476
23	-32.453	-1.304	1.397
24	-17.563	20.466	-1.556
25	2.201	44.721	-4.938
26	27.138	33.752	-3.612
27	42.212	-0.869	0.785
28	32.298	-33.125	4.512
29	0.876	-43.809	7.665
30	-25.699	-30.516	6.391
31	-45.351	-8.130	3.223
32	-22.818	33.593	-2.892

in Equation 3.1). The rate detected in the array is well above this background. This has been observed in the original 16 barrels as well as the upgraded 32 barrel array (Hudson, *et al.* 1987).

Chapter 4

Data Preparation, Calibration, and Analysis

Before the data can be analyzed for a rate excess or periodicity, all corrupted data records must be removed. Both records containing read errors and those which are seriously affected by weather or other atmospheric fluctuations are removed first. After this initial data selection, a calibration is performed in preparation for further analysis. In this chapter, we will begin by discussing this initial data selection and calibration process. Finally, the processes by which the rate excess calculations and the periodicity search are performed is described.

4.1 Preliminary Data Preparation

The data record is checked for bad or incorrectly recorded records. Status registers which indicate whether all CAMAC modules responded correctly during the event read are written into the event record for each CAMAC crate. This word is compared to the correct value for a complete read, and any incorrect events are disregarded. The event length (the total word count of the event) is also checked for each event. The word count of each event is written as the first word of that event, and it is the same for similar event types (i.e. normal data events and environmental events). This is frequently a redundant check (if the word count in incorrect, then it is likely that one of the CAMAC modules did not respond completely so one of the CAMAC status words is also incorrect). The percentage of bad events (bad status words and/or incorrect word counts) is much less than 1% of all events recorded. In Figure 4.1, events with a word count of 249 represent normal events*, while those with a word count of 146 are environmental events, which record the scaler rates for each tube. Note that on this log scale, the number of bad word count events are almost a factor of 10^3 below the number of correct word count events. Currently, the addition of energy trigger information (latches and ADCs recording sum of the total charge of the event if an energy trigger interrupt was generated) has increased the total word count to 263. This change makes no difference for data analysis routines, since they read the first word to get the length of the event, then read offset words in the header of the event to determine where each data area begins. The data record for the new telescope is conveniently divided into 3 parts for every event: The header and indicative area containing the offset words (or "pointers" mentioned above) the clock, and other information common to all events; the barrel area for the particle counters; and the main telescope area.

The environmental records may be used as a preliminary check for weather contamination such as clouds, moisture on the mirrors, or rain which will reduce the recorded scaler rates. As we will see, an increase in light levels (moonrise, for

---

*This is the correct word count during the 1989 Her X-1 season.

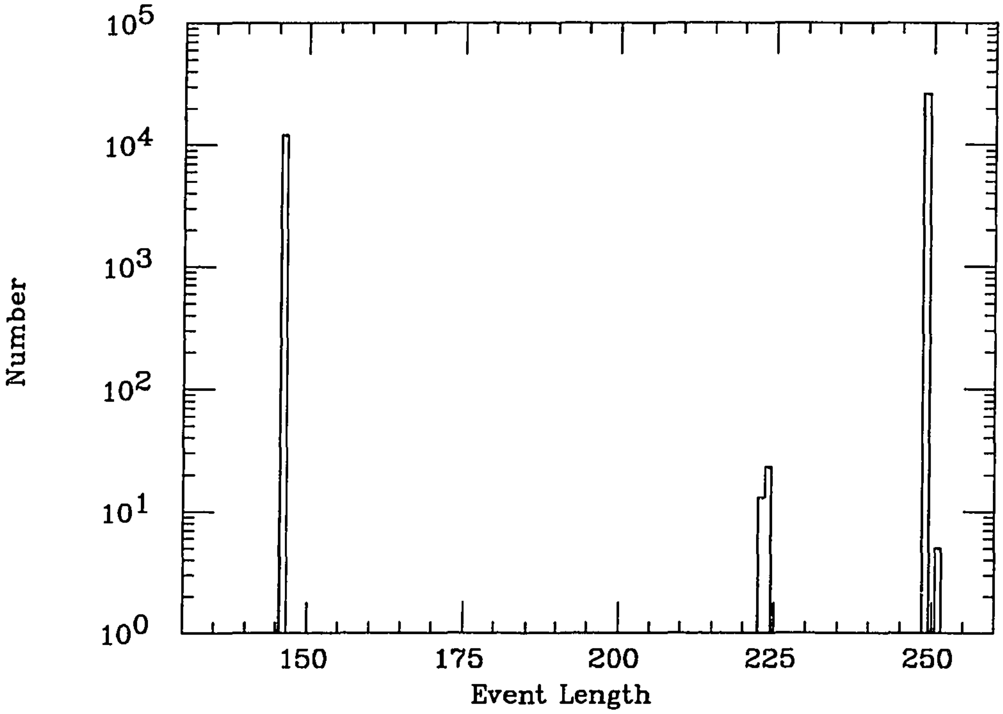

Figure 4.1: The word count (on a log scale) for a typical event.

example) is also reflected in these rates. Figure 4.2 is an example of a run that was ended due to rain. The first small dip at 1500 s may be clouds or fog beginning to blow over the observatory, and the final plunge at 1700 s reflects the mirrors or filters beginning to get wet. Although the scalers provide a good indication of serious weather problems, they are not as useful for determining small fluctuations in viewing conditions. A determination of the rate as a function of the zenith angle of the telescope based upon off-source data is a more sensitive measure of observing fluctuations (Section 4.5.2).

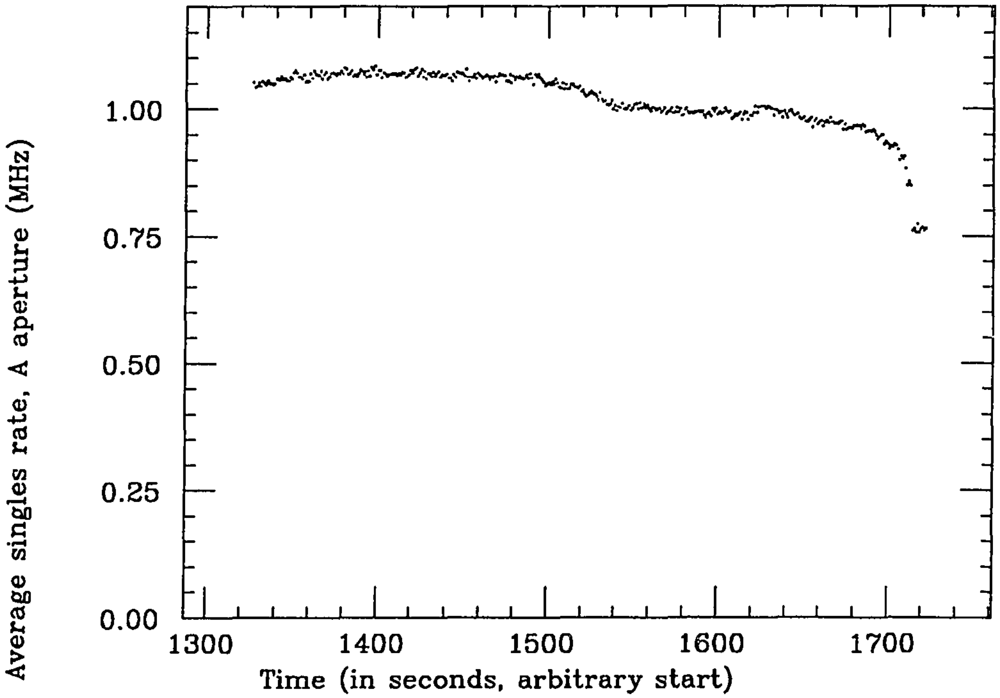

Figure 4.2: An example of weather contaminated data.

Although the scalers do register the change in background light levels brought on by the sun or moon rise, the new telescope can continue to operate when the moon is less than about half full, as long as the telescope is pointed far enough away from the moon so that the scaler rates are below about 3 MHz for the 0.35° apertures. This was tested during May '89 with the moon at about 1/4 full. The telescope was moved in right ascension from 45° East of zenith, through zenith to 45° West of zenith in 10° steps and the scaler rates were recorded at each position. During this test, the moon was at near to setting at about 25° – 15° above the horizon. Although the average scaler rate at ~ 45° East (2.61 ±0.03 MHz) was slightly higher than was observed the previous night with no moon up (2.21 ±0.03 MHz) the uncertainties in the means quoted here do not take into account possible differences due to local star light in the two regions. The rate did not increase significantly as the telescope was moved toward the moon, though, by the time the telescope was moved over to 45° West of zenith (30° from the moon), the moon was very low on the horizon and partly obscured by thin clouds. Figure 4.3 shows the scalers rates during a moon rise, compared to the raw event rate, and the event rate after imposing a higher multiplicity requirement of 12 hits in a 5 ns window. The cut event rate does not change appreciably in this example, though a small increase in the uncut data rate is observed. The plot of average scaler rates and that of the uncut rate have a suppressed zero.

4.2 Pulse Height and Timing Calibration

In order to use the information collected by the ADCs and TDCs, a calibration of these units must first be performed. We do not use a controlled source (such as a calibration laser) to determine the calibrations for each channel, but instead we use normal data runs, and extract the calibration parameters from them. This calibration is made possible partly by our capability to trigger on a shower in one part of the sky, while recording only random light* in the other aperture.

---

*We assume!

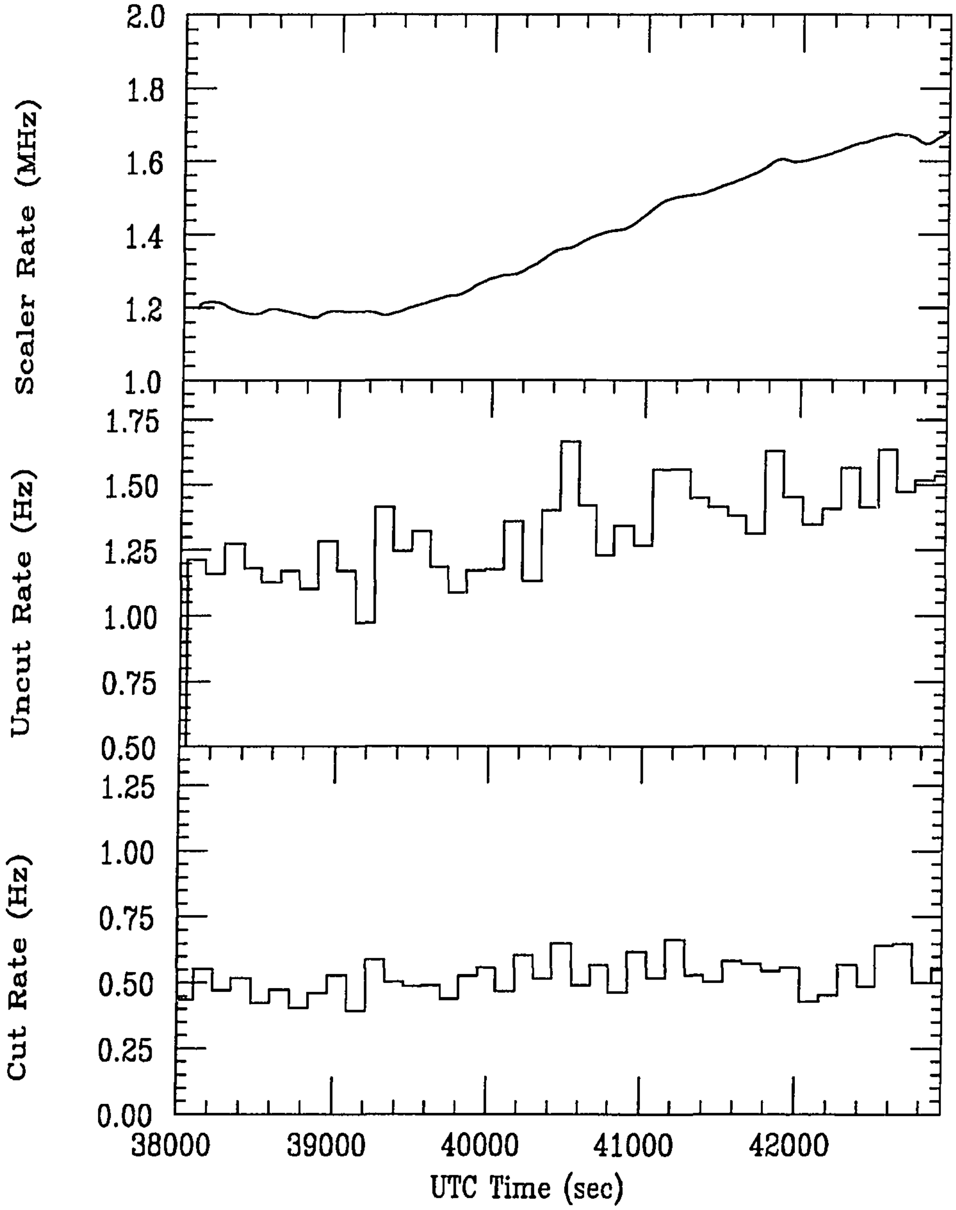

Figure 4.3: The change in scaler rates, raw event rates, and cut event rates with the rise of the moon.

4.2.1 ADC Calibrations

The minimum ADC value for each channel corresponds to no charge recorded by the ADC. It is a property of the individual ADC units rather than any input from the data stream. This value, which known as the channel's ADC pedistal, is easy to determine by averaging the ADC value for each channel when either the TDC does not receive a stop, or the channel is not latched, or both. Every hit within the latch gate will have a latch associated with it, so checking only the latches is sufficient to determine if the TDC received an in time stop. Requiring the TDC to be in overflow as well is just an additional check on this to exclude any out of time pulses. Out of time (non-latched) pulses account for less than .1% of the total pulses for each channel.

The ADC value corresponding to one photo-electron produced by the PMT photocathode is called the one PE level for the channel. To determine this value from a normal data run, the latched tubes in the *non-triggered* side of the telescope are examined. It is assumed that these channels which did not participate to form a trigger, registered only one photon from random light. Figure 4.4 shows a typical pedistal, one PE, and total ADC distribution (in this case, for channel AC). Although larger pulse height hits are seen in the total distribution, the bulk of the hits in the total distribution are consistent with one PE. Recall that since the one PE level is calculated from the non-triggered hits, the total number of events making up this distribution will be relatively small, as can be seen by the scales on the first two plots in this figure. It can also be seen from the second and third plots that the gain of the amplifier is low so that there is very little separation between the pedistal, one PE, etc. levels. On the average, the one PE levels correspond to ~ 15-60 ADC counts for the new telescope.

4.2.2 TDC Calibrations

It is necessary to perform a timing calibration to compensate for small differences in cable lengths, PMT response, and other delays between the channels. To perform this calibration, one must consider the time slewing from several sources. Trigger slewing is a result of differences in how quickly a trigger forms. This is a function of the multiplicity of the trigger. With the multiplicity setting during 1989 of 9-folds, it is the ninth hit occurring within a ~ 7 ns window that causes an event trigger to be produced. In the case of a high multiplicity event, the ninth hit will usually come in more quickly than the ninth hit in a low multiplicity event. Thus, this slewing affects the relative TDC average *between* these two events but not the relative time of hits within a single event. Assuming that this slewing does not significantly affect the timing calibration values for each channel, trigger slewing is not a problem, as long as one only uses the relative time between events rather than absolute times. This is what is done when one uses a sliding window to make timing cuts on the data, rather than choosing a fixed window beginning at a specific TDC value for each event. The small effect of multiplicity slewing on the timing calibration for each channel can be minimized by choosing only similar multiplicity events as a basis for the calibration.

ADC, or pulse height slewing, is a result of the affect of the size of the PMT pulse on the recorded time of the hit. After the PMT anode pulse goes through its

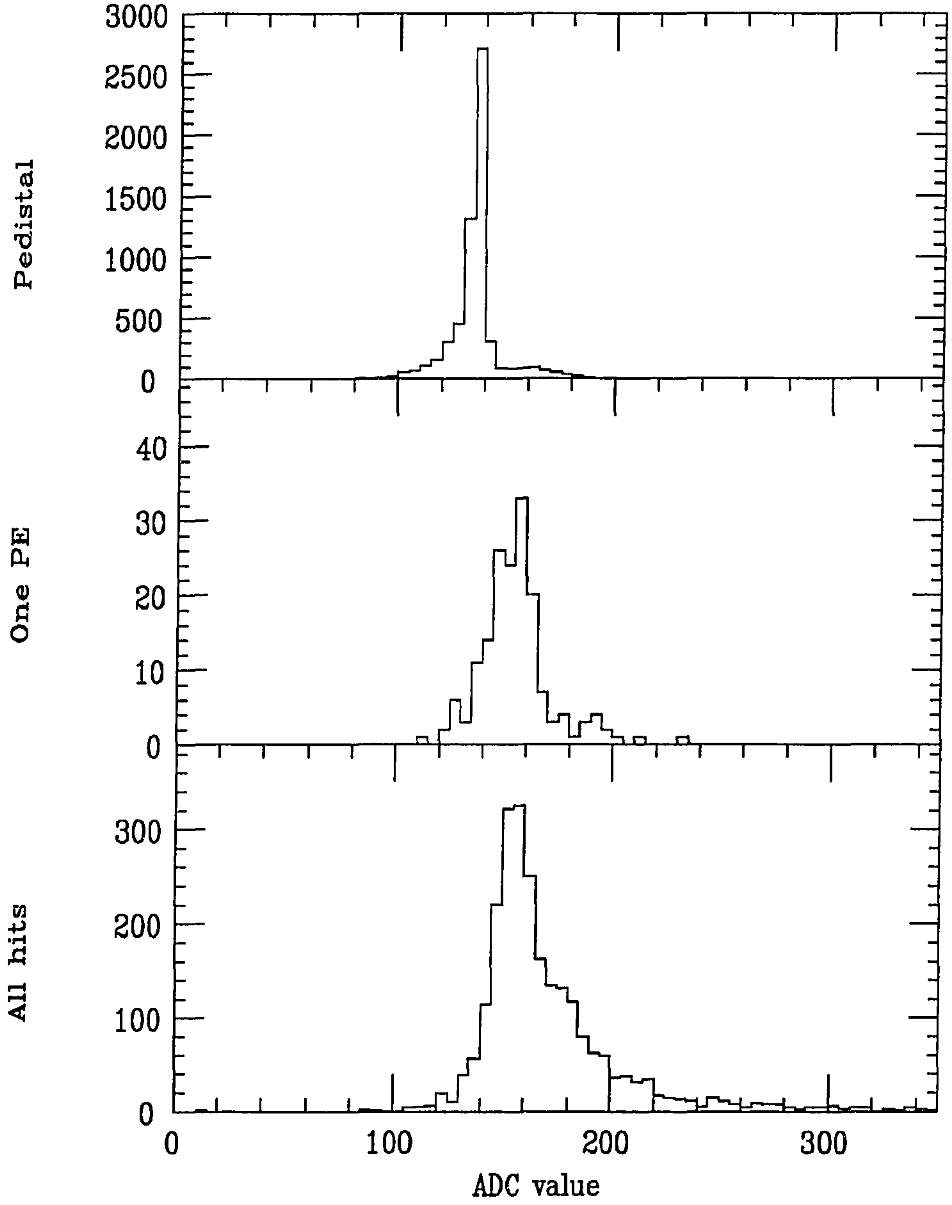

Figure 4.4: The pedistal, one PE, and total ADC distributions for a typical channel (AC).

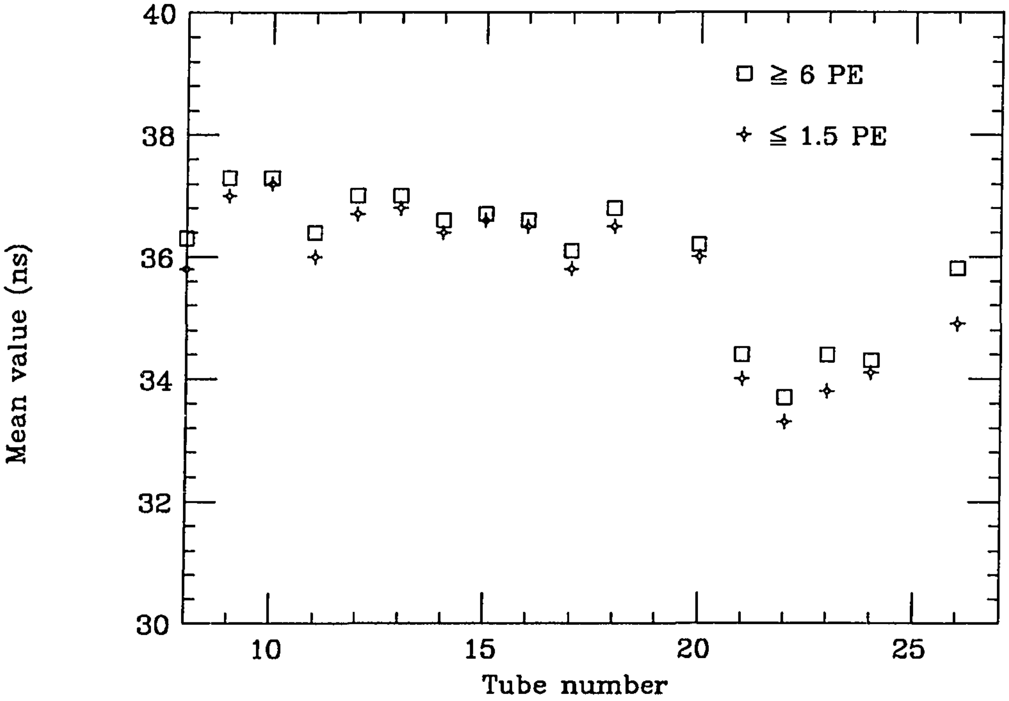

Figure 4.5: Pulse height slewing in the new telescope.

final amplification in the analog fan-out, it is discriminated before being sent to the TDCs. The discriminator is designed to produce a pulse when the input anode pulse drops below a certain, threshold value. For a very large pulse, the time taken to drop below the discriminator threshold is shorter than for a smaller pulse. To determine if pulse height slewing is a problem for the new telescope, a plot of TDC value for low (≤ 1.5) and high (≥ 6) PE hits is presented in Figure 4.5. It can be seen from this figure that the affects of pulse height slewing are small, well within 1 ns for every channel. Because of this, a slewing correction was not made for the data that will be discussed in this dissertation.

By requiring that all events used for the timing calibration are of high multiplicity (greater than 18) trigger slewing is minimized, and by requiring that each channel within this high multiplicity event have a large (greater than 360 count) ADC value, the pulse height slewing is reduced. Thus, employing these two requirements, a TDC calibration can be performed that is relatively free of the effects of slewing. After imposing these requirements, very few hits make up the timing calibration for each run, but since one can use all of the runs during a dark shift (as long as a PMT, amplifier, or other component was not changed during this time, which will change the calibration values) enough events are left to provide satisfactory statistics for each channel. Typically, one calibration file is produced for the entire month's data set. The 1 σ errors in the distribution of TDC values for each channel is shown along with the calibration correction applied to the channel in Figure 4.6. This plot is for the July '89 data. From this figure, uncertainties in the individual hit times are seen to be on the order of 1–2 ns. The uncertainty in the average calibration values themselves is on the order of 0.02–0.04 ns for this data set.

4.3 Barycentering

The time analysis of signals from relatively short period sources necessitates a careful treatment of event times. Corrections for the movement of the earth and the orbital motion of the neutron star, in the case of a binary system, must be made. Most of what I about to discuss may be found in Laurence Taff's book on spherical astronomy (Taff, 1981) or in the Astronomical Almanac for each year (for

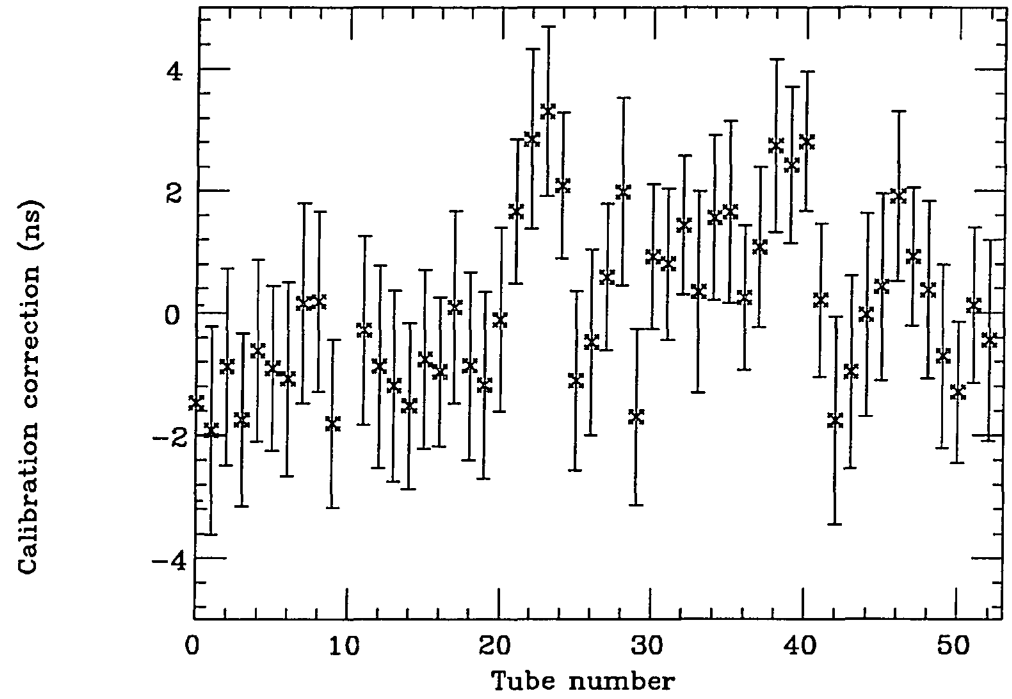

Figure 4.6: Calibration corrections and 1 σ errors for July '89.

example: Astronomical Almanac, 1988). The abbreviations defined below are, for the most part, those used in the Astronomical Almanac.

There are very many different time scales in astronomy.* At the HGRO, the time of each event is recorded in coordinated universal time (UTC). This time scale is the basis for broadcast time signals. A one leap second correction is made to this periodically, inserted either on July 1st or January 1st which allows International Atomic Time (TA1) to be calculated from UTC. In principle, a leap second could need be subtracted to obtain TA1, but so far this has never been necessary. TA1 is based upon atomic standards (one second in this time scale is defined in terms of the frequency of radiation from a hyperfine transition in the cesium atom). This atomic standard represents the most accurate measure of time we currently use. It has been suggested that the measure of periodicity from short period pulsars will eventually provide an even more accurate measure of time. For the two years of data to be analyzed in this dissertation: the correction for 1987 is TA1 - UTC = 23 s added on July 1, 1985 and the correction for 1989 is 24 s added on January 1, 1988.

---

*As is stated in Taff's text, "Time can be the most confusing aspect of astronomy.".

TA1 can then be converted to Terrestial Dynamical Time (TDT), which was introduced in the mid 1980's as a time scale for geocentric ephemerides. This conversion is: January 1 0 h 1977 TA1 = January 1.0003725 h 1977 TDT. For the purpose of pulsar timing, we need to reference this geocentric time to the barycenter of the solar system. The vector from the heliocentric point to the solar system barycenter will be given by:

$$\left[1+\sum_{i=1}^{n}\left(\frac{M_i}{M_\odot}\right)\right]\mathbf{R}_B=\sum_{i=1}^{n}\left[\frac{M_i}{M_\odot}\mathbf{R}_i\right] \tag{4.1}$$

Here, M_i is the mass of the ith planet or other massive body at a radius $\mathbf{R}_i$ from the center of the sun, and a total number of n massive objects are considered in the correction. $\mathbf{R}_B$ is the vector from the center of the sun to the solar system barycenter. After corrections for the planets have been made, the barycentric point is still well within the surface of the sun. For the earth, the mass is taken as the combined earth/moon mass, and radial vector is to the earth/moon center of mass.

The final step to correct for the motion of the observer is to convert the dynamical time calculated above to a coordinate time corresponding to the solar system barycenter. From solutions to Kepler's equations in general relativity, the coordinate time can be defined. The mean anomaly may be defined as $M = n(t - \tau)$ were $n = 2\pi/T$ increases uniformly with time during the earth's orbit, T being the orbital period of the earth. τ is the time of perihelion*. Barycentric Dynamical Time (TDB) is given in equation 4.2, neglecting terms of $\geq e^3$.

$$TDB = TDT + \frac{2me}{an}\left[\sin M + \frac{1}{2}e\sin 2M\right] \tag{4.2}$$

a is the semimajor axis and e is the orbital eccentricity. Substituting into Equation 4.2 values of these constants defined for the motion of the earth:

$$TDB = TDT + 0.001658\sin M + 0.000014\sin 2M \tag{4.3}$$

The mean anomality is tabulated in the Astronomical Almanac. In practice, it is calculated directly given the day number and year.

A barycentric correction routine was written by Bob March at the University of Wisconsin, and is used for all Haleakala time analysis. This program uses the JPL DE200 barycentric ephemeris for the helocentric positions of the earth and other planets and the velocity of the earth. The barycentric position for each object is determined at a time $(t - \tau)$.

---

*Perihelion is the place of closest approach, or, more formally, in this case it is the position of the minimum in the heliocentric orbit.b

Orbital doppler corrections must be made for the motion of Her X-1. In this case, these are simplified since the orbit of Her X-1 is known to be nearly circular. The correction that must be made is just:

$$\delta t = -\frac{a \sin i}{c} \cos \phi_i \tag{4.4}$$

Where the phase, ϕ_i, is just $\frac{2\pi}{T_{orb}}(t_i - t_o)$ because of the simplified geometry and $a \sin i$ is the orbital radius. The epoch defining the zero in the phase (t_o) can be rather confusing. X-ray astronomers generally define t_o in reference to the center of eclipse of the orbiting pulsar, so that we have $\phi = 0$, 2π, 4π, ... at that point. On the other hand, at lower energies, $\phi = 0$ is often taken at the line of ascending nodes. For e=0, this corresponds to a $\pi/2$ shift between the two reference times. For Her X-1, as can be deduced from Equation 4.4, the orbital epoch is defined at the center of eclipse. Considering both this source motion, and that for the earth discussed above, we can write an event time referenced to the solar system barycenter as:

$$t_{event} = TDB + \delta t \tag{4.5}$$

TDB is given in Equation 4.3. It is this time which will be used in the search for periodicity from the source (Section 4.4). When event times are discussed in this section, it is assumed that the time is defined as t_{event} above. These barycentered times will also be used in Section 4.5 when calculating the time difference between events to investigate the behavior of the off-source aperture, which is expected to contain only random background. This is in preparation for a discussion of the DC rate excess calculations.

4.4 Periodicity Analysis

In this section, the search of data for a periodic signal is discussed. After calibration and removal of weather contaminated data, the remaining data are divided into intervals for periodicity analysis. The 1989 data divides naturally into 900 s intervals, since the two apertures were alternated between the on and off source at that period. Each alternation, we call a "wobble", so that each 900 s interval is referred to as a wobble interval.

Given a time interval of length T containing n events, we would like to test each event with time t_i in the interval for a periodic structure over a specific range of test periods. Two similar tests to perform this analysis will be described: the Rayleigh test and the H_m test. The Rayleigh test, which has been used extensively in VHE gamma-ray astronomy (Gibson, 1982), is a powerful test for periodicity at the fundamental period for a sinusoidal light curve. The H_m test is effective for a range of light curve shapes (DeJager, 1987). As will be explained, both tests have been used in the analysis of the 1987 data; however, since we have little *a priori* knowledge of the shape of the light curve expected, the H_m test is used in the final analysis of the data, and it was the sole test performed on the 1989 data set. The discussion will proceed with the description of both tests, followed by brief comments about the implementation of periodicity tests.

4.4.1 The Rayleigh Test

For a given test frequency, the Discrete Fourier Transform (DFT) can be calculated, representing a vector in the complex plane. For Her X-1, the range of frequencies to be tested is small, usually no larger than several times the independent Fourier period spacing, P^2/T where P is the test period, and T is the length of the test interval. For a 15 minute wobble interval, this corresponds to $P^2/T = 0.0017$ s for Her X-1. The DFT for a frequency ℓ can be written as:

$$J(\omega_\ell) = \frac{1}{n}\sum_{j=0}^{n-1} A_j \exp(-i\omega_\ell t_j) \tag{4.6}$$

The magnitude of the signal vector may be defined as $n|J_\ell|^2$, where $|J_\ell|$ is the magnitude of the DFT vector at the frequency ℓ.

The Rayleigh test, which was developed to test for uniformity on a circle, can be defined in a similar manner. The resultant vector corresponding to the measurements distributed around the circle, is called the Rayleigh vector. Since all measurements have the same weight, $A_j = 1$ for all j in Equation 4.6 and the magnitude of the Rayleigh vector may be expressed as:

$$R_\ell = \left[(\frac{1}{n}\sum_{j=1}^{n} \cos\phi_{j,\ell})^2 + (\frac{1}{n}\sum_{j=1}^{n} \sin\phi_{j,\ell})^2 \right]^{\frac{1}{2}} \tag{4.7}$$

Where the measured phase is given by $\phi_{j,\ell} = \frac{2\pi}{P}t_j$. $\frac{2\pi}{P} = \omega_\ell$ is the test frequency for a period P. At the fundamental we define $\ell = 1$, at the first harmonic, $\ell = 2$, and so on. $t_j = t_0 - t_i$ is the time difference between the ephemeris of the test period and the event time, assuming the period derivative is zero. In practice, $\omega_\ell t_j$ is taken to be the remainder of the division of t_j by the test period T (times 2π), since this remainder carries the entire phase information. Equation 4.7 may be rewritten as the Rayleigh power:

$$nR_\ell^2 = \frac{1}{n}\left[(\sum_{j=1}^{n}\cos\phi_{j,\ell})^2 + (\sum_{j=1}^{n}\sin\phi_{j,\ell})^2\right] \tag{4.8}$$

The sums are simple to compute. For large enough n*, the distribution of $2nR_\ell^2$ is that of a χ^2 with 2 degrees of freedom, thus the probability is given by:

$$P = \exp(-nR_\ell^2) \tag{4.9}$$

Even it is not a universally powerful test for testing an alternative hypothesis, H_A against the null hypothesis, H_o, the Rayleigh test has been widely used because of the lack of knowledge of the shape of the light curve. H_o is assumption that the "signal strength" for an interval is zero. Here, signal strength is due to any non-uniform signal or fluctuation in the data; it is not assumed to be a signal of a specific sort from the γ-ray source. Thus, rejecting H_o does not imply that a specific signal hypothesis has been accepted; it simply states that some alternative hypothesis, H_A, exists.

---

* "large enough" is $n > 100$ (DeJager, 1987) which will be true for all intervals tested.

4.4.2 The H_m Test

The H_m test was adapted by DeJager for testing the significance of a light curve. The test is as powerful as the Rayleigh test for a sinusoidal light curve, and it is more powerful than the Rayleigh test for other, sharper light curve shapes. This test is based upon the Z_m test, for which the statistic is (similar to the Rayleigh power):

$$Z_m = 2n \sum_{\ell=1}^{m} \left[(\frac{1}{n} \sum_{j=1}^{n} \cos \phi_{j,\ell})^2 + (\frac{1}{n} \sum_{j=1}^{n} \sin \phi_{j,\ell})^2 \right]^{\frac{1}{2}} \tag{4.10}$$

As with the Rayleigh statistic, the Z_m statistic is distributed as a χ^2 with $2m$ degrees of freedom. The harmonic sum over ℓ is taken up to a pre-determined value, and all harmonics above this value are ignored. This choice of m requires some knowledge of the expected light curve. It would be desirable to remove this *a priori* choice, and find the optimum value of m based upon the data. This is what the H_m test accomplishes.

The optimum value of m is given by the Hart rule (Hart, 1985) which states that the power reaches a maximum where:

$$m_{max} = max(Z_m^2 - 4m)$$

Which leads to the statistic:

$$H_m = Z_m^2 - 4(m-1) \geq 0 \tag{4.11}$$

Here m is chosen based upon the data set. The probability associated with this distribution is no longer the simple χ^2 dependence, since m is a random variable. DeJager presents the parametrized form of the probability distribution as:

$$P_m = \int_x^\infty \exp(-t)t^{r(m)-1}dt/\Gamma(r(m)) \tag{4.12}$$

Where $r(m) = H_m^2/\sigma_{H_m}^2$ and $x = (H_m/\sigma_{H_m}^2)H_m$. σ^2 is the variance of H_m. This can be converted to a similar form as the Rayleigh statistic by $Z = \ln(P_m)$, so that this number Z can be directly compared to the Rayleigh power, nR^2 .

Implementation of Periodicity tests

To apply a periodicity test to an interval of data, we must first determine the phase of an event with respect to the ephemeris time, t_o for the test period. To terms linear in $\dot{P}$, this is:

$$\phi_i = \frac{t_i - t_o}{P} - \frac{(t_i - t_o)^2}{P^2}\frac{\dot{P}}{2} \tag{4.13}$$

We assume here that here that the period derivative is a linear change over time. For Her X-1, this is true over short intervals of several months to a year, but it does not apply over the entire X-ray history of the source (Figure 2.2). If we assume that $\ddot{P} = 0s^{-1}$, then in order to have phase coherence over an observation interval T, we must have $\delta\phi = (T^2\delta\dot{P})/(2P^2) < 1$. Over a 900 s interval for Her X-1, this is not a problem since, using $\delta\dot{P} \sim 10^{-13*}$ the phase shift is negligible ($\delta\phi = 2.6 \times 10^{-8}$). Even over an entire dark shift, the phase shift is less than one complete phase. In practice, after the phase is computed for an event, its contribution to the sums in Equation 4.8 or 4.10 can be determined, leading to a rapid calculation of the Rayleigh power or H_m probability for each time interval.

4.4.3 Estimation of the Signal Strength

We can estimate the signal to background ratio if we assume we know the shape of the signal. In practice, of course, this shape is unknown, which is the advantage of the harmonic maximization of the H_m test. For now, we will assume that all of the signal is in the first harmonic ($\ell = 1$), and that our signal has a gaussian shape. In general, the length of the resultant vector for a test statistic (the Rayleigh vector, for example) can be expressed in terms of the Fourier integral as:

$$|M| = \int_0^{2\pi} \exp(i\phi) f(\phi) d\phi \tag{4.14}$$

$f(\phi)$ is the probability density function of both the signal and the background. The true magnitude, $|M|$, differs from $R_{\ell=1}$ defined in Section 4.4.1 slightly (De-Jager, 1987), so that:

---

*This is the period derivative for Her X-1 when it is undergoing spin up.

$$|M|^2 = \frac{nR^2 - 1}{n - 1} \tag{4.15}$$

For large n, we can see that $|M|^2 \sim R^2$ for typical values of nR^2. The density function can be constructed from the signal and background parts as:

$$f(\phi) = \frac{n_s f_s(\phi)}{n} + \frac{(n - n_s)}{(2\pi n)} \tag{4.16}$$

The total number of events can be divided into a *known* number of signal events, n_s, and a number of background events, n_b, which include both background and noise events. The background is assumed to be randomly distributed. The integral in Equation 4.14 can then be performed using the probability density function for a gaussian signal.

$$|M| = \frac{n_s}{n} \int_0^{2\pi} \frac{1}{\sqrt{2\pi}\sigma} \exp(i\phi) \exp\left(\frac{-\phi^2}{2\sigma^2}\right) d\phi \tag{4.17}$$

$$|M| = \frac{n_s}{n} \exp\left(\frac{-\sigma^2}{4}\right) \tag{4.18}$$

In practice, σ is the width of the signal peak multiplied by its duty factor. From Equations 4.15 and 4.18 we find that the signal to background ratio, defined as $n_s/\sqrt{n}$, can be written as:

$$\frac{n_s}{\sqrt{n}} \simeq \left[\frac{nR^2 - 1}{\exp(-\sigma^2/2)}\right]^{1/2} \tag{4.19}$$

We have taken $(n-1) \simeq n$ for large n. Assuming a duty factor of 30% and a signal peak standard deviation of 1.6 radians, we would find that the signal to noise ratio expected for a Rayleigh power of 10 to be 3.2 σ. A maximum likelihood estimate of the expected number of signal events for a given Rayleigh power, and the consistency between n_s observed and that expected has been presented recently by D.A. Lewis (Lewis, 1989). The parameter $\alpha = 2Z + \sigma^2$ is distributed as a chi-square with three degrees of freedom in the case where background fluctuations in the Rayleigh power, Z, and the rate excess, σ, are not correlated. From α, the probability that the observation is due to random background can be calculated. Using a general signal density function, $f_s(\phi)$, he calculates the probability of obtaining the observed values of the Fourier amplitudes (Equation 4.14) and the number of signal events. The exponent of the likelihood function is minimized by varying the expected number of events and the phase, reducing the exponent of the probability equation which has three degrees of freedom to an equation with one degree of freedom for the expected number of signal events. The consistency between the observed Rayleigh power and the rate excess is then given by the function:

$$\gamma = \frac{(n_s - \sqrt{nP}/g_s)^2}{[\sqrt{n} + n/(2g_s^2)]} \tag{4.20}$$

The function g_s depends upon the assumed signal light curve, thus γ may be calculated rapidly for a range of light curves. γ is also distributed as a chi-square with one degree of freedom (as was the expected number of signal events). The probability of obtaining a Rayleigh power producing an individual probability P and n_s signal events can be determined from γ.

4.5 DC Analysis

In this section, the process by which a counting excess is determined for each interval is described. First, the final stage of data selection for the DC counting rate excess calculation must be performed in order to remove any fluctuations in the background causing a deviation from the expected random distribution. The Gini-test is used to test the data for randomness. Then, the background rate is estimated from fitting the off source using the expected zenith angle dependence. The justification for the equation used to describe the rate as a function of zenith angle is presented. This is followed by a discussion of the errors associated with the fit. This analysis will be used primarily for the 1989 data set, since this data was taken in track wobble mode, allowing a background estimate to be made for each aperture. The 1987 data was taken with the same aperture on source throughout the entire run (track normal operation).

4.5.1 The Gini-test

In order to use the off source to determine the background rate, we would like to verify that these events represent a random data set. The Gini-test has been proven to be a powerful test of the randomness of a set of events in time (Gail and Gastwirth, 1978). This test was applied to VHE γ-ray measurements by DeJager as a test for the randomness of off source events (DeJager, 1987). Events in time can be described by the Poisson probability:

$$P_n(t) = \frac{1}{n!}(t/\tau)^n \exp(-t/\tau) \tag{4.21}$$

Where t is the time interval and n is the number of events, so this represents the probability of n events occurring in the time interval t. If one considers the time interval *between* two events in the time ordered set, then the probability associated with this interval is the probability of $n = 0$ events occurring during this interval, $\Delta t = t_{i+1} - t_i$, or:

$$P_0(\Delta t) = \exp(-\Delta t/\tau) \tag{4.22}$$

Therefore, the time difference between events should be exponentially distributed if the original set of events are randomly distributed in time. The gini-test tests a set of *time ordered* Δt's for agreement with the expected exponential distribution. The gini statistic is:

$$G = (g_n - \frac{1}{2})[12(n-1)]^{\frac{1}{2}} \tag{4.23}$$

where g_n is given by:

$$g_n = \frac{\left[\sum_{i=1}^{n-1} i(n-i)(\Delta t)\right]}{\left[(n-1)\sum_{i=1}^{n} t_i\right]}$$

Assuming that the Δts are time ordered, G represents the number of standard deviations this interval in the data set is away from the expected exponential probability distribution. If G, which is called the Gini-number, is calculated for each wobble interval, then those intervals which deviate from the expected, normal distribution by more than a certain amount may be disregarded. For this analysis, all intervals with $\mid G \mid \geq 1.96$ are eliminated from the DC analysis. This corresponds to a 5% probability.

The Gini test will be valid for any interval of reasonable length that we will wish to test*. It may be applied to the off source data before any analysis has been performed with the on source data set. Because of this, any intervals containing environmental or instrumental fluctuations, causing a deviation from the expected, distribution of the off source, can be discarded before any bias may be introduced from a prior "peek" at the on source data.

4.5.2 The Cosmic Ray Rate as a Function of Zenith Angle

It is necessary to determine the expected rate as a function of zenith angle in order to estimate the correct cosmic ray background rate. Although this dependence can be approximated as $\cos^n \theta$ or by a similar polynomial distribution, a better, more exact dependence can be obtained from considering how the observed detection of cosmic ray induced photons changes with changing zenith angle. The largest variations are caused by the change in the target area of the telescope and the attenuation and divergence of Čerenkov photons as a function of zenith angle. These arguments have been presented in a more complete form elsewhere (Learned, 1986 and Matthews, 1986) and they were excellently summarized and expanded recently (Sinnis, 1990). Here, I will sketch these arguments to justify the fitting procedure used to determine the background rate at a given zenith angle.

---

*DeJager states that this test is valid for intervals with as few as 10 events. Typically, each 900 s interval contains 200-500 events, depending on the cuts employed and the zenith angle of the telescope.

We first consider the known form of the differential cosmic ray spectrum. From this, we can deduce that the flux of cosmic rays from zenith goes as $\Phi(E) = \Phi_o \, (\frac{E}{E_o})^{-\gamma}$. Where here the value of γ is simply assumed to be constant. We will not fix this to be the spectral index, ~ 2.5, instead, this will be fit from the data. γ is expected to be influenced by the response function of the telescope, so it will not be exactly equal to the spectral index. We will assume that the cosmic ray background is isotropic, so that the only variations in the rate with zenith angle are an effect of the change in the distance traveled in the atmosphere and the change in our collection area.

The rate detected by our telescope above an energy threshold E_{th} can be written as:

$$R(\theta) = \int_{E_{th}}^{\infty} \Phi_o \left(\frac{E}{E_o}\right)^{-\gamma} A(E,\theta) dE \tag{4.24}$$

where $A(E,\theta)$ is the collection area of the telescope at shower maximum. This integral can be done if the variation of the collection area with energy is assumed to be small, allowing us to separate the angle and energy dependent parts of the

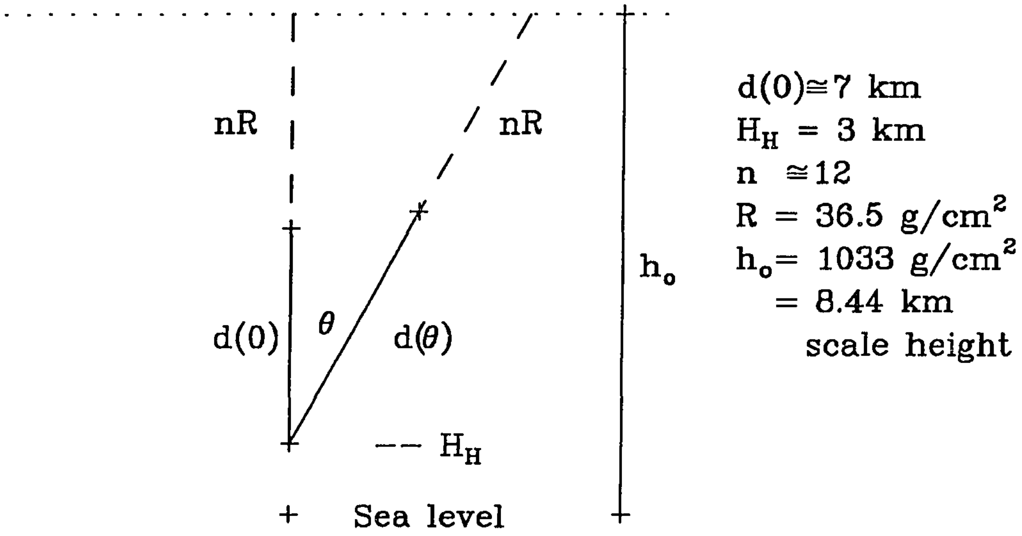
nR
nR
d(0)
θ
d(θ)
-- H_H
+ Sea level
h_o
d(0)≅7 km
H_H = 3 km
n ≅12
R = 36.5 g/cm²
h_o= 1033 g/cm²
= 8.44 km
scale height

Figure 4.7: The distance to shower maximum, d, at a given zenith angle, θ. the dotted line is the top of the "flat" atmosphere, n is the number of radiation lengths, R.

integral. The rate at a given zenith angle can then be determined as a function of the rate at zenith.

The variation of the area at shower maximum as a function of θ will be proportional to $d(\theta)^2$, where $d(\theta)$ is the distance to shower maximum (Figure 4.7). This can be determined assuming a flat atmosphere model, and assuming that the point of the maximum extent of the shower will be determined by the amount of atmosphere that the shower has transversed since the initial interaction in the atmosphere. This thickness, t, is given by:

$$t = \frac{\rho_o}{\cos\theta} \int_{d(\theta)\cos\theta}^{\infty} \exp\left(\frac{-r}{h_o}\right) dr \tag{4.25}$$

Here, h_o is the scale height of the atmosphere (8.44 km), and ρ_o is the photon density at sea level. Since t will always be the same independent of the zenith angle, $t_\theta = t_0$ gives:

$$\frac{\rho_o h_o}{\cos\theta} \exp\left(\frac{-d(\theta)\cos\theta}{h_o}\right) = \rho_o h_o \exp\left(\frac{d(0)}{h_o}\right)$$

or:

$$A(E) \propto \left[\frac{d(\theta)}{d(0)}\right]^2 = \frac{1}{\cos^2\theta}\left[1 - \frac{h_o \ln(\cos\theta)}{d(0)}\right]^2 \tag{4.26}$$

The dependence of the area on energy is absorbed into the energy ratio, so that the value of γ in Equation 4.24 is no longer exactly equal to the cosmic ray spectral index.

Since we will need it soon, lets convert this distance from shower maximum to an atmospheric thickness. If $\tau(\theta)$ is the thickness of atmosphere between the altitude of the Haleakala telescope, $H_H = 3km$, and shower maximum, then we can directly use Equation 4.25 with the appropriate limits:

$$\frac{\tau(\theta)}{\tau(0)} = \frac{\frac{\rho_0}{\cos\theta}\int_{H_H}^{d(\theta)\cos\theta} \exp(\frac{-r}{h_o}) dr}{\rho_o \int_{H_H}^{d(0)} \exp(\frac{-r}{h_o}) dr}$$

$$\frac{\tau(\theta)}{\tau(0)} = \frac{1}{\cos\theta}\left[\frac{\exp(\frac{-H_H}{h_o}) - \exp(\frac{-d(\theta)\cos\theta}{h_o})}{\exp(\frac{-H_H}{h_o}) - \exp(\frac{-d(0)}{h_o})}\right] \tag{4.27}$$

Assuming that the photon density varies linearly with energy, we can write the energy ratio in terms of a ratio of the photon densities. The two factors affecting the observed photon density are the atmospheric attenuation and the geometric divergence of the photons produced in the cascade. This second factor is proportional to $1/d(\theta)^2$. We can write the photon density attenuation as (Learned, 81):

$$\rho(E,\theta) \propto \left(1 + \frac{\tau(\theta)}{\tau(0)}\right)^{-a} \exp(-b\tau(\theta)) \tag{4.28}$$

Here, $\tau(\theta)$ is the thickness to shower maximum defined in Equation 4.27, a is determined to be 0.574, and b is the attenuation coefficient. The atmospheric attenuation has been measured over Mauna Kea on the island of Hawaii*. From these measurements, the absorption length to shower maximum ($b\tau(0)$) will be 0.07 for the B-370 filters used in 1987. During the 1989 observation season, U-340 filters were used. When the spectral response of these filters are folded with the response function of the PMTs and the expected cosmic-ray spectrum (Section 3.2), the wavelength of maximum response is about 350nm. The absorption length at this wavelength is 0.10. The ratio $\rho(E,0)/\rho(E,\theta)$ may be written as:

---

*This data from the Canada-France-Hawaii Telescope was obtained for us by Gus Sinnis (Beland, *et al.* 1988).

$$\frac{\rho(E,0)}{\rho(E,\theta)} = \left[\left[\frac{1+\tau(\theta)/\tau(0)}{2}\right]^{a} \exp[b(\tau(\theta)-\tau(0))]\right] \tag{4.29}$$

Assuming that the number of photons observed at zenith ($\propto \rho(E,0)(\theta)^2$) is proportional to E_{th}, after performing the integration of Equation 4.24, Equation 4.29 and the factor of $d(\theta)^2$ for depletion due to geometric divergence may be substituted in for the ratio E_{th}/E_o. Finally, the area at shower maximum determined in Equation 4.26 is inserted and we get that:

$$R(\theta) = R(0)\left[\frac{d(\theta)}{d(0)}\right]^{4-2\gamma} \left[\frac{1+\tau(\theta)/\tau(0)}{2}\right]^{-a(\gamma-1)} \exp\left[-b\tau(0)\left(\frac{\tau(\theta)}{\tau(0)}-1\right)(\gamma-1)\right] \tag{4.30}$$

Where the ratios $d(\theta)/d(0)$ and $\tau(\theta)/\tau(0)$ are given in Equations 4.26 and 4.27. It is possible to simplify this equation for small zenith angles. Taking $\cos\theta \sim 1$ we find that $d(\theta)/d(0) \sim \tau(\theta)/\tau(0) \sim 1/\cos\theta$. So:

$$R(\theta) \sim R(0)\cos^{2\gamma-4}\theta \exp\left[-b\tau(0)\left(1/\cos\theta-1\right)(\gamma-1)\right] \tag{4.31}$$

In practice, this is a good approximation out to zenith angles of $\sim 35°$; however, as expected, this approximation fails badly out at large zenith angles. Only a very small part of the Her X-1 data set during both 1987 and 1989 was taken at zenith angles larger than 35°, thus for the 1987 sample, this approximation to the rate is used. Because the 1987 data was taken in track normal mode, a careful DC rate excess analysis could not be performed. Thus, the zenith angle fit was used only for run selection for the 1987 data. For the 1989 data sample, the full form of the rate as given in Equation 4.30 was used.

From Equation 4.30 or 4.31, the expected number of background events may be determined over a time interval $T = t_2 - t_1$ by integrating over the interval:

$$N_b = \int_{t_1}^{t_2} R(\theta)dt \tag{4.32}$$

The zenith angle is also a function of time during the run. In practice, this integral is evaluated numerically, with dt being the interval spacing between events.

4.5.3 Errors in the Rate Excess Calculations

$R(\theta)$ is determined by a fit of Equation 4.30 or 4.31 to the off source data for one data run or several runs taken during the same evening. The fitting process using the CERNLIB fitting routine MINUIT will be further discussed in Section 5.2, here the errors in the rate excess determination are explained. There are two main sources of error in the DC calculations. There is an error associated with the zenith angle fit, including both the error in the off source data and the correlated error in the fitting process, and there is the Poisson error in the number measured during an on source interval.

In order to help to eliminate variations caused by the changing atmospheric conditions overhead, or scattering caused by clouds near the horizon, the fit to the rate was performed on a night by night or a run by run basis. In principle, the atmosphere will change on time scales much shorter than the length of a run, or even the length of a wobble interval; however, these fluctuations are usually small, and cause no noticeable disturbance in the rate. The exception to this is the passing of a dense cloud overhead, or condensation forming on the mirrors. These conditions are often detected while the data is being taken, and are evident in the scaler rates when the data is analyzed. The column height of water above the telescope will change from night to night. Unless the moisture content becomes large enough to form visible clouds, this variation will go unnoticed while the data is taken, necessitating a nightly fit to eliminate the errors caused by this variation of the background rate.

The errors associated with a nightly zenith angle fit can be estimated from the error in the fit parameters. From Equation 4.30, all parameters are known except $R(0)$ and γ. γ, which is proportional to the spectral index, is not expected to vary from night to night, so we will eliminate this as a free parameter in the final fit. It is thus the error in $R(0)$, which is typically 1.5% - 3.5%, that will contribute to the error in each fit.

Chapter 5

Time Series and DC Analysis of the Haleakala Data

The observation of a number excess in the direction of a source when that direction is compared to the background cosmic ray rate expected for the zenith angle of observation is taken as a measure of the VHE γ signal from that source. This may be in the form of steady emission over a long period of time, a short transient burst of photons, or pulsed emission at a characteristic frequency (usually the neutron star rotation frequency). This number excess (or DC excess) is a very straightforward quantity to define: it is merely the number of events observed from the source above the expected background; however, the expected background to which the on source must be compared is a difficult quantity to determine. Even though the Haleakala telescope has the capability to observe an off source region of the sky and the on source concurrently, this simultaneous off source is at a slightly different zenith angle, so it may not be directly compared to the on source. In addition, the two apertures behave slightly differently, even after cuts have been applied to the data, as is seen in the plots of expected rate as a function of zenith angle for the two apertures (Figure 5.1). Points plotted as square boxes differ from the fit by more than 2σ. The presence of dead channels (a problem in the 1987 Her X-1 data set) will also increase the difference between the two apertures.

If the telescope is operated in a track wobble mode, where the instrument will alternate between having the A aperture and the B aperture viewing the source, then it is possible to determine the expected rate in each aperture by using the intervals during which the aperture was not viewing the source. The 1987 data was only taken in a track normal mode, where the instrument views the source with only one aperture during the entire run, so this is not possible for the '87 data set. The 1989 data was taken in track wobble mode, thus a more complete DC analysis will be performed on this data. For the '87 data, it is still possible to use the zenith angle fit for the on source to look for a short term rate increase, or burst, during a run; however, this excess may be partially masked since it is contributing to the overall fit. If no short term excess exists, but instead a low level constant flux is present, this will be nearly impossible to detect if the instrument is in track normal mode. Its detection will be especially difficult if the same aperture is usually used to view the source. As we will see, all but two of the '87 Her X-1 runs analyzed were taken with the A aperture viewing the source. The reason for this asymmetry is simple result of the definition of zenith for the old telescope, which was set up to be the A aperture pointed at zenith. Movement of the telescope from zenith to a guide star, then (after a raster to fix the position of the telescope on the guide star) from the guide star to the source were conducted with the guide star and then the source in the A aperture. One could, before beginning a run, wobble the telescope once to put the B aperture on source, but this was usually not done.

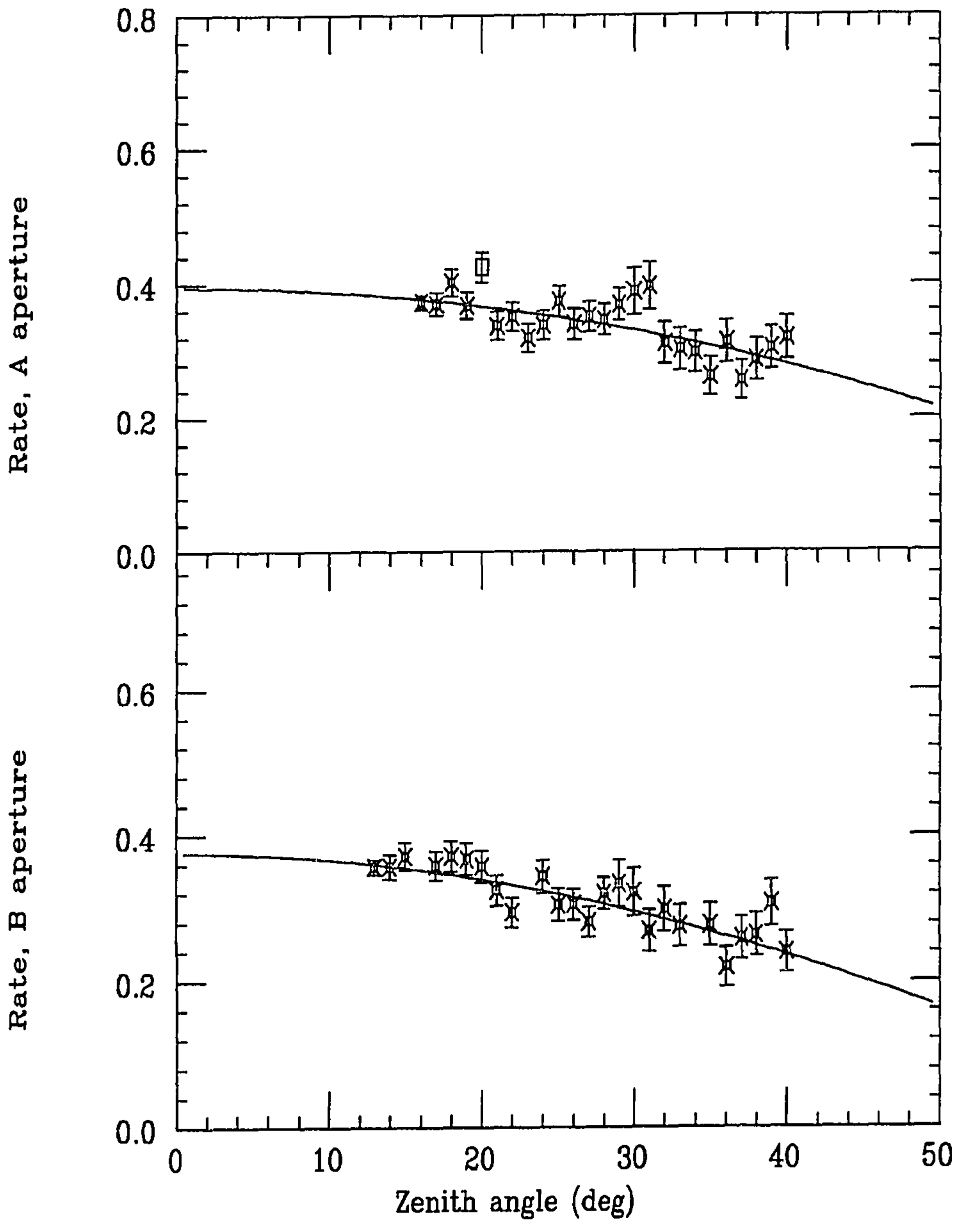

Figure 5.1: Rate as a function of zenith angle for run 1162, A and B apertures.

If one knows the pulse period and corresponding ephemeris for a source, then a more sensitive test for VHE γs may be performed through periodicity searches of the data. The two tests that will be employed, the Rayleigh test and the H_m test, have been discussed in Chapter 4.4. Both track wobble and track normal data are equally suitable for periodicity searches. The wobble interval was chosen to correspond to a reasonable length of data upon which to perform a periodicity search. For the new telescope, this interval is 900 s long.

For the old telescope data, a 900 s interval was also chosen for periodicity searches. This choice of interval was based upon observations in 1986 by the Haleakala group, showing an approximately 900 s long interval of anomalous periodicity from Her X-1 (Slane, 1988). In principle, since the '87 Her X-1 data was all taken in the track normal mode, any other reasonable length interval could have been chosen for the periodicity search.

First, I will discuss the 1987 data set, and the periodicity search and DC analysis performed on these data. The periodicity search is the main part of the analysis, since the background rate could only be poorly estimated due to the track normal mode of data taking employed. The periodicity search on these data revealed one interval of significant periodicity. The period detected during this interval is in agreement with the anomalous period discovered in the '86 data. Next, the 1989 searches will be discussed. No intervals of significant periodicity were found either at the X-ray pulse period or at the anomalous period in the '89 data set, but a small overall DC excess was present in these data.

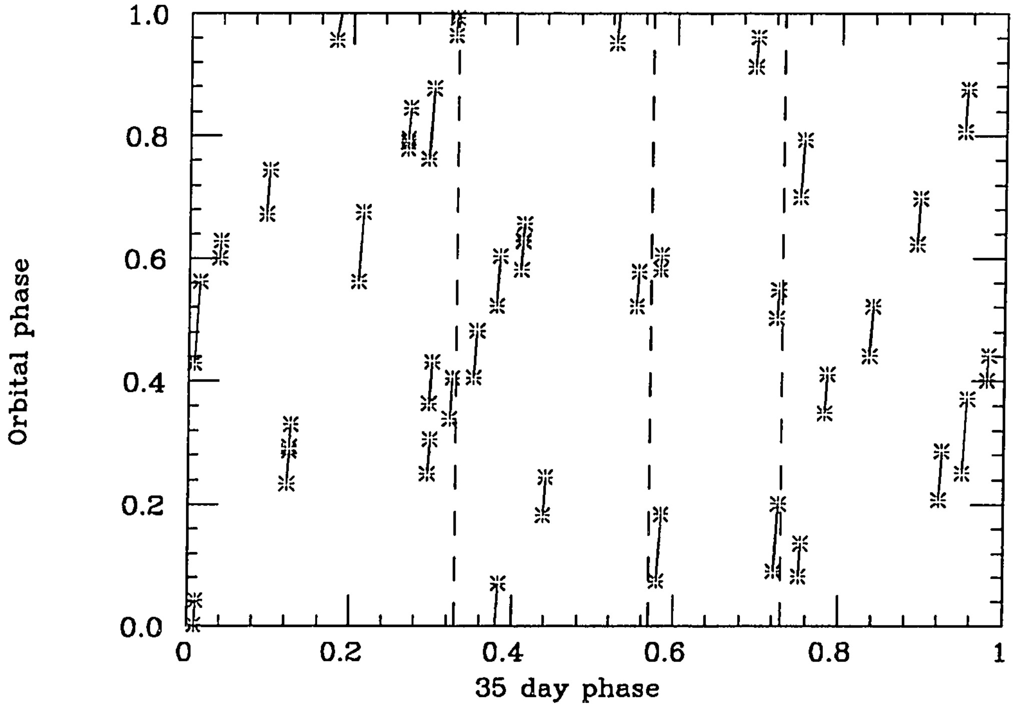

Figure 5.2: Orbital phase and 35-day phase of all 1987 Her X-1 runs.

5.1 1987 Data

During part of the '87 Her X-1 season, which on Haleakala stretches from March through July or August of each year, the telescope experienced several problems with the PMTs and amplifiers out on the telescope mount. During one month, as many as 3 of the 18 on source channels were malfunctioning. The remaining channels were analyzed for signal in the same manner as the fully operative telescope was analyzed.

Since the approximate 35-day phase is known, we used this information during data taking. A slight preference was given to Her X-1 when it was in the high and low X-ray on portions of the 35-day phase. When it was in an X-ray off phase, approximately equal preference was given to Her X-1, and any other potential sources (such as PSR1133 or SS433) in our observation window at that time. A plot of our orbital vs 35 day coverage is shown in Figure 5.2. Figure 5.3 are these same data runs presented in histogram form, showing the coverage as a function of orbital phase and 35-day phase.

5.1.1 Preparation of the 1987 Her X-1 Data

Preliminary calibrations and zenith angle fits were performed on the data in order to eliminate weather contamination. The data were divided into six intervals for calibration, one each month during March, April, May, and July and two during June. These intervals were selected so that during each of the calibration periods, the status of the telescope remained constant, thus a reliable calibration could be determined for each channel.

The rate on and off source was fit to determine the expected rate at a given zenith angle (θ) using Equation 4.31, under the assumption that θ is not large ($< 40^\circ$). A summary of the zenith angle fits for each run is compiled in Table 5.1. R_o is the rate at zenith and γ is proportional to the spectral index. The fit was performed with both of these as variables. Those runs with a χ^2/dof which was greater than 2 for the off source aperture were rejected. These runs have an X in the status column in the table. In one case, the on source aperture had would have

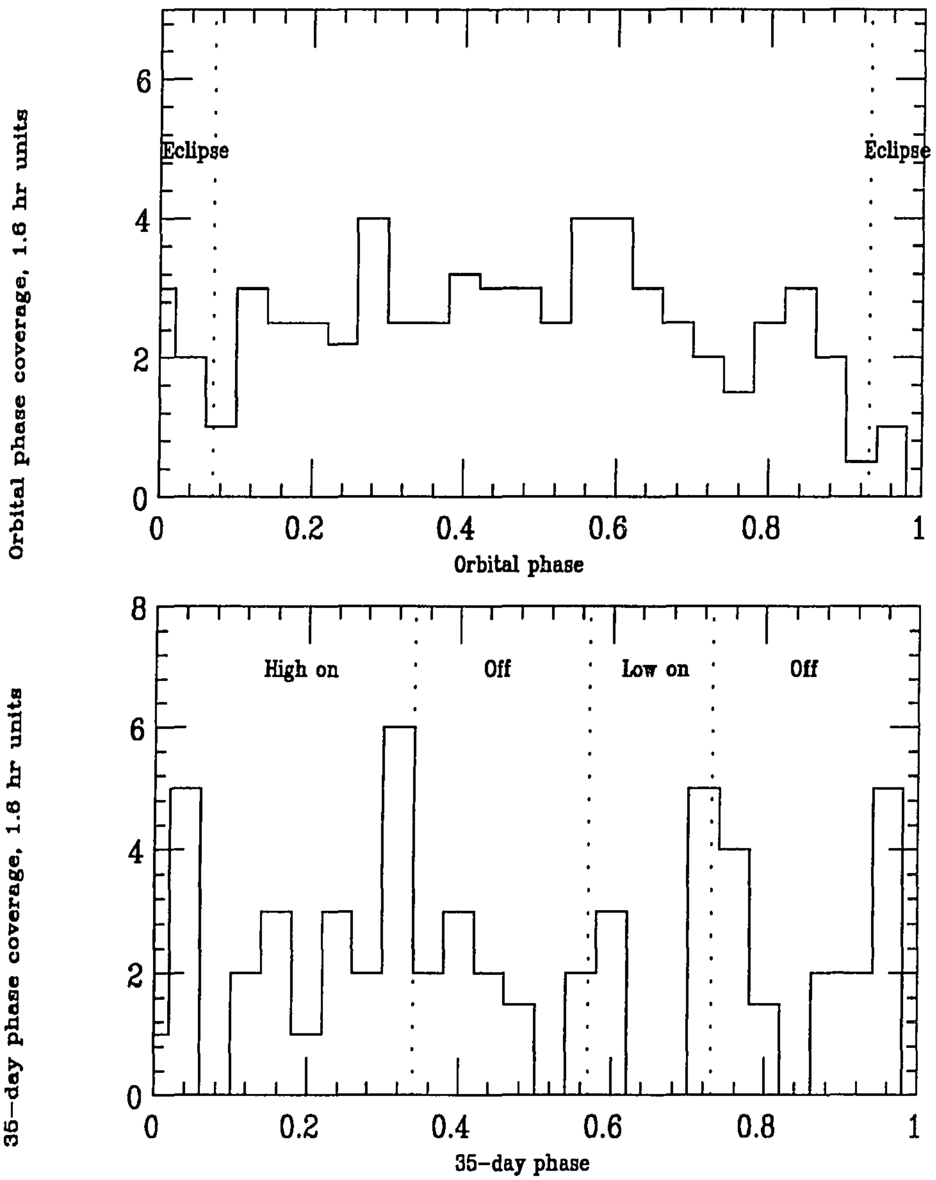

Figure 5.3: Orbital phase and 35-day phase coverage of all 1987 Her X-1 runs.

failed this cut (run 1131), but since the off source did not show a rate variation, this run was accepted. Run 1127 spanned only 2 degrees in zenith angle, thus a fit could not be performed. Since this run was so short (< 1 hr) it was not analyzed. Run 1144 was also short (1 1/2 hr) but since it spanned three degrees in zenith, a fit was possible. Even though the variables R_o and γ are not well determined for this run, it was accepted.

Of the runs passing the chi-square cut (those with a $\surd$ in the status column) only 1123 and 1143 had the B aperture viewing the source. In the remainder of the runs, the A aperture was on source. So, approximately 72 hours of A on source data and 4 hours of B on source data were analyzed from the '87 data set.

The initial data cuts included both a tight timing and a PE cut. At least 9 channels were required to have at least 0.5 PE within a 5 ns sliding window. These cuts were employed for the initial zenith angle fits, the periodicity tests, and the DC excess determination. In terms of the number of events saved, this cut is very similar to a 10-fold minimum multiplicity cut with no PE requirement. The low PE cut was originally made in an attempt to reduce the number of promotion (and accidental) triggers. Promotion triggers are a combination of a lower energy shower, producing hits below the telescope threshold and one or more noise hits, pushing this shower over the multiplicity threshold for a trigger. This low PE cut was eliminated for the 1989 analysis, since it is selecting hits more on the basis of the random PMT response to one PE rather than the accidental hit rate.

Table 5.1: Zenith angle fit parameters for 1987.

	A			B			
Run	R_o	γ	χ^2/dof	R_o	γ	χ^2/dof	Status
March							
1100	0.4392	2.1561	13.7/18	0.3334	2.2890	8.0/18	√
1104	0.4416	2.2101	19.9/17	0.3384	2.3157	12.6/17	√
1106	0.4400	2.2563	30.1/21	0.3227	2.3174	25.7/21	√
April							
1116	0.3635	1.9203	13.8/13	0.4206	2.3002	10.9/13	√
1120	0.4362	2.2224	18.4/22	0.4054	2.2656	15.1/22	√
1123	0.4198	2.0991	12.0/16	0.3999	2.1761	17.1/16	√
1126	0.4484	2.2860	19.7/15	0.4426	2.3371	12.2/15	√
1127	Too short to fit						X
1131	0.4455	2.2337	27.2/13	0.3952	2.1356	6.6/13	√
1133	0.4068	1.9604	20.8/9	0.4208	2.2093	23.2/9	X
1135	0.4373	2.2556	11.2/15	0.4157	2.2016	27.1/16	√
1137	0.4145	2.2270	36.0/33	0.4043	2.2361	29.2/33	√
May							
1141	0.4092	2.1290	15.2/14	0.3961	2.2131	17.1/14	√
1143	0.4456	2.3640	17.3/20	0.3829	2.2563	24.5/20	√
1144	0.4768	3.0000	0.3/1	0.4047	3.0000	1.0/1	√
1155	0.4165	2.2331	19.4/21	0.3822	2.2300	14.7/21	√
1157	0.3830	2.1318	67.5/27	0.3512	2.1114	55.4/27	X
1159	0.4230	2.2589	25.7/22	0.3919	2.2142	21.7/21	√
June 1							
1162	0.3950	2.1634	32.1/23	0.3858	2.2575	21.5/23	√
1164	0.4177	2.1881	24.0/20	0.3818	2.1659	44.8/20	X
1174	0.3863	2.1679	18.2/17	0.3724	2.2297	13.8/17	√
June 2							
1176	0.3355	2.2410	27.6/23	0.3093	2.2581	29.2/24	√
1178	0.3842	2.3021	18.5/19	0.3136	2.1224	13.2/19	√
1180	0.4170	2.6980	6.7/5	0.2997	1.5000	16.4/5	X
July							
1182	0.0356	3.0000	684/8	0.0988	3.0000	429/8	X
1183	0.4079	2.2218	40.9/22	0.3748	2.2211	15.4/22	√
1184	0.4351	2.4553	8.4/12	0.3878	2.2853	21.7/12	√
1185	0.4019	2.2364	33.5/24	0.3753	2.2086	55.3/24	X
1189	0.4036	2.2850	13.9/20	0.3962	2.3715	24.3/20	√
1194	0.3950	2.1645	8.0/15	0.3727	2.2393	12.7/15	√
1196	0.3684	2.1440	14.1/18	0.3455	2.0535	17.2/19	√
1199	0.4189	3.0000	23.8/11	0.3766	2.8593	22.3/11	X
1201	0.3724	1.9684	2.0/7	0.3873	2.5826	5.6/7	√

5.1.2 Periodicity Analysis

Using event times corrected to the solar system barycenter (Chapter 4.3), each run was divided into 900 s intervals. There were a total of 293 such intervals in all of the good runs listed above. Only intervals longer than 600 s were analyzed, so the total amount of data analyzed for periodicity was just over 73 hours, less than the total amount of data available (76 hours).

A range of 19 periods around the interpolated X-ray period, 1.237773 s were searched. This corresponds to a total of approximately ± 3 independent periods scanned, where one independent period is defined as P^2/T for a test period, P, and an interval length, T (in our case 900 s). The search range was oversampled, with an interval between test periods of $P^2/3T$ to assure that a signal would not be missed if it occurred at a period between two independent Fourier test periods. This broad search window, which is ± 7 times the maximum Doppler shift, was chosen to span both the expected X-ray period and the anomalous period. The anomalous period is 1.2 independent periods below the X-ray period, or about three times the expected Doppler shift.

The periodicity test employed initially was the Rayleigh test. Each 900 s interval was tested for periodicity in the range of periods mentioned above using this test. The most significant periodicity occurred during the 12th interval of run 1162. This interval, which began on May 23rd, at UT = 40485. s, had a Rayleigh power of 11.9 in the initial search. This corresponds to an overall chance probability of $293 \cdot 3 \cdot 3\ \exp(-11.9) = 2\%$, including the total number of intervals searched (293) the number of independent periods spanned (3) and an additional factor of 3 for oversampling. The period detected was 1.23578±0.00020 s, which is 2.9 times the orbital Doppler shift away from the interpolated X-ray period. The Rayleigh power during this interval is shown in Figure 5.4 for the on and off source. Deviation from the X-ray period is obvious in this figure. The light curve is shown in Figure 5.5. The solid curve lying over the light curve histogram is the Kernel Density Estimator (KDE) (DeJager, 1987). The KDE error band is plotted in dashed lines. The ephemeris for the determination of the pulsar phase was taken to be 0 h TDB for May 23rd. The light curve has a sinusoidal modulation with a higher population bin near phase 0.25. A comparison of this detected period with previous observations is shown in Figure 5.6, it can been seen from this figure that the '87 period is in very good agreement with those reported the previous year. This interval occurred at $\phi_{orb} = 0.32$ and at a 35-day phase consistent with the start of the high on X-ray variation.

The light curve can be determined for the period reported by Ooty (Chapter 2.3) which produces phase linking between their four measurements and those of the Cygnus Air Shower Array at ultra-high energies (Dingus, *et al.* 1988). This light curve, presented in Figure 5.7 does not resemble the emission reported at higher energies, which was concentrated in the phase range 0.11 – 0.38. One reason for this may be a phase shift caused by a small $\dot{P}$, since the UHE measurements were taken approximately one year before the measurement reported here. The Ooty group does not detect a $\dot{P}$ in their data, but a period derivative on the order of 10^{-15} would produce a phase shift of 0.4 over one year for Her X-1. The Ooty

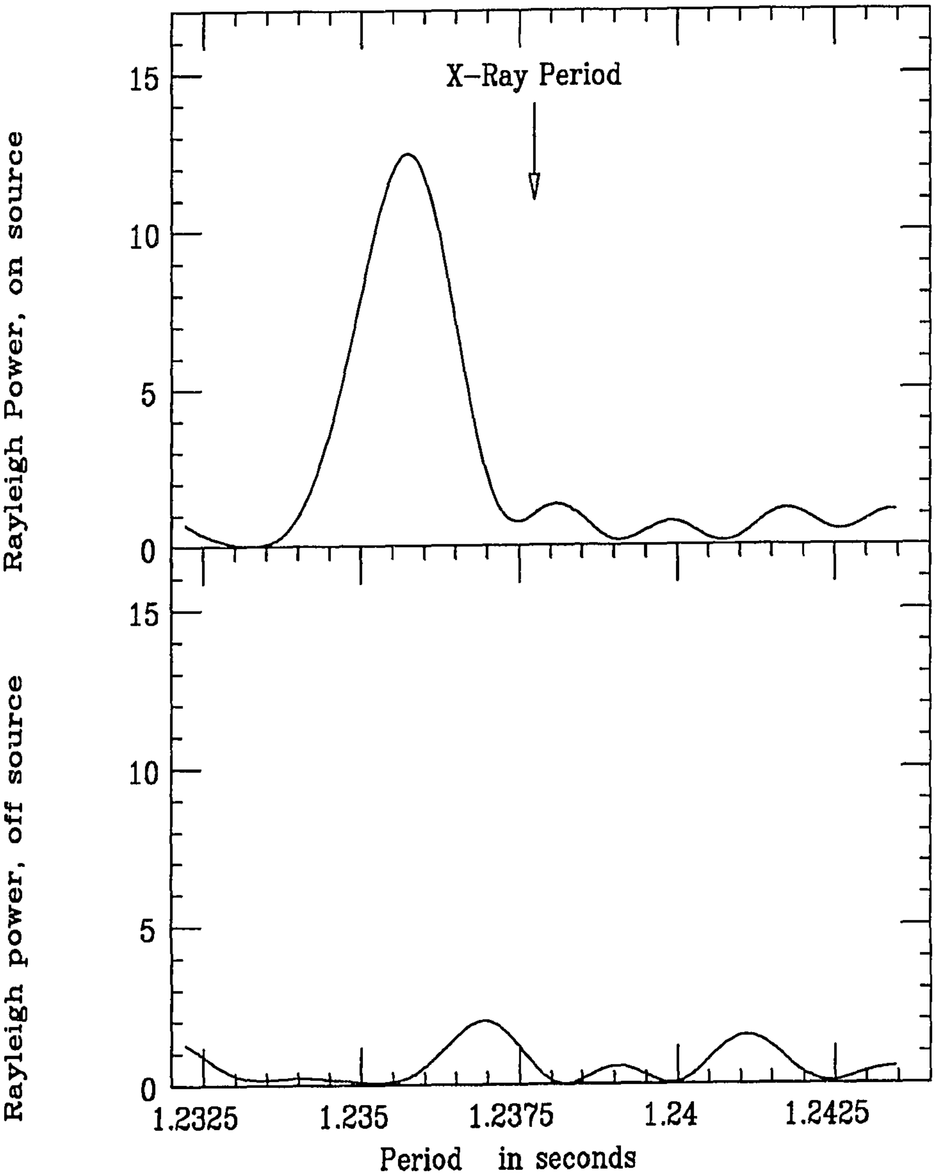

Figure 5.4: On and off source Rayleigh distributions for run 1162.

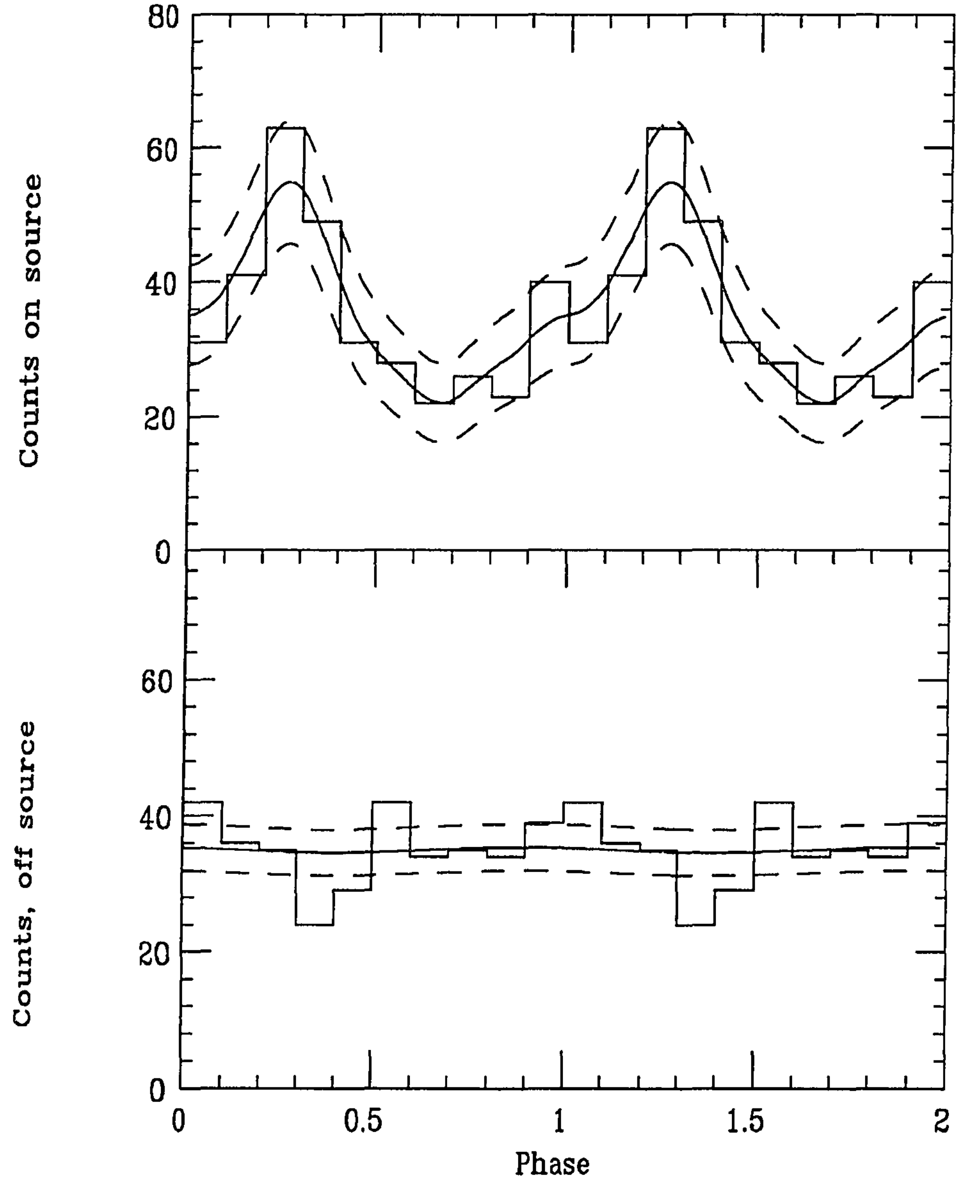

Figure 5.5: Light curve for the 12th interval of run 1162 at P=1.23578 s.

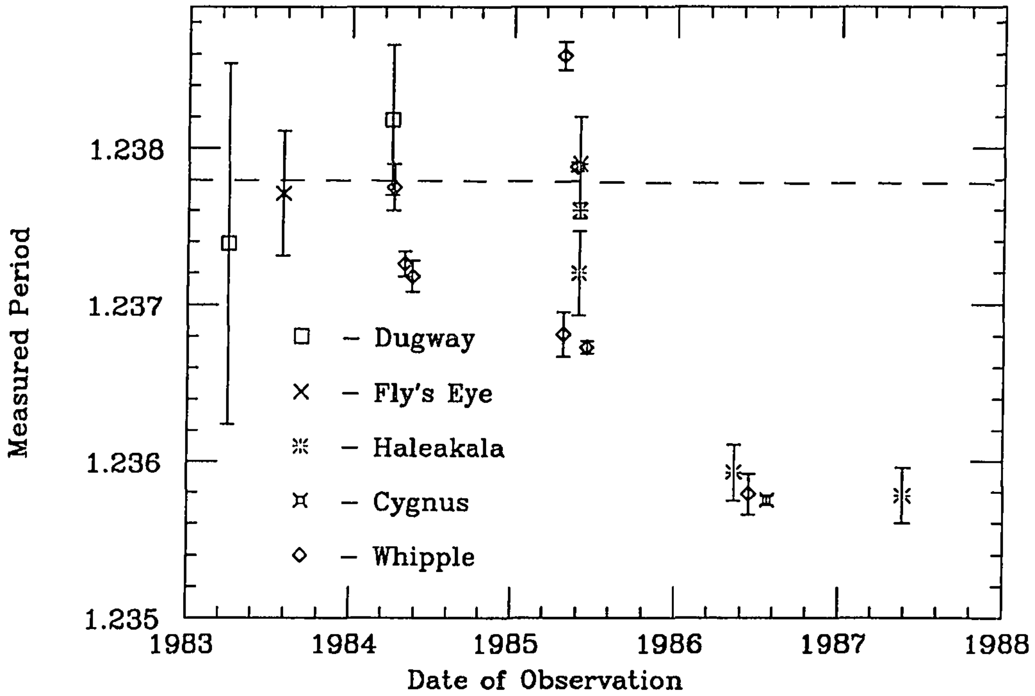

Figure 5.6: All reported VHEGR detections of Her X-1 through 1987.

group may not have detected this small of a period shift, since it would correspond to a phase shift of 0.2 over their detection interval. The step size they used when searching for a $\dot{P}$ was about 4 times larger than the $\dot{P}$ needed to produce the phase observed in figure 5.7, so the phase disagreement is not surprising. In Appendix B, we discuss the investigation of the anomalous period interval found by Pat Slane in the 1986 data for phase coherence at the Ooty period and ephemeris.

A closer examination of this interval during run 1162 was conducted. First, the interval was searched with a finer period spacing corresponding to $P^2/15T$ near the detected period in order to determine the 1 σ uncertainly in this period. The

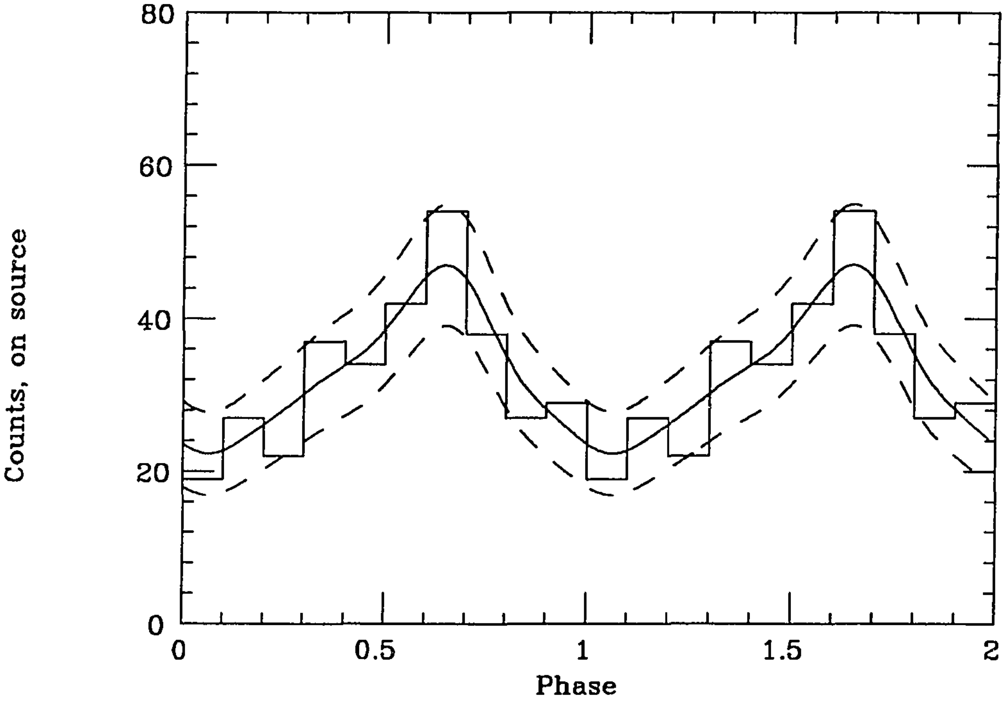

Figure 5.7: Run 1162, on source light curve for t_o = 6613.17379361 JD.

maximum Rayleigh power found in this search was 12.4 (Figure 5.4), at the period quoted above. The error in this period was determined from the width of the peak, assuming its shape to be Gaussian. To determine the beginning and duration of the interval of periodicity, the start of the 900 s interval was then decreased by 30 s intervals revealing that the burst actually began about 150 s before the start of the test interval, at UT=40335. s and continued for approximately 900 s. This interval produces a Rayleigh power of 15.2. This maximized interval was also investigated as a function of the multiplicity requirements on the data. The highest Rayleigh power occurred at the initial search multiplicity of 9 hits in 5 ns (Figure 5.8).

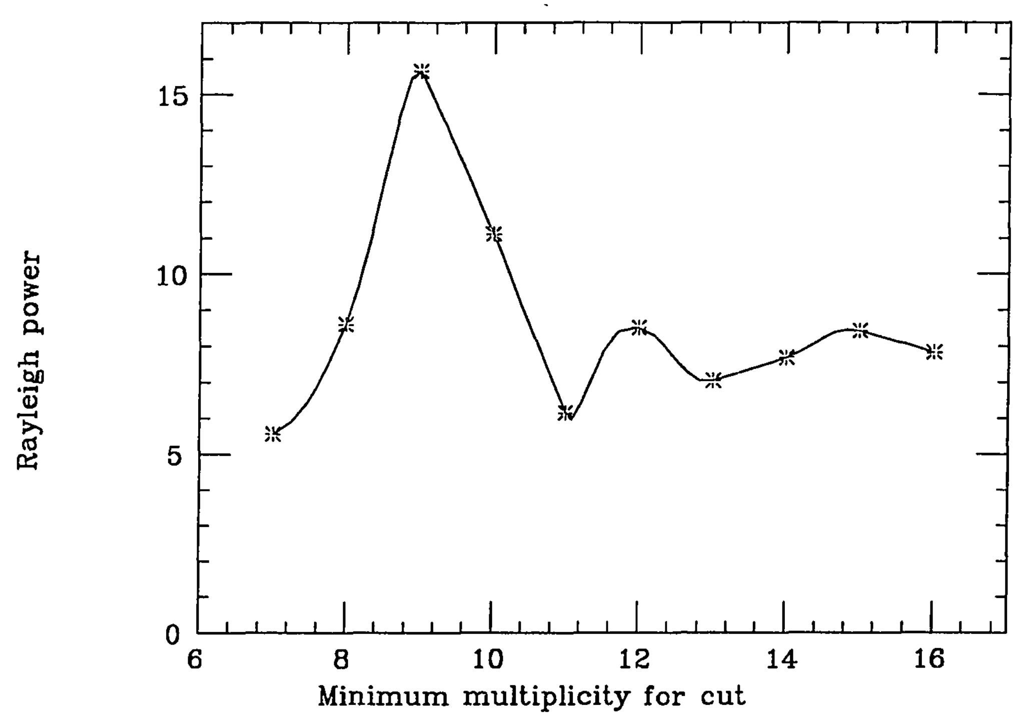

Figure 5.8: Rayleigh power as a function of the multiplicity cut.

It should be noted that it is the initial search probability (11.9) that is quoted in the final result. The overall probability associated with the further investigation of this interval is difficult to correctly assess. Although it is instructive to further 'tune' this peak, the detection probability does not automatically increase through this tuning.

The interval with the second highest Rayleigh power in the on source occurred at the end of run 1178. The power displayed during this interval was 9.7 at a period of 1.237774 s, corresponding to an overall chance probability of 16%. Although this interval is not significant, it is curious that the two highest Rayleigh powers observed in the '87 data set appear at the anomalous period and at the interpolated X-ray period. Figure 5.9 is the Rayleigh power spectrum for all on and off source intervals tested. The second peak from run 1162 at 11.3 is from oversampling of the peak in interval 12.

5.1.3 DC Analysis

The entire off source data set, divided as above for the periodicity analysis, was tested for exponentiality using the Gini test (Section 4.5). This was done as an check of the randomness of the background data, though no overall rate excess can be calculated. The distribution of off source Gini numbers is presented in Figure 5.10. This is almost exclusively a measure of the exponentiality of the B aperture. There are 14 Gini numbers greater than the 5% probability value $|G| > 1.96$, while 14.65 are expected. The width of this distribution (1.03) is in agreement with the expected width of 1; however, the mean is shifted to 0.09 ± 0.05. The distribution is in acceptable agreement with the expected distribution for random background data. Just as a note, the two intervals mentioned above show no unusual background fluctuations according to the Gini test: the interval in run 1162 and run 1178 have Gini numbers of 0.55 and -0.74 respectively. The curve drawn in Figure 5.10 is the fit of the data to a Gaussian distribution.

The 12th interval of run 1162 was investigated for a DC rate excess. The rate excess was determined by using the zenith angle fit for the A aperture for runs 1162 and 1174; this was the on source for both of these runs. The expected number of background events was then determined by numerically integrating Equation 4.32

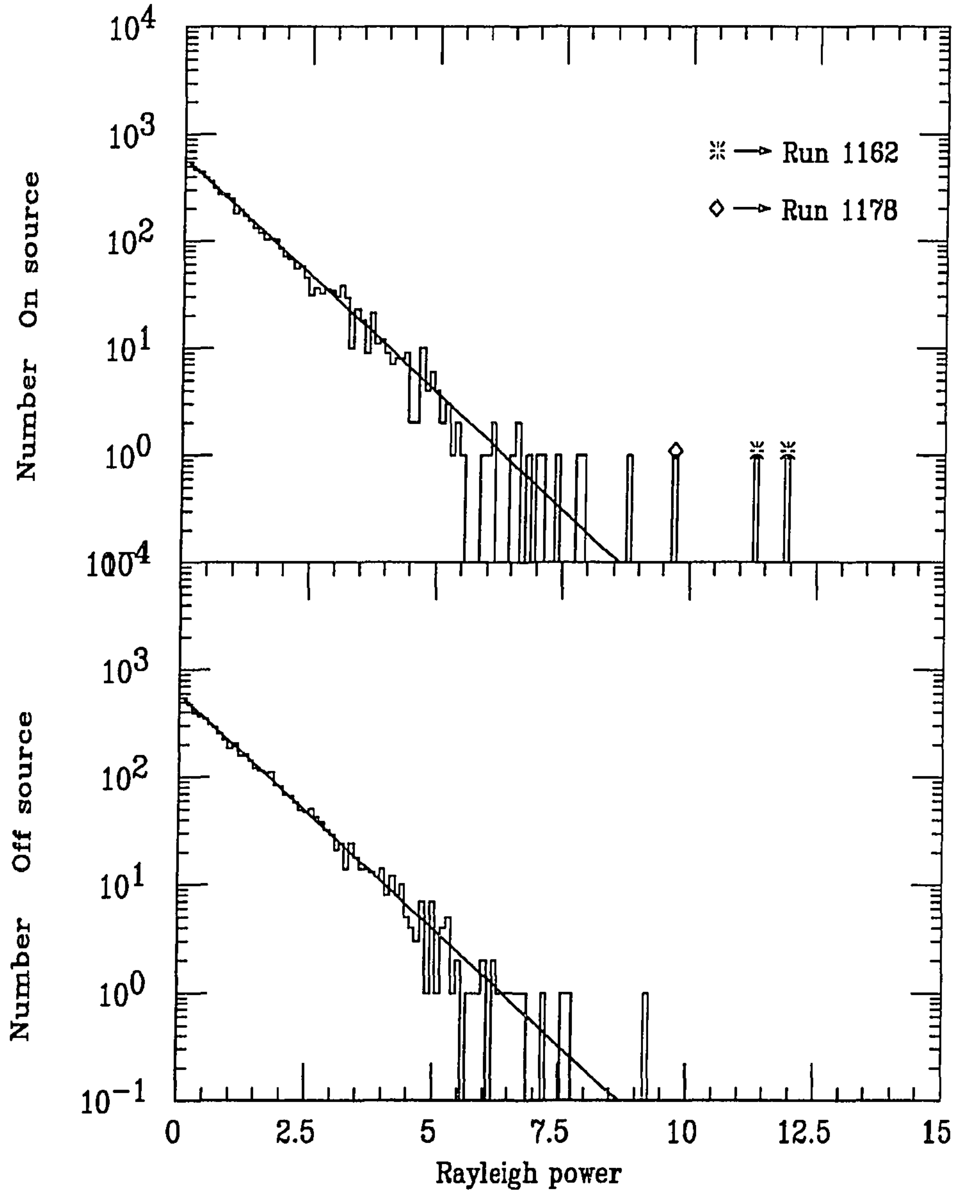

Figure 5.9: Rayleigh power spectrum for the on and off source for all '87 data tested.

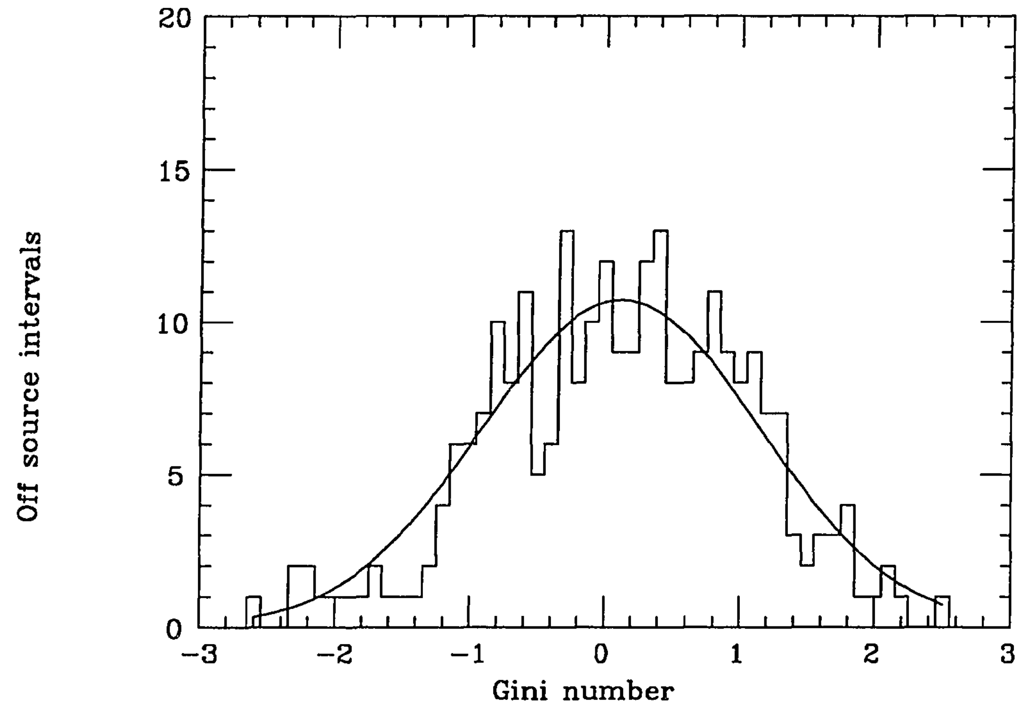

Figure 5.10: Distribution of Gini numbers for the 1987 off source data set.

over the time interval. The values for R_o and γ are given for the individual runs in Table 5.1.

Using this fit, the rate excess during this interval is consistent with zero (0.5 σ). If only run 1162 is used in the zenith angle fit, which eliminates any night to night variations which may be present but it also reduces the number of points in the fit, a similar result is obtained. The zenith angle fit for run 1162 was presented in Figure 5.1. The number excess, expressed in units of sigma for runs 1162 and 1174 is presented in Figure 5.11 for both the on and off source. As can be seen from this figure, there is not an obvious bias of the fit to enhance or diminish the observed rate excess. Because of the low statistics, neither distribution looks exceedingly Gaussian; however, both distribution means are in agreement with zero (on source: 0.10 ± 0.17 σ and off source: 0.02 ± 0.15 σ), and both widths are in agreement with one (0.99 σ and 0.93 σ).

To investigate the rate as a function of time in greater detail, a plot of the DC excess, divided into 180 s intervals, is presented in Figure 5.12. As can be seen from this figure, a slight excess is present during the beginning of the interval of highest Rayleigh power, and a slight deficit appears during the final ~300 s of this interval. None of these 180 s intervals are statistically significant, suggesting that either, if this is a detection of periodic gamma-rays, the signal is at a very low level, and the periodicity observed is signal enhanced by "periodic" noise, or that there is simply no signal present. Periodic noise may be a random or pseudo-random background which produces a Rayleigh vector in the same direction as the signal vector. The chance probability we calculated assumed the random background, no signal (H_o) hypothesis, which is violated when we have a low level signal.

To test the hypothesis of a constant, low level periodic signal, the highest Rayleigh power found in the interval of ± 1 independent Fourier period (IFP) around the anomalous period, and ± 1 IFP around the interpolated X-ray period was determined. A similar analysis was performed by the Whipple group on their entire data set (Section 2.3), revealing an apparent low level signal near the X-ray period. These Rayleigh power distributions (Figures 5.13 and 5.14) were tested for agreement with background estimates using the Fisher test based on the maximum likelihood estimation (Eadie, *et al.* 1971):

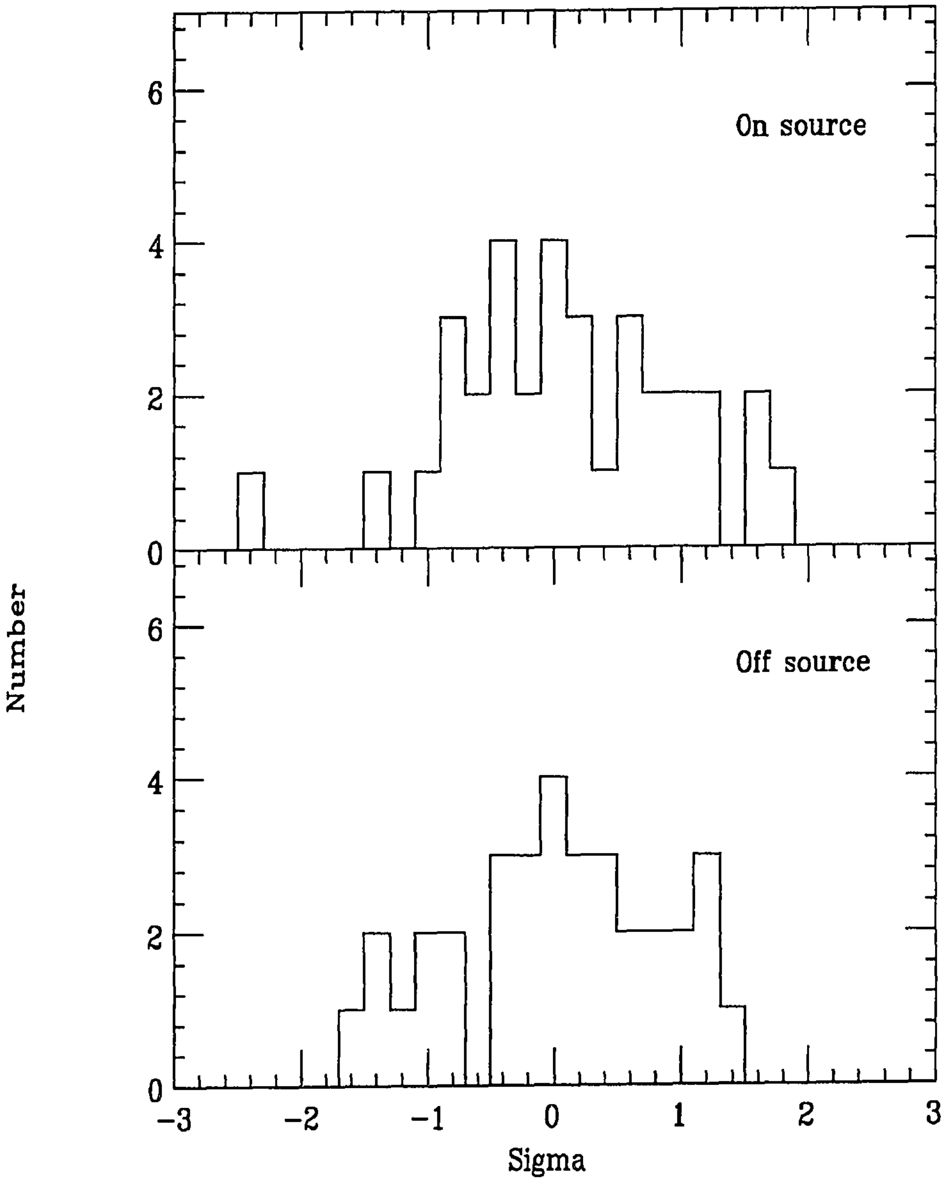

Figure 5.11: The sigma rate excess for each interval in runs 1162 and 1174.

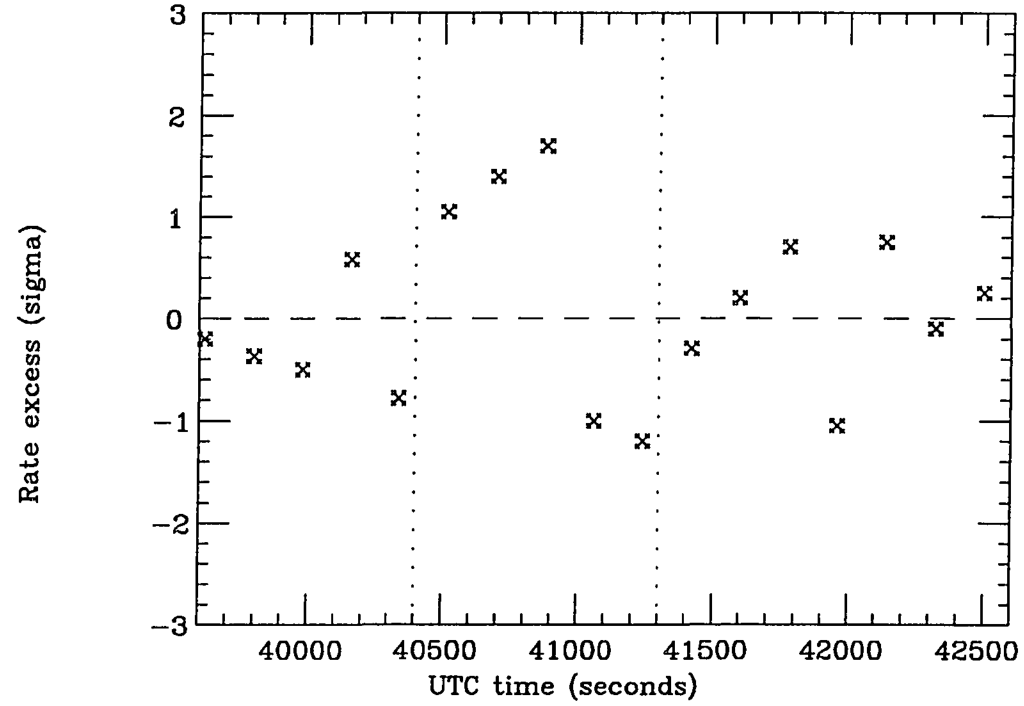

Figure 5.12: Rate as a function of time for a portion of run 1162. The 12th interval is inclosed in dotted lines.

$$H_f = -2\log\left[\prod_{i=1}^{N} p_i\right] \tag{5.1}$$

H_f is distributed as a χ^2 with $2N$ degrees of freedom, where N is the total number of trials. In the case of an ideal data set, p_i would be just the Rayleigh probability, $p_i = \exp(-nR_i^2)$. Since our distribution includes both oversampling and the selection of the largest power in each oversampled interval, p_i is determined from the background (off source) distribution. If the highest on source Rayleigh powers are removed (those above $nR^2 = 8$) and the lowest is 2.5, then there is no significant difference between the on and off source distribution according to the

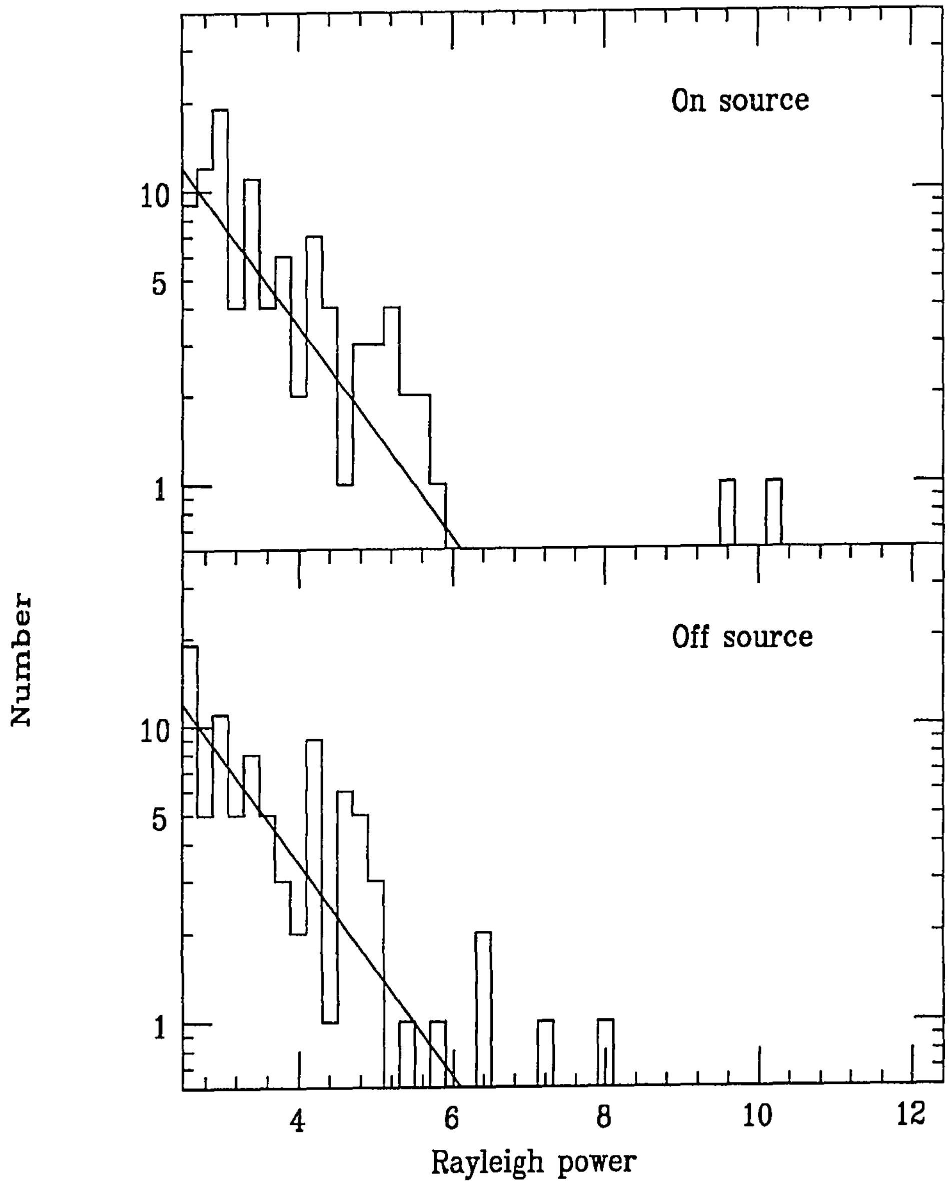

Figure 5.13: Rayleigh distribution for ± 1 IFP around the interpolated X-ray period.

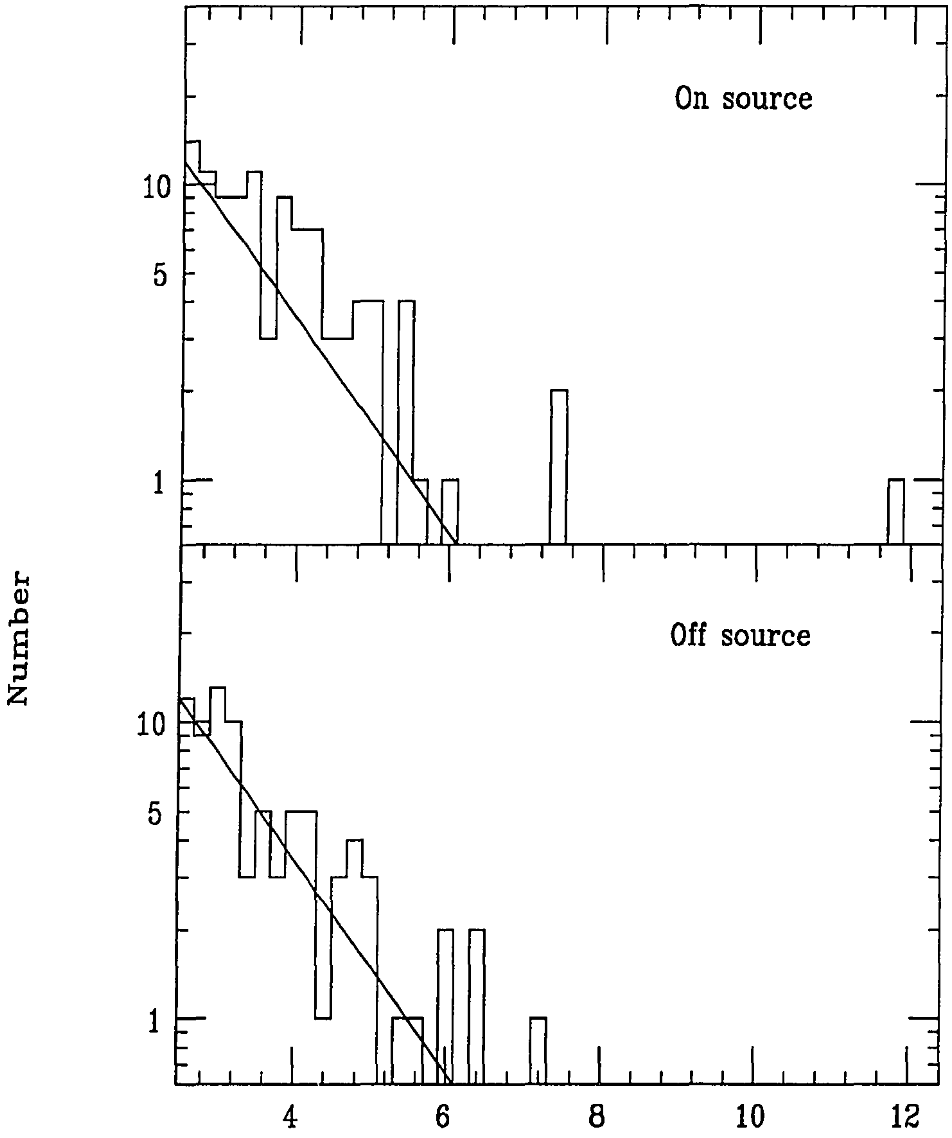

Figure 5.14: Rayleigh distribution for ± 1 IFP around the detected anomalous period.

Fisher test. The lower limit on the Rayleigh power reduces low nR^2 background, and makes no difference in the final probability. If the Rayleigh probability is substituted in for p_i, then both on and off source distributions are still in reasonable agreement with what is expected. Again, taking Rayleigh powers from 2.5 to 8, the χ^2 probability is in the range of .2 – .4 for all distributions, so none of these differ significantly from an exponential distribution in this power range, even though they are not expected to be *purely* exponential.

We can determine the probability of obtaining both a Rayleigh power of 11.9 and a rate excess of 0.5 σ, as well as the consistency of these two values using three parameters formulated by Lewis from the maximum likelihood estimation of the product of the individual probabilities for the Fourier amplitudes and the number excess (Section 4.4). Using the observed number excess (10 ± 21 events), the following summary can be compiled:

Table 5.2: Combined probabilities for run 1162.

lc	α	β	γ	Prob	Consistency
sine	24.	56.	12.4	2.4×10^{-5}	0.00043
δ fn.		49.	4.8		0.028

Here, α is a combination of the Rayleigh power and rate excess as $\alpha = 2Z + \sigma^2$, which is distributed as χ^2_3. The individual chance probability of observing Z and σ calculated from α is listed as "prob" in the table. β is the estimated number of signal events expected from the measured periodicity, given the excess observed for a sinusoidal light curve and a delta function light curve. The consistency between the observed periodicity and rate excess can be found from γ, which is distributed as χ_1^2. This consistency is listed as "consistency" in the table. Again, this is determined for a sine wave and delta function light curve. Therefore, from this table, even for a delta function light curve, the overall chance probability and the consistency of the DC and periodic measurement are on the same order. Since, according to this estimate, the low rate excess for the observed Rayleigh power is just as improbable as the high Rayleigh power itself, and since there does not appear to be any low level periodic signal present in a large part of the 1987 data, it is improbable that the observed periodicity is solely the result of pulsed VHE γ emission from Her X-1.

That is not to say that this interval is not interesting, nor is it to say that this interval is abnormal considering recent observations of periodicity from Her X-1 in the VHE range. The occurrence of a reasonably significant periodicity, with an unusually low rate excess is not new for Her X-1. Both of the VHE detections of Her X-1 in 1986 reported a lower than expected rate excess associated with the observed period (Resvanis, *et al.* 1988, Lamb, *et al.* 1988). In the case of our '86 detection, the observed rate excess (1.4 σ) was nearly as significantly low, as compared to the strength of the Rayleigh power observed, as the Rayleigh power its self was significantly high (Slane, 1988). Including observations by the Whipple group since 1984 (Gorham, 1986) and Haleakala, Table 5.15 represents the difference in units of sigma, from the expected number of events and the observed number*. The expected number is calculated assuming an observed rate excess of zero. The error

---

*A summary of these detections is presented in Appendix C for reference.

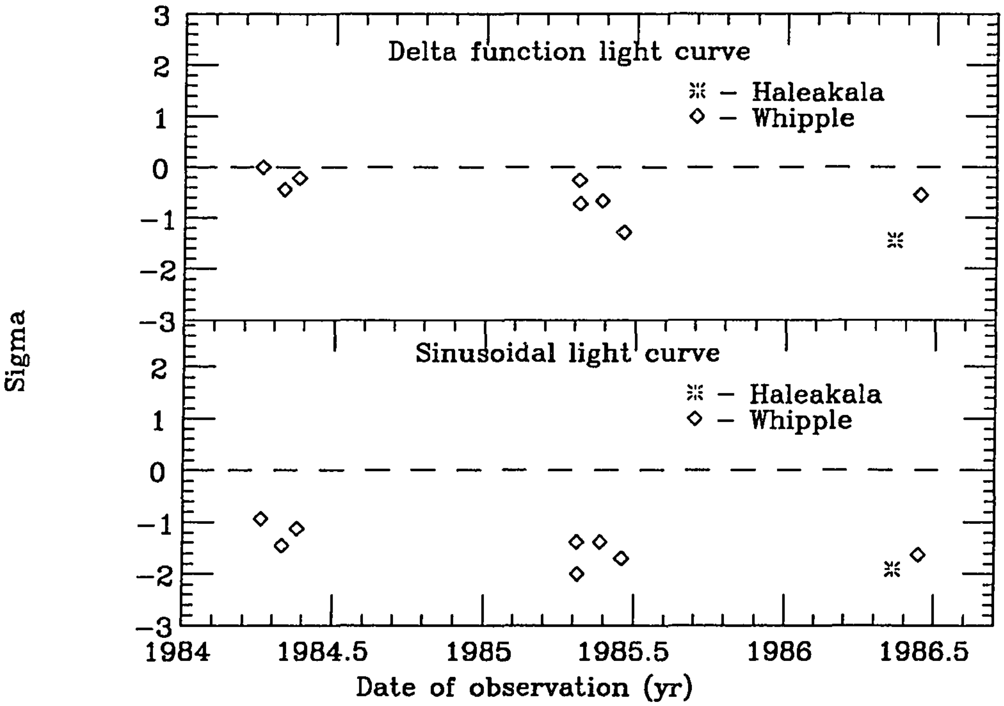

Figure 5.15: The difference between the expected and observed number of events for both a delta-function and sinusoidal light curve.

is taken as the uncertainty in the observed number of events. As can be seen in the figure, even for a delta function light curve, at least 7 of the 9 intervals have an observed excess lower than expected according to this calculation, though none of the intervals are more than 1.4σ low.

In all the detections mentioned above, it is intervals with the highest Rayleigh power that are selected, without any initial consideration of the rate excess. For this reason, the expected excess calculated from β, as is shown in Table 5.2 may not be the correct estimate for the rate expected given the selection criteria. In Figure 5.15, the expected rate is calculated from the individual probability of the observed Rayleigh power, assuming that the observed rate excess is equal to zero. Under this assumption, the maximum likelihood function gives a value for the expected number of γ events (or the expected rate excess) of:

$$\beta_R = \frac{2g_s\sigma^2\sqrt{Zn}}{2g_s\sigma^2 + n} \tag{5.2}$$

We have used the notation β_R to represent the expected number of excess events considering the Rayleigh power with no rate excess. Figure 5.16 is plotted to show the noise origin probability contours. The dashed line corresponds to β_R expressed in units of σ^2 for a given $2Z$. In this plot, all number excesses were greater than zero. In practice, if σ is less than zero, resultant probability is lowered, and Figure 5.16 may be extended to include values of $-\sigma^2$, with probability contours which increase linearly along a negative diagonal axis (recall that information about the sign of σ is thrown away when the noise origin probability is calculated). A plot with negative values of σ does not correctly depict the consistency between the observed values of Z and σ, which will become smaller as σ becomes more negative.

As has been stated above, the rate excess is not a simple quantity to calculate, and it is possible that the uncertainty in its determination is larger than we realize. The agreement of this measurement with those of the pervious year is encouraging; however, the low rate excess associated with the measurement presented above does cast some doubt on this as a detection.

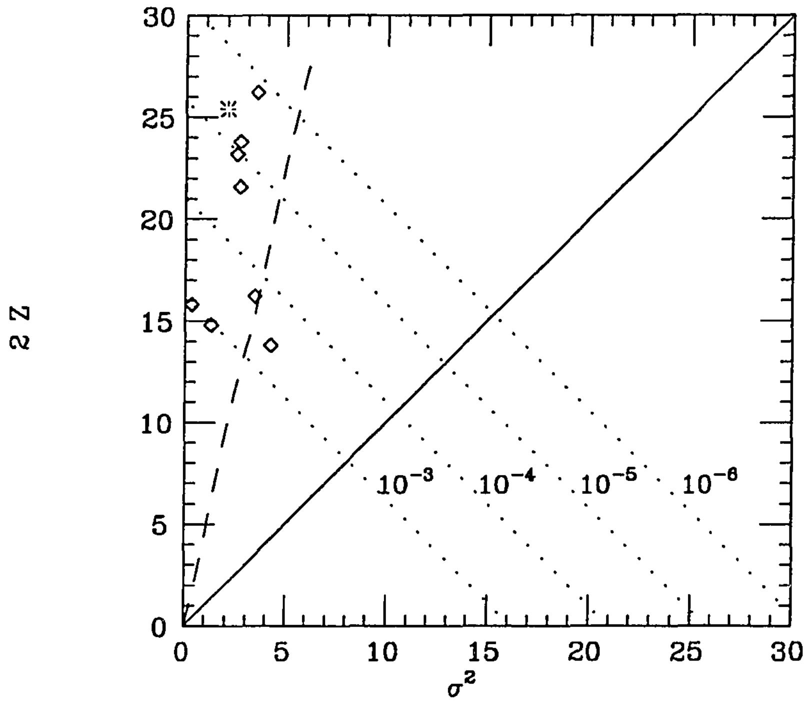

Figure 5.16: The distribution of the Rayleigh power and rate excess (from Figure 5.15). The dotted line is the expected excess.

5.1.4 A Look at the Barrels During 1987

While data was being taken with the main Čerenkov telescope, the 16 barrel air shower array was also recording events. These events were recorded only in coincidence with the Čerenkov telescope events. Here, I will summarize a brief study performed using the barrel array in an attempt to find an excess of PeV γ showers from Her X-1.

The only data selection criteria applied to the barrel data were the following:

- Only events with three or more barrels hit were used, so that a direction fit could be performed each event.
- Of these events, on source telescope triggers were designated as on source barrel events, and off source telescope triggers were designated as off source barrel events.
- Finally, only events within a 5° radius around the expected aperture were accepted.

In principle, one can resolve the two apertures with the barrels (Figure 5.17), so that the information concerning the telescope trigger would not be needed; however, this information allows for a lower energy threshold, since low multiplicity barrel triggers cannot be fit to an accuracy of ±1.8° necessary to separate the apertures. Even at higher multiplicities, this separation is difficult, as can be seen in this figure, which shows an apparent aperture separation which is larger than expected ($\sim$ 5°) and a large amount of scatter. The 5° radius circle around the aperture is an attempt to limit contamination from off axis showers. This will also tend to eliminate an event containing a random (out of time) or poorly calibrated PMT, since the fitting process is non-iterative.

Each run was divided into 30 minute intervals, and the number of barrel hits corresponding to on and off source triggers were compared. An interval twice as long as that for the Čerenkov telescope data was chosen to increase the counting statistics at these higher energies. Additionally, bursts of UHE γs have been observed recently lasting for $\sim$ 30 minutes (Dingus, 1988). Figure 5.18 shows

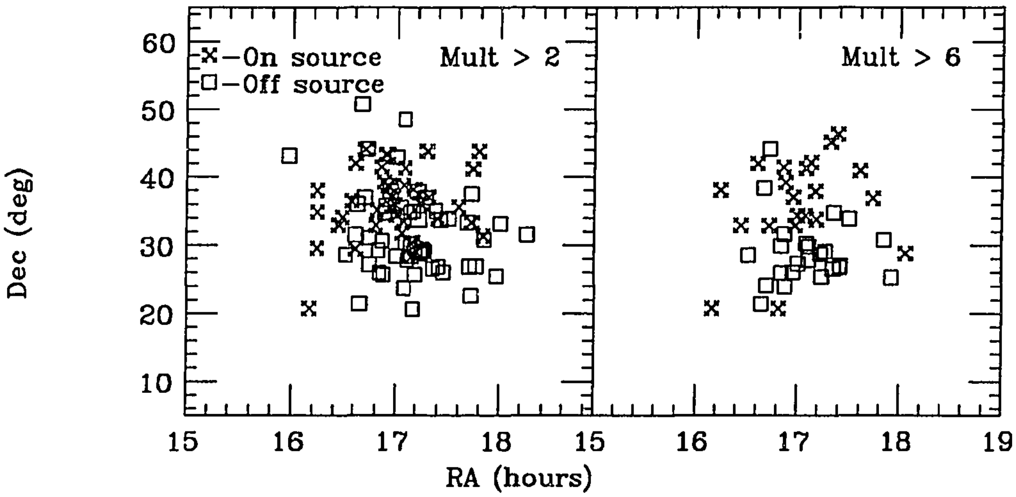

Figure 5.17: Barrel events for run 1116.

both the interval by interval excess expressed in σ, and the integrated number excess. For both of the plots in this figure, σ is calculated as:

$$\sigma = \frac{N_{on} - N_{off}}{\sqrt{N_{on} + N_{off}}} \tag{5.3}$$

N_{on} and N_{off} being the number of on and off source events respectively (Li and Ma, 1983). Thus the conservative estimate of the number excess error is taken as $\sqrt{N_{on} + N_{off}}$ rather than $\sqrt{N_{on}}$.

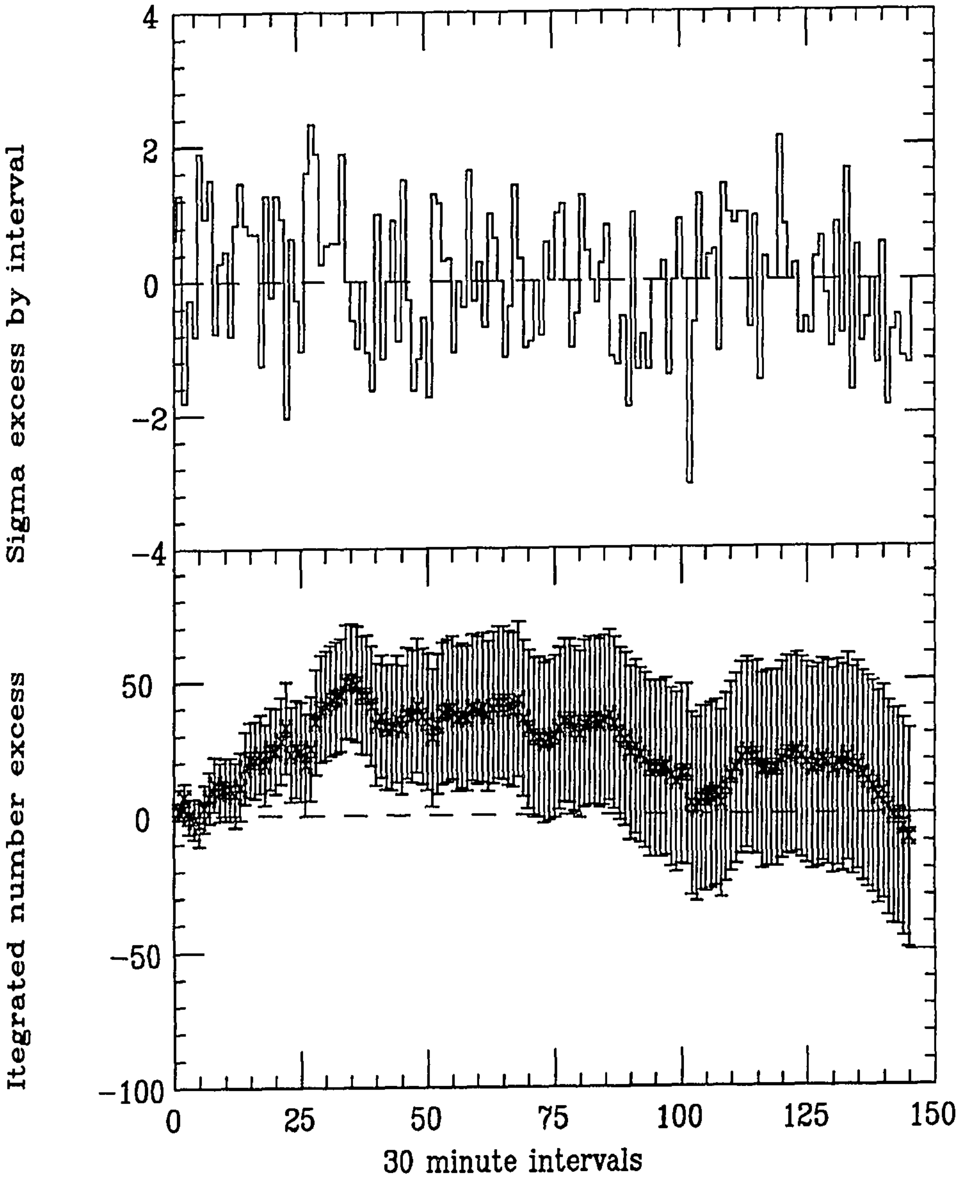

Figure 5.18: Individual interval excess and integrated number excess for the barrels.

The single most significant interval contains a negative excess of -3.0σ. For a total of 145 intervals, the overall significance of this negative point is 40%. Intervals 26 – 33, which correspond to run 1135 and half of run 1137, all show some excess, with a combined counting excess of 2.0σ. This excess occurs near the start of a low-on X-ray phase. Apart from the integrated 2.2σ enhancement ending near interval 33, the overall number excess is in good agreement with zero.

The barrel events are plotted as a function of pulsar*, orbital, and 35 day phase in Figure 5.19. Here, the number excess is plotted in units of σ (where σ is defined in Equation 5.3). No significant correlation is seen as a function of pulsar or orbital phase for all events. The enhancement at a 35-day phase of 0.6 arises largely from the excess seen in intervals 26 – 33 in Figure 5.18. This excess is at the 10% chance level. Both intervals 26 – 33 and the barrel 30 minute interval encompassing the 15 minute interval of anomalous periodicity during run 1162 were investigated individually for phase correlations at both the X-ray and anomalous period. In both cases, no periodicity was detected. Also, no rate excess was observed by the barrels during the anomalous periodicity interval.

In summary, the barrel data taken in coincidence with the Čerenkov telescope data on Her X-1 during 1987 does not appear to show an overall correlation with the expected pulsar or orbital phase. There is some evidence for a rate increase corresponding to the start of the low on 35-day phase, though these excess events do not appear to be pulsed at either the X-ray or anomalous period. Unfortunately,

---

*The pulsar period was precessed to the start of day number 85. $\dot{P}$ was assumed to be -2×10^{-13} throughout the entire data set.

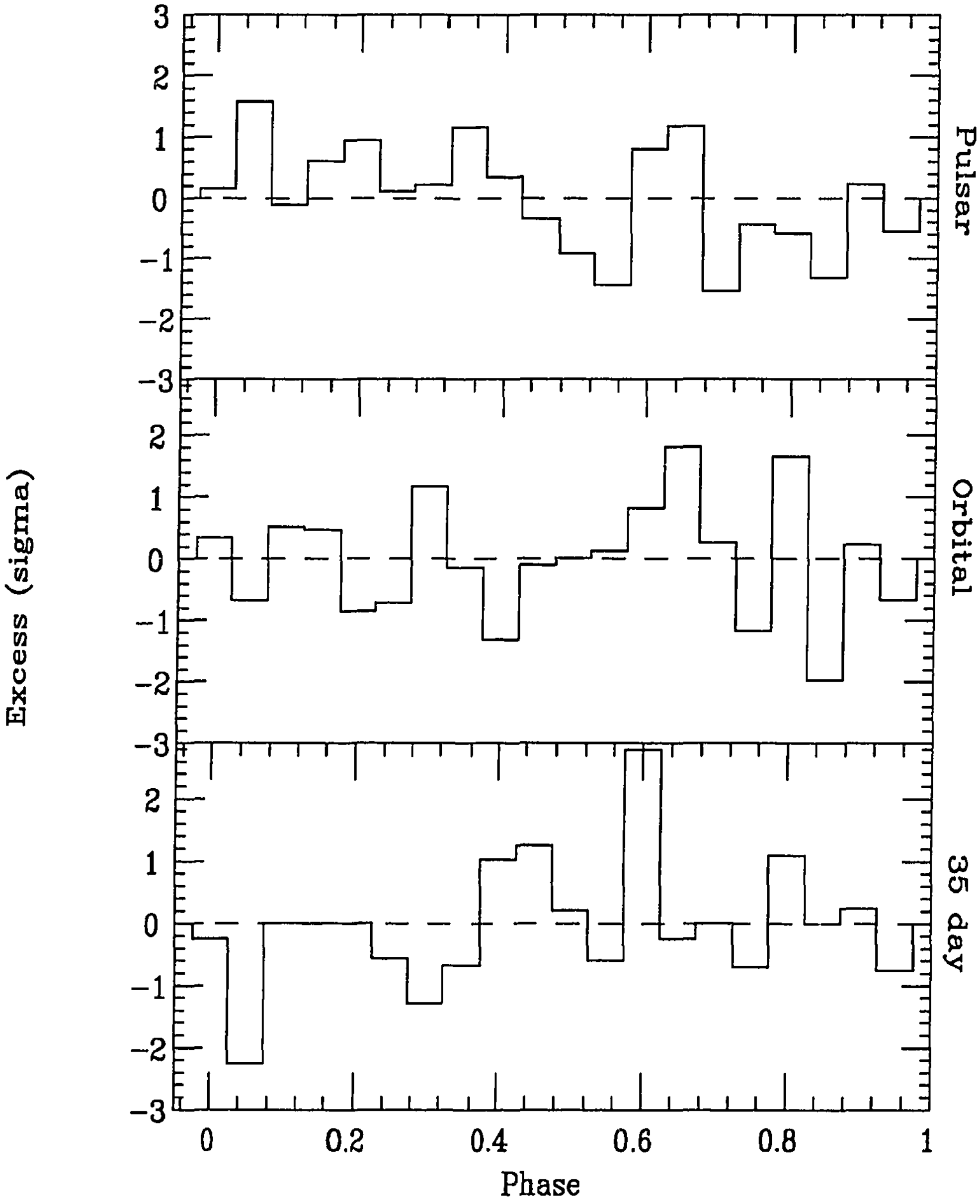

Figure 5.19: Pulsar, orbital, and 35-day phase plots for all Her X-1 barrel data.

because of difficulties encountered in the upgrade of the barrel array (which occurred at the same time as the telescope upgrade), reliable barrel data was not available for the 1989 Her X-1 season.

5.2 The 1989 Data

At the start of the 1989 Her X-1 season, construction of the new telescope had not yet been fully completed. For the first 2 months of this season, hardware changes were still being made. The apertures and filters were changed, and final alignment was made in March, and during April, bad weather permitted only a total of two runs to be taken. The instrument began stable operation at the beginning of May, and took data on Her X-1 from May–August. It is only data from these months that are used in the analysis. Because of the shortened season, Her X-1 was viewed exclusively when it was in or near an X-ray on phase, and at a zenith angle of $\leq 30°$. The 35 day and orbital phase coverage of all of the data taken on Her X-1 during 1989 is presented in Figure 5.20. Here, the 35 day phase preference is obvious, with over half of the total data taken during the high-on X-ray phase, which comprises only about 35% of the total 35 day variation

5.2.1 Preparation of the 1989 data

The calibration and run selection for the 1989 data set was performed in a similar manner as for the 1987 data. The primary differences in the analysis occur as a result of the track wobble mode of operation for all 1989 Her X-1 data. Because of

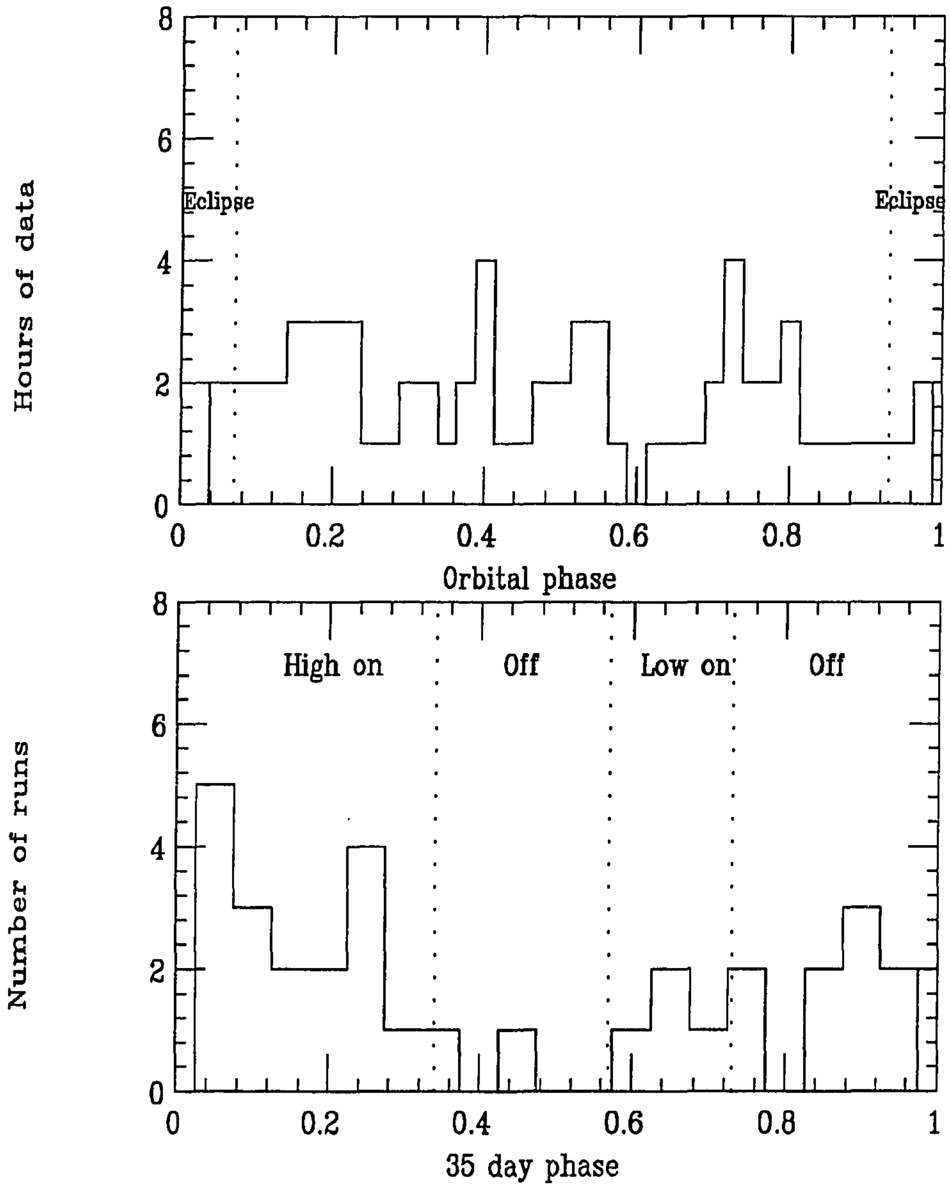

Figure 5.20: Orbital phase and 35-day phase coverage of all 1989 Her X-1 runs.

this, a better determination of the background rate can be made for the 1989 data set. For this data sample, a fit of the off source data to the expected zenith angle dependence (Equation 4.30) was performed in two steps. First, a fit was done for both the rate at zenith (R_o) and a value proportional to the spectral index (γ) on a night by night basis, using all nights during which Her X-1 data was taken as long as the runs do not show large scaler fluctuations indicative of clouds and rain. Next, from this fit, an average value of γ is determined after those runs with a $\chi^2/\text{dof} \geq 3$ have been removed. Finally, this value of γ was fixed in the fit, and a final one parameter fit to the data was made. A histogram of the values of γ for which $\chi^2/\text{dof} \geq 3$ (Figure 5.21) shows that γ is very stable from night to night as is expected, since γ should not depend on small fluctuations in the nightly observing conditions.

The one parameter fit for R_o is very stable, since the shape of the curve is fixed when γ is fixed. The background rate can then be well determined for runs with as few as 3 data points in the zenith angle distribution (or a run where one aperture spans as few as 3° from the start to the end of the run).

The average χ from each of the selected runs is in good agreement with zero for both apertures (Figure 5.22). A representative plot of the χ determined at each zenith angle during a long run is plotted in Figure 5.23. There is no systematic difference in the observed and expected rate for small or large zenith angles which would occur if the shape of the curve were incorrect.

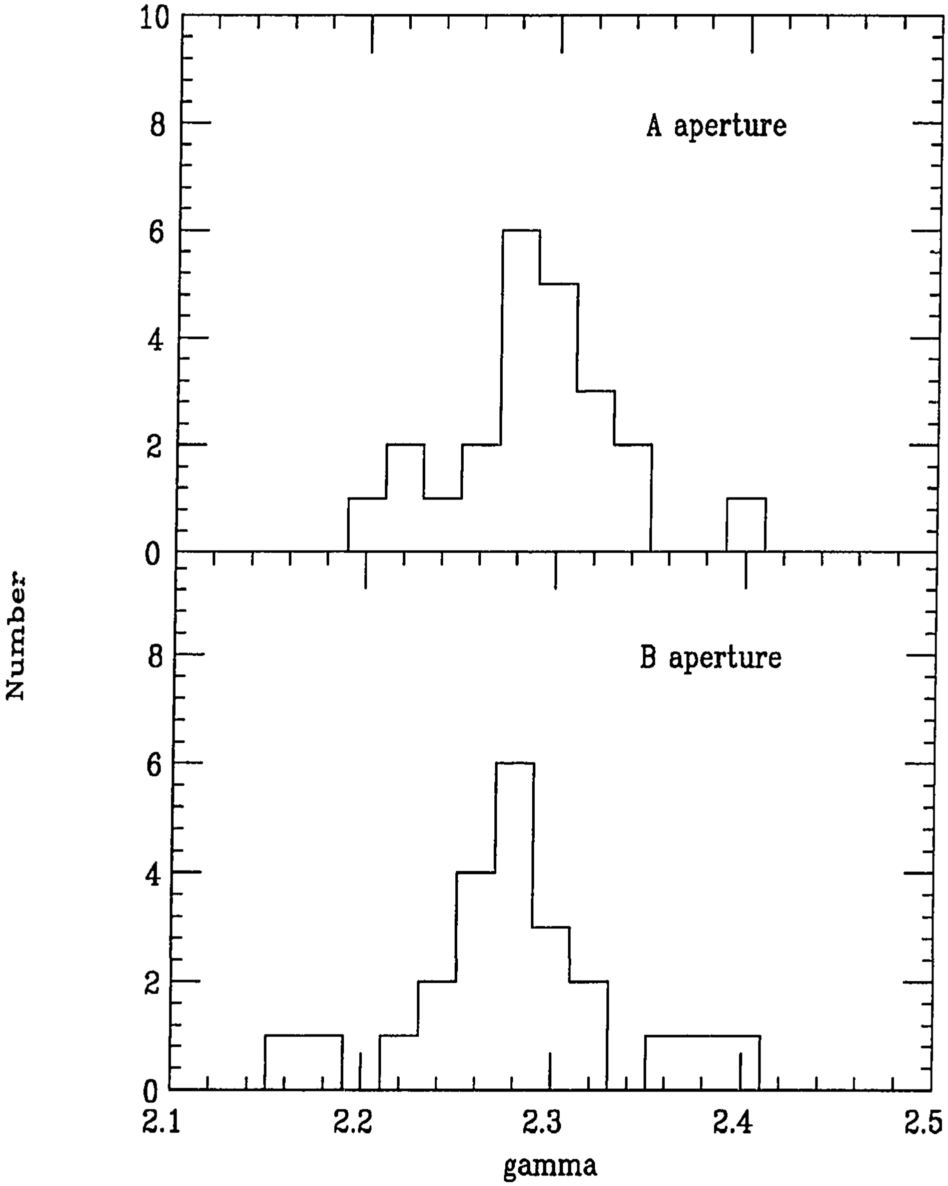

Figure 5.21: The distribution of γ, A and B aperture.

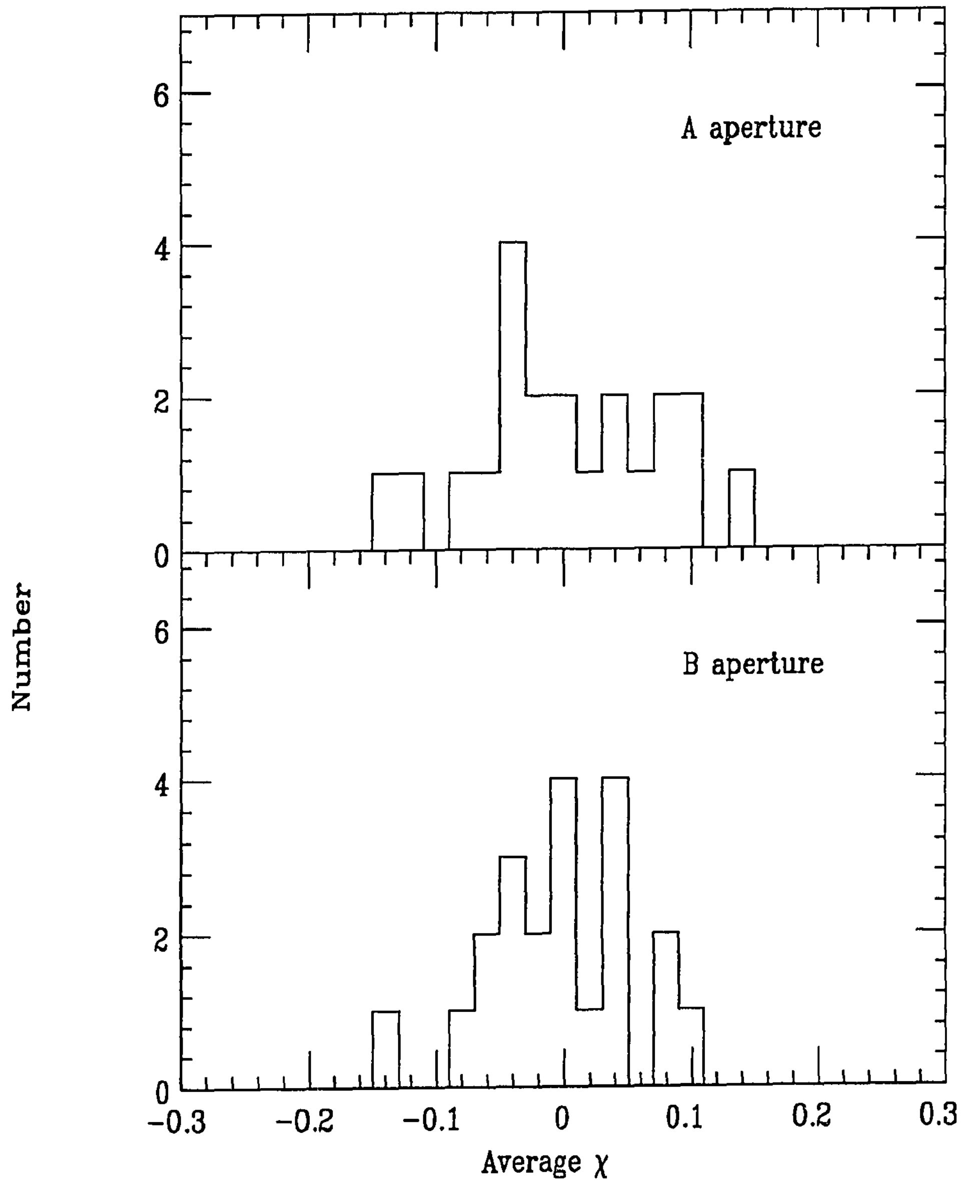

Figure 5.22: Average χ for each zenith angle fit.

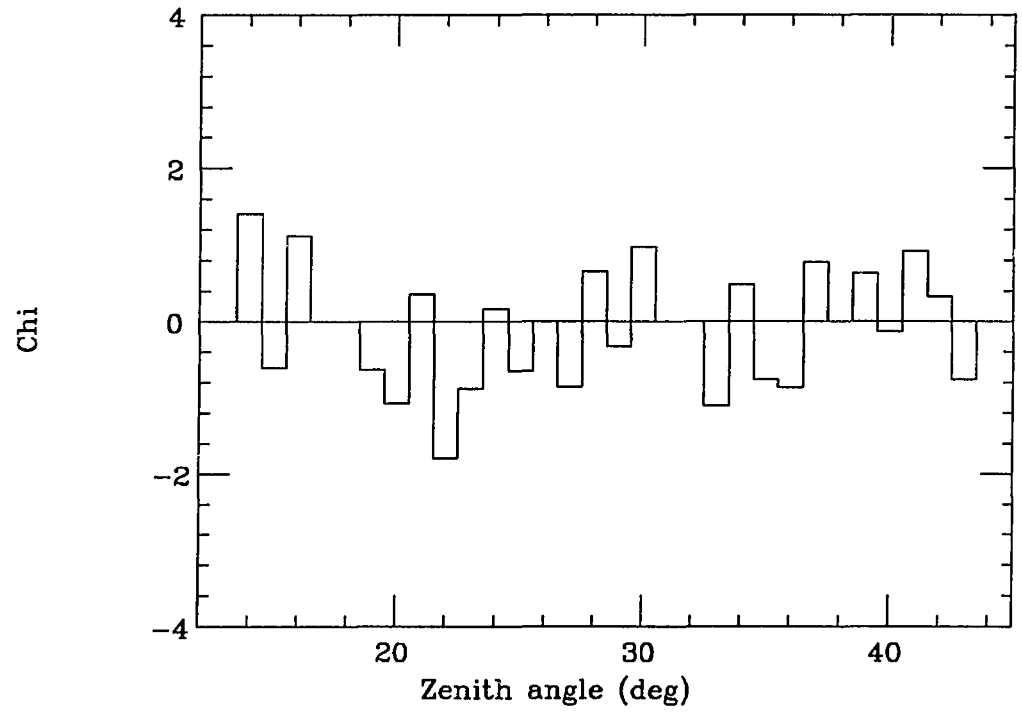

Figure 5.23: χ as a function of zenith angle during one run.

The rate at zenith and χ^2/dof for each run is presented in Table 5.3. These zenith fits were performed with $\gamma = 2.284$ for both apertures. For the DC analysis, an additional requirement that the final χ^2/dof be less than 2.0 for both apertures is imposed. Those runs that did not pass this cut are marked with an X in the status column. This table only includes runs in May – August which pass the initial cuts based upon fluctuations in the average scaler rate.

Table 5.3: Zenith angle fit parameters for 1989

	A		B		
Run	R_o	χ^2/dof	R_o	χ^2/dof	Status
May					
1589	0.609 ± 0.009	24.5/17	0.600 ± 0.009	24.3/21	√
1591	0.612 ± 0.010	31.1/19	0.630 ± 0.009	26.7/21	√
1593	0.620 ± 0.010	15.5/17	0.601 ± 0.011	35.6/21	√
1594	0.642 ± 0.022	2.8/4	0.650 ± 0.021	5.0/5	√
1597	0.622 ± 0.012	38.4/14	0.616 ± 0.011	23.0/18	X
1598	0.635 ± 0.017	7.4/8	0.640 ± 0.016	6.9/8	√
1601	0.595 ± 0.013	11.8/17	0.556 ± 0.013	38.0/19	√
June					
1613	0.644 ± 0.009	13.7/18	0.636 ± 0.009	17.6/19	√
1615	0.644 ± 0.014	21.1/16	0.667 ± 0.015	31.2/17	√
1619	0.581 ± 0.016	62.0/11	0.675 ± 0.018	4.3/8	X
1620	0.664 ± 0.024	4.8/5	0.556 ± 0.031	4.9/2	X
1622	0.659 ± 0.010	14.7/14	0.657 ± 0.011	46.0/15	X
1624	0.638 ± 0.024	1.7/5	0.613 ± 0.024	9.4/6	√
1625	0.653 ± 0.012	12.8/14	0.627 ± 0.011	13.1/14	√
1628	0.636 ± 0.016	15.9/8	0.616 ± 0.013	4.2/7	√
July					
1636	0.650 ± 0.016	2.0/5	0.615 ± 0.017	6.1/5	√
1638	0.693 ± 0.015	8.1/10	0.652 ± 0.014	8.5/10	√
1648	0.650 ± 0.016	8.5/8	0.643 ± 0.019	0.2/4	√
1650	0.646 ± 0.015	13.3/8	0.622 ± 0.014	3.4/8	√
1658	0.636 ± 0.015	10.1/6	0.601 ± 0.014	9.3/7	√
1660	0.649 ± 0.020	7.6/4	0.600 ± 0.019	2.4/5	√
August					
1669	0.604 ± 0.019	2.5/2	0.579 ± 0.025	1.2/2	√
1671	0.632 ± 0.016	0.3/2	0.539 ± 0.014	0.6/4	√
1673	0.608 ± 0.016	0.4/2	0.552 ± 0.018	0.1/1	√
1676	0.581 ± 0.015	1.8/2	0.552 ± 0.016	0.6/3	√

5.2.2 DC Analysis

The DC analysis of the '89 data was performed in two pieces: first, a burst search was performed on each wobble interval, looking for short γ bursts of 900 s. Next, an overall DC excess search was performed, looking for low level, longer duration γ emission. The rate as a function of 35-day and orbital phase was also investigated.

The zenith angle fit determines the background rate well on a run by run basis. In order to perform a careful burst search on an interval by interval basis, a better measure of the fluctuations of the off source on this time scale is desirable. The Gini test (discussed in Section 4.5) is used to check each interval for exponentiality. For this analysis, intervals for which the absolute value of the off source Gini number greater than 1.96 (or 5% probability) were eliminated from the final data set. A total of 9 of these intervals were expected from the data sample, and 8 were seen. The distribution of all of the off source Gini numbers is shown in Figure 5.24. The mean of this distribution is shifted from zero by $+1.2\delta$, where δ is the standard deviation of the mean. This is seen as a larger than expected number of values between +1.3 and +1.8. As one would guess from looking at the distribution, removing those Gini numbers outside of ±1.96 does not significantly change the shift in the mean. After this final cut on the data, 184 intervals remained to be analyzed.

Using the value of γ determined in the initial two parameter zenith angle fit to the data, and the values of R_o determined in subsequent one parameter fit, the expected number of events during a given 900 s interval may be determined

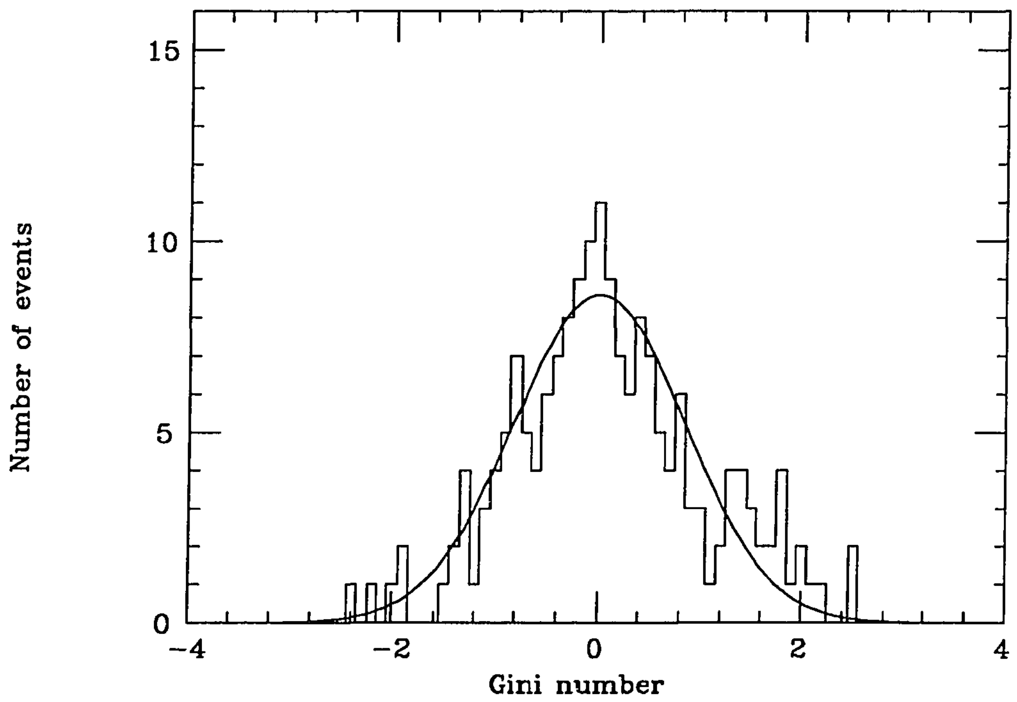

Figure 5.24: The Gini numbers for all off source Her X-1 data passing zenith angle fit cuts.

from the expected rate, R(θ), by approximating the integral (Equation 4.32) by $N_{exp} = \Delta t\ R(\theta)$ where Δt is the time interval between events, as was done for the 1987 analysis. The error in the number excess (N_{obs} - N_{exp}) is found from both the Poisson error in N_{obs}, and the error in the fit (Section 4.5). The number excess is calculated for each interval for the on source aperture. As a check of the analysis procedure and the expected behavior of the background, the off source aperture number excess is also determined. Since it is the off source that was used to determine the expected number of events, the off source number excess distribution should fit well to the expected distribution.

As can be seen in Figure 5.25, there are no burst intervals in either the on or the off source. The most significant number excess in the on source, 3.5σ corresponds to about 10% chance probability. This is of the same magnitude as the largest off source excess. The on source distribution is noticeably wider, with a width corresponding to 1.06σ. The most significant feature of the on source distribution is the deviation of the mean, which is $+2.3\delta$ from zero. As is indicated on the plot, the off source distribution mean (0.03 ± 0.07) and width ($0.98\ \sigma$) agree well with what is expected for a Gaussian distribution.

A plot of the number excess as a function of wobble number (Figure 5.26) does not show any evidence that the observed number enhancement occurs during a continuous set of wobble intervals. Since the magnitude of the shift is not very large, such a shift is difficult to observe on an interval by interval excess plot.

The integrated number excess may be determined, as a running total of the excess throughout the data set (Figure 5.27). Since this is plotted as a function of wobble number, the x axis is not linear in time, thus the 35 day phases are not the correct length in the figure. Several things can be noted: during two of the three high-on 35 day phases during which we have data, the rate on source is higher than the expected background. During both the 35 day off phases and the low on phase, the integrated rate is consistent with no excess. The overall integrated excess from Figure 5.27 is 707 ±314 events, or 2.25σ. The (non-integrated) rate as a function of wobble number for the high on, low on, and off 35 day intervals is presented in Figure 5.28. The integrated rate for these same intervals is plotted in Figure 5.29. The 3 σ jump in the high on distribution near wobble number 77 in the high on

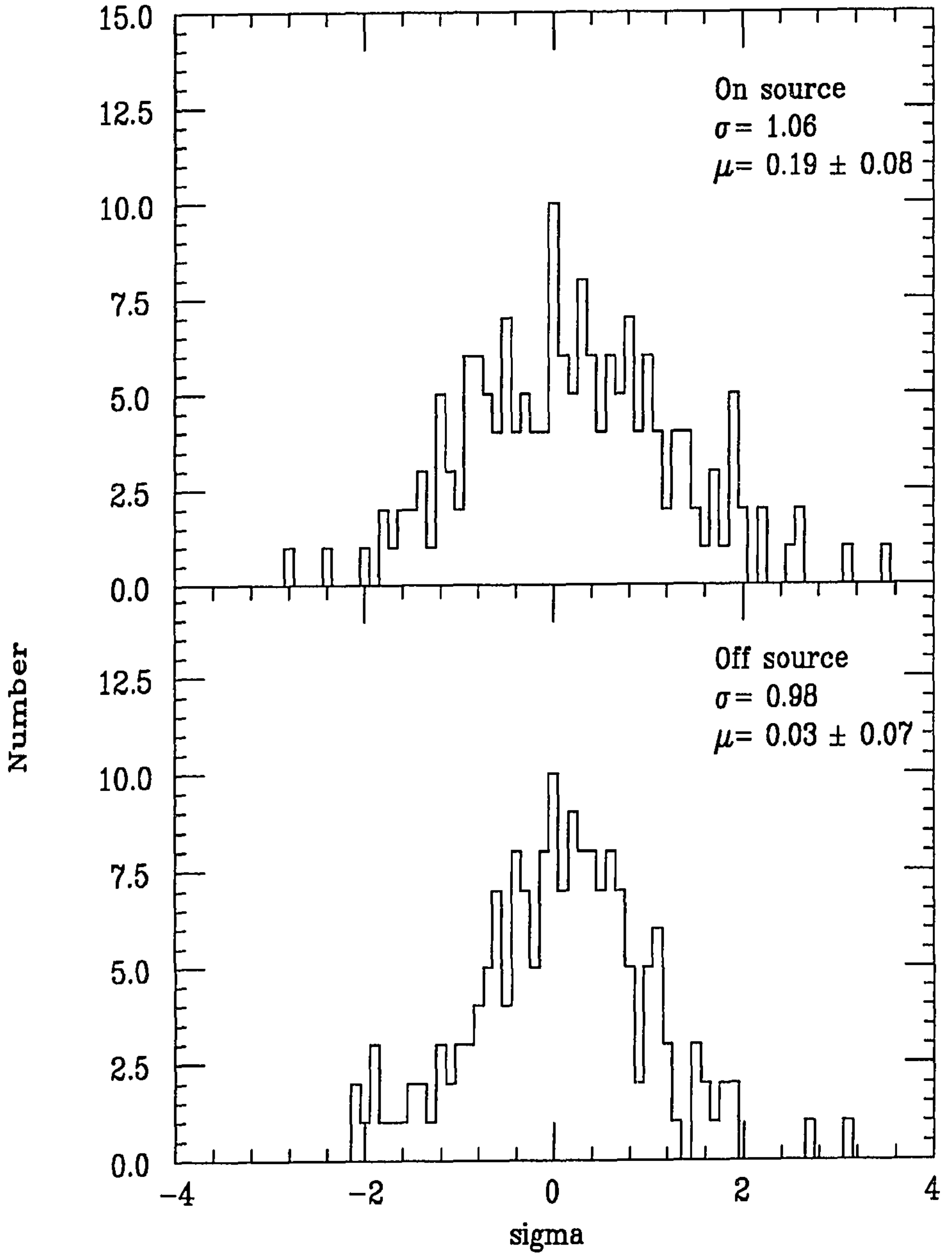

Figure 5.25: Distribution of the number excess for each 900 s interval, expressed in σs.

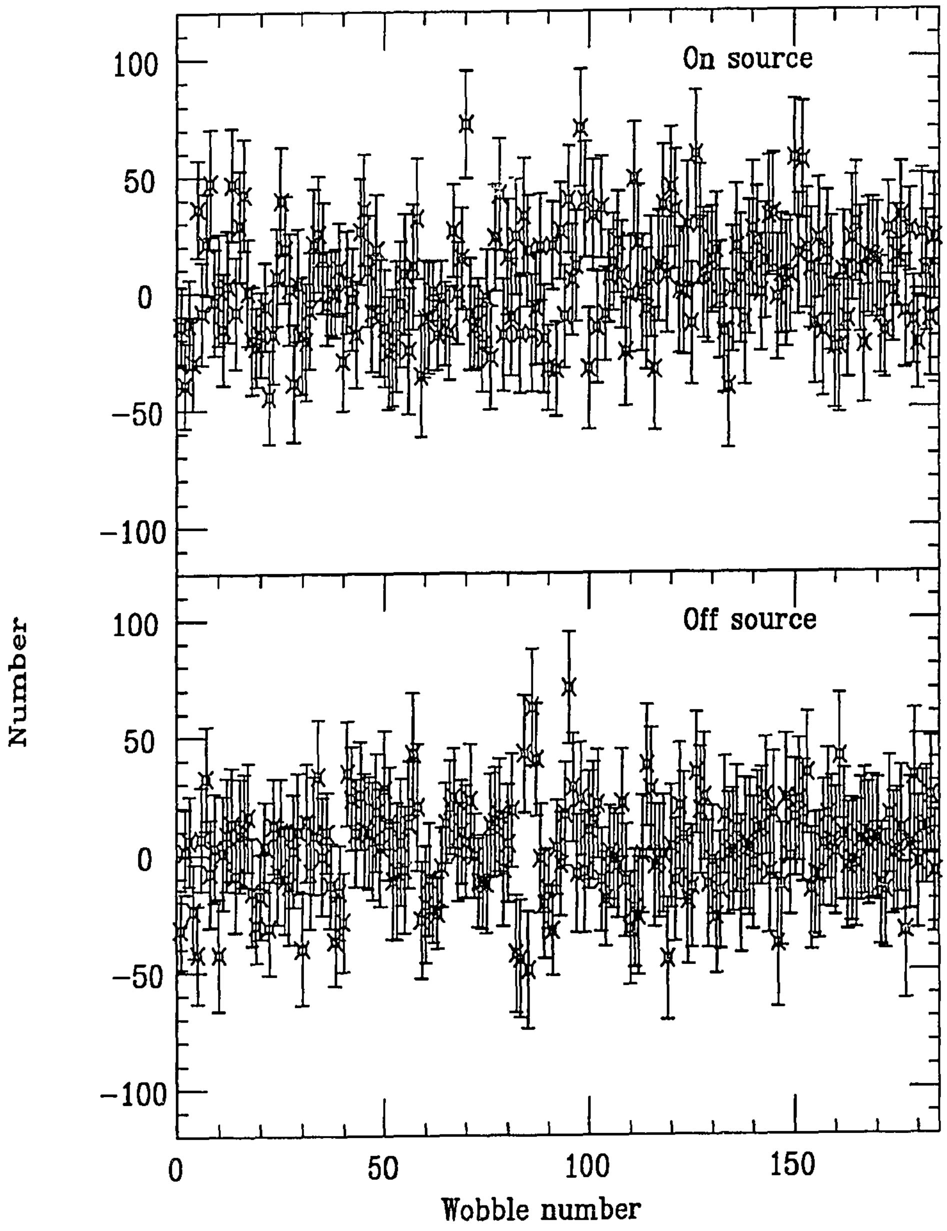

Figure 5.26: Number excess as a function of wobble number.

plot in Figure 5.28 is obvious in the integrated excess as well. From about wobble number 96 on in this plot through wobble number 117, all but 4 intervals show a small excess rate. The low on and off intervals are all consistent with no excess. Table 5.4 summarizes the final rate excess in each interval mentioned above.

Table 5.4: Integrated number excess for each 35 day phase.

35 day phase	On excess	σ_{on}	Off excess	σ_{off}
High-on	543 ± 256	2.1	76 ± 256	0.3
Low-on	14 ± 91	0.2	51 ± 92	0.6
Off	150 ± 158	0.9	62 ± 158	0.4
Total	707 ± 314	2.3	189 ± 314	0.6

Even though every off source interval is consistent with no excess, each integrated excess is greater than zero. Also, it can be seen that the 35 day off interval is contributing to the total on source excess. As we noted in Section 4.1, clouds and moisture during a run will, by decreasing the rate at zenith calculated in the fit, tend to overestimate the rate excess during the run. A small amount of weather contaminated data may introduce an systematic offset, such as what is seen in the integrated off source excess.

The number excess is also plotted as a function of the 1.7 day orbital phase, and of the 35 day phase (Figures 5.30 and 5.31). The excess is not correlated with the orbital phase. Bins near the start and the end of the 35 day high on interval contain most of the observed on source excess. The interval from about the start

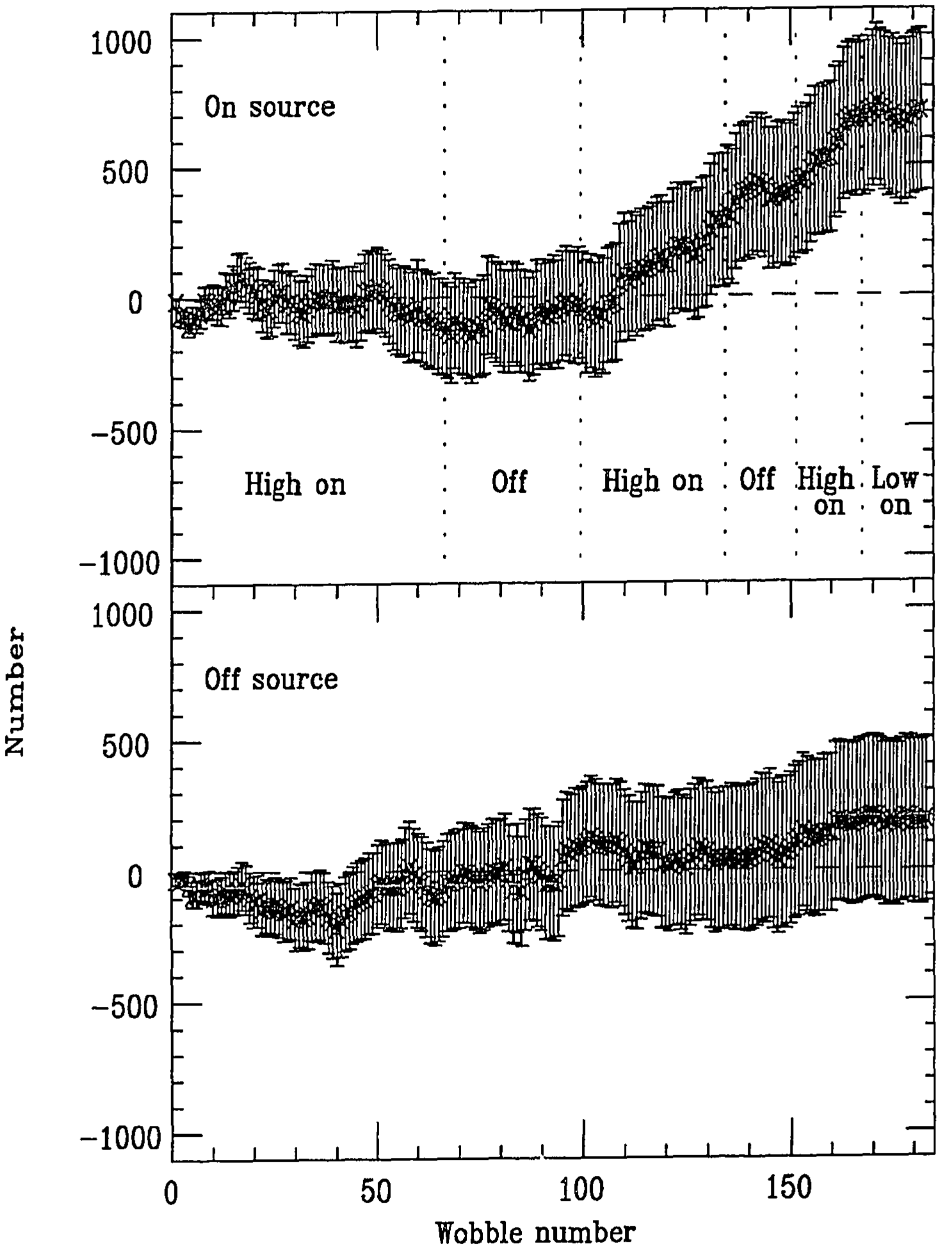

Figure 5.27: Integrated number excess as a function of wobble number.

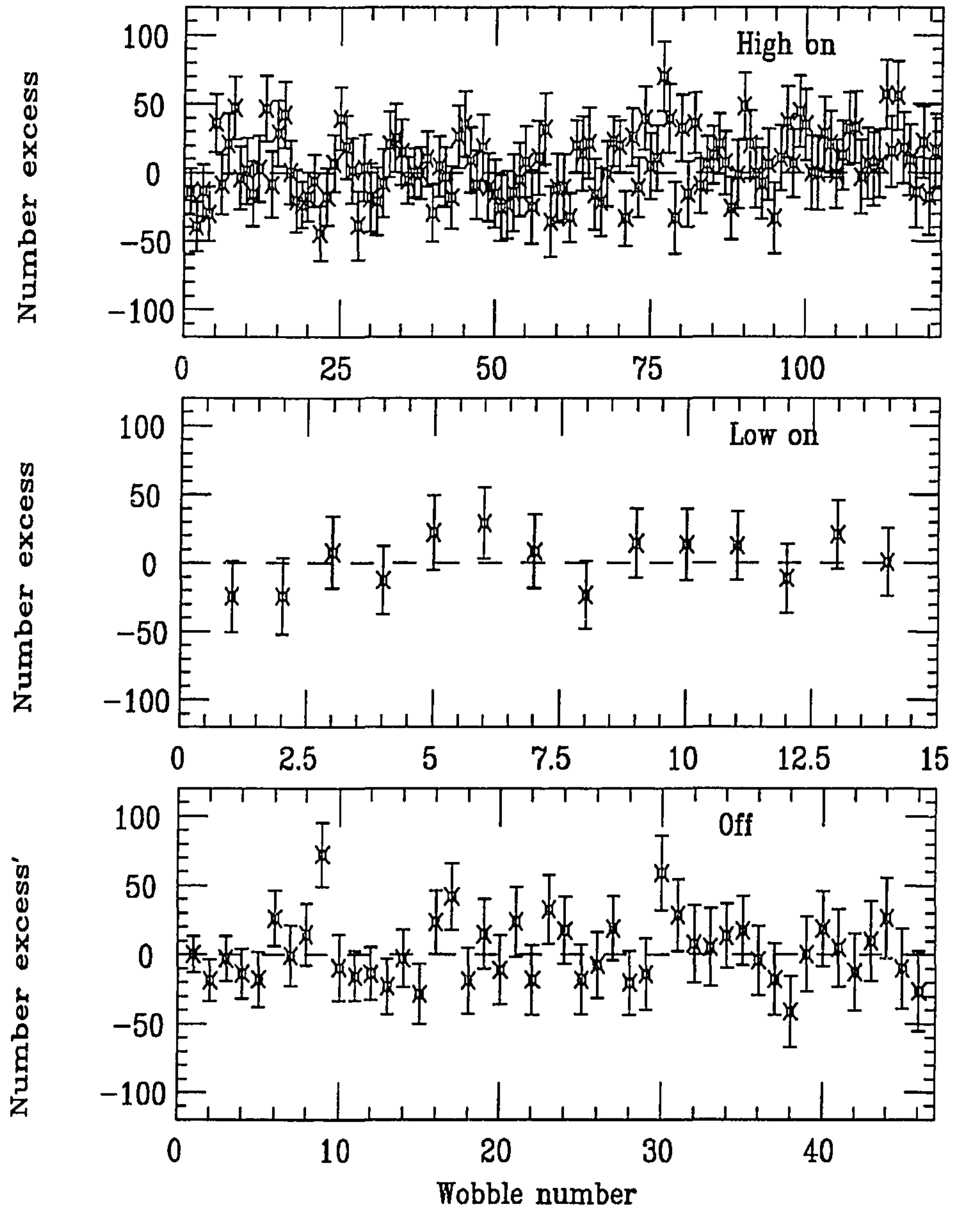

Figure 5.28: Rate as a function of wobble number for the high on, low on, and off 35 day variation phases.

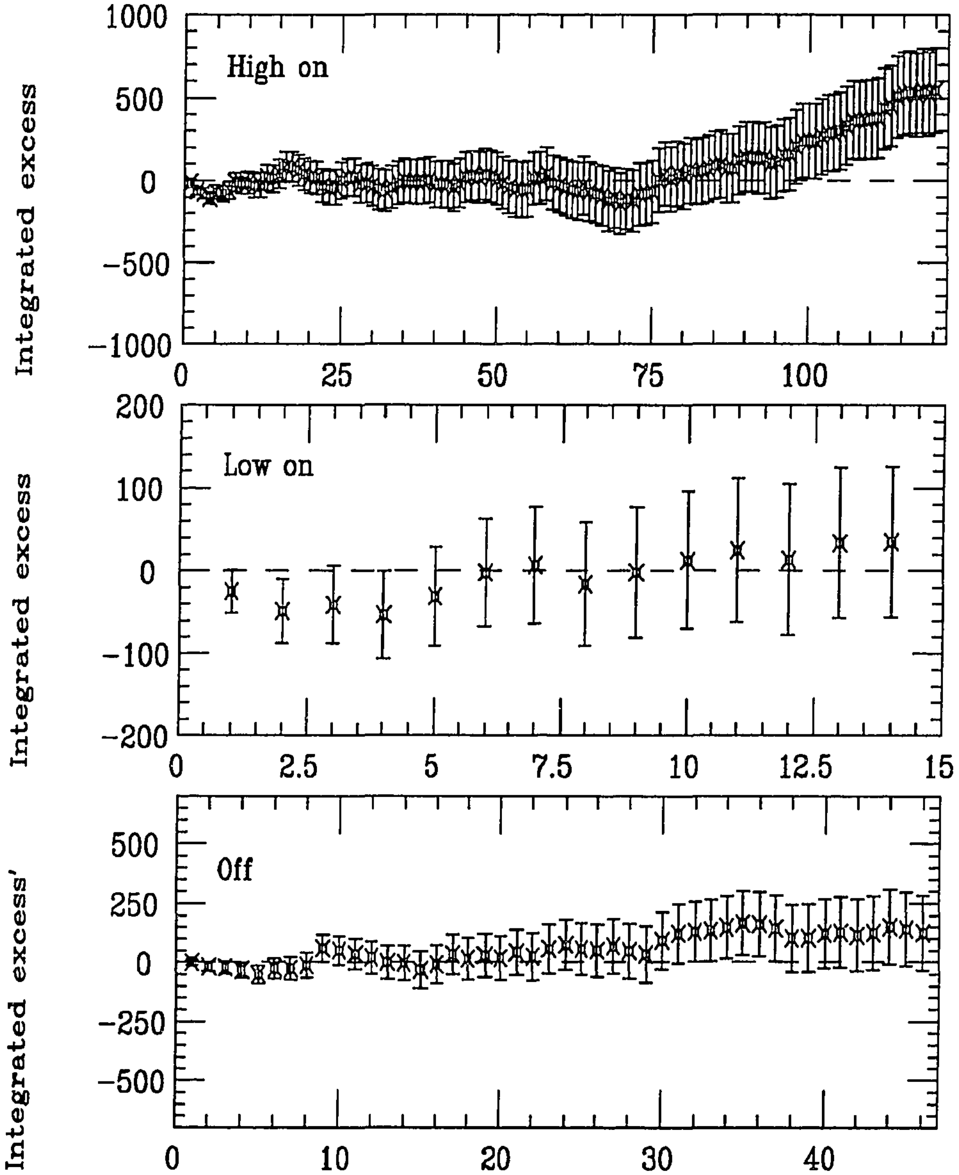

Figure 5.29: Integrated rate as a function of wobble number for the high on, low on, and off 35 day variation phases.

of the 35 day phase to a phase of 0.1 shows a 2.7σ excess, and the final bin of the high on interval is 1.8σ above zero.

5.2.3 Periodicity Analysis

The periodicity search of the '89 data proceeded in a similar fashion as the search of the '87 data. Using all intervals of 600 s or longer which passed the zenith angle fit cuts discussed in the previous section, the H_m test was performed on the 192 intervals using the same search interval and oversampling factor.The Rayleigh test was not performed on these data.

The H_m power distribution (Figure 5.32) reveals the two intervals with the highest powers are in the on source distribution. Both of these have a periodicity close to the interpolated X-ray period. The highest, Z=9.1, occurred during run 1591, on day number 122, beginning at 39230 s UT with the A aperture on source. The period detected was 1.23719 s. This run was taken at a 35-day phase of 0.2. The second highest peak occurred during run 1669, on day 207 beginning at 24695 s UT with the B aperture on source, at a 35 day phase of 0.6. The period detected here was 1.237760 s. After all trials were taken into account, the overall chance probability of the highest peak is 18% and for the second highest peak, it is 37%, so neither of these are significant individual peaks. The combinatorial probability is about 5% chance.

Each 900 s interval was also investigated for a low level signal, producing a excess in the power distribution at lower H_m power. Following the same steps as

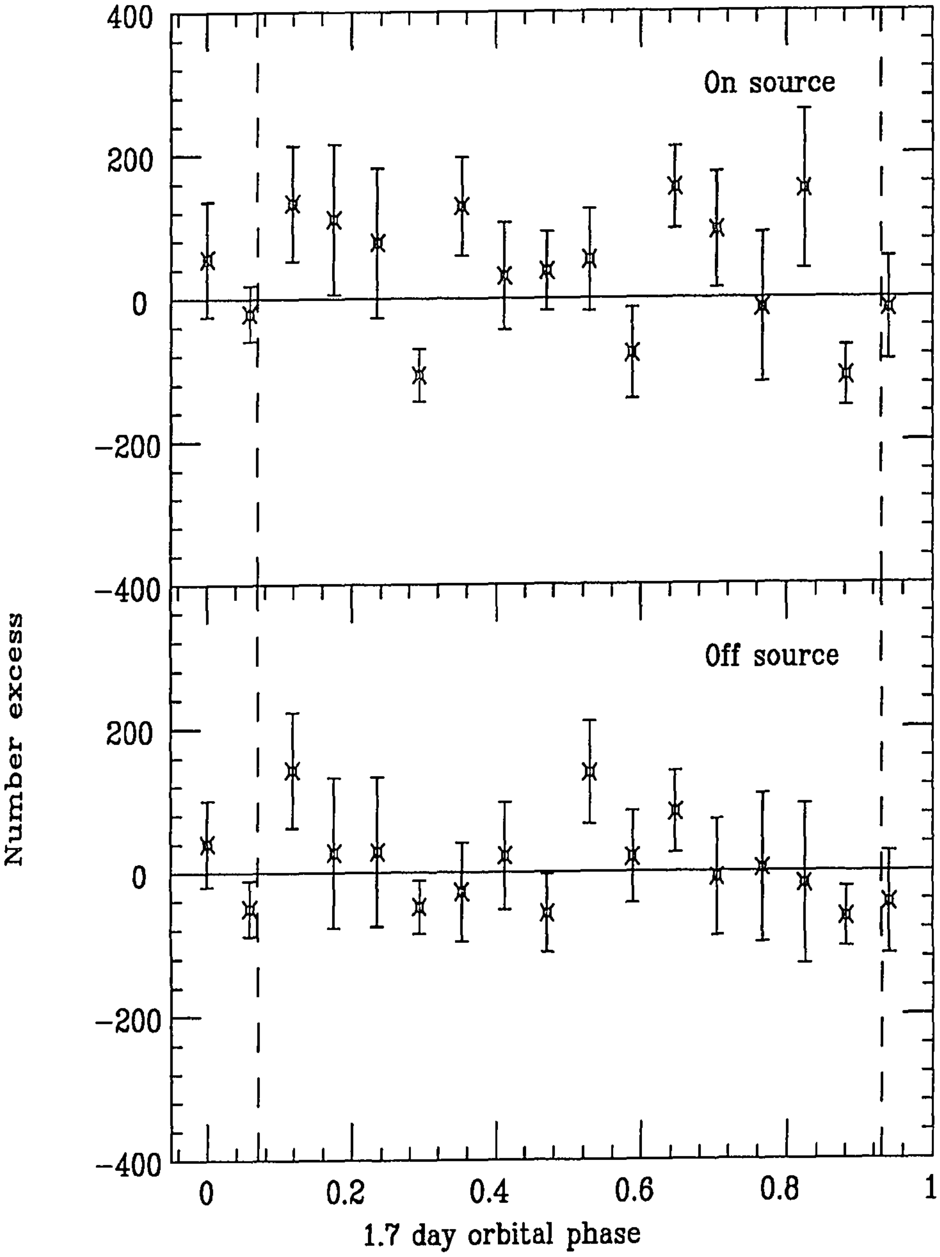

Figure 5.30: The number excess as a function of the orbital phase.

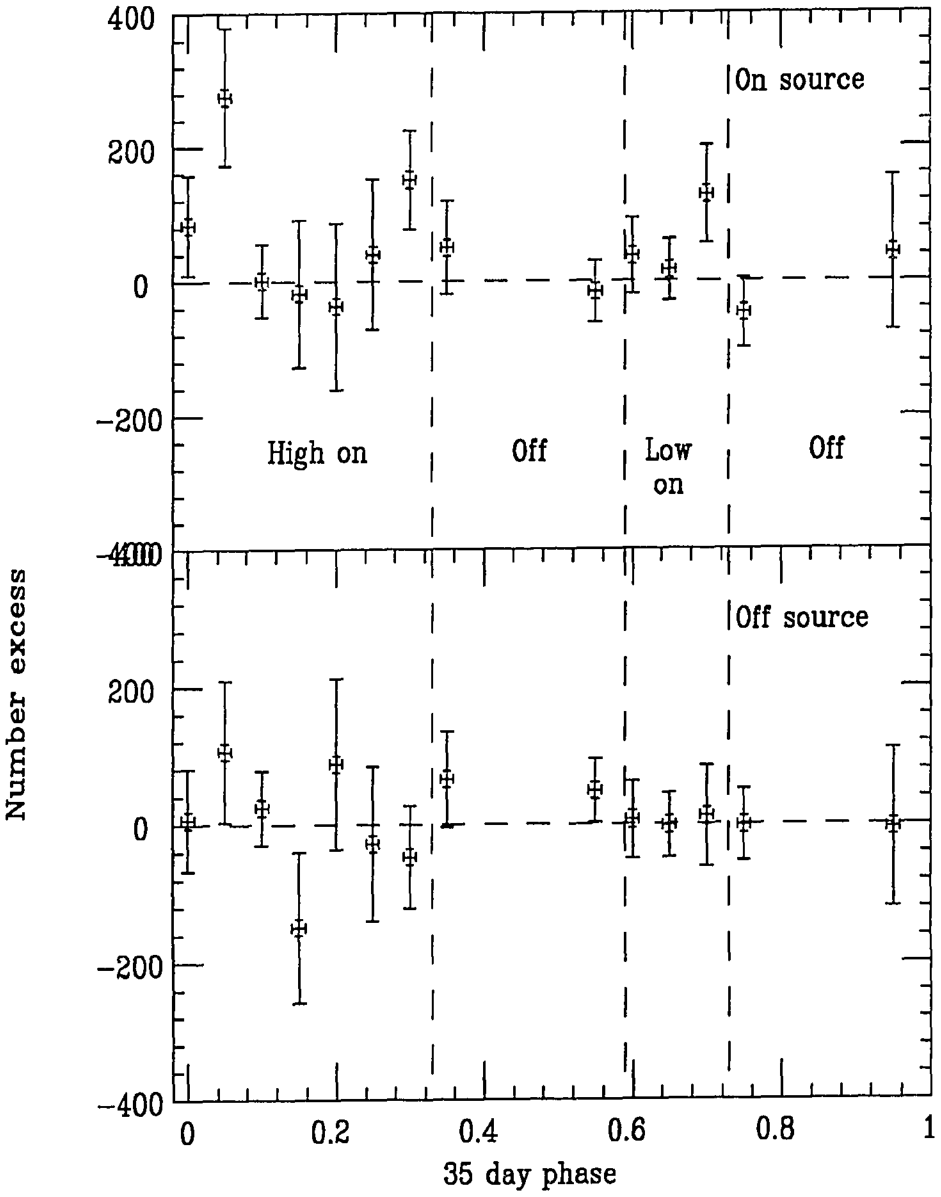

Figure 5.31: The number excess as a function of the 35 day phase.

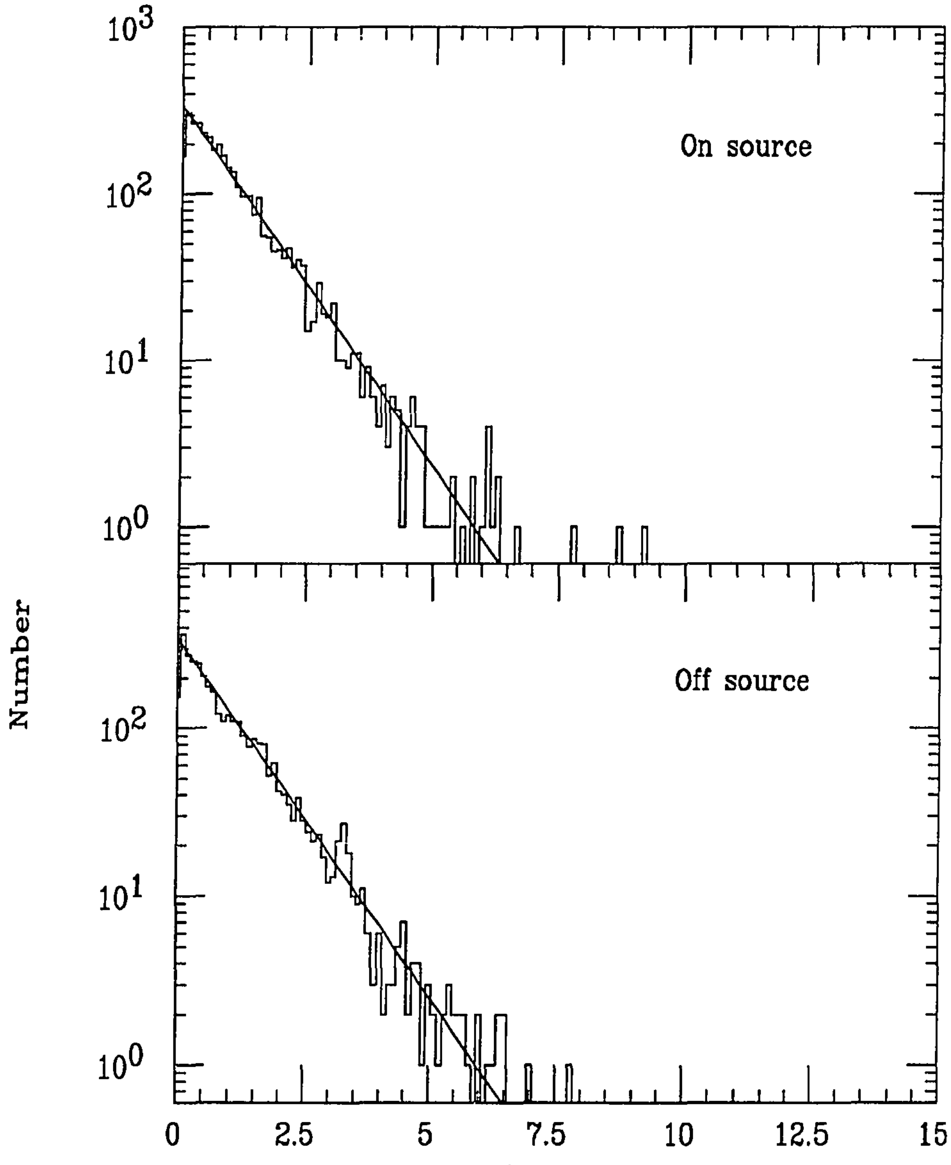

Figure 5.32: On and off source H_m distributions.

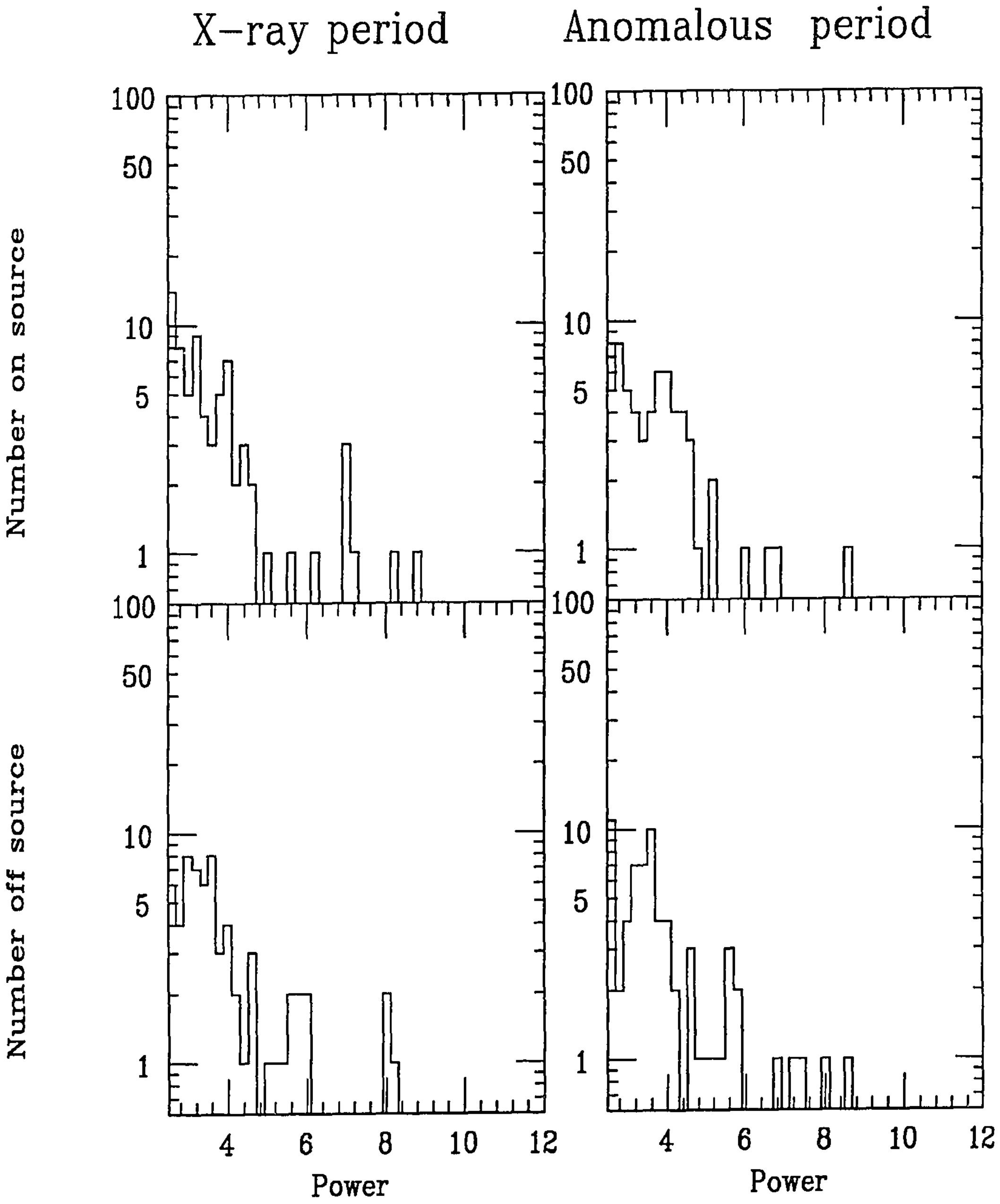

Figure 5.33: On and off source H_m distributions for ±1 IFP around the X-ray and the anomalous period.

with the 1987 data (Section 5.1) maximum power in the range of ± 1 IFP around both the expected X-ray period and the anomalous period as determined in run 1162. No evidence for an excess at lower H_m power was seen. The distributions for the on and off source are shown in Figure 5.33. Further oversampling by a factor of 5 in these distributions have increased the highest power near the anomalous period so that it is nearly as large as the highest at the X-ray period; however, none of these are significant. When both the 1987 and 1989 data sets are combined and tested in a similar manner, no evidence for a low level periodic signal is seen.

5.3 Summary and Conclusions

In this section, I will briefly summarize the results presented in the earlier sections of this chapter and present observations and conclusions based upon these results. Most of these observations have been made, or at least hinted at, throughout this chapter. In this concluding section, I will attempt to assemble them into a coherent structure.

1987 Summary

The most significant observation of Her X-1 at the HGRO during 1987 leads to a contradiction. The rate excess observed from the source is not in agreement with the observed level of periodicity during run 1162. The probability of obtaining a rate excess of 0.5σ given a Rayleigh power of 11.9 is at best the same order of magnitude as the overall probability of the observed periodicity. A possible explanation for this (perhaps the most straightforward explanation) is that there is no signal present from the source. It is solely a fluctuation in the background that is producing the observed periodicity. This explanation is impossible to dismiss; though, when the overall chance probability is calculated from the Rayleigh power, Z, this explanation is only $\sim 2\%$ probable.

In addition, if we assume that the calculated number of excess events for a sine wave light curve is a reasonable approximation to the actual number of signal events expected, then the event deficit is on the order of 2σ according to the estimate made in section 5.1.3. This implies that the null (no signal) hypothesis is approximately equally as probable as a negative fluctuation in the number of background events producing an apparent lack of rate excess assuming the periodicity observed is from signal events. Both of these explanations are consistent on only the several percent level, so neither is highly probable. Figure 5.12 does show a 1.2σ negative rate fluctuation during two, 3 minute intervals, which is preceeded by a 1.7σ rate excess during the first three, 3 minute intervals on this plot, making up the 900 s interval of highest periodicity during run 1162. Although this periodicity is observed to be present throughout all of the 900 s interval, a shorter burst is not ruled out in this case, where a periodic signal from the source is combined with a contribution along the same phase direction from the noise vector. The excess, over only the first three intervals, would be consistent with a Rayleigh power of 10.2 at the 50% level for a delta function light curve. As we observed in Figure 5.15, an agreement to the predicted rate on this order (within -1σ of expected) is not uncommon based upon previous measurements of Her X-1.

Given the observed rate as a function of time during this interval, the possibility of a low level signal combined with a periodic fluctuation in the background causing the strength of the observation to be enhanced should also be considered. There are several supportive and contradictory points to be made here. In support of this explanation, if such a low level signal were present through a large part of the data set, then the observation of Z=11.9, σ=0.5 is made more plausible both because it makes achieving the observed value of Z more likely if this observed signal strength is a combination of signal and a "periodic" background, and because the estimate of σ would then be incorrect. Recall that the on source rate is determined from a zenith angle fit of the on source data during 1987, so that any *small* overall DC excess will be lost in this fit. The observation of a small overall DC excess in the 1989 data, partially corresponding to the X-ray on portions of the 35 day phase, also lend support to this hypothesis. Since the 1989 data set is substantially different from the 1987 set, due to the changes at the mount producing a lower energy threshold, the two sets should not be directly compared. The period observed here and that detected in 1986 by four groups can be directly compared. The excellent correlation among these five measurements lends support to the hypothesis that at least part of the detected periodic signal is a characteristic of the source.

The lack of an observation of a low level periodic signal from Her X-1 as determined by the agreement of the maximized Rayleigh power distribution near both the X-ray and anomalous period to what is expected from the background

(Figures 5.13 and 5.14), contradicts the low level signal hypothesis. For this explanation to be valid, we must assume that:

1. The anomalous period is not stable.
   Models developed to explain the anomalous periodicity do not predict a stable period; however, all reported detections of an off-period since 1986, including measurements at higher energies by Cygnus and Ooty, contradict this.
2. Even though DC emission may be present, it is not always pulsed.
   The 1989 measurements support this claim. No intervals of significant periodicity or a low level periodicity was observed during this year, yet a small overall DC excess was observed. This hypothesis cannot be fully tested since the rate as a function of zenith angle cannot be determined for the A aperture using purely off source data during 1987.

In the process of investigating this interval further, different cuts, such as multiplicity cuts described in Section 5.1.2, Figure 5.8, as well as cuts based upon the uniformity of the light over the mirrors in each event, were employed in an attempt to better understand the interval. Throughout these investigations, and those performed by other members of our collaboration, the significance of this interval was diminished or enhanced, but it did not completely disappear. Although we cannot claim that we observe periodicity consistent with Z=11.9 from Her X-1 because of the conflicting rate excess measurement, given the relative unlikelihood of the chance probability, the rate excess during the first two-thirds of the interval, and the agreement of the observed period with that found in 1986, a combination of a periodic signal and noise is plausible. Certainly, this is a very interesting interval in our data set.

The air-shower data, taken in coincidence with the Čerenkov telescope, was also analyzed for rate excess and periodicity. In this data set, the most significant feature was a 3.0σ excess of events corresponding to a 35 day phase of 0.60 in a 20 bin phase plot. This excess did not appear to be correlated with the observation of a rate excess by the Čerenkov telescope, and it was not accompanied by periodicity at TeV energies.

1989 Summary

The 1989 data set contained no intervals showing significant periodicity in the range of ± 3 IFPs around the interpolated X-ray period. A small overall DC excess was observed in this data, corresponding primarily to two of the three high on X-ray intervals during which we have data. This integrated excess is 2.3σ over the entire data set.

The observed γ-ray flux from this interval may be calculated. Assuming an area of 7.5×10^7 cm^2 (Figure 1.18), and a total time of $\sim$ 161,000 s the observed excess of 707 $\pm$314 events corresponds to a flux of $(5.9 \pm 2.6) \times 10^{-11}$ cm^{-2} s^{-1} above 0.15 TeV. This flux is slightly below those observed previously (Table 2.2) given our energy threshold. If an *a postiori* choice of only the two high on intervals where a DC excess is seen is made, then an excess of 585. $\pm$153. events is observed.

When these two intervals are removed from the data set, the integrated excess is consistent with zero.

The correlation between the high on X-ray interval and an observed DC excess in VHE photons is plausible if accretion driven mechanisms, producing charged particle acceleration outward from the magnetic poles of the neutron star are assumed (Section 1.3.3). The observation of a DC excess during only two of the three intervals during which the high on state was observed is more difficult to understand. If an accelerated particle beam interacting with matter in the accretion disk around the neutron star is assumed to produce photons at very high energies, then fluctuations in the density in the disk (or at the edges of the disk) can lead to either partial transmission of the produced γs, or complete absorption of these photons, depending on the density fluctuation. All VHE sources observed to date* exhibit transient behavior, both in their pulsed and in their steady emission. The small excess we observe from Her X-1 during 1989, occurring during only two of the three intervals during which we might expect emission as described above, is indicative of a low-level, transient DC excess from the source. During these two intervals, a DC excess of 3.8σ is observed.

---

*A possible exception to this is the steady emission from the Crab observed by the Whipple group.

Appendix A

Calibration for the Waveform Tests

In order to sum the PMT pulses, a calibration taking into account timing differences due to different tube voltages and cable lengths up to the output of the AFOs must be performed. To do this, a 337 nm Laser System Industries laser was used. This laser has an output of 40 mW at 337 nm, and a pulse width of 2 ns FWHM. The laser was placed on top of the Zodiacal Light building approximately 180 ft from the telescope. A UV-transmitting diffuser placed 6 inches in front of the laser spread out the beam to about a 18 ft radius at the telescope. This provided approximately 10^{13} photons/m^2 maximum output for each pulse, which was then attenuated by two glass filters. The pulse repetition rate of the laser was set to approximately one pulse per second. Since the telescope was pointing near the horizon, the real trigger rate was very low, so that essentially all of the recorded triggers were from the laser.

Since the calibration laser was placed so close to the telescope (out of necessity: since the telescope is in a small depression at the summit), it should be impossible to trigger all of the channels at once without scattering of the light. The intensity of

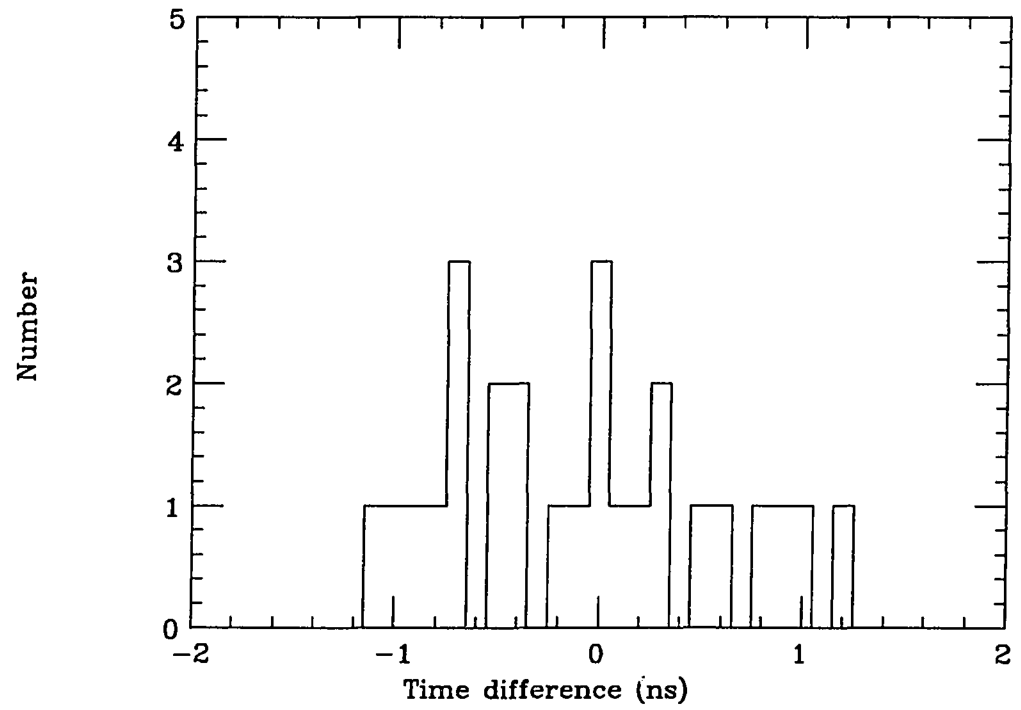

Figure A.1: The difference between standard calibrations and those obtained using the 337 nm laser.

scattered light is reduced by a factor of 10^6 at angles comparable to those necessary to trigger all channels of the telescope ($< 2°$). Considering the known intensity of the beam, prior to the insertion of the 2 attenuators, and considering the sensitivity of the PMTs, it is possible that atmospherically scattered photons could trigger some mirrors. In addition, scattering off the aluminum ring or the space frame at the center of the mirror, or imperfections in the mirror could produce triggers. All of these effects should cause only small (< 1 ns) differences in the expected and actual trigger times of each channel. Scattering off the mirror edges or off of the space frame well behind the mirrors could cause much larger fluctuations in the trigger times; however, the observed differences between the laser calibration values for each channel and those obtained in the standard manner from all of the August data runs agree to within several nanoseconds (Figure A.1). We expect that some of this timing difference could be due to components and cables up stream of the AFOs, which will effect the TDC calibration but will not be present in the laser calibration up to the AFO output. Thus, though the laser calibration performed is adequate for determining the general shape of each summed pulse, because of the width of the laser pulse and the scattering mentioned above, it is not adequate for producing an absolute calibration for use in data analysis. A summary of the timing calibrations up to the output of the AFOs for the A aperture is presented in Table A.1. The calibration times are determined with channel AA as a reference.

Table A.1: A Aperture timing calibration

channel	Timing Diff (ns)	Channel	Timing Diff (ns)
A	0.0	N	0.5
B	-1.0	O	0.0
C	-0.5	P	0.0
D	0.0	Q	-1.0
E	0.0	R	-0.5
F	0.0	S	-1.0
G	0.0	T	-0.5
H	-0.5	U	0.0
I	-1.0	V	-2.0
J	0.5	W	-1.0
K	-1.0	X	-1.5
L	0.0	Y	-1.0
M	0.0	Z	-0.5

Appendix B

Phase Linking of the 1986 Anomalous Period Data

As an extension of part of the analysis performed in Chapter 5.1, the interval of periodicity reported by Pat Slane in run741 of our 1986 data (Slane, 1988) is tested at the anomalous period reported by the Ooty group. This interval occurs about 40 days before the first interval reported by Ooty. These measurements are close enough in time so that a small $\dot{P}$ will not effect the relative phase of these intervals. The Ooty group was unable to detect a period derivative in the anomalous period over 6 months.

Using the ephemeris provided by Ooty, and their phase-linked period, we find that our 1986 interval does not appear to be correlated in phase to the Ooty intervals. At the period of 1.2357701 s, the light curve from run 741 is sinusoidal, whereas near the maximum Rayleigh power period the curve is sinusoidal with one high population bin (see Figures B.1 and B.2). The phase of events in Figure B.1 is approximately 0.6 – 1.0, which does not agree with the preferred range of pulsar phases observed by Ooty (0.11 – 0.38). I want to note here that the period maxi-

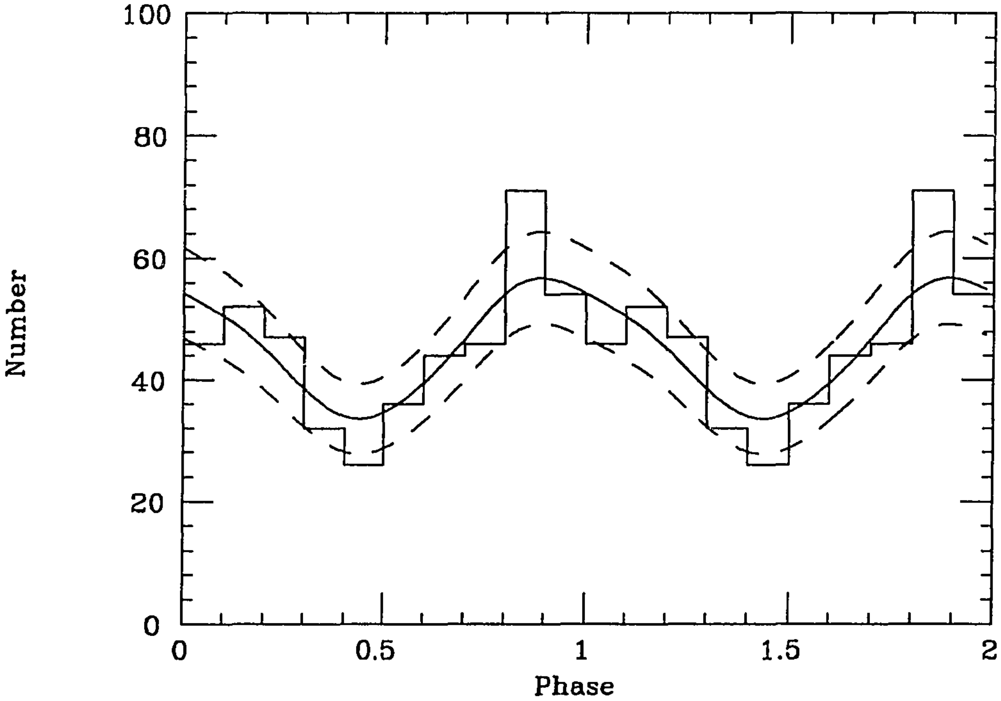

Figure B.1: The light curve at P=1.2357701 s for run741, using an ephemeris of $t_0 = 2446613.17379361$ JD.

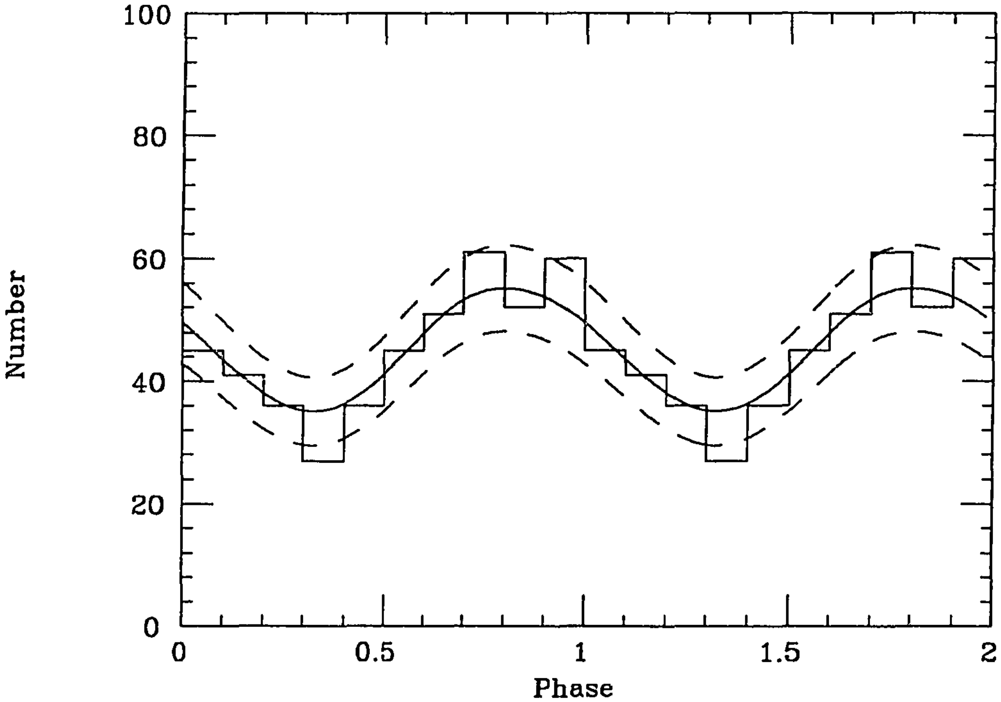

Figure B.2: The light curve at P=1.236 s for run741.

mum Rayleigh power I observe for this interval differs by $1/20^{th}$ of an independent period from the period reported by Slane. Although this difference is only 0.4 σ of the reported error in the period, it suggests that a difference in the solar system or source barycenter may exist. Although the light curve in Figure B.2 looks very similar to that reported by Slane, the light curve I produced at his reported period does not have the enhanced phase bin at 0.8. Slight differences in event selection, the result of calibration differences, will also effect the light curve somewhat.

If one uses Ooty's t_0 and the detected period for our interval, then curiously enough, the high phase bin appears at a phase of 0.2; however, in this case, t_0 loses its meaning. Our barycenter routine, based on the JPL ephemerides, differs slightly from that used by Ooty (MIT-PEP-311). From calculations by Pat Slane with help from Jim Annis concerning the MIT routine, the absolute difference between our barycenter routine and MIT's is about 1% of the pulsar phase on day 133 of 1986. This would be nearly undetectable in our light curve plots, apart from small binning effects. The phase drift over a 900 s interval at this time is also negligible, since the time derivative difference between the two routines is about $2\mu s/900$ s.

Appendix C

Summary of Periodicity and Rate Excess Consistency for Haleakala and Whipple data, 1984 - 1986

The following Table C.1 presents a summary of the reported Rayleigh power and number excess, and the predicted number of excess events based upon the observed Rayleigh power and consistency between this and the observed number excess. Information concerning the first seven Whipple intervals from 1984 and 1985 is from P. Gorham's Thesis (Gorham, 1986c). For these measurements, the number of excess events was inferred from the interval time, telescope area, and calculated flux values reported in the Thesis. The eighth entry in the table is the sole Haleakala data point in the group, (Slane, 1988). The final entry is the anomalous interval from the Whipple group (Lamb, *et al.* 1988).

In this table, Z is the reported Rayleigh power, and β and γ are the Lewis coefficients defined in Chapter 4.4. The consistency between the observed Rayleigh power and number excess is presented as P_γ assuming a sine wave and then a delta function light curve. The difference between the expected number of events for both of the two trial light curves (β) is listed for first a sine wave and second a delta function light curve. The difference between the observed and expected number of events is plotted in Figure 5.15 in Chapter 5, and it is presented here for reference.

Table C.1: Summary of Whipple and Haleakala results.

Date	Z	Excess	β	γ	P_γ
4/4/84	6.9	144 ±70	209	1.9	0.17
			144	1.2×10^{-5}	1.0
5/5/84	10.8	181 ±111	342	3.9	0.048
			230	0.24	0.63
5/23/84	8.1	135 ±73	217	2.7	0.10
			150	0.054	0.82
4/23/85	7.9	54 ±94	216	6.8	0.0089
			174	2.2	0.14
4/24/85	7.4	117 ±103	259	3.9	0.049
			185	0.55	0.46
5/21/85	11.6	222 ±141	576	2.0	0.16
			324	0.14	0.70
6/16/85	11.9	378 ±232	698	3.1	0.078
			440	0.08	0.77
5/13/86	12.7	30 ±21	72	11.0	0.00093
			62	3.1	0.076
6/11/86	13.1	165 ±88	308	5.3	0.021
			214	0.39	0.53

Bibliography

Astronomical Almanac 1988, Naudical Almanac Office, U.S. Gov. Printing Office.

Baltrusaitis, R.M. *et al.* 1985, *Ap.J. Lett.*, **293**, L69.

Beland, S. *et al.* 1988, *CFHT Info. Bull.*,**18**, 16.

Cassiday, G.L. *et al.* 1989, *Phys. Rev. Lett.*, **62**, 383.

Chadwick, P.M. *et al.* 1985, *Nature*, **318**, 642.

Cheng, K.S. and Ruderman, M. 1988, *Ap.J. Letters*, **337**, L77.

Cohen, J.M. and Mustafa, E. 1987, *Ap.J.*, **319**, 930.

Davidsen, A. *et al.* 1972, *Ap.J. Lett.*, **177**, L97.

Deeter, J.E. *et al.* 1981, *Ap.J.*, **247**,1003.

De Jager, O.C. 1987, *The Analysis and Interpretation of VHE Gamma Ray Measurements*, Ph.D. Thesis, Potchefstroom Univ.

Dingus, B.L. *et al.* 1988, *Phys. Rev. Lett.*, **61**, 1906.

Dowthwaite, J.C. *et al.* 1984, *Nature*, **309**, 691.

Eadie, W.T. *et al.* 1971, *Statistical Methods in Experimental Physics*, North-Holland Publishing Company.

Eichler, D. and Vestrand, W.T. 1985, *Nature*, **318**, 345.

Gail, M.N and Gastwirth, J.L. 1978, *J. Roy. Sta. B*, **30(3)**, 350.

Gaisser, T.K., Harding, A.K., Stanev, T. 1989, *Ap.J.*, **345**,423.

Ghosh, P., Lamb, F.K., and Pethick, C.J. 1977, *Ap.J.*, **217**, 578.

Ghosh, P. and Lamb, F.K. 1979 *Ap.J.*, **232**, 259.

Ghosh, P. and Lamb, F.K. 1979 *Ap.J.*, **232**, 296.

Giacconi, *et al.* 1971 *Ap.J. Lett.*, **167**, L67.

Gibson, A.I. *et al.* 1982, *International Workshop on Very High Energy Gamma Ray Astronomy*, Smithsonian Institution, 97.

Goldreich, P. and Julian, W.H. 1969 *Ap.J.*, **157**, 869.

Gorham, P.W. *et al.* 1986a, *Ap.J.*, **309**, 114.

Gorham, P.W. *et al.* 1986b, *Ap.J. Lett.*, **308**, L11.

Gorham, P.W. 1986, *Ground Based Detection of Gamma-rays Above 250 GeV from Hercules X-1.*, Ph.D. Thesis, University of Hawaii.

Gorham, P. and Learned, J.G. 1988, *Nature*, **323**, 422.

Gupta, S.K. *et al.* 1990, *Ap.J. Lett.*, **354**, L13.

Gupta, S.K. *et al.* 1991, Submitted to *Ap.J.*

Hart, J. 1985, *J. Stat. Comp.*, **21**, 95.

Hewish, A., *et al.* 1968, *Nature*, **217**, 709.

Hudson, J., *et al.* 1987, *The Barrel Extensive Air Shower Telescope*, HGRO internal memo.

Hutchings, J.B., *et al.* 1985 *Ap.J.*, **292**, 670.

Jackson, J.D. 1975, Classical Electrodynamics, Second Edition, John Wiley and Sons.

Jelley, J.V. 1967, *Čerenkov Radiation from EAS. Elementary Particle and Cosmic Ray Physics*, **9**, 39.

Johnson, P. A. 1989, *Cosmic Gamma Rays, Neutrinos, and Related Astrophysics*, Kluwer Academic Publishers, 259.

Joss, P.C. *et al.* 1980, *Ap.J.*, **235**, 592.

Király, P. and Mészáros, P. 1988, *Ap.J.*, **333**, 719.

Kraushaar, W. *et al.* 1965, *Ap. J.*, **141**, 845.

Kwok, P.W. 1989, *Very High Energy Gamma Rays from the Crab Nebula and Pulsar*, Ph.D. Thesis, University of Arizona.

Lamb, R.C., *at al.* 1988, *Ap. J. Lett.*, **328**, L13.

Learned, J.G., 1981 *Internal memo*, HDC–81–10.

Learned, J.G., 1986 *Internal memo*, HGR–1–86.

Lewis, D.A. 1989, *Astron. Astrophys.*, **219**, 352.

Lewis, D.A. *et al.* 1991, Submitted to *Ap. J.*.

Li, P.P and Ma, Y.Q. 1983 *Ap J.*, **272**, 317.

Longair, M.S. 1981, em High Energy Astrophysics, Cambridge University Press.

Macomb, D.J. and Lamb, R.C. 1990, XXI ICRC, **2**,435.

Matthews, J. 1986 *Internal memo.*

Michel, F. Curtis, 1982, *Rev. of Mod. Phys.*, **54**, 1.

Nagase, *et al.* 1984, *Astron. Soc. Japan*, **36**, 667.

Nagase, F. 1989, *Astron. Soc. Japan*, **41**, 1.

Ögelman, H., *et al.* 1985, em Space Sci. Rev., **40**, 347.

Ostriker, J.P. and Gunn, J.E. 1969, *Ap.J.* **157**, 1395.

Ramana Murthy, P.V. and Wolfendale, A.W. 1986, *Gamma Ray Astronomy*, Cambridge University Press.

Rawat, H.S. *et al* 1990, XXI ICRC, **2**, 104.

Resvanis, L.K., *et al.* 1988, *Ap. J. Lett.*, **328**, L9.

Reynolds, P.T. *et al.* 1990, XXI ICRC, **2**, 99.

Ruderman, M.A. and Sutherland, P.G. ApJ, **196**, 51 1975.

Samorski, M. and Stamm, W. 1983, *Ap, J. Letters*, **268**, L17.

Schlickeiser, R. 1981 *Astron. Astrophys.*, **94**, 57.

Sinha, S. *et al.* 1990, XXI ICRC, **2**, 126.

Slane, P. 1988, *A Search for Very High Energy Gamma Rays from Hercules X-1*, Ph.D. Thesis, University of Wisconsin.

Slane, P. and Fry, W.F. 1989 *Ap.J.* **342**, 1129.

Sombeck, M.V. 1982, *Handbook of Space Astronomy and Astrophysics*, Cambridge University Press.

Sutantyo, W. *et al.* 1986, *Astron. Astrophys.*, **169**, 133.

Szentgyorgyi, A.H. 1986, em A search for Very High Energy Gamma Ray Emission from Cygnus X-3, Ph.D. Thesis, University of Wisconsin.

Tananbaum, et al. 1972 ApJ Letters, 174,L143.
Trümper, J., em et al. 1986, *Ap.J. Lett.*, **300**, L63.

Tumer, O.R., *et al.* 1990, XXI ICRC, **2**, 155.

Vishwanath, P.R. *et al.* 1989, *Ap.J.*, **342**, 389.

Wdowczyk, J. and Wolfendale, A.W. 1983 *Nature*, **305**, 609.